Liquid Argon Time Projection Chambers for Dark Matter and Neutrino Experiments

Laura Manenti

A Dissertation
Presented to the Faculty
of University College London
in Candidacy for the Degree
of Doctor of Philosophy

Recommended for Acceptance
by the Department of
Physics and Astronomy
Adviser: Dr. Chamkaur Ghag

April 2016

Declaration

I, Laura Manenti confirm that the work presented in this thesis is my own. Where information has been derived from other sources, I confirm that this has been indicated in the thesis.

Abstract

This thesis illustrates the contribution of the author to experiments using liquid argon Time Projection Chambers (LAr TPCs), a technology already widely used, that is becoming the dominating detection technique in dark matter (DM) and neutrino searches.

The results of the SCENE experiment, a dual-phase LAr TPC exposed to a low- energy pulsed narrowband neutron beam, are reported. These comprise the scintillation efficiency, $\mathcal{L}_{\text{eff}}$, and the ionisation yield, $\mathcal{Q}_y$, of nuclear recoils in LAr. While previous measurements only included $\mathcal{L}_{\text{eff}}$ at zero electric field, SCENE measured $\mathcal{L}_{\text{eff},\,^{83\text{m}}\text{Kr}}$ ($\mathcal{L}_{\text{eff}}$ relative to $^{83\text{m}}$Kr) in the drift field range 0–970 V/cm for energies between 10.3 and 57.3 keV. $\mathcal{Q}_y$ was also measured by SCENE with unprecedented precision and for a wide range of low-energy nuclear recoils, namely 16.9–57.3 keV, between 96.5 and 486 V/cm. The data collected are not only valuable to the DM field, but more in general to the design and calibration of any LAr TPC which exploits scintillation and ionisation signals of nuclear recoils in liquid argon.

The description of the liquid argon test facility constructed at UCL, named "LARA", is also reported. The first measurement performed with LARA has been the scintillation quenching for electron recoils in LAr, S_e. For the purpose, a TPC and a cryogenic PMT have been designed and built by the author. The measurement of S_e has established correct electric field operation of the TPC in the chamber. The LARA test stand has also been used in the context of dark matter R&D, for testing a novel cold high-voltage feedthrough design, with a focus on the LZ experiment in particular. The research progressed designs for novel cold feedthroughs, which so far have proved to satisfy the critical vacuum sealing aspect of the feedthrough. This opens up gains for noble gas TPCs in terms of low background and compact constructions that could greatly simplify HV delivery in future experiments.

To my parents.

Acknowledgements

My deepest thanks goes to my supervisor Dr. Chamkaur Ghag, who first offered me the possibility of embarking on this PhD. I could not have dreamed for a better supervisor, both from an academic point of view and a personal one. His support was fundamental throughout these three years and a half. From him I learned how to responsibly and independently manage my work, and become, as he has recently told me, a proper "scientist".

I am extremely grateful to my friend and former colleague Dr. Lea Reichhart who thaught me how to run a lab and "do hardware". Thanks for always demanding so much from me, you have definitely been the best colleague to work with.

I would like to greatly thank the SCENE collaboration, especially as this was the experiment that marked my first public scientific contribution.

I thank my colleague Dr. Anna Holin, for providing funds and help for the LAr system; the MAPs workshop, for constructing all the custom-made parts of the detector; and Mr. Derek Attree, for his help and precious advise when building the LARA setup. I equally thank all the colleagues of the HEP group, in particular Dr. Samer Kilani for his support in designing the PMT circuit board. Together with Matthew Warren, they have thaught me all that I know about electronics. Thanks to Prof. David Waters for the early PMT calibrations and for the good advice when coming to the lab. Thanks also to Dr. Andreas Korn for the support in the lab when needed.

I thank Sally Shaw for teaching me her "secret" GEANT4 tips and sharing with me her expertise, which has made my MC simulation work a lot easier.

Thanks to the LZ collaboration, in particular to Dr. James Dobson for the ICP-MS sessions and for always keeping me safe from hazards in the lab!

Thanks to all my PhD colleagues, in particular to Maciej Pfutzner, who spent time with me discussing the results of my analysis and was always there when I needed a favour (that being handing in documents for the thesis submission or simply some good company in the lab); to Xin, for showing me how to use the 3D printer and teaching me to always "have fun".

Thanks to Prof. Ruben Saakyan for sharing with me his expertise on photomultiplier tubes and his precious help in the lab. I would also like to thank him as my examiner along with Dr. Simon Peeters. Thanks for the discussion during the viva and the corrections to my thesis, which have proved extremely useful.

Last but not list, I would like to thank all of my family: my husband Alberto for his support and love during these years and my son Marco for came into being and teaching me what time management and sacrifice mean, especially when you are a

working mother.

The last thanks goes to my “native” family: to my brother Riccardo for being such an inspiring physicist, and to my parents, Marco and Lina, who have always believed in my potential since I was a child and to whom this work is dedicated.

Contents

List of figures

List of tables

Preface

In recent years noble gas Time Projection Chambers (TPCs) have attracted increasing attention, showing their potential in both dark matter and neutrino searches. The next generation of direct dark matter detectors will see the presence of two-phase liquid xenon (LXe) TPCs, while the next generation of accelerator-based long-baseline neutrino oscillation experiments will employ single- or dual-phase liquid argon (LAr) TPCs.

The present thesis focuses on argon TPCs and is an account of three years of work conducted on these detectors, on which, step-by-step, I gained knowledge and expertise thanks to the participation to experiments with international collaborations, as well as the hardware and software work conducted "in-house" at University College London.

The thesis is organised as follows. In Chapter 1, I give an introduction to the dark matter problem and outline the key points of neutrino oscillations, hereby providing the reader with the context in which liquified noble gas TPCs have developed. I then explain their operating principles by referring to completed, current and near future experiments, while showing the motivations for which LXe/LAr TPCs will be able to address future detection challenges, and become leading technologies in the dark matter and neutrino sector.

In Chapter 2, I report on the measurement of nuclear scintillation yield, $\mathcal{L}_{\text{eff}}$, and ionisation yield, $\mathcal{Q}_y$, for low-energy nuclear recoils in LAr with the SCENE experiment, to which I contributed with data acquisition and the validation of the pulse finder algorithm. SCENE's data are of fundamental importance to design experiments and calibrate nuclear recoils signals in dual-phase LAr TPCs. As previous measurements of $\mathcal{L}_{\text{eff}}$ were only available at zero field, while no measurement of $\mathcal{Q}_y$ was available for nuclear recoils at low-energy, SCENE was designed to fill these gaps. The analysis and results here presented are summarised in two papers published in Physics Review D, to which several authors have contributed.

In Chapter 3, I describe the LAr R&D test stand, named "LARA", built within the High Energy Physics group at UCL principally to facilitate tests of novel detector technologies and readouts for dark matter and neutrino physics. In the same chapter I also report on the design and construction of the TPC employed in LARA, which I personally carried out. In Chapter 5, I present the first measurement of such TPC,

whose purpose was the validation of the TPC operation and stability: the quenching of LAr scintillation for electron recoils when a drift field is applied, S_e. I describe the detector simulation performed using the GEANT4 Monte Carlo framework and the data analysis carried out using LArView, a software package I developed to enable efficient data reduction and analysis, whose details are given in Chapter 4.

Finally, in Chapter 6, I present the R&D research to investigate a novel cold high-voltage vacuum feedthrough design, whose prototype has been tested in LARA. Here, I contributed to the conductive coatings studies and sealing tests at room and cryogenic temperatures of the first prototype. I also played a major role in the argon liquefaction during the cryogenic test of the second prototype.

1
Liquified noble gas detectors

This chapter is divided into two main sections, corresponding to the two research fields that mostly use liquified noble gas detectors: dark matter and neutrino physics. In the first section, I introduce the reader to the dark matter (DM) problem and cover current DM detection techniques and experiments, with special focus on noble argon Time Projection Chambers (TPCs). In the second section, I cover questions that have remained unanswered in neutrino physics and present how large liquid argon TPCs can address detection challenges and become one of the leading techniques in the next decade of neutrino experiments.

1.1 LXe TPCs and LAr TPCs in DM detection

1.1.1 The dark matter mystery

We now know with remarkable precision that 85% of the matter that pervades our universe does not emit nor absorb electromagnetic radiation, yet, the nature of this "dark matter" (DM) is still to be discovered. The first hints for DM existence can be traced back in the '30s, with Oort in 1932 and Zwicky in 1933, but the problem of missing mass was not given much attention by the astronomical community until the '70s. By then, several 21-cm hydrogen line (Babcock, 1939; Oort, 1940; van de Hulst *et al.*, 1954; van de Hulst *et al.*, 1957; Schwarzschild, 1954; Roberts, 1965; Burbidge *et al.*, 1959; Rubin and Ford, 1970) and radio (Roberts and Rots, 1973) studies had been conducted to investigate rotation curves of galaxies. All works consistently found that the luminous rotational velocity remained constant with increasing distance from the galactic centre (see Fig. 1.1 from the work of van Albada *et al.* in 1985). This was in contradiction with the rotation speed expected by Newtonian dynamics, which predicts the velocity to be decreasing inversely as square root of the distance to the centre. To reconcile the observations with Newton's theory, the presence of a dark matter halo around the galaxies was hypothesised.

An attempt to interpret these observations without the aid of DM was first proposed in 1987 by Milgrom, through his Modified Newtonian Dynamics theory (MOND).

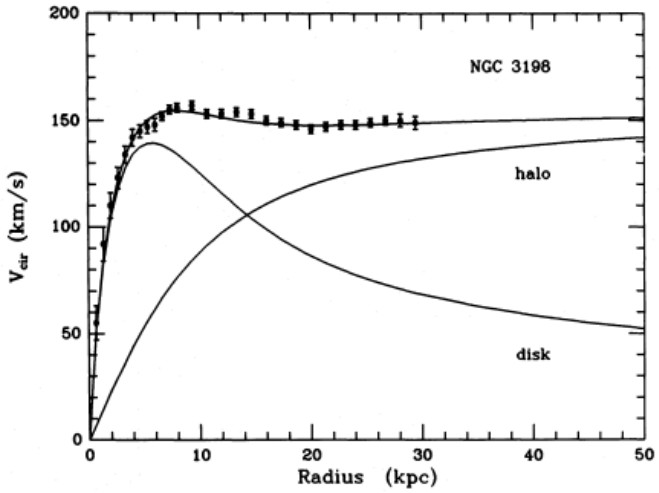

Fig. 1.1: Rotation curve of spiral galaxy NGC-3198. The dark matter halo may account for the observed rotational velocity of the the disk (van Albada *et al.*, 1985).

Although MOND is able to predict galactic dynamic studies, it cannot offer a satisfying explanation for gravitational lensing effects, among which the study of the "Bullet Cluster" (Clowe *et al.*, 2006) is surely the most compelling, and still needs the presence of some "baryonic dark matter" or neutrinos to fully account for gravitational lensing data.

So far, we have only presented observational evidences for DM, but there are also strong cosmological motivations, perhaps even more important, that support its existence. In the mid 1970s, redshift data covering all bright galaxies in the sky showed that galaxies were not uniformly distributed, but instead formed filaments and that the space between these filaments was practically empty. Most generally, we can say that structures in the universe have formed by gravitational attraction and must have started by small fluctuations of the density of matter (Einasto, 2010). If the luminous mass were the major contributor to the mass density of the universe, gravitational clustering could only have started at the end of recombination (nearly 380,000 years after the Big Bang), when radiation and baryonic matter decoupled and the universe became transparent.

The anisotropies of the emission coming from this epoch, which we now detect as a cosmic microwave background (CMB), were first measured by the Cosmic Background Explorer (COBE) satellite, launched in 1989. COBE found that the rms sky variation was a few μK, i.e. the CMB was uniform to 1 part per 10^5 (Smoot *et al.*, 1992).

Such small fluctuations, arisen from density perturbations in the baryon-photon fluid, cannot alone have accounted for the seeds of structure formation, i.e. the universe as we see it today would not have had the time to form if we solely assume the existence of a primordial baryon-photon fluid. Instead, if we suppose the presence of non-baryonic, massive particles that do not interact electromagnetically (dark matter), structure formation could have started thanks to these exotic particles prior to recombination, when the universe was still opaque (Jungman *et al.*, 1996). Neutrinos were firstly suggested as possible candidates, but they were soon ruled out, as they move too rapidly (compared to the speed of light) to have had the time to settle down and form "small" scale structures, such as galaxies and clusters of galaxies. In the mid '70s the first cosmological N-body simulations were carried out, featuring cold particles (i.e. moving slowly compared to the speed of light), and showed that a Cold Dark Matter (CMD) dominated universe would have led to the formation of the present cosmic web.

As of now, the most comprehensive description of the universe is given by the standard cosmological model, also known as ΛCDM. Λ refers to Einstein's cosmological constant, while CDM stands for Cold Dark Matter. The underpinning point of the model is the assumption that the universe is both isotropic and homogenous on the large-scale. This is also known as the Copernican principle and leads to the Friedmann-Lemaitre-Robertson-Walker metric (FLRW metric). Friedmann's equations are the set of equations that solve Einstein field equations ($G_{\mu\nu}+\Lambda g_{\mu\nu} = 4\pi G T_{\mu\nu}$, with $G_{\mu\nu}$ being the Einstein tensor, $g_{\mu\nu}$ the metric tensor, and $T_{\mu\nu}$ the energy-momentum tensor) assuming the FLRW metric and that govern the expansion of the universe. These are:

$$\frac{\ddot{a}}{a} = -\frac{4\pi G}{3}(\rho_m + 3p) + \frac{\Lambda}{3} \tag{1.1}$$

and

$$H^2 \equiv \left(\frac{\dot{a}}{a}\right)^2 = \frac{8\pi G}{3}\rho_m - \frac{k}{a^2} + \frac{\Lambda}{3} \tag{1.2}$$

where G is the gravitational constant, ρ_m is the universe energy-mass density, and p is the universe pressure. The function $a(t)$ (with $\dot{a}$ and $\ddot{a}$ being the first and the second derivative, respectively) is known as the scale factor, and it tells us "how big" the space-like hyper-surface of the universe is at time t. The ratio $\dot{a}/a$ is the so-called Hubble parameter H, which measurable value at the present epoch t_0 is denoted H_0. The last term, $\Lambda/3$, comes by introducing the cosmological constant Λ in Einstein's equations and describes vacuum energy. This is called dark energy and acts as a repulsive force (conversely to dark matter that is attractive) causing an expansion of space at an

increasing rate. k represents the curvature parameter of space-time, taking the value 0, +1 or −1 for a flat, closed or open universe, respectively. Equation (1.2) says that three competing terms drive the universal expansion: a matter term, a cosmological constant term, and a curvature term (Carroll *et al.*, 1992). It is useful to assign symbols to each fractional contribution at the present epoch. We define:

$$\begin{aligned} \Omega_m &\equiv \rho_m/\rho_c = \frac{8\pi G}{3H^2}\rho_m \\ \Omega_\Lambda &\equiv \frac{\Lambda}{3H^2} \\ \Omega_K &\equiv -\frac{k}{a^2H^2} \end{aligned} \tag{1.3}$$

where $\rho_c = 3H^2/8\pi G$. This quantity is called critical density as it is the density the universe would have if it were flat and the cosmological parameter Λ were zero (set $\Lambda = 0$ and $k = 0$ in eqn 1.2). From eqn (1.2) it follows that:

$$\Omega_m + \Omega_\Lambda + \Omega_K = 1 \tag{1.4}$$

It is sometimes convenient to write eqn (1.4) as:

$$\Omega_m + \Omega_\Lambda = 1 - \Omega_k \equiv \Omega \tag{1.5}$$

As such, the sign of k is determined by whether Ω, also called cosmological parameter, is less than, equal to, or greater than 1:

$$\begin{aligned} \Omega < 1 \quad &\leftrightarrow \quad k = -1 \quad \leftrightarrow \quad \text{open} \\ \Omega = 1 \quad &\leftrightarrow \quad k = 0 \quad \leftrightarrow \quad \text{flat} \\ \Omega > 1 \quad &\leftrightarrow \quad k = +1 \quad \leftrightarrow \quad \text{closed} \end{aligned} \tag{1.6}$$

The smoothness of the CMB, measured by a number of independent experiments including QMAP, MAT/TOCO, Boomerang, Maxima, DASI, WMAP, and Plank, has showed that Ω is very close to 1, meaning the universe is spatially flat.

The latest Planck CMB power spectrum, giving the most precise measurement of Ω, is shown in Fig. 1.2. Small multipoles correspond to early times in the universe, while larger multipoles to more recent times. Bumps are "snapshots" of acoustic oscillations of primordial plasma at the moment of recombination. In the early universe over-dense regions were frozen, as their physical size was equal to or larger than the

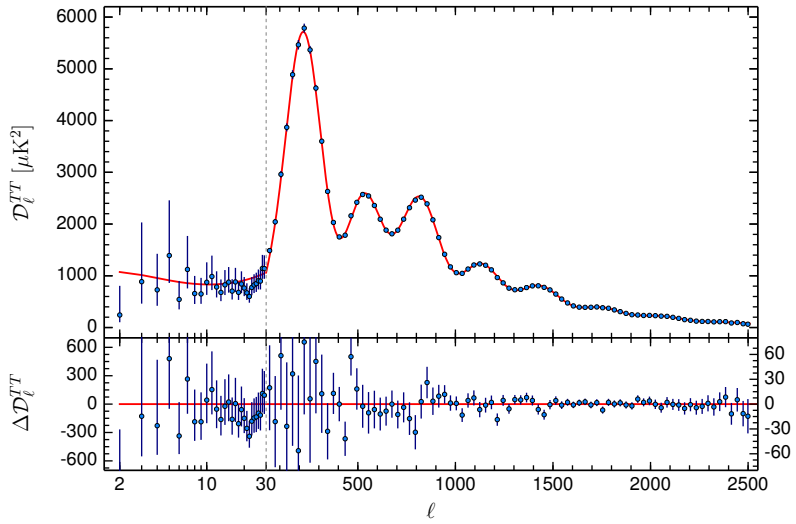

Fig. 1.2: CMB power spectrum as a function of angular scale from latest Planck measurements (Planck Collaboration, 2015).

Hubble radius. Because of the universe expanding, the size of these over-dense regions became smaller than the growing Hubble radius and they began to evolve. Under the gravitational force they collapsed, but, as temperature increased, they responded to radiative pressure by bouncing back. As they bounced back, they became less dense, because of relativistic particles trying their best to smooth out anisotropies and reach equilibrium. After expanding, they could have collapsed and bounced back again, and what one obtains is an acoustic wave. This process could have repeated until photon decoupling. The largest peak corresponds to the size of over-dense regions that had the chance to collapse and heat up, but not the chance to respond again. That is the largest achievable amount of fluctuation in temperature. The regions that bounced back and forth get progressively damped (this is called "Silk damping"). So, *a priori*, one expects a sequence of peaks, one smaller than the other, as they get damped and damped all over again. Originally DM and ordinary matter were over-dense in the same places. They both collapsed under the force of gravity and heated up, but while ordinary matter heated up and bounced back, DM kept collapsing, as it does not interact with radiation. At peaks that correspond to odd values of multipoles, ordinary and dark matter were in phase with each other and were working together. At the peaks that correspond to even values of multipoles, ordinary and DM became out of phase and began working against each other. As such, the effect of dark matter is to boost the third peak and shrink the second peak, so that, instead of a uniform

decrease, there is a dip from the first to the second, while the second and the third are almost at the same scale. This is the prediction in a model with DM in it and the fit to the data gives the constraint $\Omega_K = -0.052^{+0.049}_{-0.055}$, consistent with the inflationary prediction of a spatially-flat universe.

Thus, given nowadays the universe is flat (since Ω_k has a dependency on time, this has not always been the case):

$$\Omega_m + \Omega_\Lambda = 1 \tag{1.7}$$

The matter density Ω_m, accounting for a total of 0.3089 ± 0.0062 (Planck Collaboration, 2015) of the universe can be divided into two components: baryonic matter (Ω_b) and non-baryonic, dark matter (Ω_d). Planck CMB power spectra, in combination with lensing reconstruction, data from Baryonic Acoustic Oscillations (BAO) measurements, Joint Light-curve Analysis (JLA) of type Ia SuperNovae (SNe), and primordial nucleosynthesis, give constraints on these two constants, with $\Omega_b \simeq 4.9\%$ and $\Omega_d \simeq 26.5\%$ (Planck Collaboration, 2015), with the remaining $\sim$70% of the mass-energy content of the universe composed of dark energy. Accounting for an outstanding $\sim$85% of the mass of the universe, it is no surprise that the search for DM is a priority for both cosmology and particle physics.

It is fair mentioning that there have been numerous attempts, beyond MOND, to modify gravity in such a way to reproduce data. I present here only a few examples of alternatives to general relativity developed in recent years. In 2004, Bekenstein proposed a relativistic theory of gravity called Tensor-Vector-Scalar gravity (TeVeS), which reduces to MOND in the non-relativistic regime (for an introduction to TeVeS, I invite the reader to read Chapter 6 written by Bekenstein himself in Bertone 2010). TeVeS is derived from the least action principle by adding to the metric tensor field (the only one present through the curvature scalar in Einstein action) a scalar field and a vector field, the latter resulting in Lorentz invariance violation (Bekenstein, 2004). A year later, Skordis, Mota, Ferreira, and Boehm published their results on the evolution of the universe in such a theory (a "MONDian cosmology"), identifying its key properties and comparing it with the standard cosmology obtained in Einstein gravity (Skordis *et al.*, 2006). What they found is that to account for the observed accelerating expansion of the universe, dark energy and neutrinos had to be included. These are the same massive neutrinos (whose mass is still to be measured) MOND must invoke to account for the missing mass problem in clusters (Pointecouteau and Silk, 2005), given Big Bang Nucleosynthesis (BBN) and CMB measurements place upper limits on the amount of baryonic matter. The fit to WMAP data and other experiments using $\Omega_\Lambda = 0.78$, $\Omega_\nu = 0.17$, and $\Omega_b = 0.05$ agreed fairly well, except for

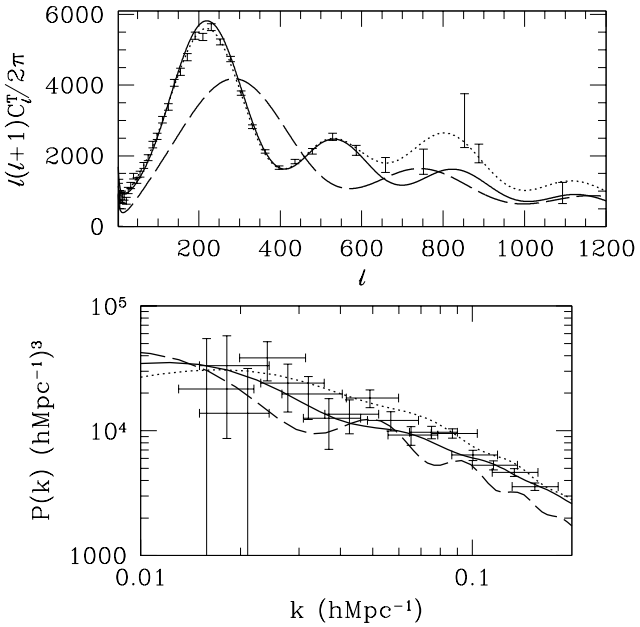

Fig. 1.3: TeVeS and the CMB power spectrum (top panel) and the power spectrum of baryon density (bottom panel) as taken from Skordis *et al.* 2006. The dashed line shows the prediction for a MOND universe with $\Omega_\Lambda = 0.95$ and $\Omega_b = 0.05$, the solid line is the for a MOND universe with $\Omega_\Lambda = 0.78$, $\Omega_b = 0.17$, and $\Omega_b = 0.05$, and the dotted line is for the ΛCDM model.

the third peak in the CMB power spectrum, for which data exceeded the model (see Fig. 1.3).

Another Modified Gravitation (MOG) theory has been proposed in 2005 by Moffat, who pursued an alternative relativistic gravity theory based on Scalar-Tensor-Vector Gravity (STVG). STVG is constructed on postulating the existence of a massive vector field ϕ_μ, coupled universally to matter. As a consequence, the theory has three constants: the ordinary gravitational constant G, the coupling constant ω, that determines the coupling strength between the ϕ_μ field and matter, and μ, which arises from considering the vector field massive. The theory then promotes G, μ, and ω to scalar fields, hereby allowing them to vary through space and time, such that the action from which the equations of motion are derived becomes:

$$S = S_{\text{Grav}} + S_\phi + S_S + S_M \tag{1.8}$$

where S_{Grav} is associated with G, S_ϕ originates from ϕ_μ, S_S arises from promoting ω and μ to scalar fields, and S_M is the matter action. STVG mainly differs from Bekenstein's theory in that the cosmological constant Λ can be set to zero, and neither dark matter nor dark energy are required (the extra added fields playing the role of dark energy). Moffat and Toth showed, in their works in 2007 and 2012, that STVG successfully predicts galaxy rotation curves, galaxy cluster masses and velocity dispersions, lensing, CMB temperature anisotropy, and supernova luminosity-distance observations without exotic dark matter. Although in Moffat and Toth's work the model successfully fitted 3 years of data taken by WMAP and data collected by the Boomerang experiment (see Fig. 1.4), to date no comparison with the latest Planck measurements has been published by the authors. Moffat has also recently published an article investigating the nature of gravitational waves in the STVG context in the light of the observation of gravitational waves from a binary black hole merger by the LIGO collaboration (LIGO Collaboration, 2016).

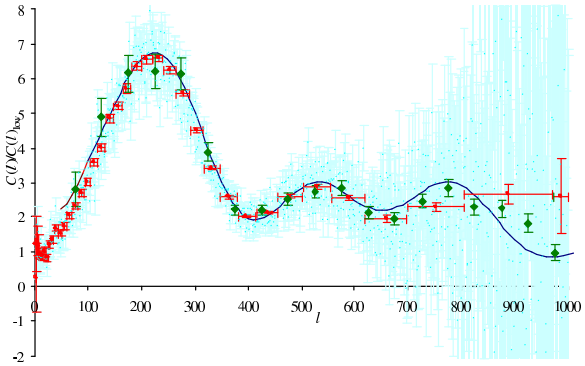

Fig. 1.4: MOG and the CMB power spectrum as taken from Moffat and Toth 2012. Fit (blue solid line) to WMAP 3-year data set (light blue) and Boomerang experiment (green) is achieved using $\Omega_m = 0.3$, $\Omega_b = 0.035$, $H_0 = 71\,\text{km/s/Mpc}$. In red the binned averages with horizontal and vertical error bars provided by the WMAP project.

Despite dark matter not being included in MOG theories, adding new fields, each propagating freely and independently through space, subtly means for these extra degrees of freedom to be sourcing the curvature of space time (i.e. Einstein's tensor) in *ad hoc* points... which is precisely what is believed dark matter does!

1.1.2 WIMPs properties and the "WIMP miracle"

The two most favourable candidates for DM are axions, motivated by a the Peccei-Quinn solution to the strong CP-violation problem (Peccei, 2008), and a general class of Weakly[1] Interacting Massive Particles (WIMPs), which are predicted by supersymmetry (or other) extensions of the standard model (Jungman *et al.*, 1996).

Axions detection relies on the prediction that axions may be converted to photons by passing through a cavity immersed in a strong magnetic field. Several experiments are currently being carried out and stringent exclusion limits have been placed on their photon coupling. Since a review on these particles is not necessary to contextualise the work of this thesis, I refer the reader to the other excellent sources on the theory of axions, such as a paper by Peccei from 2008 and—for those interested in the curious "pooltable analogy" to axions—the work of Sikivie from 1996, as well as other articles which report on the most up-to-date results of axions experiments, such as Olive *et al.* 2014, CAST Collaboration 2015, Ballou *et al.* 2015, Graham *et al.* 2016.

Let us now turn our attention to WIMPs and go through the DM properties that WIMPs must satisfy to be good DM candidates. First of all, as we have already seen earlier, DM must be cold to allow for filamentary structure formation in the universe. Secondly, as DM has not been observed to emit, reflect nor absorb light of any frequency, dark matter particles must either have a small enough electromagnetic coupling, i.e. they could be neutral, or be very heavy. From this a third property follows: DM must be very nearly dissipationless, i.e. it cannot cool down by radiating energy (i.e. photons), and, as a consequence, instead of collapsing to make galaxies, it gives rise to halos. Fourthly, DM must be collisionless, meaning it passes through itself and expands until it reaches virial equilibrium. This results in DM halos shaped as triaxial ellipsoids (Meszaros, 2010; Buote *et al.*, 2002; Schneider *et al.*, 2012) and explains what is observed in the Bullet Cluster, where the DM of the two colliding galaxies passed through each other without (or little) interaction. Finally, DM needs to be stable on time scale longer than the age of the universe, or it would have decayed already and we would not be able to see its effects.

Supposing this new type of dark matter particles, WIMPs, exist and they can annihilate with their own anti-particle, let us investigate their cosmological evolution. After inflation, WIMPs were in thermal and chemical equilibrium, with thermal equilibrium maintained by the elastic scatterings with the hot bath of Standard Model particles,

[1] It is worth noting that *a priori* the term "weakly" does not specifically refer to the electroweak force, but to the fact that WIMPs effects are mainly observable through their gravitational interaction, as they barely interact with ordinary matter

and chemical equilibrium maintained by the detailed balance between WIMP production and annihilation (Bringmann and Hofmann, 2007). As the universe expanded, the temperature decreased. When T approached the WIMP mass, $T \sim m_\chi$, the detailed balance was broken, with annihilation rates exceeding creation rates. As the temperature dropped below the WIMP mass, $T < m_\chi$, the WIMP co-moving density (i.e. ignoring universe expansion) declined exponentially as $\propto e^{-m_\chi/T}$, because of self-annihilation. Since the universe expanded (i.e. the scale factor a increased), the WIMP density was also diluted and, consequently, self-annihilation took place at a lower rate. For some $T \ll m_\chi$, the WIMP self-interaction rate $\Gamma_{\chi\bar{\chi}}$ dropped below the Hubble expansion rate H and chemical equilibrium was completely disrupted (if we define $x \equiv m_\chi/T$, we find that the WIMP abundance deviates significantly from the equilibrium abundance n_{eq}, defined at $x = 1$, when $x \simeq 10$). The temperature at which this happened is called chemical decoupling or freeze-out temperature $T_{\rm fo}$:

$$\Gamma_{\chi\bar{\chi}}(T_{\rm fo}) = H(T_{\rm fo}) \tag{1.9}$$

At this point, WIMPs were so rare that they ceased to annihilate. As the universe continued to expand, the WIMP density decreased, but its co-moving density remained constant, leaving behind a "thermal relic", as shown in Fig. 1.5.

It is interesting to calculate the current cosmological WIMP abundance as the ratio of the current WIMP density, also called cosmological relic density, over the critical density. The result varies depending on whether the particle is relativistic or non-relativistic. We now consider the latter. The left hand side of eqn (1.9) can be rewritten as:

$$\Gamma_{\chi\bar{\chi}}(T_{\rm fo}) \simeq \langle\sigma v\rangle\, n_{\rm fo} \tag{1.10}$$

where $\langle\sigma v\rangle$ is the averaged cross section times the WIMP velocity and $n_{\rm fo}$ is the WIMP number density at freeze-out. In the NR hypothesis (i.e. $m_\chi > T_{\rm fo}$), $n_{\rm fo}$ is given by:

$$n_{\rm fo} \simeq (m_\chi T_{\rm fo})^{3/2}\, e^{-m_\chi/T_{\rm fo}} \tag{1.11}$$

and the right hand side of equation (1.10) becomes:

$$\Gamma_{\chi\bar{\chi}}(T_{\rm fo}) \simeq \langle\sigma v\rangle\, (m_\chi T_{\rm fo})^{3/2}\, e^{-m_\chi/T_{\rm fo}} \tag{1.12}$$

Recalling from eqn (1.3) the relation between the total energy density of the universe and the Hubble parameter $H = \sqrt{8\pi G\rho/3}$, and assuming a radiation dominated universe at freeze-out ($\rho \sim T^4$), we may rewrite the right side of eqn (1.9) as:

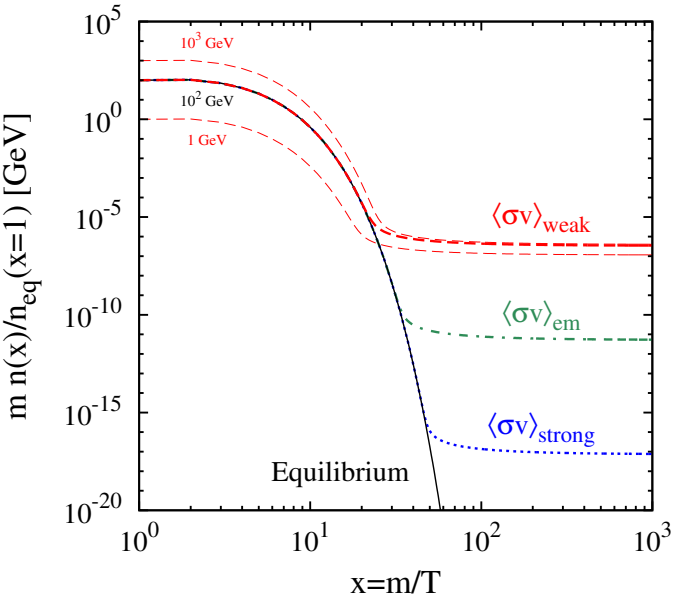

Fig. 1.5: Evolution of the cosmological co-moving (i.e. taking into account the universe expansion) WIMP density as a function of $x = m_\chi/T$. The curves show the WIMP mass density, normalised to the initial equilibrium number density at $T \simeq m_\chi$, for different choices of self-interaction cross sections, $\langle\sigma v\rangle$, and WIMP masses. For a WIMP mass of 100 GeV, results are shown in dashed red for weak interactions, $\langle\sigma v\rangle = 2\times10^{-26}\,\mathrm{cm^3 s^{-1}}$, in dot-dashed green for electromagnetic interactions, $\langle\sigma v\rangle = 2\times10^{-21}\,\mathrm{cm^3 s^{-1}}$, and in dot blue for string interactions, $\langle\sigma v\rangle = 2\times10^{-25}\,\mathrm{cm^3 s^{-1}}$. For the weak cross section, solutions for a WIMP mass of 1 GeV and 1 TeV are also shown. The black solid line represents the WIMP evolution if chemical equilibrium were not disrupted at the freeze-out temperature. This figure is taken from Steigman *et al.* 2012, and it is an updated version of the historical figure that the same author made in 1979.

$$H(T_{\rm fo}) \simeq \frac{T_{\rm fo}^2}{M_P} \tag{1.13}$$

where M_P is the Plank mass $M_P = \sqrt{1/G} \simeq 10^{19}\,\mathrm{GeV}$. By combining eqns (1.10) and (1.13), we obtain an expression for $n_{\rm fo}$:

$$n_{\rm fo} = \frac{T_{\rm fo}^2}{M_P\,\langle\sigma v\rangle} \tag{1.14}$$

By looking at eqns (1.13) and (1.12), we see that the crossing of the two terms at decoupling mostly depends on the exponential factor, $e^{-m/T_{\rm fo}}$, and that such crossing

will happen when the argument of the exponential is not too small nor too large, i.e. $m_\chi \simeq T_{\rm fo}$ (Gelmini, 2015). Thus, at $T \simeq T_{\rm fo}$ eqn (1.14) becomes:

$$n_{\rm fo} \sim T_{\rm fo}^3 \tag{1.15}$$

After chemical decoupling, WIMP thermal equilibrium is still preserved by elastic scattering processes with the bath of SM particles. Since the target density for WIMP scattering is given by the number density of relativistic SM particles, WIMP number density decreases as T^3 (Bringmann and Hofmann, 2007). Combining this result with eqn (1.15) leads to:

$$n(T \lesssim T_{\rm fo}) \sim n_{\rm fo} \frac{T^3}{T_{\rm fo}^3} \tag{1.16}$$

We can now write an expression for the current cosmological abundance of WIMPs Ω_χ, using eqns (1.16) and (1.14):

$$\begin{aligned} \Omega_\chi \simeq \frac{\rho_{0\chi}}{\rho_c} &= \frac{m_\chi n_{0\chi}}{\rho_c} \\ &= \frac{m_\chi}{\rho_c} \frac{n_{\rm fo}\, T_0^3}{T_{\rm fo}^3} \\ &= \frac{m_\chi}{\rho_c} \frac{T_0^3}{T_{\rm fo}\, M_P \langle \sigma v \rangle} \\ &= \frac{x_{\rm fo}\, T_0^3}{\rho_c M_P \langle \sigma v \rangle} \end{aligned} \tag{1.17}$$

where $x_{\rm fo} = m_\chi / T_{\rm fo}$ is the ratio that appears in the Boltzmann exponential factor and v is the WIMP velocity at freeze-out, which, in the non-relativistic limit, is given by:

$$v = (3kT_{\rm fo}/m_\chi)^{1/2} \tag{1.18}$$

and is equal to some appreciable fraction of the speed of light. The freeze-out ratio, $x_{\rm fo}$, is completely set by the cross section of the WIMP annihilation rate, the WIMP velocity at freeze-out, the WIMP mass m_χ and M_P (see eqns 1.13 and 1.12). To a first approximation though, the result in eqn (1.17) is independent of the WIMP mass and fixed primarily by the cross section of the WIMP self-interaction (Kamionkowski, 1997). Curiously enough, by plugging the value of typical electroweak cross sections in eqn (1.17), one obtains the right order of magnitude of the observed DM density for WIMP masses in the GeV–TeV range, with $x_{\rm fo} \simeq 20$ (Gelmini, 2015). By varying slightly the cross section, while matching the same observed density, one obtains different values of m_χ. The fact that for electroweak interactions eqn (1.17) gives the

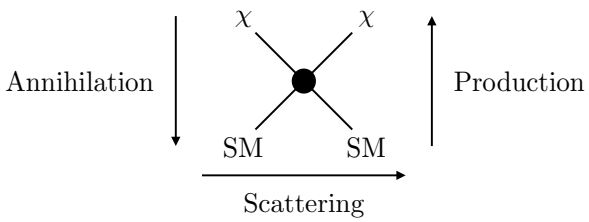

Fig. 1.6: Possible interactions of WIMPs, other than gravitational, with Standard Model particles.

right relic DM abundance is sometimes referred to as the "WIMP miracle" and is the motivation for considering WIMPs as a compelling DM candidate (for further details on how to derive the relic density see Bringmann and Hofmann 2007, Gelmini 2015, Kamionkowski 1997 and Feng 2010).

Because of spontaneous symmetry breaking in the Standard Model (SM), we do expect new particles arising at the weak scale from the supersymmetric SM or models with extra spacial dimensions. These theoretical frameworks, which developed independently of the DM issue, would greatly benefit of a WIMP discovery. This explains why WIMPs are the best motivated and most theoretically developed DM candidates.

1.1.3 WIMP detection methods

The possible non-gravitational WIMP interactions are shown in the diagram in Fig. 1.6 and are:

- **Annihilation**: $\chi + \bar{\chi} \rightarrow \mathrm{SM} + \mathrm{SM}$
  Assuming that WIMPs are their own anti-particle and may undergo pair annihilation into Standard Model particles, we expect to be able to detect their final products.
- **Production**: $\mathrm{SM} + \mathrm{SM} \rightarrow \chi + \bar{\chi} + (SM)$
  The collision of two SM particles may produce a pair of WIMPs as well as other SM products. Such reactions may be reproduced at particle colliders.
- **Scattering**: $\chi(\bar{\chi}) + \mathrm{SM} \rightarrow \chi(\bar{\chi}) + \mathrm{SM}$
  Experiments which rely on WIMPs from the galactic halo scattering off nuclei via weak interaction aim to detect their deposited energy in terrestrial detectors placed deep underground.

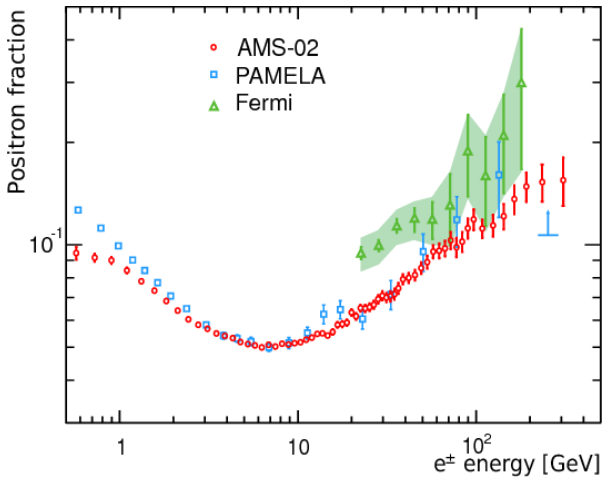

Fig. 1.7: Measurements of positron fraction in primary cosmic rays from PAMELA, Fermi-LAT, and AMS-02. An excess over the expected flux above 10 GeV may be observed. Plot taken from Corti 2014.

To each possible interaction mechanism, corresponds a different detection method, namely: indirect detection, collider detection, and direct detection, respectively. Below I present a brief overview of each class:

- **Indirect detection:** Indirect searches aim at detecting SM particles, such as photons, neutrinos, and cosmic rays (e.g. positrons, electrons, antiprotons, or deuterons), produced by WIMP annihilation processes in the galactic halo. Current experiments consist of ground-based (VERITAS, MAGIC, and HESS arrays of Imaging Atmospheric Čerenkov Telescopes [IACTs]) and space-based γ-rays telescopes (Fermi-LAT, PAMELA, and AMS-02), ground-based neutrino detectors placed under the sea (ANTARES) or ice in the South Pole (IceCube, previously AMANDA).
  Past experiments also included balloon detectors (HEAT, BESS, ATIC). The PAMELA experiment showed results on the positron abundance in the cosmic radiation for the energy range 1.5–100 GeV, which deviated significantly from predictions of positrons produced in interactions between cosmic-ray nuclei and interstellar matter ("secondary production") in the region above 10 GeV (PAMELA Collaboration, 2009). The Fermi-LAT and AMS-02 telescopes later confirmed this anomaly in 2012 and 2013, respectively. Figure 1.7 shows the experiments results. The origin of the excess in positron fraction at high energy is unknown and possibly points towards the existence of a new physical source of high energy electrons

and positron. Several interpretations have been suggested, including dark matter, but also more "ordinary" sources, such as pulsars and cosmic-rays interacting with giant molecular clouds (Fan *et al.*, 2010; Yin *et al.*, 2013; Kohri *et al.*, 2015).
To date cosmological neutrino experiments (e.g. IceCube) searching for self-annihilating dark matter in nearby galaxies and galaxy clusters have not observed an excess over the expected amount of SM products (Aartsen *et al.*, 2015).
In conclusion, as data from indirect experiments could be also explained within the SM framework, indirect searches have not offered conclusive evidences to claim a definitive discovery of DM.

- **Collider detection:** Evidence for WIMPs is also being searched for at the Large Hadron Collider (LHC) and before that at the Large Electron Positron collider (LEP). Particles created in p-p collisions are detected and reconstructed, and missing energy signatures from the escaping, undetected WIMP determined. There are three main classes of objects which can be reconstructed and are of interest for dark matter: missing transverse energy (MET), jets, and leptons. Any significant deviation from the expected Standard Model background could be an indication of dark matter. One drawback of hadron colliders is that they are relatively insensitive to dark matter that interacts only with leptons, and unable to distinguish missing momentum signals produced by a particle with lifetime ∼100 ns from one with lifetime $>10^{-17}$ s, as required for dark matter (Bauer *et al.*, 2015). So far, data have shown to be consistent with Standard Model expectations and new stringent limits have been set on the mass scale of dark matter candidates (ATLAS Collaboration, 2014).

- **Direct detection:** Direct searches of dark matter aim at detecting the signals produced by WIMPs from the galactic halo scattering off nuclei in underground detectors. This is the most straightforward methodology to verify the existence of DM and will be required for a definitive claim.
  Our Galaxy is believed to be embedded in a roughly spherical, isothermal halo of essentially static WIMPs. Because of the motion of the Solar System around the centre of the galaxy, the Earth should experience an apparent "WIMP wind". The velocity distribution of WIMPs derived within this framework, combined with the WIMP mass, defines the energy scale of WIMP scatterings. For a WIMP mass with cross sections from 10^{-40} to 10^{-50} cm^2, the kinetic energy of the scattered nuclei is found to be in the 1–100 keV range (Cushman *et al.*, 2013). Such low-energy nuclear recoils, together with very low expected rates—less than 1 event per 100 kg per day (Gelmini 2015)—require low-background, sensitive detectors, with

sufficient target mass. To help suppress background induced from cosmic-rays, experiments are located deep underground, in mines or tunnels under mountains. Direct detection prototypes have been constructed in recent years and their feasibility at larger scale has been assessed with currently-running (G1) experiments. The next generation (G2) of direct experiments will finally be capable of identifying WIMPs with a wide range of masses. The third-generation (G3) experiments will cover all the favoured WIMPs phase space and either confirm any discovery from G2 experiments with higher precision, given 100 times more sensitivity, or make a first discovery themselves, or, in the pessimistic scenario, rule out the favoured models for DM.

In the subsection below, I present in more details the methodology of direct detection, with particular focus on liquified noble gas detectors.

1.1.4 Direct detection

WIMP RATES AND CROSS SECTIONS

The underlying assumption for direct detection is that, albeit small, a probability exists for a WIMP from the local galactic halo to elastically scatter off a target nucleus in a terrestrial detector. The firsts to suggest such detection technique were Goodman and Witten in 1985. A WIMP signature would feature a single nuclear recoil, as opposed to neutrons, that are more likely to induce multiple scatterings in the detector, and to γ-rays and β-particles, which instead yield electron recoils.

The calculation of the event rate in direct WIMP detection depends on both the WIMP-matter interaction properties and on the characteristic of the dark matter galactic halo. The latter defines the WIMP velocity distribution and WIMP density, which are both necessary to calculate the WIMP flux. The simplest and most generally adopted galactic halo model is the so-called Standard Halo Model (SHM), which is compatible with a flat rotation curve (Donato *et al.*, 1998). The SHM assumes WIMPs are distributed as an isothermal sphere with an isotropic, Maxwellian velocity distribution and profile density r^{-2}, with r being the radial distance to the galactic centre (Drukier *et al.*, 1986). Other (more realistic) models assume non-spherically symmetric or flattened halo distributions, or dark matter rotating halos. Although the SHM leads to a divergent total mass and a cut-off at large radii needs to be introduced (Donato *et al.*, 1998), because of its simplicity and to allow comparison between results from different experiments, it is standard practice to adopt it for event rate and cross section calculations. I will now discuss the WIMP rate and cross section in such a simplified framework.

The differential rate for WIMP-nucleus elastic scattering, in units of events/kg/day/keV, can be expressed as (Lewin and Smith, 1996):

$$\frac{dR}{dE_r} = N_T \frac{\rho_\chi}{m_\chi} \int_{v_{\min}}^{v_{\max}} d^3\vec{v}\, f(\vec{v}) v \frac{d\sigma}{dE_r} \tag{1.19}$$

where E_r is the nuclear recoil energy, N_T is the number of target nuclei, ρ_χ is the WIMP density, m_χ is the WIMP mass, v ($\equiv |\vec{v}|$) and $f(\vec{v})$ are the WIMP velocity and velocity distribution function in the Earth frame respectively, and $d\sigma/dE_R$ is the differential cross section. In 2014, Read reported current efforts to measure the mean density of dark matter near the Sun, and showed that the Milky Way is consistent with having a spherical dark matter halo at 8 kpc from the centre of the galaxy (where our Solar System is) and a DM density of 0.2–0.56 GeV cm^{-3} (the value traditionally adopted is 0.3 GeV cm^{-3} as suggested by Lewin and Smith 1996). In the SHM, $f(\vec{v})$ follows the Maxwell-Boltzmann velocity distribution for an ideal gas at thermal equilibrium:

$$f(\vec{v}) = N \exp\left(-\frac{\langle E_{kin}\rangle}{k_B T}\right) = N \exp\left(-\frac{\langle m_\chi^2 v^2/2\rangle}{k_B T}\right) = N \exp\left(-\frac{3v^2}{2\sigma^2}\right) \tag{1.20}$$

where N is a normalisation constant and $\sigma \equiv \sqrt{\langle v^2\rangle} = \sqrt{3k_B T/m_\chi}$. Formally, in the SHM the density distribution extends to infinity and so does the velocity distribution. In reality, WIMPs with velocities larger than the escape velocity, $v_{\rm esc} = \sqrt{2\,|\Phi(\vec{r})|}$, are not bound to the galaxy by the gravitational potential (Green, 2012), and are free to escape. Practically this means that the velocity distribution goes to zero for speeds larger than the local escape speed, which, relative to Earth, was found to be $v_{\rm esc}(R_{\rm Sun}) = 544$ km/s, with $R_{\rm Sun} \simeq 8$ kpc being the Solar radius (Smith *et al.*, 2007). The $v_{\rm esc}$ constraint, equivalent to say that DM is cold, implies that all kinematic calculations are performed in the non-relativistic limit. Therefore the nuclear recoil energy transferred is given by (Drukier *et al.*, 1986):

$$E_r = \frac{\mu^2\,|\vec{v}|^2}{M_N}(1 - \cos\theta) \tag{1.21}$$

where θ is the WIMP scattering angle, M_N is the mass of the nucleus, and μ is the WIMP-nucleus reduced mass:

$$\mu = \frac{M_N\, m_\chi}{M_N + m_\chi} \tag{1.22}$$

From eqn (1.21) it is possible to derive the minimum WIMP velocity:

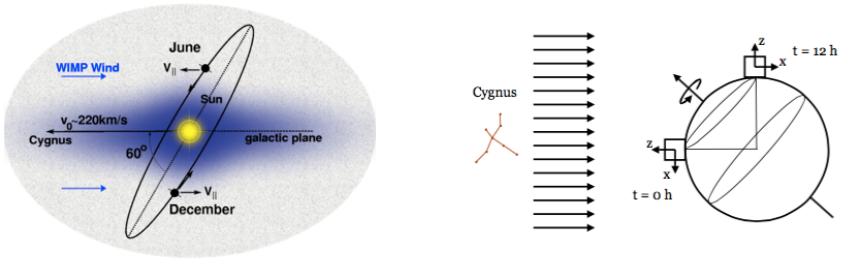

Fig. 1.8: As the Solar System moves through the galactic halo, we experience a "WIMP wind" coming from the Cygnus constellation (note that since it takes approximately 250 million years for our Solar System to complete an orbit around the galaxy, as such in a human life span the WIMP wind will always be coming from the Cygnus). Because the Earth rotates around the Sun, it adds or subtracts 15 km/s to the solar velocity, yielding a WIMP annual modulation. On top of this, the direction of the WIMP wind changes as the Earth rotates on its axis, leading to a daily modulation: initially the WIMPs appear to come overhead, while 12 hours later the wind has shifted to the horizon.

$$v_{\min} = \sqrt{\frac{M_N E_{\text{thr}}}{2\mu^2}} \tag{1.23}$$

where E_{thr} is the energy threshold specific to the detector.

The most probable WIMP velocity in our galactic neighbourhood is ~220 km/s (Dehnen and Binney, 1998), with annual modulation introduced by the Earth orbiting around the Sun and the Sun orbiting around the galactic centre. When the Earth's orbital velocity is parallel to the Sun's orbital velocity (summer), the Earth's adds roughly 10 km/s (10 km/s $= v_\oplus \cos\theta$, with $v_\oplus = 30$ km/s being the Earth's orbital velocity and $\theta = 69°$ being the angle between the Earth's axis and the galactic plane) to the solar speed. This boosts the WIMP speed distribution in the Earth's frame to higher speeds, leading to a smaller rate of low-energy recoils and an enhanced rate of high energy recoils. The expected fluctuation in rate is on the order of ±1% (Ahlen *et al.*, 2009). Although all DM detectors with sufficient target mass are sensitive to such annual variations, only DM detectors sensitive to the direction of arrival of the WIMP have the ability to observe a modulation in the recoil angle due to the daily rotation of the Earth. To date, DRIFT-II, a low pressure CS_2 gas TPC, is the only direction-sensitive WIMP detector operating underground. Although gas

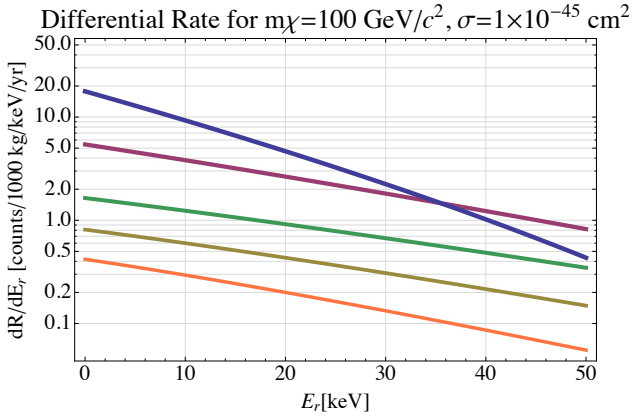

Fig. 1.9: Expected differential rate , dR/dE_r, as a function of nuclear recoil energy for 100 GeV WIMP mass assuming a spin-independent WIMP-nucleon cross section of $10^{-45}\,\mathrm{cm}^2$, shown for Xenon (blue), Germanium (purple), Argon (green), Silicon (brown), and Neon (orange) target. Figure taken from (Cushman *et al.*, 2013).

TPCs enable track reconstruction (due to the low density of the gas, ionising particles leave a reconstructable track), they have the big disadvantage of providing a low event rate. This explains why such technology still lacks behind liquid TPCs.

For a comprehensive review on directional dark matter detection see Ahlen *et al.* 2009. A picture representing annual and daily modulations, which can be used to isolate genuine WIMP signals, is shown in Fig. 1.8.

It is instructive to consider the limit of $v_{\mathrm{min}} \to 0$ (i.e. the limit of a detector stationary in the Galaxy) and $v_{\mathrm{esc}} \to \infty$, where eqn (1.19) may be written as (Lewin and Smith, 1996):

$$\frac{dR(0,\infty)}{dE_r} = \frac{R_0}{E_0 r} e^{-E_r/E_0 r} \tag{1.24}$$

where R_0 is the total event rate (in units of events/kg/day), r is a kinematic factor equal to $4M_N\, m_\chi/(M_N + m_\chi)^2$, and E_0 is the most probable kinetic energy of the incident WIMP (which, in turn, depends on the most probable WIMP velocity). It follows from eqn (1.24) that the differential energy spectrum of nuclear recoils is expected to be a featureless, smoothly decreasing exponential as recoil energy increases (Lewin and Smith, 1996). Figure 1.9 illustrates such behaviour for different target nuclei.

To obtain (1.24) we have implicitly assumed that the cross section in eqn (1.19) is a

constant ($\sigma \equiv \sigma_0$), neglecting any dependency on the recoil energy.[2] Such dependency is in reality non-zero and can be enclosed in the nuclear form factor, which takes into account the finite size of the nucleus and is dependent on nuclear radius and recoil energy. The nuclear form factor is different for spin-dependent (SD) and spin-independent (SI) interactions. The first involve a scalar coupling between the WIMP and the nucleus, while the second a coupling between the WIMP spin and the net nuclear spin. As such, the total cross section is the sum of both contributions (Baudis, 2014*a*):

$$\frac{d\sigma}{dE_r} \propto \sigma^0_{SI} F^2_{SI}(E_r) + \sigma^0_{SD} F^2_{SD}(E_r) \tag{1.25}$$

where $\sigma^0_{SI,SD}$ are the spin-independent and spin-dependent cross sections in the limit of zero momentum transfer (when the nucleus is seen as a point-like Coulomb source), $F^2_{SI,SD}(E_r)$ is the nuclear form factor as a function of the nuclear recoil energy E_r, and the subscripts SI and SD refer to spin-dependent and spin-independent couplings, respectively.

The spin-independent contribution is in general significantly larger than the spin-dependent one. In fact, as spin-independent scatterings tend to be coherent, receiving contributions from all the nucleons in the nucleus, the WIMP-nucleus cross section ($\sigma^0_{SI} F^2_{SI}$) is enhanced by the square of the target atomic mass, A^2. Although SI couplings are generally identical for protons and neutrons, in Isospin-Violating Dark Matter (IVDM) models the scattering amplitudes for protons and neutrons may interfere destructively, breaking the simple A^2 scaling (Feng *et al.*, 2011).

On the other hand, for spin-dependent scatterings, although the interaction with the nucleus is coherent, in the sense that scattering amplitudes are summed over nucleons (this is the same for the spin-independent case), the strength of the interaction vanishes for paired nucleons in the same energy state (Angle *et al.*, 2008). Thus, contributions come only from the unpaired nucleon—in the "single particle model"—or nucleons of the same type as the unpaired nucleon—in the "odd group model" (Engel *et al.*, 1992). For this reason, direct detection experiments are in general much more sensitive to spin-independent interactions than to spin-dependent interactions.

As an example, we analyse the case for argon (Ar) and xenon (Xe), the two leading noble gases for Time Projection Chambers. With 18 protons and 22 neutrons, Ar has a SI only cross section, while Xe, with 54 protons and 77 neutrons, is also sensitive to SD interactions. The effect on the event rate is illustrated in Fig. 1.10, which shows

[2] It must also be noted that since we have written eqn (1.19), we have not taken into account any of the following: the Earth motion around the Sun and its own axis, the experimental detection efficiency, instrumental resolution, and that the target may consist of more than one element.

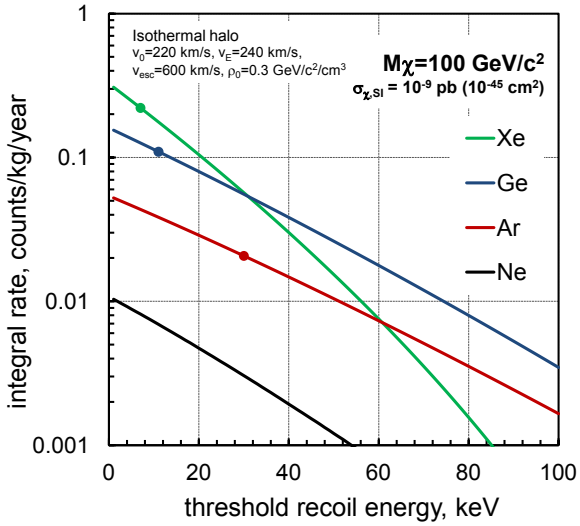

Fig. 1.10: Integral WIMP rate as a function of detector energy threshold for different target nuclei. Xenon is expected to have the largest interaction rate at low-energy thresholds.

the integrated rate as a function of threshold energy for different target nuclei. Although xenon is expected to have the largest interaction rate at low-energy thresholds (as predicted given the SI cross section dependency on A^2), the situation is reversed past 60 keV. This is due to the nuclear form factor, which decreases with transferred momentum much more rapidly for xenon than for argon (Chepel and Araújo, 2013). The SI form factor may be conveniently parametrised in terms of the product between the momentum transfer q and the nuclear radius r_n:

$$qr_n = \sqrt{2M_N E_r}\, r_n \tag{1.26}$$

where qr_n is a dimensionless quantity in natural units ($qr_n/\hbar$ gives qr_n for $\hbar = 1$). In the case of small transferred momentum ($0 < qr_n < 3$) the SD and SI form factors show falling behaviour with increasing momentum, taking approximately the following expression (Lewin and Smith, 1996):

$$F^2_{SI,SD}(qr_n) \propto e^{-\alpha(qr_n)^2} \tag{1.27}$$

where α is a constant. From eqn (1.26) and (1.27) it follows that for the same recoil energy the Xe form factor will be smaller than the Ar form factor. It should be empha-

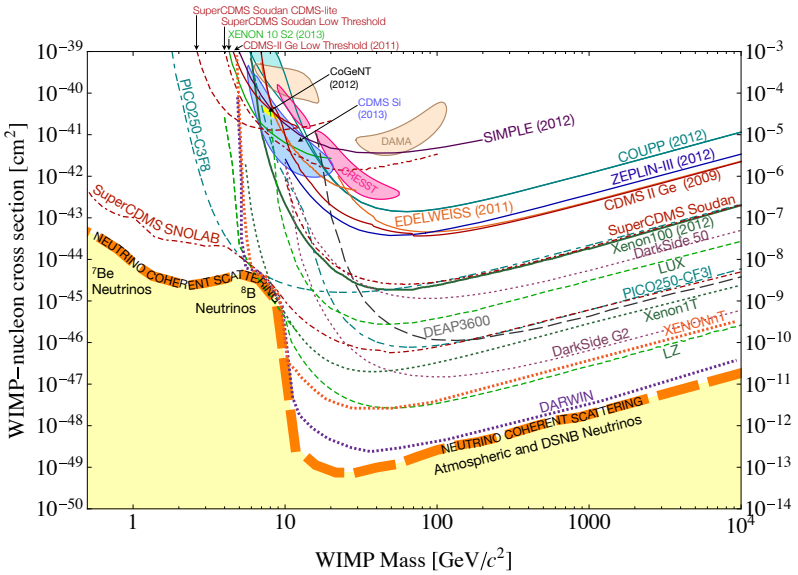

Fig. 1.11: Spin-independent WIMP-nucleon cross section limits as a function of WIMP mass for existing and future experiments. Solid lines represent existing exclusion limits, while dashed lines refer to projections of cross section limits. The figure is taken from Baudis 2014*b* and does not show the most up-to-date results from existing experiments. The latest spin-dependent and spin-independent WIMP-nucleon cross section limits are shown in Fig. 1.15 and 1.16, respectively.

sised that as the momentum transfer increases (though still in the elastic scattering regime) the coherence is lost, since the scattering amplitudes no longer add in phase, and eqn (1.27) is no longer valid. Recoil energy spectra of experiments exploiting different target nuclei may constrain the spin-dependent and -independent WIMP-nucleon couplings.

Finally, since we have seen that the galactic dark matter density and flux are approximately known, the limit on the measured total WIMP rate, which depends on the detector energy threshold (recall that $v_{\min}$ is a function of $E_{\rm thr}$), can be converted to a limit on the particle cross section as a function of the WIMP mass (Lewin and Smith, 1996), as can be seen in Fig. 1.11 (a detailed comment on this figure will be given later in the chapter).

Direct detection techniques

Given current WIMP-nucleon cross section limits as low as 10^{-45} pb (LUX Collaboration, 2016*b*), direct detection experiments face a number of non-trivial technical

challenges. To reach greater sensitivity they need to scale to larger masses (∼ton-scale), while retaining discrimination power against background, which generally falls in one of the following categories: surface α-particle radiation, β/γ radiation, cosmic ray-induced backgrounds (e.g. secondary electrons and neutrons from muons), electron recoils caused by neutrinos form the Sun or other galactic sources, and neutron radiation. Background from radioactivity can be reduced by choosing the most radiopure materials, while cosmic background can be partially diminished by locating the detectors deep underground, and further decreased by shielding the apparatus and by using veto instruments (e.g. a liquid scintillator tank surrounding the detector, so that, given WIMPs are supposed to interact via a single elastic scattering, events in coincidence in the veto and the main detector are rejected as background).

Direct detection experiments may be catalogued according to the types of signals produced when energy is deposited, namely: ionisation (secondary electrons), scintillation (photons), and heat (phonons). Figure 1.12 shows completed, current, and near-future experiments divided according to these three detection channel(s). Only

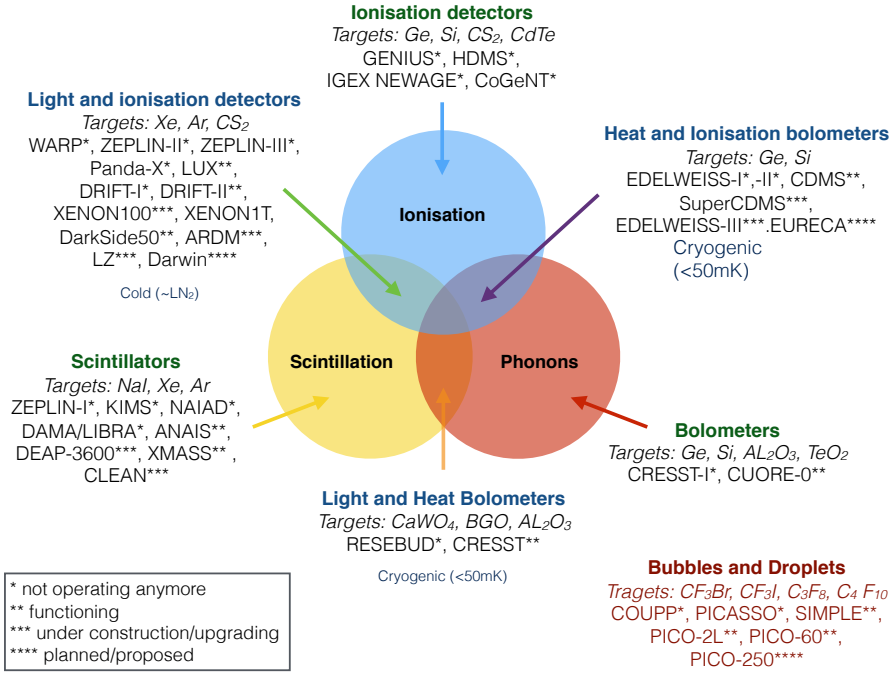

Fig. 1.12: Direct dark matter detection experiments organised by energy deposition channel(s) employed. Figure made by the author.

experiments that use bubbles and droplets to detect particles are organised separately in the right bottom corner of the figure. Many experiments employ simultaneous measurements of two signal channels to exploit different responses for electron and nuclear recoils, improving background rejection. The three most successful technologies employed to date in direct dark matter searches are cryogenic solid-state detectors, bubble chambers, and noble gas detectors:

- **Cryogenic solid-state detectors**: Cryogenic solid-state detectors aim to measure the recoil energy imparted through WIMP-nucleon collisions to target nuclei by employing sensitive phonon and ionisation detection equipment. EDELWEISS and SuperCDMS constitute an example of such methodology, both employing germanium crystals cooled to millikelvin temperatures. Contrary to liquified noble gases, for which the scintillation and ionisation yields for nuclear recoils are lower than for electronic recoils, for germanium crystals the fraction of energy deposited does not vary much with the type of incident particle. The heat quenching factor for nuclear recoils, defined as the ratio of the heat signals produced by nuclear and electron recoils of equal energy, was found to be $\sim 0.91 \pm 0.03$ for germanium recoil energies between 20 and 100 keV (EDELWEISS Collaboration, 2007). Therefore, excellent energy resolution even at low energies can be achieved. It is worth noting that among current experiments, SuperCDMS will be the most sensitive in the low-mass WIMP region ($<$6 GeV).
- **Bubble chambers**: Experiments such as PICASSO, COUPP, SIMPLE, PICO-2L, and PICO-60 use superheated droplet detectors to search for dark matter and are based on the concept of bubble chambers. Metastable, superheated droplets of fluorinated halocarbons, such as C_3F_8 or CF_3I, are dispersed in a water-based cross-linked polymer. Upon interaction with incoming radiation, droplets undergo a phase transition and are converted into bubbles. Bubbles get trapped in the polymer at the site of formation and, after expansion, collapse back into droplets. Bubbles are photographed by high resolution cameras at a rate of $\sim$50–100 frames per second and thanks to image reconstruction algorithms they can be identified and their 3D position determined (PICO Collaboration, 2016*a*). The liquid-to-vapour phase transition can be induced by nuclear recoils (following the interaction with neutrons or other particles) or by direct energy deposition (γ-rays, β- and α-particles). The number of bubbles is directly proportional to the energy deposited, but a minimal energy deposition is needed for bubble formation. This defines an energy threshold for the detector, which is usually well below 10 keV. Each bubble nucleation creates and acoustic shock wave, which can be recorded

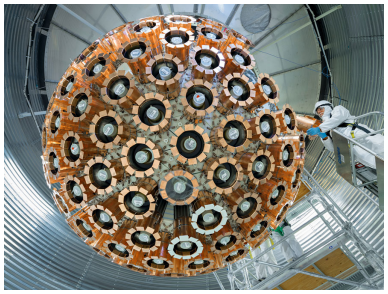

Fig. 1.13: DEAP-3600 during installation.

by piezoelectric transducers. The acoustic signal frequency spectrum differs for nuclear recoil- and radiation-induced bubbles and provides discrimination against background. Moreover, since the detector energy threshold depends on the linear energy transfer (LET) of the particle, as well as the chamber operating pressure and temperature, the detector can be set into a regime where it is mainly sensitive to nuclear recoils (PICASSO Collaboration, 2005). World-leading limits on the spin-dependent WIMP-proton cross-section that have been recently set by the PICO-2L and PICO-60 experiments are discussed below.

- **Liquid noble gas detectors**: Noble gas detectors, generally involving argon or xenon, exploit scintillation-only or scintillation accompanied by ionisation to detect particles. In the first case only the noble gas in its liquid form is employed (single-phase detectors), in the second case the gaseous phase is also used in addition (double-phase detectors).
  Noble elements are excellent detection media for a number of reasons: they scintillate when traversed by particles and are transparent to their own scintillation; when liquified they have a high enough density to serve as an effective WIMP target; ionisation charges (produced by electronic or nuclear recoils caused by the impinging particle) have great mobility in the liquid.
  The simplicity of a liquid-only based detector makes its construction relatively easier—at least compared to a double-phase detector, which involves handling of high electric fields. Examples of currently operating single-phase noble gas detectors are: DEAP-3600 and Mini-CLEAN, which exploit liquid argon, and XMASS, which operates with liquid xenon. CLEAN is yet to be constructed and is planned to operate with either argon or neon. DEAP-3600, shown in Fig. 1.13, Mini-CLEAN, and XMASS all consist of a central volume of LAr/LXe contained in a pressurised acrylic vessel surrounded by photomultiplier tubes (PMTs). To

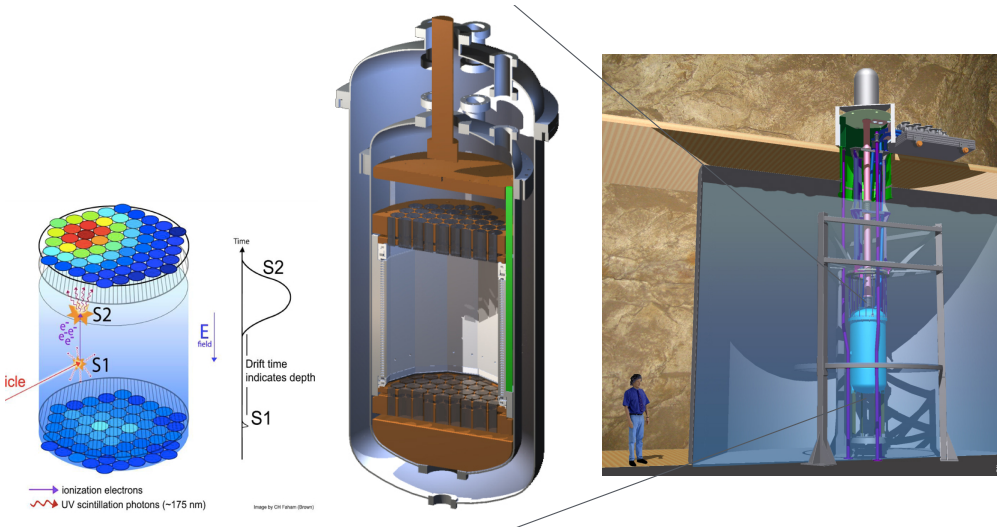

Fig. 1.14: Overview of the LUX detector system. Shown on the right are the water tank and the central cryostat. The PMTs of the muon-veto system are not shown. On the left, a zoomed-in cross-sectional view of the TPC and the cryostat, as well as the schematic of a particle interaction in the TPC (valid for any two-phase LAr/LXe detector) are shown. A particle impinging into the liquid will cause an electron recoil (ER) or a nuclear recoil (NR) in the medium. The recoiling electron/nucleus will emit scintillation light and electrons. These secondary electrons may be drifted upwards by means of an electric field and create an electroluminescence pulse (S2), after entering the gas region above the liquid level. The S1 and S2 signals are recorded with two arrays of PMTs, located below and above the active region of the detector. All figures are taken from LUX Collaboration 2013.

allow for precise vertex reconstruction and to maximise the light detection efficiency (i.e. ratio of photons detected over energy deposited), the full coverage over the 4π steradians of the detector should be aimed (usually a coverage $\sim$75% is achieved). One important advantage of LAr over LXe single-phase TPCs is that argon can also count on scintillation pulse shape as an additional background discrimination feature.

In noble gas double-phase Time Projection Chambers (TPCs), instead, the simultaneous detection of scintillation and ionisation signals allows for the event 3D position reconstruction without the need of covering the full area of the detector with PMTs. A two-phase TPC consists of a chamber filled with noble gas (xenon or argon) in its liquid and gaseous forms. A particle impinging into the liquid will cause an electron recoil (ER) or a nuclear recoil (NR) in the medium. The recoiling electron/nucleus will emit scintillation light (S1) and electrons. Whereas

in single-phase noble detectors only the photons are detected, in a double phase TPC ionisation electrons are drifted upwards by an electric drift field and, through an extraction field, they enter into the gas region where they generate secondary scintillation (S2), also called ionisation signal. Figure 1.14 shows schematically the detector system of LUX, a dual-phase xenon TPC operating at the Sanford Underground Research Facility (SURF) in South Dakota, and its operating principle, which is valid for any double-phase LXe/LAr TPC. In double-phase TPCs the ratio of energy deposition in scintillation and ionisation (S1/S2) allows for discrimination against electron recoils. As mentioned earlier, liquid argon TPCs also feature pulse shape discrimination between nuclear and electron recoils.
As noble gas double-phase TPCs have demonstrated the ability to scale to larger masses whilst retaining discrimination, they constitute the favoured technology to produce a first direct dark matter discovery.

If for no other reason than historical, it is worth spending a few words on scintillation crystal detectors. The DAMA/LIBRA experiment, employing 250 kg of iodide crystals activated with thallium NaI(Tl), is the only direct detection dark matter experiment to have strongly claimed the detection of a WIMP signal. The results obtained from a cumulative exposure of 1.17 ton × yr (equivalent to 13 annual cycles) by the former DAMA/NaI and by the more recent DAMA/LIBRA have showed evidence for a modulating signal with statistical significance of 8.9 σ, compatible with expectations of WIMPs from the galactic halo (Bernabei, 2010). This observation is very controversial, as other experiments have later excluded the DAMA/LIBRA WIMP phase space. The final stage of the ANAIS experiment, that uses the same target and detection technique of DAMA/LIBRA, is currently under-construction and will explore the authenticity of the DAMA/LIBRA signal by ruling out the possibility of a seasonal varying background with an independent experimental set-up and in a model-independent way (Amaré *et al.*, 2015).

It should be underlined that to claim for a final DM discovery, positive evidence for the presence of DM from multiple targets and techniques is mandatory, in order to rule out false signals from systematic effects, and comprehensively test particle and halo models.

Most up-to-date exclusion limits on WIMP cross sections

Figure 1.15 (LUX Collaboration, 2016*b*) shows the most up-to-date exclusion limits on the spin-dependent WIMP-neutron (left) and WIMP-proton elastic scattering cross sections (right) at 90% CL. LUX has set the most sensitive constraint on the spin-

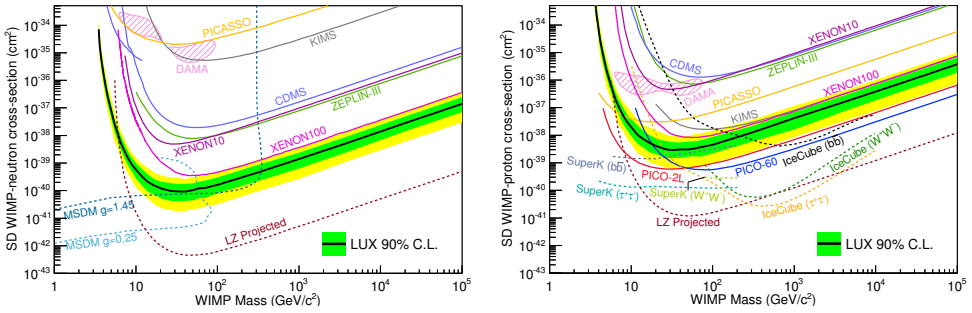

Fig. 1.15: Most up-to-date constraints on the spin-dependent WIMP-neutron (left) and WIMP-proton (right) cross section as a function of WIMP mass at 90% CL. Figures taken from LUX Collaboration 2016*b*.

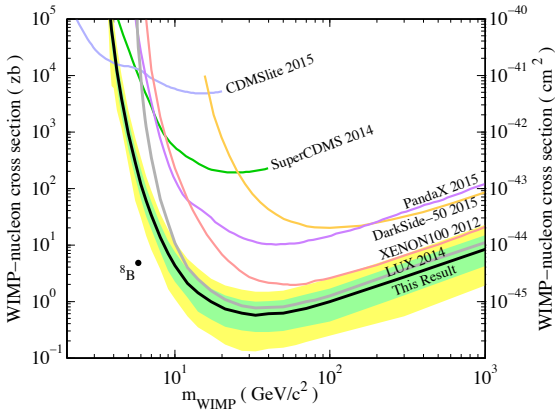

Fig. 1.16: Most up-to-date spin-independent WIMP-nucleon cross section as a function of WIMP mass at 90% CL. Figures taken from LUX Collaboration 2016*a*.

dependent WIMP-neutron cross section from an exposure of 1.1×10^4 kg $\times$ days in 2013, leading to $\sigma_n = 9.4 \times 10^{-41}$ cm^2 at a WIMP mass of 33 GeV/c^2 (LUX Collaboration, 2016*b*). Instead, the PICO Collaboration (born form the joint efforts of PICASSO and COUPP) has established world-leading limits on the spin-dependent WIMP-proton couplings for WIMP masses below 50 GeV/c^2 and above 50 GeV/c^2 using data from the PICO-2L and PICO-60 experiments, respectively. PICO-2L is a 2-liter C_3F_8 bubble chamber located in the SNOLAB underground laboratory, while PICO-60 is a bubble chamber filled with 36.8 kg of CF_3I, also located in SNOLAB, and is currently the largest bubble chamber dedicated to DM searches. Similarly to other experiments exploiting superheated fluorine-based liquids, the PICO experiments

are sensitive to proton-only coupling, because of the ^{19}F single unpaired proton and 100% abundance (PICO Collaboration, 2016*b*). The best exclusion limits on the spin-independent WIMP-nucleon scattering cross section are still held by LUX, for WIMP masses above 5.7 GeV/c^2 (LUX Collaboration, 2014), and are shown in Fig. 1.16. The 90% CL upper limit has a minimum of 0.6 zb (6×10^{-46} cm^2) at 33 GeV/c^2 WIMP mass.

The dashed lines in Fig. 1.11 show the projected limits for the spin-independent WIMP-nucleon cross section for near future experiments, among which LZ (born from the merger of the LUX and ZEPLIN collaborations) is already under construction at SURF and will be operating in 2018. The yellow region corresponds to events arising from Coherent Neutrino-Nucleus Scattering (CNNS) processes. In the light of the weak neutral current discovery, in 1973 Freedman suggested that the elastic scattering process $\nu + A \rightarrow \nu + A$ should present a sharp coherent forward peak and that for heavier nuclei the cross section should scale upward as A^2. This process has not been observed yet, but it is expected as a fundamental prediction of the SM. Unless direction-sensitive detectors are used, CNNS is considered an irreducible background to direct WIMP detectors, whose detection technique is based on coherent elastic scattering processes.

The top plots in Fig. 1.17 show the event rate (events/keV/ton/year) from solar and atmospheric neutrinos as a function of the energy recoil for argon and xenon, while the bottom plots in the same figure present the integrated count rate (events/ton/year) from solar neutrinos above recoil energy threshold as a function of energy threshold for argon and xenon (all figures being taken from Gutlein *et al.* 2010). As energy thresholds of current direct DM experiment are in the range between ∼3–10 keV, only ^{8}B- and hep-neutrinos can contribute to the WIMP background (green shaded region), with other parts of the neutrino spectrum becoming non negligible only for energy thresholds below 1 keV. However, atmospheric neutrinos have higher energies and lead to higher recoil energies, as shown in Fig. 1.18. Therefore, atmospheric neutrinos will be a serious background for detector sensitivities below ∼10–12 pb. Direction-sensitive DM detectors could be the last resource to detect WIMPs beyond the neutrino boundary, as neutrinos are not expected to produce the same WIMP daily modulation.

1.1.5 Double-phase Ar and Xe TPCs

We have already seen how a double-phase TPC works, but we have not gone much into the details of how luminescence and electroluminescence are produced. In this section I concentrate on the scintillation and ionisation mechanisms in double-phase TPCs,

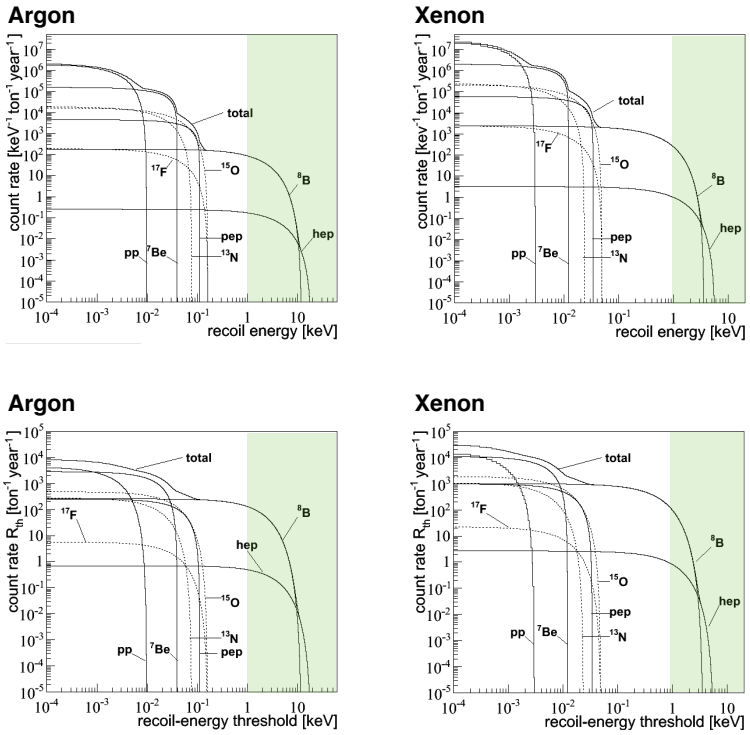

Fig. 1.17: Top: Nuclear recoil spectra from solar neutrino scattering for argon (left) and xenon (right). Bottom: Integrated count rates from solar neutrino scattering above recoil energy threshold for argon (left) and xenon (right). See the text for details. Figures are taken from Gutlein *et al.* 2010.

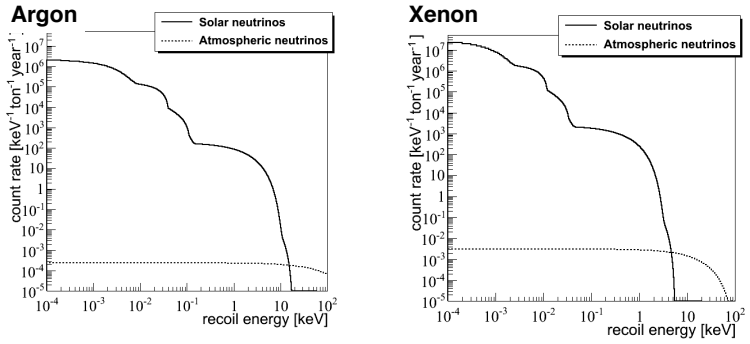

Fig. 1.18: Count rate from solar and atmospheric neutrino scattering above recoil energy threshold for argon (left) and xenon (right). Figures are taken from Gutlein *et al.* 2010.

(a) (b)

Fig. 1.19: Figure (a) is taken from the original paper of Dolgoshein *et al.* 1970 in 1970 and corresponds to a three-electrode chamber: A, G, and C represent the anode, grid, and cathode, respectively. An alpha source is placed on the cathode. Figure (b) is taken from the original paper of Suzuki *et al.* 1993 from 1993. It shows the scintillation signal seen in a xenon two-phase TPC for 5.5 MeV alphas from ^{241}Am (top) and 122 keV γ-rays from ^{60}Co (bottom).

explaining the reasons that allow for 3D-position reconstruction and discrimination between nuclear and electron recoils.

As it was not easy, nor straightforward the journey that let to the development of noble gas TPCs, before detailing the physics behind such detectors, it is due retracing the main historical steps that brought to the development of this technology, while outlining the basic concepts at the base of double-phase TPCs.

History of Double-Phase TPCs

In a paper published as early as 1948, Hutchinson had studied the mobility of electrons in liquid and solid argon. His work pointed out that, as opposed to most liquids, argon allowed great mobility of charge carriers when appropriately purified. Ten years later, Northrop *et al.* investigated the relative scintillation efficiency of various noble gas mixtures in an attempt to find a combination that would give a light yield greater than any pure gas alone, or allow a more economical use of the heavier gases. For argon, different wavelength-shifters were also tested, among which TetraPhenylButadiene (TPB). TPB is a fluorescent organic material that can wavelength-shift vacuum UV (VUV) argon scintillation, to which PMTs are blind, into the visible range ($\sim$420 nm) and constitutes the most common choice for LAr TPCs nowadays. By that time, some of the properties that make noble element scintillators unique were already known, such as transparency to their own scintillation, large light output, linearity, and large ionic mobility. But it was not until the seminal work of Dolgoshein *et al.* in 1970 that the foundations of the double-phase technique for particle detection were laid down.

Dolgoshein, Lebedenko, and Rodionov's original goal was to detect tracks of ionising particles in liquified gases in a similar manner to spark chambers. Since the idea proved too difficult, because it demanded intense electric fields to generate the discharge[3], they investigated a new method of detecting tracks of ionising particles in liquid argon. Their experimental setup, whose original drawing is shown in Fig. 1.19a, consisted of three electrodes (anode, grid, and cathode) in a chamber filled with liquid argon up to the second electrode, gas between the grid and the anode, and an alpha source on the cathode (usually modern TPCs also have conductive "shaping" rings around the argon volume to make the field more uniform). Because of the electric drift and extraction fields, the "electron image" of the track in the liquid could be transferred to the gas. A PMT was located above the anode and recorded first the scintillation flash (S1) generated by the alpha particle in the liquid argon, and then, after the electrons left the ionisation track, it registered the electroluminescence (S2)[4] produced by the electrons drifted upwards and extracted into the gas (Dolgoshein *et al.*, 1970). The drift time between the appearance of S1 and S2 determined the depth coordinate z, while from the S2 light detection they could reconstruct the image of the ionisation track on the xy-plane. This is exactly the technique used in modern TPCs for event 3D-position reconstruction, with the only exception that more than one PMT is commonly used, such that the xy-position is determined as follows:

$$(x,y)_i = \frac{\sum_i (x,y)_i \, S2_i}{\sum_i S2_i} \tag{1.28}$$

where $(x,y)_i$ is the position of the i-th PMT, $S2_i$ is the number of photoelectrons detected during the ionisation signal by that PMT, and the summation runs on all PMTs.

Although the idea of a double-phase TPC sounded appealing as a fast liquid track detector for ionising particles, it was only in 1989 that Barabash and Bolozdynya first proposed to use such technology in direct WIMP searches (although Barabash and Bolozdynya's proposal was not based on noble gases, but instead on the isoctane molecule C_8H_{18}). The principle at the base of nuclear and electron recoil discrimination, a key aspect in DM searches with noble gas TPCs, was first outlined in a paper by Suzuki *et al.* in 1993. The authors suggested that the ratio between primary and

[3] We shall see in Chapter 5, Section 5.2, that the breakdown voltage in a liquid is higher than the breakdown voltage of the same medium in its gaseous form.

[4] Electrons entering the gas region are accelerated by the extraction/multiplication electric field to sufficient energies to undergo direct excitation, herby producing secondary scintillation in the gas. Despite not being the dominant effect, sometimes electrons can even gain enough energy to ionise gas atoms, resulting in an avalanche of secondary electrons, which provides signal amplification.

secondary scintillation (S1/S2) could be used for distinguishing α-particles (heavy ionisation) from γ-rays (minimum ionisation). Using a xenon double-phase TPC chamber, it was found that while the pulse height ratio S1/S2 was considerably bigger than 1 for α-particles, it was smaller than 1 for γ-rays (see Fig. 1.19b). As such, it follows that in WIMP searches a 100% (or at least very high) charge collection efficiency is crucial, as S2 needs to be properly determined to reject electron recoil background. To achieve such efficiency, ionisation charges must not get trapped by electronegative impurities on their way up to the liquid-gas interface, i.e. LXe/LAr needs to be extremely pure, with impurities below the part-per-billion (ppb) level.

Scintillation Mechanism and Pulse Shape Discrimination

The reason S2/S1 is smaller for nuclear recoils compared to electron recoils has to be found in the scintillation mechanism of noble gases and the different structure of ionisation track generated by nuclear and electron recoils. The way light is produced is similar for both xenon and argon. If we regard the liquid as a compressed gas (which strictly speaking is not true, as LAr and LXe exhibit a band structure due to interatomic interactions), photons are emitted by relaxation of low excited molecular states to the dissociative ground states (Kubota *et al.*, 1978*b*):

$$R_2^* \rightarrow R + R + h\nu \tag{1.29}$$

where R can refer either to Ar or Xe and $h\nu$ is the energy of the emitted VUV photon. Such diatomic excited molecules, R_2^*, may be formed in two different ways, called excitation and recombination, which proceed as follows:

Excitation	Recombination
	$^{i)}\ X + R \rightarrow R^+ + e^- + X$
	$^{ii)}\ R^+ + R \rightarrow R_2^+$
	$^{iii)}\ R_2^+ + e^- \rightarrow R^{**} + R$
$^{1)}\ X + R \rightarrow R^* + X$	$^{iv)}\ R^{**} \rightarrow R^*$
$^{a)}\ R^* + R \rightarrow R_2^{*,\nu}$	$^{a)}\ R^* + R \rightarrow R_2^{*,\nu}$
$^{b)}\ R_2^{*,\nu} + R \rightarrow R_2^* + R$	$^{b)}\ R_2^{*,\nu} + R \rightarrow R_2^* + R$
$^{c)}\ R_2^* \rightarrow R + R + h\nu$	$^{c)}\ R_2^* \rightarrow R + R + h\nu$

where X can be a nuclear or electronic recoil and the superscript ν refers to excited states with vibrational excitation ($R_2^{*,\nu}$), as opposed to purely electronic excitation with $\nu = 0$ (R_2^*). An excited atomic state, R^*, can be produced either directly by collision with the incident particle (1) or by ionisation (i) followed by recombination (iii). Steps *a,* *b*, and *c* are common to both scintillation mechanisms: the excited atomic state collides with one of the surrounding atoms, undergoes excimer formation (a), then relaxation (b), and finally emits light (c).

Xenon and argon scintillation spectra both lie in the vacuum ultraviolet wavelength region, with xenon peaking around $\lambda \simeq 178\,\text{nm}$ and argon around $\lambda \simeq 127\,\text{nm}$. The scintillation photons are emitted in a transition of R_2^* from one of the two lowest electronic excited states, namely the singlet state ${}^1\Sigma_u^+$ or the triplet state ${}^3\Sigma_u^+$, to the ground state ${}^1\Sigma_g^+$. As the ground state is repulsive—i.e. the potential energy for ${}^1\Sigma_g^+$ shows no minimum, but, instead, it decreases smoothly with the interatomic distance, resulting in the atoms repelling each other (Hollas, 2004)—the molecule becomes unstable and immediately disassociates. Spectroscopically, the two transitions are indistinguishable, but their decay times are quite different, especially in liquid argon (Chepel and Araújo, 2013). The transition ${}^1\Sigma_u^+ \rightarrow {}^1\Sigma_g^+$ accounts for the fast component of the scintillation signal, while ${}^3\Sigma_u^+ \rightarrow {}^1\Sigma_g^+$ accounts for the slow one. Multiplicity would forbid transaction from ${}^3\Sigma_u^+$ to ${}^1\Sigma_g^+$, but the decay becomes allowed thanks to the mixing of the ${}^1\Pi_u^+$ state with the ${}^3\Sigma_u^+$ state due to spin-orbital coupling (Kubota *et al.*, 1978*a*). As the strength of such coupling increases with increasing atomic number, the triplet component decay time of argon is rather long ($\sim$1 µs) compared to xenon ($\sim$27 ns) (Chepel and Araújo, 2013).

Table 1.1 summarises some of the optical properties of LAr and LXe specific to electron and nuclear recoils (from alpha particles), as well as properties which do not depend on the nature of the recoil. Figures 1.20 and 1.21 show instead the observable distribution of the luminous energy in LAr and LXe for electron recoils and nuclear recoils, respectively. As the relative contribution of the fast component (singlet state) is greater for nuclear recoils than electron recoils, the pulse shape discrimination parameter, defined as the fraction of primary scintillation that arrives in the first 90 ns ($\mathtt{f}_{90}$), can be used to distinguish electronic recoils from nuclear recoils ($\mathtt{f}_{90\text{n}} > \mathtt{f}_{90\text{e}^-}$). Since, as mentioned before, LAr has a higher slow decay lifetime compared to LXe, pulse shape discrimination is more effective in Ar based detectors. The current generation of liquid xenon detectors does not rely on pulse shape discrimination for the primary scintillation signal (Chepel and Araújo, 2013). As pointed out by Chepel and Araújo 2013, it should be noted that strong recombination, due to a greater charge

Table 1.1 The table summarises optical properties of LAr and LXe specific to electron and nuclear recoils (from alpha), as well as properties which do not depend on the nature of the recoil.

Liquid	Particle	τ_S [ns]	τ_T [ns]	I_S/I_T	Electric field [kV/cm]	Reference
LAr	electron	6 ± 2	1590 ± 100	0.3	0	Hitachi *et al.* 1983
		6.3 ± 0.2	1020 ± 60	0.083	0	Kubota *et al.* 1978*a*
		5 ± 0.2	860 ± 30	0.045	6	
		34 ± 2			0	
	α	7.1 ± 1.0	1660 ± 100	1.3	0	Hitachi *et al.* 1983
		5	1200 ± 100		0	Kubota *et al.* 1978*c*
LXe	electron	34 ± 2			0	Kubota *et al.* 1978*a*
		2.2 ± 0.3	27 ± 1	0.05	4	
	α	4.3 ± 0.6	22 ± 1.5	0.45	0	Hitachi *et al.* 1983
		3	22		0	Kubota *et al.* 1982

Liquid	N_{ex}/N_i (electron recoils)	N_{ex}/N_i (nuclear recoils)	W [eV]	Scintillation wavelength [nm]	Reileigh scattering[a] [cm]	Index of refraction
LAr	0.21[b]	0.19[c]	$23.6^{+0.5}_{-0.3}$[d]	126.8[e]	55 ± 5[f]	1.46 ± 0.07[f]
LXe	0.06[g]	~ 1[h]	15.6 ± -0.3[g]	178[i]	36.4 ± 1.8[i]	1.69 ± 0.2[i]

[a] at the corresponding triple point and scintillation wavelength

[b] Kubota *et al.* 1978*b*

[c] Joshi *et al.* 2014

[d] Miyajima *et al.* 1974

[e] Heindl *et al.* 2010

[f] Grace and Nikkel 2016

[g] Takahashi *et al.* 1975

[h] Sorensen and Dahl 2011

[i] Solovov *et al.* 2004

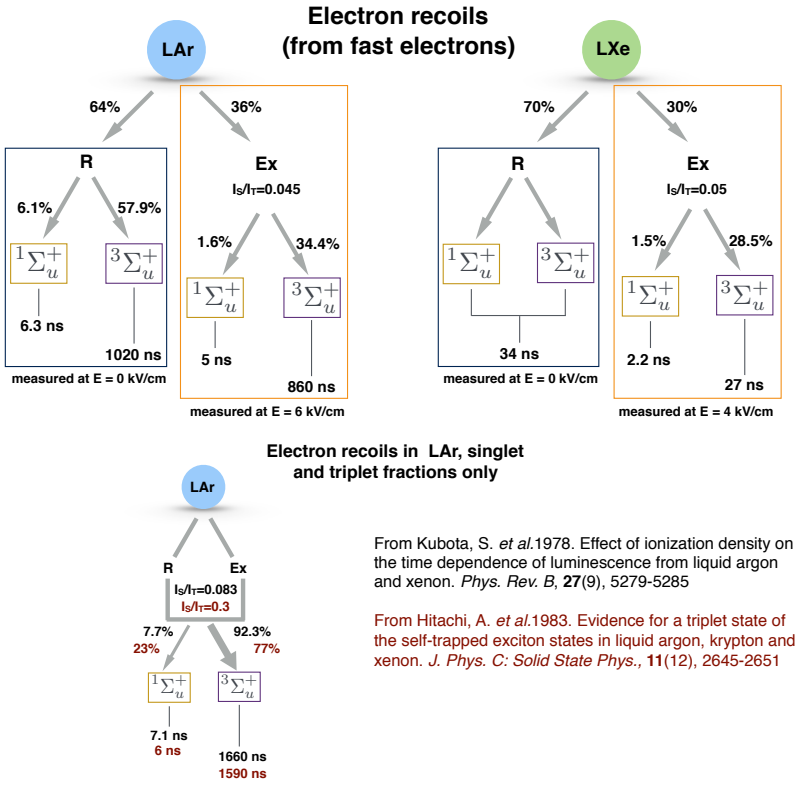

Fig. 1.20: Observable distribution of the luminous energy for electron recoils generated by fast electrons. The top diagrams show the scintillation percentages in LAr and LXe according to the recombination and direct excitation channels, as well as the triplet and singlet states (fast and slow scintillation components). All data are taken from Kubota *et al.* 1978*a*. The bottom diagram shows the scintillation distributions only according to the singlet and triplet states for LAr at zero electric field. The measurements performed by Hitachi *et al.* 1983 are also shown for comparison.

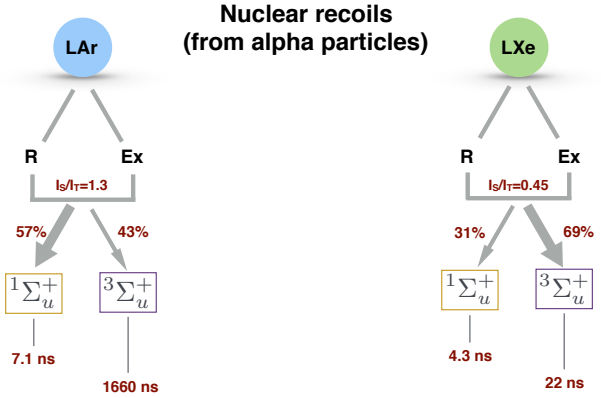

Fig. 1.21: Observable distribution of the luminous energy for nuclear recoils generated by alpha particles. The diagrams show the scintillation percentages in LAr and LXe according to the triplet and singlet states (fast and slow scintillation components). All data are taken from Hitachi *et al.* 1983.

density along the recoil track (i.e. greater LET), does not explain *perse* why the relative contribution of the fast component is enhanced for nuclear recoils. So far an exhaustive explanation is still missing. One possible mechanism is the quenching of singlet states in super-elastic collisions with thermal electrons, resulting in transitions from the singlet to the triplet state (Chepel and Araújo, 2013). The fact that these transitions are more probable for electron recoils, due to slower recombination, could potentially motivate the larger singlet component for nuclear recoils.

The minimum possible energy needed to produce a scintillation photon (maximum number of photons) with no quenching processes is:

$$W_s^{min} = \frac{W}{1 + N_{ex}/N_i} \tag{1.30}$$

where W is the average energy expended to produce an ion pair and N_{ex}/N_i is the ratio between excitons and number of ionised atoms. W has been measured to be 23.6 eV by Miyajima *et al.* and W_s^{min} is the inverse of the (maximum) scintillation yield:

$$\frac{dL}{dE} = \frac{1}{W_s^{min}} \tag{1.31}$$

with dL/dE usually expressed in units of ph/keV.

Whenever an electric field is applied ($E \neq 0$), some of the electrons produced through ionisation may be drifted away before recombination takes place, not contributing to S1, but, instead, to S2. This leads to an S1 quenching, S_e for electron recoils and S_{nr} for nuclear recoils, which varies with recoil energy and electric field. In Chapter 2, I present the results for nuclear quenching (relative to electron recoils) obtained by the SCENE experiment and in Chapter 5 the measurements I took for S_e in liquid argon.

Recombination luminescence and S2/S1 discrimination parameter

The dynamic of recombination luminescence effects the S2/S1 ratio and depends on the structure of the track, which is different for electron recoils and nuclear recoils. Let us describe the case for electron recoils first.

For electron recoils produced by fast ^{207}Bi internal-conversion electrons, in 1979 Kubota *et al.* found that the secondary electrons track structure could be approximated by a cylindrical tube of radius equal to the Onsager radius R_C and length equal to the true range R_0 of the primary recoiling electron. The Onsager radius corresponds to the distance between the secondary electron and its parent ion for which the Coulomb

energy equals the thermal energy:

$$R_C = \frac{e^2}{4\pi\epsilon_0\epsilon kT} \tag{1.32}$$

where e is the electron charge, ϵ_0 is the vacuum permittivity, ϵ is the dielectric constant of the liquid, k is Boltzmann's constant, and T the absolute temperature (Kubota *et al.*, 1979). This means that, as far as the secondary electron stays inside R_C, it cannot escape the electrostatic attraction of its parent ion and will eventually recombine with it, contributing to S1. However, if it diffuses outside R_C, it is free from the influence of the parent ion. As a consequence, when no electric field is applied, the electrons that lie outside the cylinder can either diffuse to the chamber walls (and get captured by electronegative impurities) or recombine with ions other than their parents, but only after a considerable amount of time (>ms), well above the usual observation time of an oscilloscope. As such, the scintillation produced by recombination of escaping electrons from the parent ions is responsible for the scintillation quenching observed at zero electric field for electron recoils. This is shown in Doke *et al.* 1988, where the scintillation yield (dL/dE) is divided into three parts:

$$\frac{dL}{dE} = \left(\frac{dL}{dE}\right)_{\mathrm{v}} + \left(\frac{dL}{dE}\right)_{\mathrm{g}} + \left(\frac{dL}{dE}\right)_{\mathrm{ex}} \tag{1.33}$$

where the first term is the contribution from recombination between electrons and ions other than the parents (the so-called "volume recombination"), the second is the scintillation yield for photons generated by geminate recombination (i.e. within the Onsager radius), and the third is the scintillation yield for light generated directly through excitation by the primary recoiling electron. Note that in this context dL/dE is not the absolute scintillation yield in ph/keV, but instead the scintillation yield of electron recoils relative to ^{210}Po (i.e. unitless), which is assumed to be unity:

$$\frac{dL}{dE} \equiv \frac{(dL/dE)_{e^-}}{(dL/dE)_{^{210}Po}} \tag{1.34}$$

Assuming dE/dx is proportional to the initial density of secondary electrons produced along the ionisation track (valid only for a cylindrical geometry, i.e. long tracks), Doke *et al.* write the total scintillation yield in eqn 1.33 as:

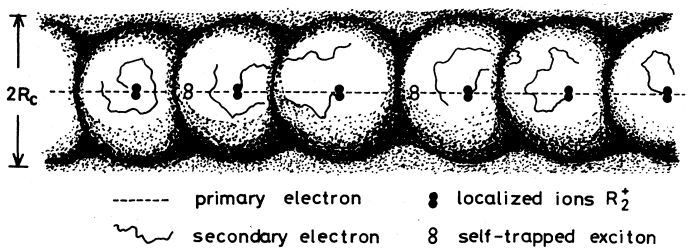

Fig. 1.22: Illustration of secondary electrons in a cylindrical tube of Coulomb attraction with radius R_C and length R_0 as taken from (Kubota *et al.*, 1979). Each secondary electron leaves behind a R_2^+ molecular ion, which in turn defines a sphere of Coulomb attraction of radius R_C. Since the intervals between neighbouring R_2^+ ions are nearly equal and R_C is of the same order of these intervals, the set of spheres forms a cylinder of radius R_C and length equal to the true range of the primary electron.

$$\begin{aligned}\frac{dL}{dE} &= \left(\frac{dL}{dE}\right)_{\mathrm{v}} + \left(\frac{dL}{dE}\right)_{\mathrm{g}} + \left(\frac{dL}{dE}\right)_{\mathrm{ex}} \\ &= \left(\frac{(1-\eta_0)(dE/dx)}{1+C(dE/dx)} + \eta_0\right)\end{aligned} \tag{1.35}$$

where C is a constant and $\left(\frac{dL}{dE}\right)_{\mathrm{g}} + \left(\frac{dL}{dE}\right)_{\mathrm{ex}} = \eta_0$. From eqn 1.35 it is apparent that $(dL/dE)_{\mathrm{v}}$ is responsible for the variation of the scintillation yield between unity and η_0. In fact, if $\eta_0 = 1$, then $dL/dE = 1$. The analysis in Doke *et al.* found $\eta_0 \simeq 0.75$ to be the most probable value.

When an electric field is applied, the secondary diffused charges are drifted and extracted in the gas region, where they contribute to S2, none of them being lost (this assumes the drift field is strong enough, the extraction efficiency is unity, and no electronegative impurities are present in the liquid). The diffusion distance is determined by the electrostatic attraction to the parent ion as well as the thermalisation length. The latter is estimated ∼4000–5000 ns in LXe (Mozumder, 1995*b*) and ∼1500–1800 ns in LAr (Mozumder, 1995*a*), both of which are way above the corresponding Onsager radius (125 ns for LAr and 49 ns for LXe), meaning that a good fraction of the electrons will not recombine (or will recombine with other ions after a long time) (Doke *et al.*, 2002).

Conversely, the track structure found for nuclear recoils (generated by alpha particles) suggests a different recoil track structure (no longer cylindrical), with more secondary electrons concentrated around the core track. This leads to a smaller probability for secondary electrons to escape their parent ion, even when an electric field is applied. Thus, secondary electron diffusion cannot alone justify the light quenching

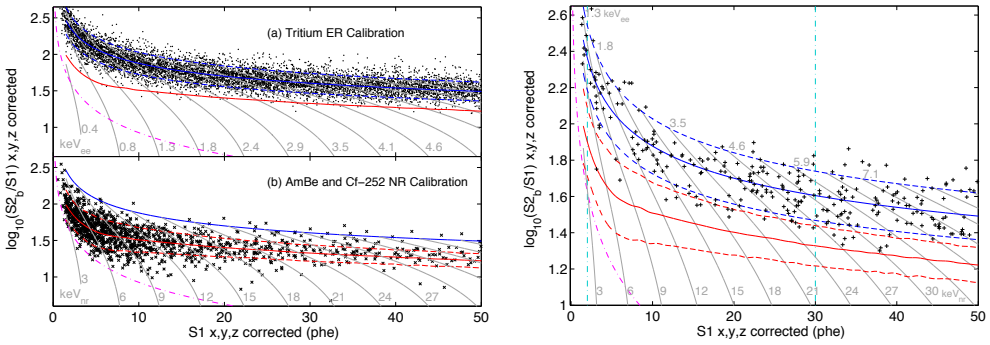

Fig. 1.23: Left: Calibrations of LUX detector for ER (tritium, top panel) and for NR (AmBe and ^{252}Cf, bottom panel), showing $\log_{10}$(S2/S1) as a function of photoelectrons (phe). The solid lines indicate the means and the dashed lines the ± 1.28 contours. The ER plot shows the NR band mean and vice versa. Grey contours indicate constant energies using an S1–S2 combined energy scale (same contours on each plot). The dot-dashed magenta line indicates the approximate location of the minimum S2 cut. Right: LUX WIMP signal region as of 2014. 160 events between 2 and 30 phe (S1) were observed within the fiducial volume in 85.3 live-days exposure. All events are consistent with the predicted background of electron recoils. As the average discrimination (with 50% NR acceptance) for S1 from 2–30 phe was $99.6 \pm 0.1\%$, 0.64 ± 0.16 events from ER leakage were expected below the NR mean. Both figures are taken from LUX Collaboration 2014.

observed at zero electric field for nuclear recoils and the theoretical model developed in Doke *et al.* 1988 to describe scintillation efficiency cannot be used anymore (dE/dx in not a good parameter to characterise dL/dE). Instead, alternative theories apply, namely Lindhard's theory (Lindhard *et al.*, 1963) and Birk's (Birks and Black, 1951) saturation law. The first explains energy loss due to nuclear inelastic collisions (providing an empirical formula for nuclear recoil energy that is transferred to electrons), while the second explains scintillation quenching caused by high ionisation and excitation density induced by nuclear recoils (a more detailed description of nuclear scintillation quenching will be given in Section 1.1.6).

Due to greater LET, when an electric field is applied recombination will be more dominant for nuclear recoils than for electron recoils, leading to a smaller S2/S1 ratio (as less electrons are being drifted, S2 will consequently be smaller). This feature is extremely useful in DM searches, as can be used to discriminate against background (see Fig. 1.23).

Single-phase TPCs

As it is from secondary scintillation that we extrapolate the xy-position of the event, dual-phase TPCs need costly, cryogenic, radiopure, and highly efficient PMT arrays, fully covering the top and bottom of the detector. Moreover, precise monitoring and control of the liquid-gas interface is needed, as variations in the liquid level can change the S2 signal for the same amount of charges extracted. Especially for future multi-ton experiments (e.g. DARWIN), more affordable solutions might come in handy.

One concept, exploiting the use of Liquid Hole-Multipliers (LHMs), was suggested by Breskin in 2013, and consists of a cascade of three CsI-coated perforated electrodes (e.g. Gaseous Electron Multipliers [GEMs] or Thick Gaseous Electron Multipliers [ThGEMs]) immersed in the liquid, replacing the extraction grid. If successful, such configuration would allow for easier detector designs and more cost-effective experiments, simpler to scale to multi-ton dimensions.

GEMs consist of a frame and an active area. The latter is a thin mesh, realised by photolithographic methods. A thin (∼25-50 µm) insulating polymer foil (such as Kapton) is coated on both sides with a conductive (e.g. copper) layer (∼5-20 µm). The metal is passivated with photoresist and exposed to light to create the geometric pattern from the photomask. Through an acid etching process, the conductor is perforated with 30–80 µm diameter holes 100-200 µm apart. A second etching of the insulator opens the holes all the way through. Finally, the photoresist is removed (Sauli, 1997; Buzulutskov *et al.*, 2000; Breskin *et al.*, 2011).

ThGEMs are thicker versions of GEMs, constructed by mechanically drilling submillimeter diameter holes, spaced by a fraction of a mm in a thin (generally a fraction of a mm) printed circuit board (PCB), followed by Cu-etching of the hole's rim (typically 0.1 mm) (Breskin *et al.*, 2009). As such, ThGEMs are a lot cheaper than GEMs and the complex operations of framing and stretching specific of GEMs can be avoided. The only constraint is given by position resolution, which is ∼500 µm.

In both GEMs and ThGEMs, an electric potential is applied between the conductive plates, creating a strong dipole electric field within the holes. In LHMs the perforated electrodes are covered with CsI photocathodes, which allow for photoelectric conversion. A schematic of a cascade of ThGEMs with CsI photocathodes immersed in LXe/LAr is shown in Fig. 1.24. Photons from primary scintillation and drifting ionisation electrons are collimated through the holes, where they accelerate, producing electroluminescence photons. Depending on the strength of the field, S1 photo-induced electrons and S2 ionisation electrons may undergo charge multiplication (avalanche). With sufficient amplification, final charges can be recorded directly; alternatively, photons can be detected as usual by PMTs. Other less standard photodetectors are also

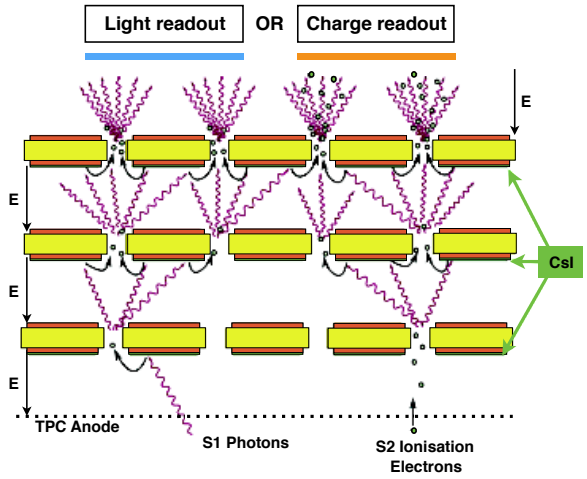

Fig. 1.24: Schematic of Liquid Hole-Multiplier (LHM) principle, here shown with three ThGEMs. S1 photons impinging on the first CsI-coated ThGEM electrode are converted into electrons. These are collected by the strong electric field within the holes, where they undergo electroluminescence. The process of light amplification is from one ThGEM to the next one. Similarly, drifting S2 ionisation electrons are focused into the holes and follow the same amplification path. The resulting S1 and S2 light signals are recorded by photodetectors. If sufficiently charge amplification is provided, photon-induced electrons from the final stage can be simply collected by charge readouts.

being studied, such as silicon photomultipliers (Lightfoot *et al.*, 2008). A different configuration has been investigated in 2011 by Spooner *et al.* in LAr , where ThGEMs with no CsI coating were used to generate electroluminescence in the liquid and SiPMs were employed for detecting the light.

In 2014, Aprile *et al.* have derived electric field thresholds of 412^{+10}_{-133} and 725^{+48}_{-139} kV/cm in LXe for proportional scintillation and electron multiplication, respectively, using a single 10 µm diameter gold plated tungsten wire. Spooner *et al.* have claimed to have observed electroluminescence using a ThGEM mounted within the liquid. More recents results in 2015 by Erdal *et al.* in LXe suggest, however, that this electroluminescence might be due to bubbling of the liquid under the ThGEMs. In such case the secondary scintillation would be explained by the same mechanism as in double-phase TPCs: direct excitation of gas atoms by accelerating electrons (Arazi *et al.*, 2013; Arazi *et al.*, 2015).

At UCL, we have started gathering experience with ThGEMs and we aim at testing

them in LAr in the near future to investigate whether the behaviour observed by Erdal *et al.* applies to argon as well.

Xenon or Argon?

We have already mentioned that xenon, given its higher atomic number, shows a greater spin-independent WIMP-nucleon cross section and, given its odd number of neutrons, has the advantage of being sensitive to spin-dependent WIMP-neutron interactions. Moreover, absence of long-lived radioisotopes in natural xenon make it even more suitable for DM detectors. Perhaps, the only drawback of xenon is its cost, especially when one has to build multi-ton LXe detectors.

Argon offers a cheaper alternative, and, given the large difference between the decay times of the singlet and triplet scintillation components, allows for higher electron recoil discrimination based on $\mathtt{f}_{90}$. However, as it is usually the case, "one gets what it pays for", as low-cost natural atmospheric argon contains the radioisotope ^{39}Ar, with activity of 1 Bq/kg (Chepel and Araújo, 2013). ^{39}Ar decays β^-, has a half-life of 269 years, and is produced in the atmosphere by cosmic ray interactions, principally through the $^{40}\mathrm{Ar}(\mathrm{n},2\mathrm{n})^{39}\mathrm{Ar}$ reaction. As such, sourcing from underground natural gas reservoirs is necessary to obtain argon depleted in ^{39}Ar (Acosta-Kane *et al.*, 2008). Underground sourced argon has a cost of approximately ~\$500–1000/kg, slightly cheaper than the cost of liquid xenon, which is also around ~\$1000/kg.

Although radioactive decays constitute a problematic background in the search for WIMPs, they do not harm noble gas TPCs used in neutrino oscillation experiments, the energies involved being much higher than the energy deposited from radon or other radioactive materials. As such, liquid argon is definitely the best and cheapest option for ton-scale neutrino TPCs.

1.1.6 $\mathcal{L}_{\mathrm{eff}}$ and $\mathcal{Q}_y$ for LAr

The scintillation yield for liquid argon has been investigated across a wide range of linear energy transfers by Doke *et al.* 1985, Doke *et al.* 1988, and Hitachi and Doke 1992. In 1988, Doke *et al.* showed that the maximum scintillation yield is obtained for relativistic heavy ions in the Ne-La group (LET between 200 and 5000 $\mathrm{MeV\,cm^2\,g^{-1}}$) and it drops on both sides of this LET interval (see Fig. 1.25). The decrease of the scintillation yield on the low LET side (relativistic electrons and γ-rays) is explained, as seen before, by a higher probability for electrons escaping recombination and thus not contributing to photodetectable light. On the high LET side, the reduction in scintillation yield is observed for fission fragments and particles which generate nuclear

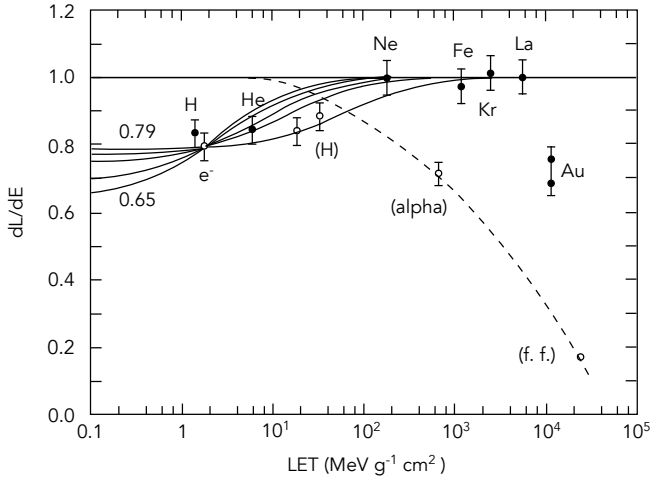

Fig. 1.25: Scintillation yield in liquid argon relative to α-particles from ^{210}Po as a function of LET as reported by (Doke *et al.*, 1988). The solid curves represent the fit to the data points of 0.976 MeVelectrons using different values for the light yield quenching, namely 0.65, 0.70, 0.75, 0.77, and 0.79. Doke's work analysis showed that the most probable value is 0.75 for electron recoils in LAr. The scintillation curve for α-particles and fission fragments is given as the product of the solid curve and the dashed curve. The light yield for α-particles and fission fragments dramatically decreases because of quenching processes.

recoils (NR), such as neutrons or alphas. There are two main mechanisms responsible for this light loss: non-radiative collisions and collision between excited states. The first process results in heat being produced. The second regards autoionisation of one of the two colliding excitons ($R^* + R^* \rightarrow R + R^+ + e^-$), which yields, at best, only one emitted photon (from R^+ through recombination) instead of two (Chepel and Araújo, 2013). In fact, since the electron generated in the collision of the two excited species has a kinetic energy close to the difference between twice the excitation energy $\mathrm{E_{ex}}$ and the band gap energy $\mathrm{E_g}$, it may rapidly lose its energy through thermalisation, or easily escape before recombining (Hitachi *et al.*, 1983).

The relative scintillation efficiency for nuclear recoils, denoted $\mathcal{L}_{\mathrm{eff}}$, is a unitless quantity and is usually measured with respect to the scintillation signal produced by the 122 keV ^{57}Co γ-ray source at zero field as follows:

$$\mathcal{L}_{\mathrm{eff},^{57}\mathrm{Co}}(E_{nr}, \mathcal{E}_d) = \frac{S1_{nr}(E_{nr}, \mathcal{E}_d)/E_{nr}}{S1_{^{57}\mathrm{Co}}(\mathcal{E}_d = 0)/E_{^{57}\mathrm{Co}}} \tag{1.36}$$

E_{nr} corresponds to the true nuclear recoil energy in keV fixed by the kinematics

(often denoted as "keV$_{\rm ne}$", i.e. "keV nuclear equivalent"), while $E_{^{57}\rm Co}$ is the observed electronic recoil equivalent energy (E_{ee}) based on ^{57}Co γ-rays, i.e. 122 keV$_{\rm ee}$. The "keV$_{\rm ee}$" stands for "keV electron equivalent" and stresses the fact that the energy measured is based on gamma calibration, i.e. electron recoils. $S1_{nr}(E_{nr}, \mathcal{E}_d)$ is the primary scintillation for the nuclear recoil at energy E_{nr} and electric drift field $\mathcal{E}_d$ in units of p.e. (photoelectrons). $S1_{^{57}\rm Co}(\mathcal{E}_d = 0)$ is the primary scintillation for 122 keV at zero electric drift field in units of p.e. The dependence on the nuclear recoil energy and electric (drift) field $\mathcal{E}_d$ of $\mathcal{L}_{\rm eff}$ must be considered *a priori* and has been expressed explicitly in eqn (1.36).

Equation (1.36) implies that to convert the nuclear recoil energy from keV$_{\rm ee}$ (calibrated with ^{57}Co γ-rays) to keV (or keV$_{\rm ne}$), one needs simply to divide keV$_{\rm ee}$ by $\mathcal{L}_{\rm eff}$

$$E_{nr}[\text{keV}] = \frac{E_{nr}[\text{keV}_{\rm ee}]}{\mathcal{L}_{\rm eff,^{57}Co}(E_{nr}, \mathcal{E}_d = 0)} \tag{1.37}$$

This relation holds true only at zero electric field, but inclusion of non-zero electric field can be done by multiplying the right hand side by the scintillation quenching for electron recoils when an electric drift field is applied, S_e, and using the corresponding value of $\mathcal{L}_{\rm eff}$ at that electric field. The reconstructed nuclear recoil energy deposited, E_{nr} in units of keV, is then given by:

$$E_{nr} = \frac{S1_{nr}(E_{nr}, \mathcal{E}_d)}{L_{y,^{57}\rm Co}(\mathcal{E}_d)} \times \frac{1}{\mathcal{L}_{\rm eff,^{57}Co}(E_{nr}, \mathcal{E}_d)} \times S_{e,^{57}\rm Co}(\mathcal{E}_d) \tag{1.38}$$

where $L_{y,^{57}\rm Co}$ is the measured light yield using ^{57}Co at zero electric field in units of p.e./keV$_{\rm ee}$, $S_{e,^{57}\rm Co}(\mathcal{E}_d)$ is the field quenching factor for electronic recoils as measured with ^{57}Co source as a function of the drift field, and $S1_{nr}(E_{nr}, \mathcal{E}_d)$ is the measured primary scintillation at nuclear recoil energy E_{nr} and drift field $\mathcal{E}_d$. We can also explicitly express the quenching for nuclear recoils when an electric field is applied (S_{nr}), by rewriting $\mathcal{L}_{\rm eff}$ in the following way:

$$\mathcal{L}_{\rm eff,^{57}Co}(E_{nr}, \mathcal{E}_d) = \mathcal{L}_{\rm eff,^{57}Co}(E_{nr}, \mathcal{E}_d = 0) \times S_{nr,^{57}\rm Co}(\mathcal{E}_d) \tag{1.39}$$

From now on, when referring to $\mathcal{L}_{\rm eff}$ I will implicitly imply the energy and electric field dependence $(E_{nr}, \mathcal{E}_d)$. Despite its scintillation efficiency also not being equal to 1, ^{57}Co is usually used when defining $\mathcal{L}_{\rm eff}$, as this γ-source has been traditionally used for electron recoil calibration. However, one can in principle choose any reference energy as far as all the other quantities are referred to that same energy (e.g. S_e).

Direct nuclear recoil energy calibration is particularly difficult to perform *in situ*,

as a neutron beam is needed and the detector has to be large enough to contain the double-scatter neutron event in order to measure the scattering angle and kinematically constrain the recoil energy. In such case, the detector would essentially serve the double function of TPC and neutron detector of a typical experiment measuring $\mathcal{L}_{\text{eff}}$. AmBe sources (Americium Beryllium) produce a broad nuclear recoils spectrum and together with Monte Carlo simulations can be used to directly calibrate a detector for nuclear recoils. However, the calibration with AmBe sources is less precise than one using a neutron generator and that is why it is usually preferred to use gamma calibration combined with $\mathcal{L}_{\text{eff}}$ to convert from p.e. to keV_{ee} (using $L_{y,^{57}\text{Co}}$), and then from keV_{ee} to keV (using $\mathcal{L}_{\text{eff}}$). The only detector which has a dedicated collimated beam of mono-energetic neutrons for *in situ* nuclear recoil calibration is LUX.

Analogously to the (relative) scintillation yield for S1, also the ionisation yield for S2, $\mathcal{Q}_y$, may be measured. $\mathcal{Q}_y$ is expressed in detector-independent units of extracted electrons per unit of recoil energy (e^-/keV) and is related to S2 through the following equation:

$$\mathcal{Q}_y = S2 \times \frac{1}{E_{nr}} \times \frac{1}{g_2} \tag{1.40}$$

where E_{nr} is in units of keV, $S2$ in p.e. and g_2, in units of $\text{p.e.}/\text{e}^-$, is the detector specific single electron S2 gain. In Chapter 2, I will present the measurement of light and ionisation yields from nuclear recoils in LAr at keV energies performed by the SCENE experiment (SCintillation Efficiency of Noble Elements) that I worked on. Prior to this work, these quantities were not well understood in LAr, despite their importance in understanding the response of argon targets to WIMPs.

1.2 Large LAr TPCs for neutrino detectors

This section is divided into two parts. In the first I provide the reader with a brief introduction to neutrino physics, focusing only on the aspects that are relevant to LAr TPCs. In the second part I describe the features that make LAr TPCs so attractive to neutrino searches and present current and near future experiments that use this technology, underlying the main differences in design against dark matter experiments.

1.2.1 Current status of neutrino physics

Neutrinos might not be as much enigmatic as dark matter particles, but they surely are one of the most puzzling particles in particle physics. We now know that neutrinos are chargeless, colourless, and massive particles, hereby only interacting through gravity and the weak nuclear force. First postulated by Pauli in 1930 as neutral particles to explain the continuos spectrum of β decay (while preserving the conservation of energy principle), their observation came only in 1956 with the work of Reines and Cowan (Cowan *et al.*, 1956). Strictly speaking, the first neutrino to be found was the electronic antineutrino in the reaction $\bar{\nu}_e + p \rightarrow e^+ + n$. By that time it was already well known that to each particle corresponded an antiparticle with (almost) identical properties, so that the discovery of ν_e also implied the existence of $\bar{\nu}_e$. In 1962, Lederman, Schwartz, and Steinberger found that there also existed a muon neutrino. When a third type of lepton, the tau, was discovered by Perl *et al.* in 1975, it was already clear that it had to have an associated neutrino. As such, the discovery of ν_τ in 2000 did not come unexpected (Feldman, 1992).

Although Pontecorvo had already suggested in 1957 the possibility of neutrino flavour transformations, and experiments in the '60s had detected an unexplained deficit in the flux of solar neutrinos against the prediction given by the Standard Solar Model (Davis *et al.*, 1968), it was only in recent years that the hypothesis of neutrino flavour oscillations has been confirmed thanks to the Super-Kamiokande experiment and data from the Sudbury Neutrino Observatory.

The core idea of neutrino favour oscillations is that two basis of neutrino eigenstates exist, one of them being flavour. Assuming the other base is composed of mass eigenstates, namely $|\nu_1\rangle, |\nu_2\rangle, |\nu_3\rangle$, and that each $|\nu_e\rangle, |\nu_\mu\rangle, |\nu_\tau\rangle$ is a superposition of $|\nu_1\rangle, |\nu_2\rangle, |\nu_3\rangle$, then, as the Hamiltonian generates time evolution, neutrinos propagate as mass eigenstates. However, since their interactions are weak interactions, we can only observe them as flavour eigenstates, i.e. with a specific flavour (at the moment of measurement, the quantum state "collapses" in a flavour eigenstate). This is in contrast to the Standard Model, which, at the time it was constructed, assumed

neutrinos had zero mass. As such, neutrino oscillations point to new physics beyond SM predictions. The neutrino flavour eigenstates $|\nu_\alpha\rangle$, with $\alpha \in (e, \mu, \tau)$, can be expressed as a combination of the mass eigenstates $|\nu_i\rangle$, with $i \in (1, 2, 3)$, using the Pontecorvo-Maki-Nakagawa-Sakata (PMNS) unitary matrix U (Ahmad *et al.*, 2001):

$$|\nu_\alpha\rangle = \sum_{i=1}^{3} U^*_{\alpha i} |\nu_i\rangle \tag{1.41}$$

where the PMNS matrix is a 3×3 unitary complex matrix, which can be parameterised by three mixing angles, $\theta_{12}, \theta_{23}, \theta_{13}$, and a single CP-violating phase δ (or δ_{CP}):

$$U = \begin{pmatrix} 1 & 0 & 0 \\ 0 & c_{23} & s_{23} \\ 0 & -s_{23} & c_{23} \end{pmatrix} \begin{pmatrix} c_{13} & 0 & s_{13}e^{-i\delta} \\ 0 & 1 & 0 \\ -s_{13}e^{+i\delta} & 0 & c_{13} \end{pmatrix} \begin{pmatrix} c_{12} & s_{12} & 0 \\ -s_{12} & c_{12} & 0 \\ 0 & 0 & 1 \end{pmatrix} \begin{pmatrix} 1 & 0 & 0 \\ 0 & e^{i\alpha} & 0 \\ 0 & 0 & e^{i\beta} \end{pmatrix} \tag{1.42}$$

where $s_{ij} = \sin\theta_{ij}$, $c_{ij} = \cos\theta_{ij}$, and α and β are Majorana phases that have no effect on neutrino oscillations. Similarly, the mass eigenstates can be expressed as a combination of the flavour eigenstates:

$$|\nu_i\rangle = \sum_{\beta} U_{\beta i} |\nu_\beta\rangle \tag{1.43}$$

where the index β runs over all possible favours (e, μ, τ). The time evolution of a neutrino produced at time $t = 0$ in the state $|\nu_\alpha\rangle$ is given by:

$$|\nu_\alpha(t)\rangle = \sum_{i=1}^{3} U^*_{\alpha i} e^{-iE_i t} |\nu_i(t=0)\rangle \tag{1.44}$$

where $\hbar = 1$ and the operator Hamiltonian $\hat{\mathcal{H}}$ has already been evaluated, giving the energy eigenvalue E_i. Using eqns (1.43) and (1.44), we can express $|\nu_\alpha(t)\rangle$ in the basis of the flavour eigenstates $|\nu_\beta\rangle$:

$$|\nu_\alpha(t)\rangle = \sum_{\beta} \sum_{i=1}^{3} U_{\beta i} e^{-iE_i t} U^*_{\alpha j} |\nu_\beta\rangle \tag{1.45}$$

From eqn (1.45) it follows that the oscillation probability for $\nu_\alpha \to \nu_\beta$ is :

$$P(\nu_\alpha \to \nu_\beta) = |\langle \nu_\beta | \nu_\alpha(t) \rangle|^2 = \left| \sum_{i=1}^{3} U_{\beta i} e^{-iE_i t} U^*_{\alpha j} \right|^2 \tag{1.46}$$

Since neutrinos are highly relativistic, the p_i with $i \in (1,2,3)$ are all approximately equal to the beam energy E and the following holds true:

$$E_i = \sqrt{p_i^2 + m_i^2} \simeq p_i + \frac{m_i^2}{2p_i} \simeq E + \frac{m_i^2}{2E} \tag{1.47}$$

Also, given the neutrino velocity is approximately equal to c, the time travelled equals the distance travelled in natural units ($t \simeq L$). Using these approximations and separating out the real and imaginary parts of eqn (1.46), the probability of $\nu_\alpha \to \nu_\beta$ transitions becomes (Kayser, 2008):

$$\begin{aligned} P(\nu_\alpha \to \nu_\beta) = \delta_{\alpha\beta} &- 4\sum_{i>j} \Re(U^*_{\alpha i} U_{\beta i} U^*_{\alpha j} U^*_{\beta j}) \sin^2(1.27\,\Delta m^2_{ij} \frac{L}{E}) \\ &+ 2\sum_{i>j} \Im(U^*_{\alpha i} U_{\beta i} U^*_{\alpha j} U^*_{\beta j}) \sin(2.54\,\Delta m^2_{ij} \frac{L}{E}) \end{aligned} \tag{1.48}$$

Here, L is the distance in km travelled by the neutrino, E is neutrino beam energy in GeV, $\Delta m^2_{ij} \equiv m^2_i - m^2_j$, and the factors 1.27 and 2.54 stem from expressing Δm^2_{ij} in eV^2, L in km, and E in GeV with natural units recovered. It should be emphasised that eqn (1.48) is only valid in vacuum. In fact, when traveling through matter, neutrino propagation is modified by coherent forward scattering with other particles. Mikheyev, Smirnov, and Wolfenstein (MSW) were the first to study neutrino oscillations through matter (Wolfenstein, 1978; Smirnov, 2003). The MSW effect arises from the fact that electron (anti)neutrinos interact with matter differently than muon and tau anti(neutrinos). In fact, $\nu_e(\bar{\nu}_e)$ can undergo both current and neutral current elastic scattering with electrons, whereas $\nu_\mu(\bar{\nu}_\mu)$ and $\nu_\tau(\bar{\nu}_\tau)$ can only interact with matter via neutral currents. From measurements of neutrinos from the Sun, reactors, atmosphere, and accelerators, we have been able to derive the following parameters:

$$\begin{aligned} \sin^2(2\theta_{12}) &= 0.846 \pm 0.021 \\ \sin^2(2\theta_{23}) &= 0.999^{+0.001}_{-0.018} \\ \sin^2(2\theta_{13}) &= 0.093 \pm 0.008 \\ \Delta m^2_{21} &= (7.53 \pm 0.18) \times 10^{-5}\,\text{eV}^2 \\ |\Delta m^2_{32}| &= (2.52 \pm 0.07) \times 10^{-3}\,\text{eV}^2 \quad \text{assuming IH} \\ \text{or } &(2.44 \pm 0.06) \times 10^{-3}\,\text{eV}^2 \quad \text{assuming NH} \\ \delta_{CP} &\in (-\pi, \pi) \text{ unknown} \end{aligned}$$

while θ_{12} and θ_{13} can be determined without ambiguities, the survival probability $P(\nu_\mu \to \nu_\mu)$, through which we measure θ_{23}, does not allow us to know which octant θ_{23} lives, leading to two degenerate solutions: either $\theta_{23} \leq 45°$ (in the first octant) or $\theta_{23} > 45°$ (in the second octant) (Nunokawa, 2007). All data reported above are taken from the Particle Data Group in Olive *et al.* 2014.

So far we still do not know if the δ_{CP} phase is non-zero, and, if so, what its value is. If CP symmetry were preserved in all physical processes, the laws of Nature would be the same for matter and antimatter. Most phenomena are indeed C- and P-symmetric, hence also being CP-symmetric. In particular, these symmetries are respected by the gravitational, electromagnetic, and strong interactions (this is called "strong CP problem", see Quinn 2004). On the other hand, while weak interactions violate C and P separately, CP is still preserved in most weak interaction processes. The CP symmetry is, however, violated in certain rare processes involving hadron decays via the weak interaction (Olive *et al.*, 2014). So far, flavour-changing CP violation has been observed in the quark sector, but never for leptons. Measuring δ_{CP} could cast light on the CP violation in the lepton sector and help to explain the matter-antimatter imbalance in the universe.

Furthermore, since we ignore the absolute neutrino mass scale, we do not know if neutrinos mass hierarchy is normal ($m_1 < m_2 \ll m_3$), inverted ($m_3 \ll m_1 < m_2$) or degenerate $m_1 \simeq m_2 \simeq m_3$. Finally, whether neutrinos are Dirac or Majorana particles and whether sterile neutrinos exist remain unanswered.

Accelerator-based long-baseline neutrino oscillation experiments use GeV muon neutrinos produced by pion decay in an accelerator complex to precisely measure the parameters of the PMNS matrix. For the best possible detector design it should be noted that the asymmetry between the probability of oscillations of neutrinos and antineutrinos in vacuum and in matter suggests a CP asymmetry increasing from the first to higher oscillation maxima. For the vacuum case, we can see from eqn (1.48) that the probability of conversion is maximum for multiple choices of L/E. Assuming an energy threshold around 1 GeV, it follows that the experiment baseline should be greater than 1500 km in order to detect the second maximum (LAGUNA-LBNO Collaboration, 2014). A next generation of large scale neutrino experiments is on its way and several ideas have been proposed worldwide. These experiments will provide simultaneous and complementary studies, with unprecedented precision, of the channels $\nu_\mu \to \nu_\mu$, $\nu_\mu \to \nu_e$, and $\nu_\mu \to \nu_\tau$ for charged current events, yielding a definitive resolution of the mass hierarchy and CP violation problem.

1.2.2 Large LAr TPC neutrino detectors

Dark Matter vs Neutrino LAr TPCs

Although the underlying concept of LAr TPCs for WIMPs and neutrinos experiments is the same, the two detector designs are substantially different. This is due to the fact that, while in direct dark matter searches we look for small energy depositions leaving behind a few keV in nuclear recoils, in neutrino experiments we aim at detecting relatively high energy events of the order of the GeV.

Figure 1.26, taken from Formaggio and Zeller 2012, shows the existing muon neutrino (left) and antineutrino (right) charged-current cross section measurements as a function of neutrino energy. The different contributing processes in this energy region include quasi-elastic (QE) scatterings, resonance productions (RES), and deep inelastic scatterings (DIS). Predictions for each channel are provided by the NUANCE generator (Casper, 2002). Since next generation neutrino experiments aim at studying accelerator-produced muon neutrinos with energies $\lesssim$(1–5) GeV, detectors will be sensitive to quasi-elastic scatterings, resonance production, and even deep inelastic scatterings. Thus, while WIMP-induced nuclear recoils in LAr are so faint they can only generate a feeble scintillation signal, neutrinos deposit enough energy to produce a clear ionisation track. As such, an "electron image" of the track can be derived directly from the ionisation electrons produced in the liquid, with no need for extra signal amplification through charge extraction and multiplication in the gas (to improve the image resolution WA105, a double-phase LAr TPC, is trying to do so by exploiting LHMs in the gas region—see end of the chapter for more details on the

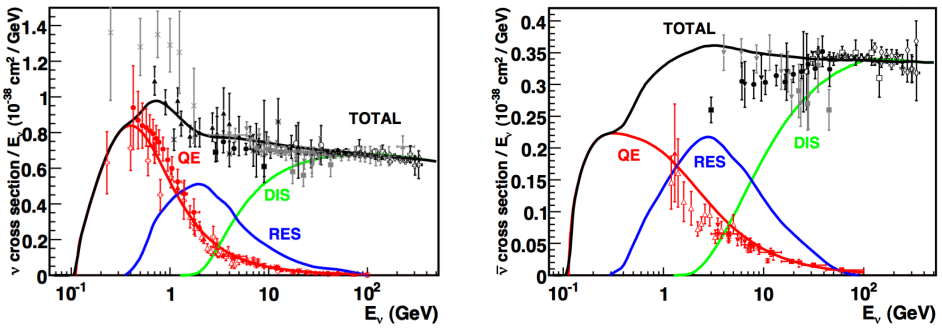

Fig. 1.26: Total muon neutrino and muon antineutrino per nucleon CC cross sections (for an isoscalar target) divided by neutrino energy and plotted as a function of energy. Note that the quasi-elastic scattering data and predictions have been averaged over neutron and proton targets and hence have been divided by a factor of two for the purposes of this plot. Figure taken from Formaggio and Zeller 2012.

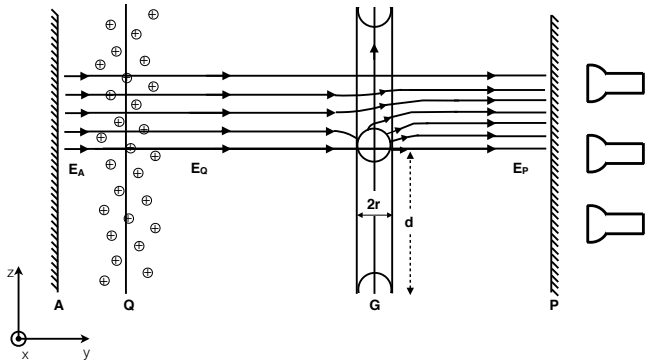

Fig. 1.27: Electric field in grid ionisation chamber. Positive ions and electrons are produced by an ionising particle along Q (ionisation track). A grid (G) shields the collecting electrode (the anode P) from the induced effect of positive ions moving to the cathode (A). A set of PMTs behind the collecting electrode detects the scintillation photons, providing the reference time of the event. Note that the electric field has been defined as the positive gradient of the potential. Figure taken from Bunemann *et al.* 1949.

WA105 experiment). For this reason all neutrino LAr TPCs are single-phase TPCs, without any internal gain mechanism (as such differing from a single-phase TPC that would use ThGEMs).

Design of neutrino LAr single-phase TPCs

Let us now go through the details of LAr TPCs for neutrino detection, initially following the notes of the first ever published paper on "the design of grid ionization chambers", by Bunemann *et al.* in 1949. The simplest LAr TPC chamber would consist of a rectangular volume filled with liquid argon, containing two parallel wire plane[5] electrodes with an electrostatic field applied between them, that is a high (negative) voltage electrode (cathode) and a collecting electrode (anode) connected to a suitable read-out electronic system. When an ionising particle (e.g. a muon produced in the reaction $\nu_\mu + n \rightarrow \mu^- + p$) passes through the parallel plates, it deposits its energy in the form of secondary electrons and scintillation light. The scintillation photons are measured through arrays of PMTs coated with TPB, placed behind the collecting electrode. The scintillation, analogously to DM experiments, provides the trigger signal and the reference time for the interaction. To permit the drift of ionisation electrons

[5] A wire plane is an array of thin conductive parallel wires, spatially separated by typically 2 to 4 mm

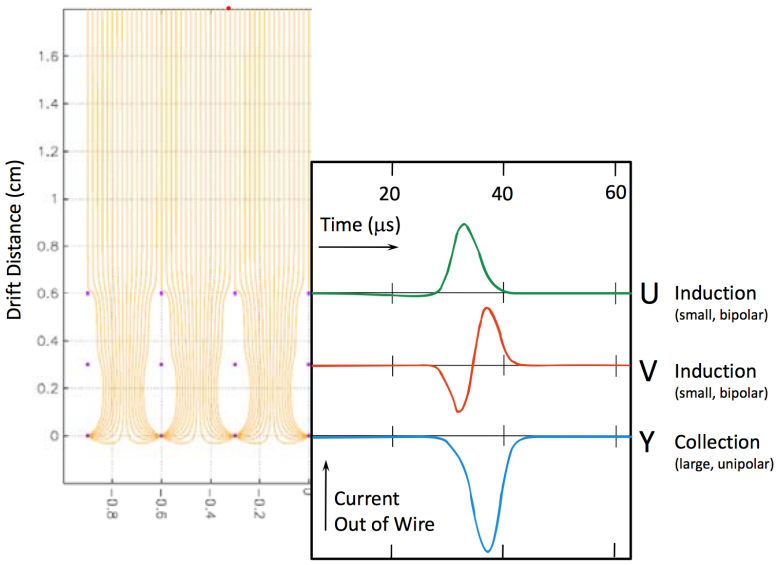

Fig. 1.28: Planar illustration of electric field lines (i.e. drifting electron trajectory) and the signals induced by an ionising track at 90° to the wire direction and 0° to the normal identifying the wire planes U, V, and Y. Figure taken from Cressler and Mantooth 2013.

to the collection plane, the filling liquid must not form negative ions by electron attachment, as it is for argon, and it must be free of electronegative impurities. Positive ions moving to the cathode induce on the anode a signal of the same polarity as that from electrons moving to the anode. It was shown, theoretically and experimentally by Bunemann *et al.*, that this induction effect can be eliminated by inserting a grid in front of the collecting wire plane, hereby restoring the proportionality between the electron pulses collected and the ionisation charges produced (i.e. energy deposited). Figure 1.27 shows schematically the anode A, the shielding grid G, and the cathode P, where the z-axis indicates the direction of the impinging particle and the y-axis points towards the direction of the drifting electrons. Note that in Fig. 1.27 the electric field has been defined as the positive gradient of the potential, with the field lines oriented in the direction of motion of the electrons. Bunemann *et al.* also demonstrated that, while shielding from the effect of the positive ions, the potential between the grid and the collector could be tuned in such a way that the collection of electrons by the screening grid could be avoided. The condition for all the drift field lines to by-pass the grid, so that it is fully transparent for the drifting electrons, is given by:

$$\left|\frac{\vec{E}_P}{\vec{E}_Q}\right| > \frac{1+\rho}{1-\rho} \tag{1.49}$$

where $\vec{E}_Q$ is the electric field between the the ionisation track and the grid, $\vec{E}_P$ is the electric field between the the grid and the collecting plane, and $\rho = 2\pi r/d$, with r and d being, respectively, the wire radius and the wire spacing of the grid. Equation (1.49) can be generalised to any two regions i and j, by simply replacing $E_G \to E_i$ and $E_Q \to E_j$.

The collection electrode in modern TPCs exploits exactly the same principle, with the only difference that, instead of one grid and one anode, three wire planes (U, V, Y) are used, with a minimum of two (V, Y) being instrumented to realise readout of charges along different spatial coordinates. The two innermost electrodes (U, V) are called induction planes and, when appropriately biased according to (1.49), they allow electrons to travel through them, while providing signals in a non-destructive way—i.e. no net charge is collected (Schenk, 2015). Signals on the induction-planes are produced from induced currents, which are positive when the drift electrons move towards the wire, and opposite in sign when the electrons move away from it, resulting in a bipolar signal (Joshi and Qian, 2015). The first plane U, which has usually either a vertical (90°) or horizontal (0°) orientation with respect to the horizontal beam direction, serves primarily the purpose of shielding the other two electrodes from the positive ions charge effect explained earlier (sometimes the U plane is not even supplied with readout electronics, playing only the role of shielding such as in ArgoNeuT). The second wire plane V is oriented at some angle θ (e.g. 60° in ICARUS) with respect to the horizontal direction. Finally, the third wire plane Y, oriented as $-\theta$ (e.g. −60° in ICARUS) with respect to the horizontal direction, collects the charge, hereby generating a unipolar signal and enabling precise measurement of the ionisation produced by the particle transversing the medium. Figure 1.28 illustrates the electric field lines (i.e. drifting electron trajectory) and the signals induced on the the U, V, and Y planes. Combining the electron drift velocity ($v_D \simeq 1.5\,\mathrm{mm}/\,\mu\mathrm{s}$) with the time of each ionisation signal relative to the zero time given by the primary scintillation, information on the depth of the track along the electric field direction can be computed at each sampled time, achieving a 3D image resolution of less than $1\,\mathrm{mm}^3$.

Completed, current, and future neutrino LAr TPCs

The first ever built large scale liquid argon detector for studies of neutrinos was ICARUS-T600 (Antonello *et al.*, 2015). Located at the INFN Gran Sasso Underground

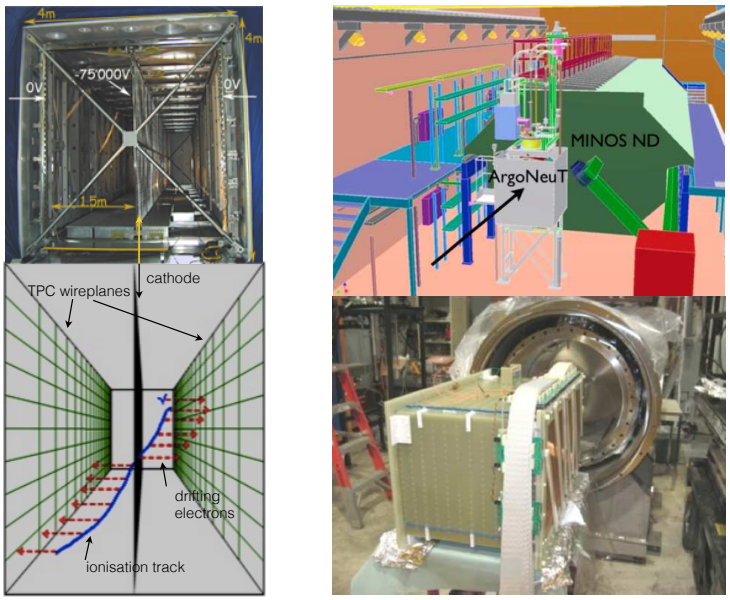

ICARUS-T600 ArgoNeuT

Fig. 1.29: Left: Vertical cross-sectional view of ICARUS. The picture is taken from the ICARUS website `http://icarus.lngs.infn.it/DetectorOverview.php`. Right: Photo of the ArgoNeuT TPC right before entering the inner cryostat (Palamara, 2011) and schematics of the location of the ArgoNeuT detector in the NuMI beam, in front of the MINOS detector (Guenette, 2011).

Laboratory (LNGS), it comprised a total argon mass of ∼760 t (∼480 t active mass) and two read-out chambers (two TPCs for each half-vessel) mounted on the internal walls and separated by a common cathode, with a drift length of 1.5 m. Figure 1.29 (left) shows the ICARUS-T600 vertical cross section. ICARUS collected data using the CERN Neutrinos to Gran Sasso (CNGS) beam between 2010 and 2013, and it has now been relocated upstream the MicroBooNE near detector (MicroBooNE Collaboration, 2012) in the Booster Neutrino Beam (BNB) line at Fermilab. ICARUS, together with MicroBooNE and SBND, is part of the Short-Baseline Neutrino (SBN) program at Fermilab, using the BNB. In such program, ICARUS will serve as the far detector, MicroBooNE as the intermediate, and SBND as the near detector (see Fig. 1.30). The motivation for the SBN program is to investigate the unexplained low-energy excess

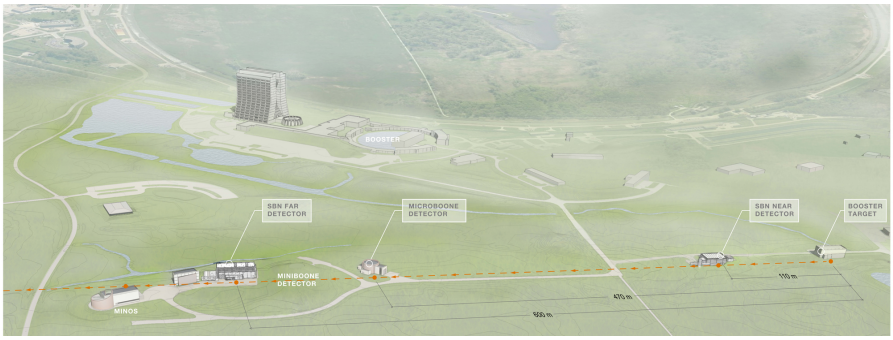

Fig. 1.30: Map showing the location of the three LAr TPC experiments that are part of the Short Baseline Neutrino program at Fermilab.

of electron neutrinos in $\nu_\mu/\bar{\nu}_\mu$ beam seen by the MiniBooNE experiment (and before by LSND), which is compatible with sterile neutrino oscillation models (MicroBooNE Collaboration, 2008). MiniBooNE looked for appearance of ν_e and $\bar{\nu}_e$ ($\nu_\mu \to \nu_e$ and $\bar{\nu}_\mu \to \bar{\nu}_e$) above the background prediction, under a two-neutrino mixing approximation. Since MiniBooNE is a Čerenkov detector, it cannot tell the difference between a single outgoing electron or single outgoing gamma, hence, the observed excess could be explained by unaccounted background, not hinting at radically new physics. As liquid argon TPCs can distinguish between electrons and photons using 3D image reconstruction, they will be able to assess the nature of the MiniBooNE excess. Excavation work for the SBN far detector building, housing the refurbished ICARUS detector, began in July 2015. The building is scheduled to be completed in late 2016.

Let us now describe the second ever built LAr TPC operating in a neutrino beam: ArgoNeuT. ArgoNeuT is a 175 litre liquid argon TPC, exposed to the NuMI muon neutrino beamline at Fermilab and located just upstream of the MINOS Near Detector (ND) (see Fig. 1.29, top, right). Constructed to gain experience building and operating LAr TPCs in a real beam environment, its goal was also to collect real data to be used for developing simulation and reconstruction code (Soderberg, 2009) as a first step in a program towards ton-scale long-baseline neutrino oscillation experiments (Palamara, 2011). Data-taking concluded in March 2010, and analysis is still ongoing. Given the small dimensions of the TPC, ArgoNeuT could not contain the majority of the muons produced in neutrino interactions. As such, it used data from MINOS to obtain information on long-track muons for its data analysis. The detector followed the ICARUS design and differed mainly in that only one read-out module was used, consisting of three wire planes with 240 wires each, separated by 4 mm (Guenette, 2011).

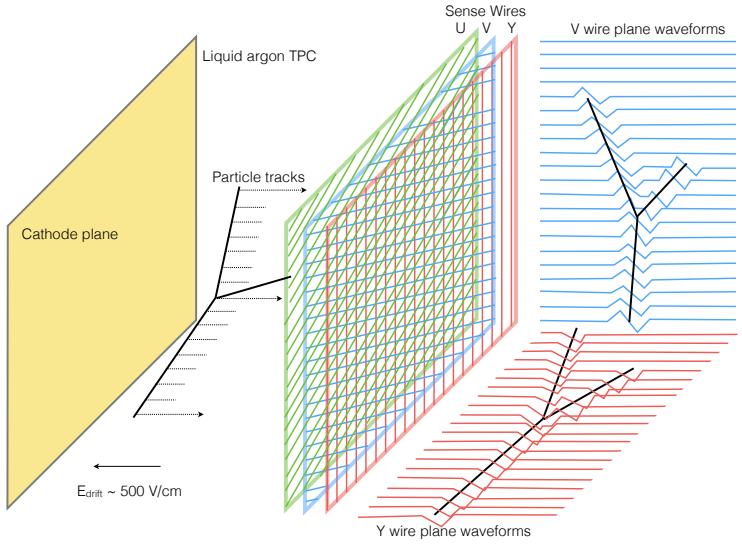

Fig. 1.31: Illustration of ArgoNeuT signal readout. Figure taken from (Radeka *et al.*, 2009).

ArgoNeuT's rectangular volume ($90 \times 40 \times 48$ cm) was enclosed in a cryostat, featuring a closed-loop Ar re-liquefaction and purification system, which guarantees high purity for large electron mobility. The operating cathode voltage of 25 kV ensured an electric field of 500 V/cm, for which the electron speed was 1.55 mm/ µs. Figure 1.29 (right, bottom) shows ArgoNeuT's TPC right before entering the inner cryostat.

The dominant interaction modes for neutrinos in the GeV-region are: charge current quasi-elastic (CCQE), neutral current quasi-elastic (NCQE), charge current resonant pion production (CCRES), neutral current resonant pion production (NCRES), charged current coherent pion production (CCCOH), and charge current deep inelastic scattering (CCDIS). While CC neutrino interactions (Fig. 1.32) produce an outgoing lepton, NC interactions often generate a π_0, which immediately decays into two gamma particles, each of which can turn into an electron-positron to create electromagnetic showers. Electron showers can be discriminated from gamma showers in LAr TPCs, but an experimental measure of the efficiency of this technique has never been carried out (Foreman, 2015).

ArgoNeuT mostly focused on the CCQE channel, as it aimed at measuring the cross section of muon neutrinos and anti-neutrinos for such interactions, although a paper on the measurement of neutral current π_0 production in ν_μ-argon and $\bar{\nu}_\mu$-

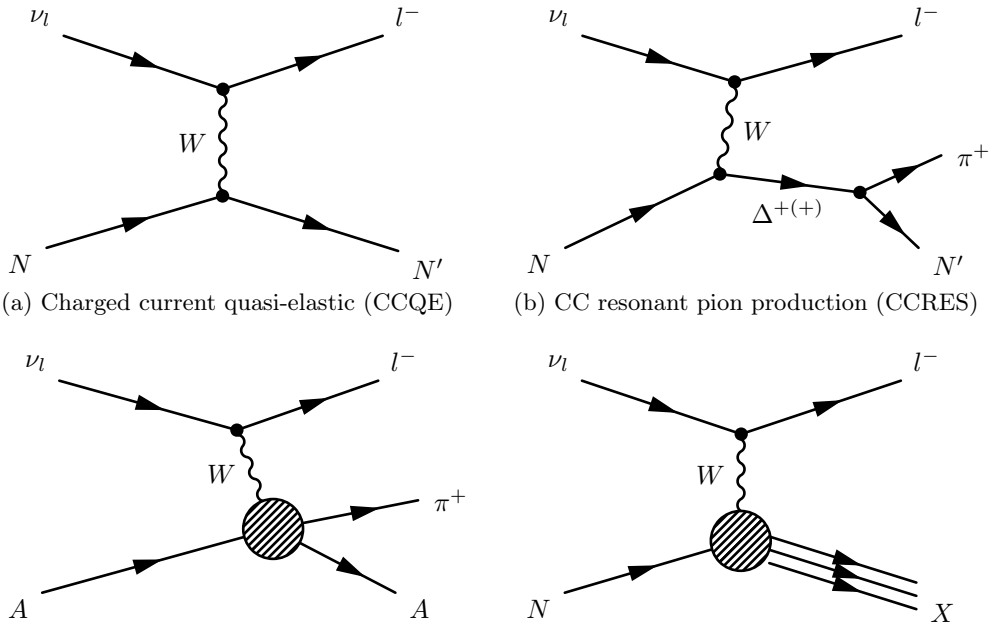

(a) Charged current quasi-elastic (CCQE)
(b) CC resonant pion production (CCRES)
(c) Charged current coherent (CCCOH)
(d) CC deep inelastic scattering (CCDIS)

Fig. 1.32: Feynman diagrams of the main neutrino-nucleon interactions relevant to long-baseline neutrino oscillation experiments. N and N' indicate nucleons, A indicates that the reaction occured with the whole nucleus. For neutrinos produced in

argon scattering has been recently published (Acciarri, 2015). For its data analysis, the ArgoNeuT collaboration used an analysis software called LArSoft (Church, 2014), specifically designed for all LAr experiments in the US. This software was developed by the ArgoNeuT collaboration, together with MicroBooNE and DUNE collaborations. The event reconstruction in LArSoft proceeded as follows (Palamara, 2011):

1. Hit construction and identification from raw data signal information.
2. Clustering among nearby hits.
3. 3D track reconstruction.
4. Calorimetric reconstruction.
5. Particle identification (from the energy deposited per unit length along the track, dE/dx).
6. Escaping muon momentum reconstruction using the downstream MINOS detector.

An example of the raw data for a neutrino candidate event is given in Fig. 1.33. Calorimetric measurements can be combined with 3D track reconstruction to allow a

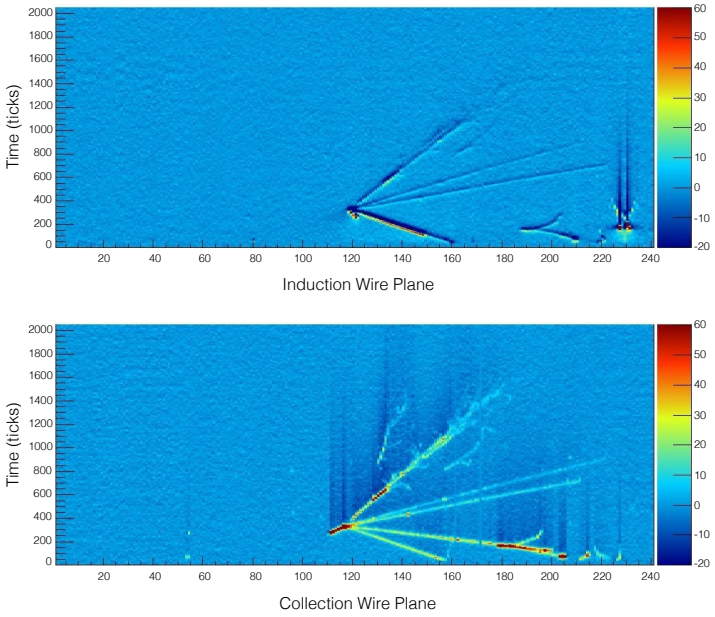

Fig. 1.33: Neutrino event candidate from ArgoNeuT. The raw data for the induction (V) and collection (Y) planes are displayed. (Soderberg, 2009).

powerful topological tool to discriminate against background. Moreover, the neutrino energy deposition can be reconstructed using two independent and complementary methods, namely calorimetric and kinematic (Ankowski *et al.*, 2015).

Since the neutrino oscillation parameters depend on the neutrino energy beam (see eqn 1.48), it is crucial to correctly reconstruct the unknown incoming-neutrino energy E_ν. The kinematic method reconstructs E_ν from the measured kinematics of the outgoing leptons, hereby assuming the beam particle interacts with a single nucleon at rest:

$$\begin{aligned} \nu_\mu + n &\rightarrow \mu^- + p \\ E_\nu &= E_\nu(E_\mu, \theta_\mu) \end{aligned} \tag{1.50}$$

where θ_μ is the scattering angle of the outgoing muon with respect to the direction of the incoming neutrino. Instead, the calorimetric technique reconstructs E_ν by summing the measured energies of the particles in the final state and can be applied to any type of CC interaction. So, in the case of a single muon in the final state, we have:

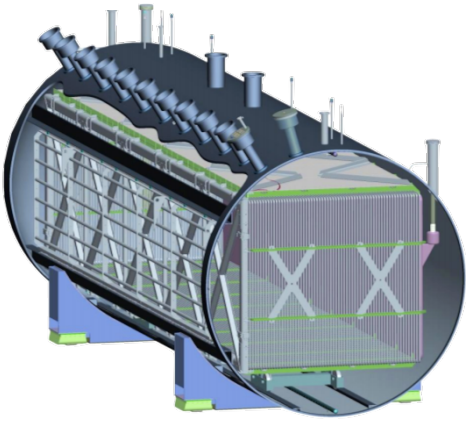

Fig. 1.34: MicroBooNE's TPC ($2.5 \times 2.3 \times 10.2\,\mathrm{m}$, with $2.5\,\mathrm{m}$ being along the drift direction) inside the cryostat looking along the beamline from the downstream side. The cathode pane is on the right of the picture (beam-left). The wire planes and PMT array are on the left (beam-right).

$$\begin{aligned} \nu_\mu + n &\to \mu^- + X \\ E_\nu &\simeq E_\mu + E_X \end{aligned} \tag{1.51}$$

The advantage of such approach is that no *a priori* assumption is made on the underlying interaction, although an accurate reconstruction of hadrons is surely not trivial.

ArgoNeuT was refurbished in 2015 and it is now part of the LArIAT (LArTPC In A Test beam) experiment, whose aim is to explore particle response calibration, technical R&D, and several physics topics relevant to current and future liquid argon detectors (Foreman, 2015).

The MicroBooNE experiment, which we have mentioned earlier, is located 470 m from the BNB source and holds 170 t (86 t) of liquid argon. The TPC size is $2.5 \times 2.3 \times 10.2\,\mathrm{m}$, with $2.5\,\mathrm{m}$ being along the drift direction. A schematic is shown in Fig. 1.34. Similarly to ArgoNeuT, MicroBooNE uses only one read-out module, consisting of three wire planes with 3 mm wire separation and 8,256 wires in total. 30 PMTs provide the signal trigger and the event reference time. MicroBooNE's goal is twofold: investigating the nature of the low-energy excess in the electron neutrino energy spectrum measured by MiniBooNE and providing an R&D base for next generation liquid argon neutrino experiments, such as the Deep Underground Neutrino Experiment (DUNE) (Karagiorgi, 2013). MicroBooNe has started taking data in 2015.

The last detector being part of the BNB line complex is the Short-Baseline Near Detector (SBND), a TPC of 112 t of active liquid argon volume, located 110 m from the neutrino source. SBND is currently in its design/construction phase and is planned to be working by 2018. Being the closest experiment to the beam, SBND will have very high interaction rates, herby allowing precision cross section measurements. Albeit its primary goal is to serve as the near detector for the MicroBooNE experiment, SBND will also play the role of the engineering prototype for DUNE, as it employs the "membrane cryostat" design of the DUNE far detector (Karagiorgi, 2013). UCL, together with Yale University, leads the design and construction of the SBND high voltage feedthrough. The LARA test stand I built at UCL (see Chapter 3) will provide the testing facility, with my cold high-voltage R&D (see 6) also improving designs of the feedthrough.

Finally, the DUNE experiment (whose Conceptual Design Report [CDR] can be found in DUNE Collaboration 2016) will be part of the next generation of long-baseline neutrino experiments using LAr TPC technology. The DUNE far detector will be installed 1457 m underground at the Stanford Underground Research Facility and will detect the neutrino beam coming from the Long-Baseline Neutrino Facility (LBNF) at Fermilab, after traversing 1300 km of earth.

An experiment aimed at testing new technologies to be implemented in DUNE is the Long Baseline Observatory Demonstration (LBNO-DEMO) at CERN, also called WA105 experiment (Galymov, 2015; Agostino *et al.*, 2014). One of the main goals of LBNO-DEMO is to demonstrate the operation and scalability of dual-phase LAr TPCs (DP LAr TPC) for long-baseline neutrino searches. A prototype two-phase LAr TPC detector (WA105 detector), with 5 ton (fiducial) argon mass and dimensions of $3 \times 1 \times 1$ m, is currently under construction and will be operational in a few months (a second prototype with dimensions $6 \times 6 \times 6$ m is already being developed).

As DUNE will be able to constrain the neutrino oscillation parameters of the PMNS matrix, the mystery of their mass and of matter generation in the early universe will be unravelled. Unfortunately, we will have to wait until 2024 for DUNE to be operational.

2
The SCENE experiment

The experimental measurement of light and ionisation yields from nuclear recoils in LAr at keV energies has to be known precisely in order to design experiments, define the energy scale for DM searches, establish detector sensitivity to nuclear recoils, and interpret LAr signal response from WIMPs. Past measurements of scintillation yield of nuclear recoils in liquid argon were only available at zero electric field (Regenfus *et al.* 2012; Gastler *et al.* 2012; Creus *et al.* 2015), and no measurement of ionisation yield was available for nuclear recoils at low-energy (relevant to WIMP searches). The SCENE experiment that I worked on was built to fill in these gaps, performing direct measurements to determine these important quantities at low energies and with unprecedented precision. $\mathcal{L}_{\text{eff}}$ and $\mathcal{Q}_y$[1] were measured by resembling WIMPs impact with LAr atomic nuclei in a LAr TPC using a neutron beam. For the purpose only single elastic scatterings were studied and their deposited energy in keV_{ee} was determined by combining the information on the incident neutron energy with the scattering angle measured with liquid scintillator neutron detectors. The relative scintillation efficiency was measured with respect to $^{83\text{m}}$Kr, which, due to its short half-life of 1.83 hours, does not contaminate the detector. $^{83\text{m}}$Kr decays into stable ^{83}Kr by emitting two sequential gammas of energy 9.4 and 32.1 keV for a total energy deposition of 41.5 keV. Light yield for electron recoils shows a linear response above 30 keV as reported by Creus *et al.* 2015. This allows to directly compare the results obtained from SCENE to those from other experiments using a ^{60}Co source (Gastler *et al.*, 2012) or a ^{241}Am source (Regenfus *et al.* 2012; Creus *et al.* 2015). The results presented in this chapter, of significance to entire DM community, have been published in Alexander *et al.* 2013*a* and Cao *et al.* 2015.

2.1 Experimental setup

The experiment was performed at the University of Notre Dame Institute for Structure and Nuclear Astrophysics in two runs in June, when $\mathcal{L}_{\text{eff}}$ was measured, and Octo-

[1] For the definition of $\mathcal{L}_{\text{eff}}$ and $\mathcal{Q}_y$, see Chapter 1, Section 1.1.6

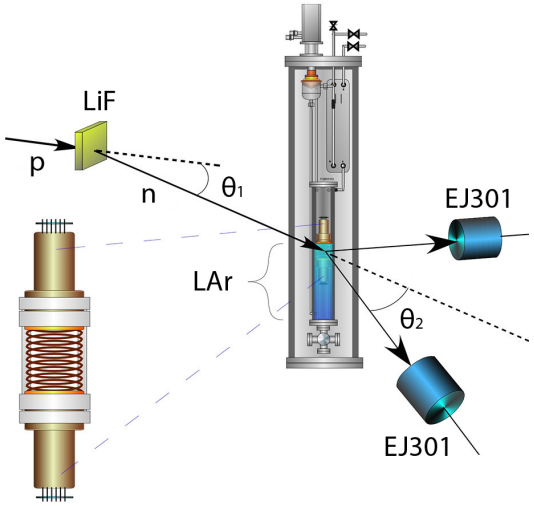

Fig. 2.1: Schematic of the experiment setup and a zoom-in on the TPC with the PMTs, field cage and PTFE case. θ_1 is the angle between the proton beam and the neutron beam axis. θ_2 is the neutron scattering angle. Figure taken from Cao *et al.* 2015.

ber 2013, when $\mathcal{Q}_y$ was determined. Neutrons were generated through the reaction ^{7}Li(p,n)^{7}Be using a proton beam from the Tandem accelerator striking a 20 mg/cm^2 thick LiF target deposited on a 1-mm-thick aluminium backing. The proton beam was pulsed into bunches of 6.3×10^4 protons spanning 1 ns in time, with intervals of 101.4 ns between bunches. The accelerator pulse selector was set such that only one every two proton pulses stroke the LiF target, leading to a neutron beam pulse every 203.0 ns. During the S2 studies, the pulse selector was instead set to allow one of every four, five, or eight pulses.

The LAr TPC was placed 73.1 cm from the LiF target in the first run and 82.4 cm in the second. To determine the light and ionisation yields as a function of nuclear recoil energy, we measured the neutron scattering angle using three EJ301[2] 12.7 × 12.7 cm cylindrical liquid scintillator neutron detectors, which also provided timing information and pulse shape discrimination, both of which suppressed the background from γ-ray interactions.

As can be seen from Fig. 2.3, the neutron detectors on the sides, at a distance of 71 cm from the LAr target, were placed on a two-angle goniometer-style stand to form the same scattering angle with respect to the neutron beam axis (thus measuring

[2] http://www.eljentechnology.com/index.php/products/liquid-scintillators/71-ej-301, EJ301 liquid scintillator from Eljen Technology, Inc.

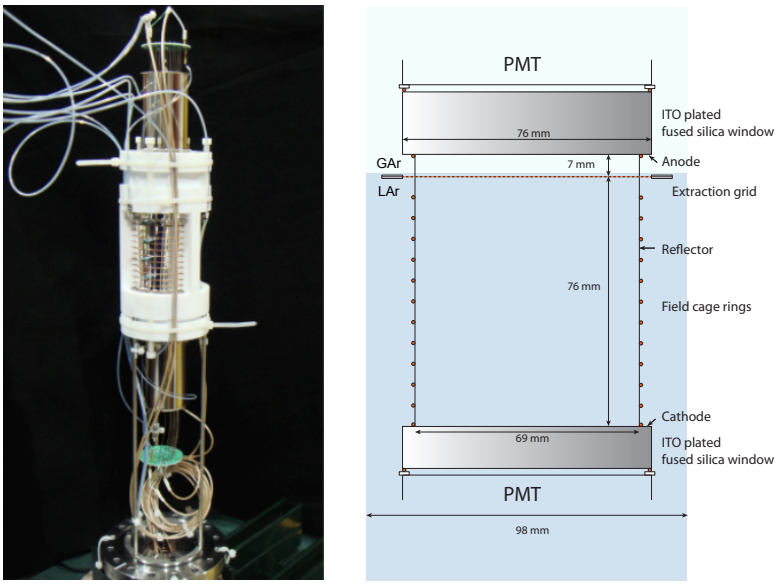

Fig. 2.2: Left: Photo of the LAr TPC. Right: Sectional drawing of the TPC.

events corresponding to the same energy deposition). By moving the detectors along the stand, an event with a specific scattering angle can be selected, and consequently a specific recoil energy be chosen. This is schematically illustrated in Fig. 2.1.

The two-angle goniometric mount also allowed the EJ301 detectors to be placed at positions corresponding to a single scattering angle but at different azimuthal angles (this is practically done by sliding the horizontal structure upwards or downwards), corresponding to recoil nucleus directions parallel or perpendicular to the drift field (Cao, 2014). As the vertical structure of the goniometric stand prevents the neutron detectors on the sides to be placed at a scattering angle equal to zero, a third detector had to be added (this can slide upwards and downwards, but cannot move horizontally).

In the non-relativistic limit, which holds true for incoming neutrons with energies below 939.6 MeV, conservation of momentum and energy in the centre-of-mass frame leads to the following equation:

$$E_r = E_n \frac{4M_n M_{Ar}}{M_n + M_{Ar}} \frac{1 - \cos\theta_{CM}}{2} \tag{2.1}$$

which relates the nuclear recoil energy E_r to the centre-of-mass frame scattering angle θ_{CM} and the incident neutron energy E_n, with M_n being the neutron mass and M_{Ar}

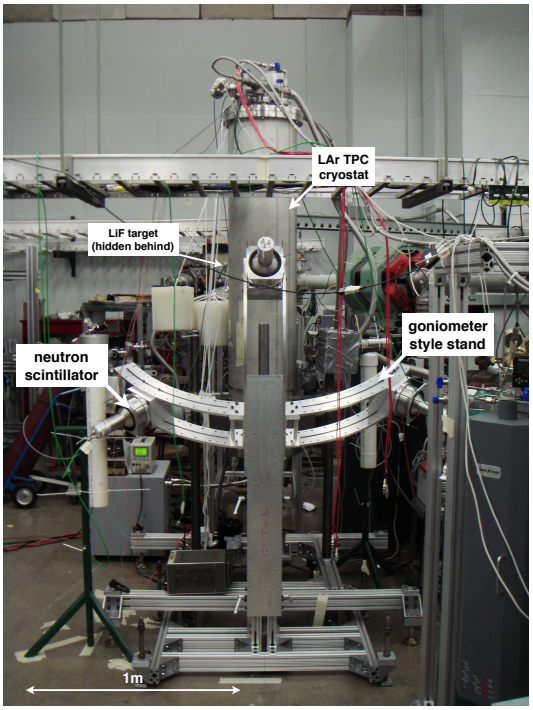

Fig. 2.3: Real setup during the June run.

the Ar atomic mass. The relation between θ_{CM} and the scattering angle in the lab frame θ_{LAB} is given by:

$$\tan\theta_{LAB} = \frac{\sin\theta_{CM}}{M_n/M_{Ar} + \cos\theta_{CM}} \tag{2.2}$$

Use of eqn (2.1) to determine the nuclear recoil energy only relies on the incident neutron energy (calculated from the measured proton energy beam) and the measured scattering angle. To take full account of all materials and geometry of the detectors and estimate the nuclear recoil energy more realistically, we performed a Monte Carlo (MC) simulation of neutron scattering in our apparatus. From the energy distribution computed for each measured scattering angle, we obtained the median nuclear recoil energy of single scattering component, and the plus/minus band in which 68% of the scatters are contained. Table 2.1 lists the configurations of beam energy, scattering angle, and the corresponding median nuclear recoil energy in the TPC at which data have been taken.

Table 2.1 Proton energy, neutron energy, and scattering angle for the two runs. The neutron production angle, θ_1, was 25.4°in June and 35.6°in October. The fourth column lists the median energy of the single scattering distribution as computed by the MC simulation of neutron scattering in our apparatus. For completeness, the nuclear recoil energy calculated using eqns (2.1) nad (2.2) is also shown in the last column labeled "Geometric energy". Data sets marked with an asterisk (*) were taken with the TPC AND trigger requiring the coincidence of the top and bottom PMTs. All other data set required triggering only of one of the two PMTs.

	Proton energy [MeV]	Neutron energy [MeV]	Scattering angle [°]	Nuclear recoil energy [keV]	Geometric energy [keV]
Jun 2013	2.376	0.604	49.9	$10.3^{+1.5}_{-1.4}$	10.8
	2.930	1.168	42.2	$14.8^{+2.7}_{-2.6}$	15.2
	2.930	1.168	49.2	$20.5^{+3.0}_{-2.8}$	20.8
	2.930	1.168	59.9	$28.7^{+2.8}_{-2.8}$	29.0
	2.930	1.168	82.2	$49.7^{+3.4}_{-3.4}$	49.9
Oct 2013	2.316	0.510	69.7	$16.9^{+1.5}_{-1.5}$	16.5
	3.607	1.773	45.0	$^{*}25.4^{+3.2}_{-2.9}$	26.1
	3.607	1.119	69.7	$^{*}36.1^{+3.1}_{-3.1}$	36.3
	3.607	1.773	69.7	$^{*}57.3^{+5.0}_{-4.9}$	57.6

The design of the LAr TPC closely resembled the one used in DarkSide10 (Alexander *et al.*, 2013*b*). Figure 2.2 shows the real TPC (left) and the TPC sectional drawing. The liquid argon active volume was enclosed in a polytetrafluoroethylene (PTFE) cylinder 68.8 mm in diameter and 76.2 mm in height, lined with 3M Vikuiti enhanced specular reflector and capped by fused silica windows. The choice of the height and diameter of the liquid argon volume is a design trade-off between contamination from multiple scatterings and adequate statistics from single scattering events. A Monte Carlo simulation of the apparatus showed that for 10.3 keV nuclear recoil energy multiple scattering accounts for less than 32% of the total event rate between 5 and 16 keV and the position of the single scattering peak is not affected by background. The LAr target was viewed through the fused silica windows by two 3" Hamamatsu R11065 photomultiplier tubes (PMTs). Since liquid argon scintillates in the VUV range, peaking at 127 nm, and PMTs are practically blind in this bandwidth, all internal surfaces of the TPC were coated through vacuum deposition with the wavelength-shifter TetraPhenylButadiene (TPB).

The fused silica windows, coated with the transparent conductive material indium tin oxide (ITO), functioned as anode and cathode in the TPC. To make the field more uniform, copper field rings were embedded in the PTFE cylinder and resistors

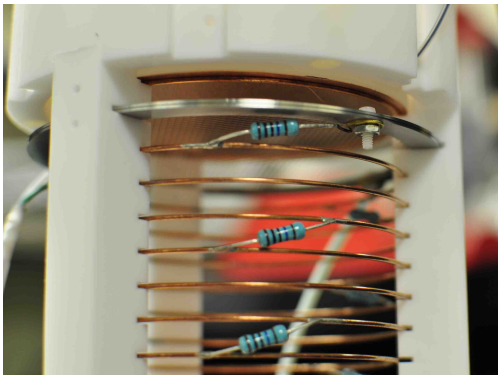

Fig. 2.4: Zoomed-in picture of the TPC, showing the stainless steel mesh, the field rings, and the PTFE support. The Vikuiti reflector is not installed in the picture and the anode window is replaced by a copper disk for clear view.

were soldered between adjacent race tracks to allow a step-by-step drop in voltage (see Fig. 2.4). A hexagonal stainless steel mesh, fixed 7 mm below the top window, was connected to the ground to provide the electric drift field, between the bottom window and the grid, and the extraction and multiplication fields, between the mesh and the top window. The cathode and the anode voltages were applied independently, which allowed us to collect data with or without ionisation signal at our choice. The LAr level was maintained 2 mm below the mesh in June and 1 mm above the mesh in October to ensure proper production of S2 signals (see Fig. 2.5). It is worth noting that in the second configuration light yield and resolution are worsened, as scintillation photons undergoing internal reflection at the liquid-gas interface would also have to pass multiple times through the mesh.

To monitor the liquid level three parallel plate capacitive level sensors 10×10 mm were positioned equidistantly along the circumference of the mesh (see Fig. 2.6). Nominal drift voltages of 50, 100, 200, 300, 500 and 1000 V/cm were applied. The electrostatic potential in the detector was calculated using ELMER[3], which took as in input a 3D model of the TPC generated in GMSH (Geuzaine and Remacle, 2009), convolved with the GEANT4 (Agostinelli *et al.*, 2003) simulation of the neutron scatter position to obtain the neutron-weighted median field at each voltage setting. Table 2.2 summarises these values and also lists for each nominal electric field the ranges in which 68% of the neutron scattering are contained. From now on, when referring to the electric drift field settings, I will implicitly mean the neutron-weighted median values.

[3] www.csc.fi/elmer/

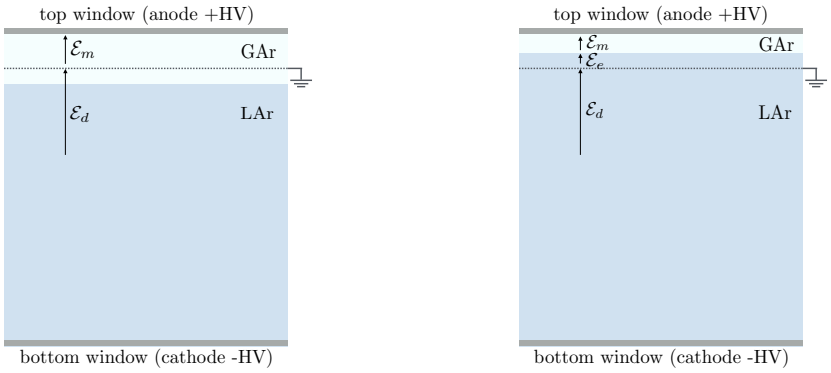

I configuration II configuration

Fig. 2.5: In the first configuration, where the liquid level is below the mesh, the electric drift field $\mathcal{E}_d$, at the liquid-gas boundary is not strong enough to extract electrons (and that is why the extraction field between the liquid surface and the mesh is not indicated in the picture). In the second configuration the liquid level is above the mesh and we distinguish an extraction and multiplication field ($\mathcal{E}_e$ and $\mathcal{E}_m$, respectively). Here the voltage across the grid and anode is sufficient to pull electrons out of the liquid. Although produced from the same voltage, the fields in the liquid and gas regions have different values due to dielectric constants of LAr and GAr being different (since $\epsilon_{GAr} > \epsilon_{LAr}$ it follows that $\mathcal{E}_m > \mathcal{E}_e$).

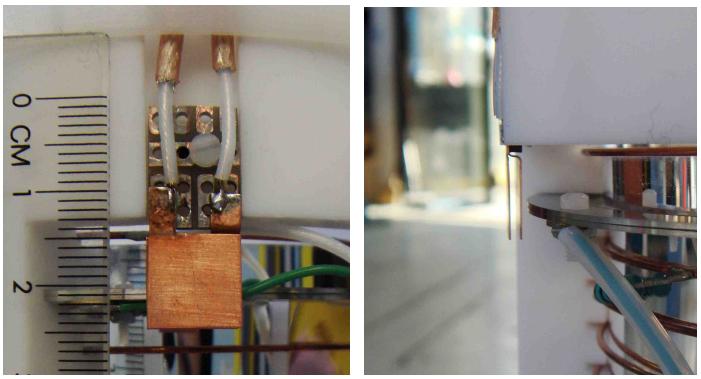

Fig. 2.6: Photos of the parallel-plate capacitive level sensor.

Finally, Fig. 2.7 shows the gas system setup. Gas argon was fed to the TPC chamber after being cooled by a Cryomech PT-60[4] connected via a heater block to a condenser.

[4] www.cryomech.com

Table 2.2 Nominal electric drift field values, neutron-weighted median field obtained by combining an ELMER finite element simulation of the electrostatic potential in the TPC with a GEANT4 simulation of neutron scattering 3D reconstruction. The last column shows the ranges which include 68% of all neutron scatters at each nominal electric drift field setting.

Nominal $\mathcal{E}_d$ [V/cm]	Neutron-weighted median $\mathcal{E}_d$ [V/cm]	68% coverage $\mathcal{E}_d$ range [V/cm]
50	49.5	45.5–53.5
100	96.4	92.5–108
200	193	189–212
300	293	285–322
500	486	476–536
1000	970	954–1073

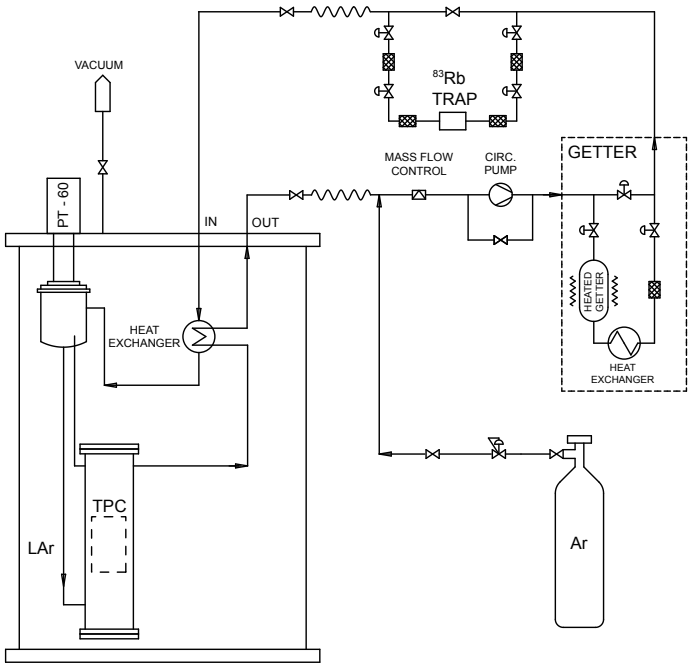

Fig. 2.7: Gas system used for continuos purification of the liquid argon and the ^{83}Rb trap for injection of ^{83m}Kr. Figure taken from Cao *et al.* 2015.

Grade 6.0 (99.9999% purity) gas argon was recirculated through a SAES MonoTorr PS4-MT3-R1 getter and further purified from both the gas bottle and the LAr TPC.

2.2 Data acquisition and trigger efficiency

Data from the PMTs in the TPC, the neutron detectors, and the accelerator RF signal were acquired using a 250 MS/s digitiser. Data were recorded using the in-house daqman data acquisition and analysis software[5]. When the TPC was operated without ionisation signal, the waveforms were recorded over a time window of 16 µs, including 5 µs before the hardware trigger to allow for baseline calculation. At the times when the TPC was operated with the ionisation signal, the length of the digitiser waveforms was set to the maximum drift time plus 45 µs to allow for full S2 recording.

Data were acquired only when a coincidence between the TPC trigger and one of the neutron detectors occurred. Besides these coincidence events, events triggered by the TPC only, which mainly consisted of ^{83m}Kr events, were also recorded at an arbitrary rate, 12 Hz in June and 5 Hz in October, to constantly monitor the stability of the system (more on this in Section 2.3). The TPC trigger could be chosen as either the OR or the AND of the top and bottom TPC PMTs (i.e. TPC trigger set to "AND" if both PMTs in the TPC observe an event at the same time; TPC trigger set to "OR" if any of the two PMTs records something). The PMTs thresholds were both set to ∼0.2 p.e.

Trigger efficiency may affect the observed energy and, as a consequence, introduce a distortion in the S1 and S2 spectra, leading to a major systematic uncertainty in $\mathcal{L}_{\text{eff}}$ and $\mathcal{Q}_y$. As reported by Manalaysay in 2010, a falling of the trigger efficiency in the low-energy region will effect the position of the energy spectrum of low-energy recoils by shifting the observed peak to higher energies (contrary to high-energy events, low-energy event are less efficiently collected and thus get suppressed). It follows that as the recoil energy decreases, the measured peak will approximately stay at constant value. Not taking into account the trigger efficiency or underestimating it will result in a higher reconstructed $\mathcal{L}_{\text{eff}}$ at low recoil energies (where the trigger efficiency effects are more significant). Vice versa, if one overcompensates the observed spectrum by overestimating the trigger efficiency, the resulting $\mathcal{L}_{\text{eff}}$ will fall with decreasing energy (see Fig. 2.8).

To determine the efficiency of our trigger setup we used the procedure described in Plante *et al.* 2011, where a ^{22}Na source (β^+ emitter) is positioned between the TPC and a neutron detector, such that the solid angle subtended by the neutron counter was larger than the one subtended by the TPC. This ensures that the whole active LAr volume of the TPC is probed. The annihilation of the ^{22}Na positron with an electron occurs with the positron practically at rest. The back-to-back pair of gammas

[5] github.com/bloer/daqman

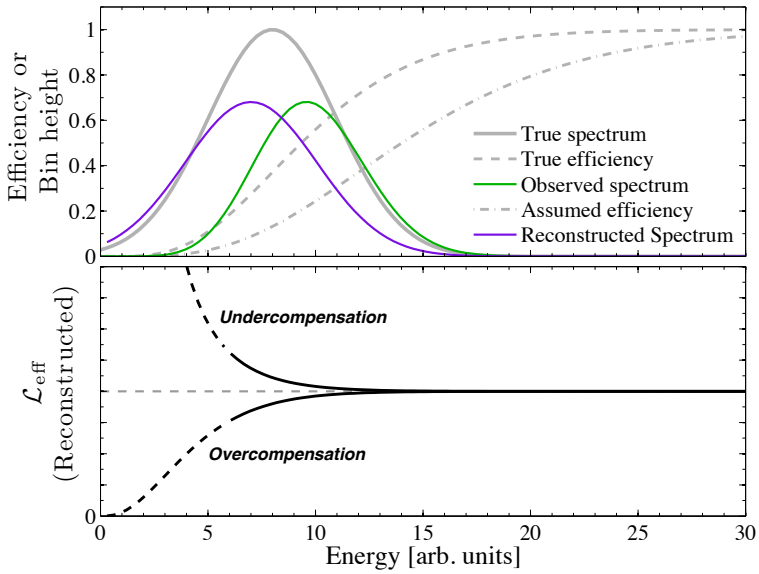

Fig. 2.8: Plot taken from Manalaysay 2010. The top plot shows how detection efficiency (trigger efficiency) may affect the position of the peak. The solid curve is an hypothetical true peak, which, due to a falling detection efficiency in the low-energy region (grey dashed), is observed as the green curve. If the wrong detection efficiency is assumed (grey dot-dashed, efficiency is overestimated), the resulting peak (purple) will be shifted below the true one. The bottom plot shows how a constant $\mathcal{L}_{\rm eff}$ would be affected if one undercompensates or overcompensates for the detection efficiency.

emitted from the e^+e^- annihilation should be detected at the same time in the LAr TPC and neutron detector. The trigger efficiency for both the OR and AND trigger setups was computed as the number of events collected by the TPC (in the OR or AND mode) over the the number of events detected by the neutron detector, as a function of the number of photoelectrons measured by the TPC. Figure 2.9 shows that the TPC trigger efficiency obtained with this method was above 90% for pulses above 1 p.e with the OR trigger and above 10 p.e with the AND trigger.

To further assess the effects of the trigger setup we analysed two subsets of 20.5 keV nuclear recoils data taken with both OR and AND TPC triggers. As can be seen from Fig. 2.10 the only alteration in the S1 spectrum between the two trigger configurations is below 12 p.e, which agrees with what was independently found using the ^{22}Na source. A Gaussian plus first polynomial fit to the peaks gave a mean of 22.3 ± 0.6 p.e with the OR trigger and 22.9 ± 0.7 p.e with the AND trigger. Since the results are statistically compatible, we conclude that data collected with the AND trigger provided undistorted

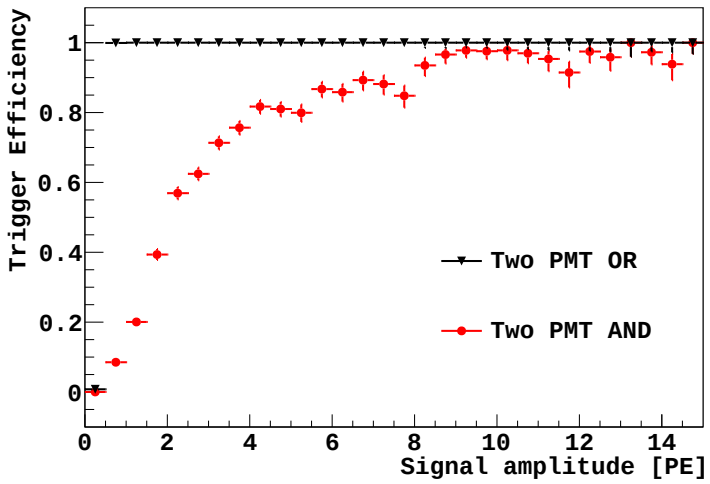

Fig. 2.9: Efficiency for the OR (black triangles) and AND (red, solid dots) trigger configurations. Figure taken from Cao *et al.* 2015.

Table 2.3 Lower fit boundaries for the S2 spectra analysis at each drift field, obtained by finding the corresponding S2 value for an S1 of 4 p.e for the the OR trigger and 12 p.e for the AND trigger. Table taken from Cao *et al.* 2015.

Electric field [V/cm]	S2 lower bound OR [p.e]	S2 lower bound AND [p.e]
49.5	n/a	163
96.4	104	174
193	123	196
293	142	224
486	183	255

spectra above 12 p.e. and could be used reliably. Setting the AND between TPC PMTs has the advantage of saving space on the disk as less data is written to it. In fact, many of the background events, which become dominating below 5 p.e, are in this way rejected. The lower fitting bounds in the S1 spectra were set to 4 p.e for data taken with the OR trigger and 12 p.e for data taken with the AND trigger. These lower fit boundaries on S1 correspond to higher values in the S2 signal. To preserve the same fitting bounds, for each drift field setting we determined the values of S2 corresponding to an S1 of 4 p.e for the OR trigger and 12 p.e for the AND trigger. These S2 values form the lower fitting bounds for the S2 spectra analysis in each trigger configuration and are summarised for all drift fields in table 2.3.

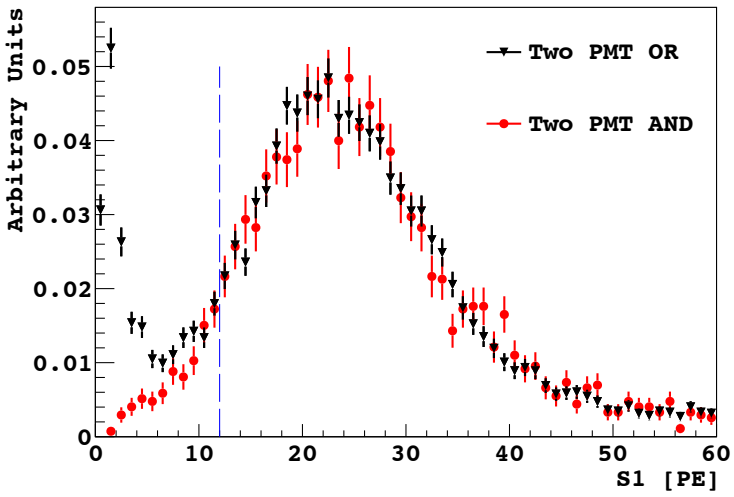

Fig. 2.10: Comparison of S1 spectra for the 20.5 keV recoil energy data at 970 V/cm taken with the OR trigger (black triangles) and the AND trigger (red, solid dots). The integral between 12 and 60 p.e for both spectra is normalised to 1. The AND trigger has no effects on the shape of the spectrum below 12 p.e. Figure taken from Cao *et al.* 2015.

2.3 Calibration and monitoring

2.3.1 SPE calibration

The single photoelectron (SPE) calibration of each PMT was performed in two distinct ways. The first method exploited pulses in the tails of scintillation events from ^{83m}Kr continuously inserted in the TPC through a ^{83}Rb trap in the recirculation loop, shown in Fig. 2.7. The single PE response was measured every 15 minutes and showed a slow decrease of 15% (26%) in the top PMT and 10% (26%) in the bottom PMT over the 6 (13) days of data acquisition in June (October). The uncertainty was measured to be 1% in both runs.

The second method was only used in the October run, when an optical fibre feedthrough was installed in the chamber and light pulses 1 ns wide at a rate of 1 Hz were sent into the TPC from a 355 nm LED though an optical fibre. Data from the PMT was acquired by triggering on the LED pulse. Assuming perfect stability from the LED, the SPE signal of the bottom PMT shifted ±4% from its mean value over the entire run.

Whenever the extraction field was turned on, the mean response due to LED pulses (normalised to the SPE response) from the top PMT would decrease by a factor of 2

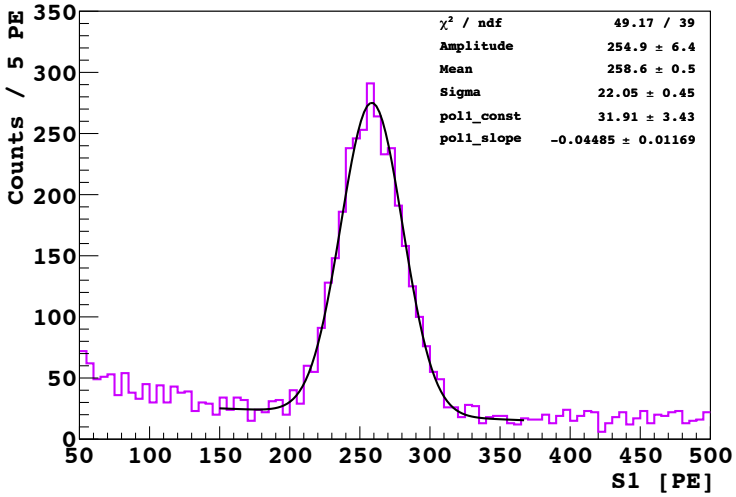

Fig. 2.11: Example of S1 light yield calibration with ^{83m}Kr source. Figure taken from Cao 2014.

and recover only after 30 minutes. Signals from the bottom PMT did not exhibit such change and remained stable within a few percent even in the presence of ionisation signals. A decrease in the PMTs response to the LED light was not observed when the drift field was turned on with no extraction field. We explained this by a decline in quantum efficiency of the top PMT at the high light levels generated by the S2 signals in the top gas layer. To correct for this variation in response, we divided the data into 15-minute blocks and within each block, normalised the top PMT signals to the LED response. To account for this variation in response, for each 15-minute block of data, we scaled the signals of the top PMT by the ratio of its response to the LED during that interval to the dataset with the lowest response to the LED. The SPE response changed by maximum 10% when the ionisation signal was turned on, with the bottom PMT being more affected than the top one. Since the SPE calibration was performed every 15 minutes (and the the beginning and end of each run), any change due to the SPE response was taken into account and accordingly corrected for.

2.3.2 S1 light yield calibration and e^- drift time

The ^{83m}Kr source was used to both calibrate the electron recoil light yield (p.e./keV) and monitor the stability of the TPC throughout the run. At zero field, the ^{83m}Kr 41.5 keV peak position was measured to be 260 (200) p.e. in the June (October) run, which leads to a measured light yield of 6.3 (4.8) p.e./keV. The peak position was stable

within 4% throughout both runs. As already mentioned above, in October we operated the TPC with the argon level 1 mm above the mesh to allow proper S2 production. This, in turn, caused photons reflected at liquid-gas interface to pass multiple times through the grid obstruction, which explains the light yield decrease compared to the June run when the liquid was kept below the mesh. Figure 2.11 shows an example of S1 light yield calibration with ^{83m}Kr source. The peak was fitted with a Gaussian plus a first order polynomial.

When S2 was produced, we also tracked the electron-drift lifetime τ_d, with ^{83m}Kr. τ_d determines the electrons neutralisation rate, which is given by $[e_0]/\tau_d$, with $[e_0]$ the initial electron concentration (Bakale *et al.*, 1976), and gives an indirect measurement of the liquid argon purity. For stable observation of ionisation signals with high ionisation yield, it is essential to keep the concentration of electronegative impurities (mainly O_2) below 1 ppb (Aprile and Doke, 2010). In fact, the attachment of an electron to an impurity leads to the formation of a negative ion, with subsequent reduction in the S2 signal. The decrease of electron concentration, $[e(t)]$, is given by the following equation (Aprile and Doke, 2010):

$$\frac{d[e(t)]}{dt} = -k_S\,[S]\,[e(t)] \tag{2.3}$$

where $[S]$ is the concentration of electronegative impurities in units of mol/L and k_S is the electron attachment rate constant given in L/(mol s). Solving eqn (2.3) for $[e(t)]$ leads to:

$$[e(t)] = [e_0]\exp(-t/\tau_d) \tag{2.4}$$

with the drift lifetime τ_d given by:

$$\tau_d = (k_S\,[S])^{-1} \tag{2.5}$$

From eqns (2.4) and (2.5) it is clear why monitoring τ_d is important for assessing the purity of the system and the quality of S2. We determined τ_d by measuring the correlation between the S2 signal (p.e.) and drift time (difference between the start time of S1 and S2 in µs). Figure 2.12 (top) shows the 2D distribution of S2 *vs* drift time for the events which contained a second pulse (S2) that started at least 7 µs after the first pulse (S1). Data were taken at 200 V/cm. The profiles of 3 µs-wide bins were plotted across the entire drift time range and the mean S2 was determined for each µs-wide bin. The results are plotted in Fig. 2.12 (bottom). The data points were fitted to an exponential function. The "lifetime" parameter is the input for Fig. 2.13,

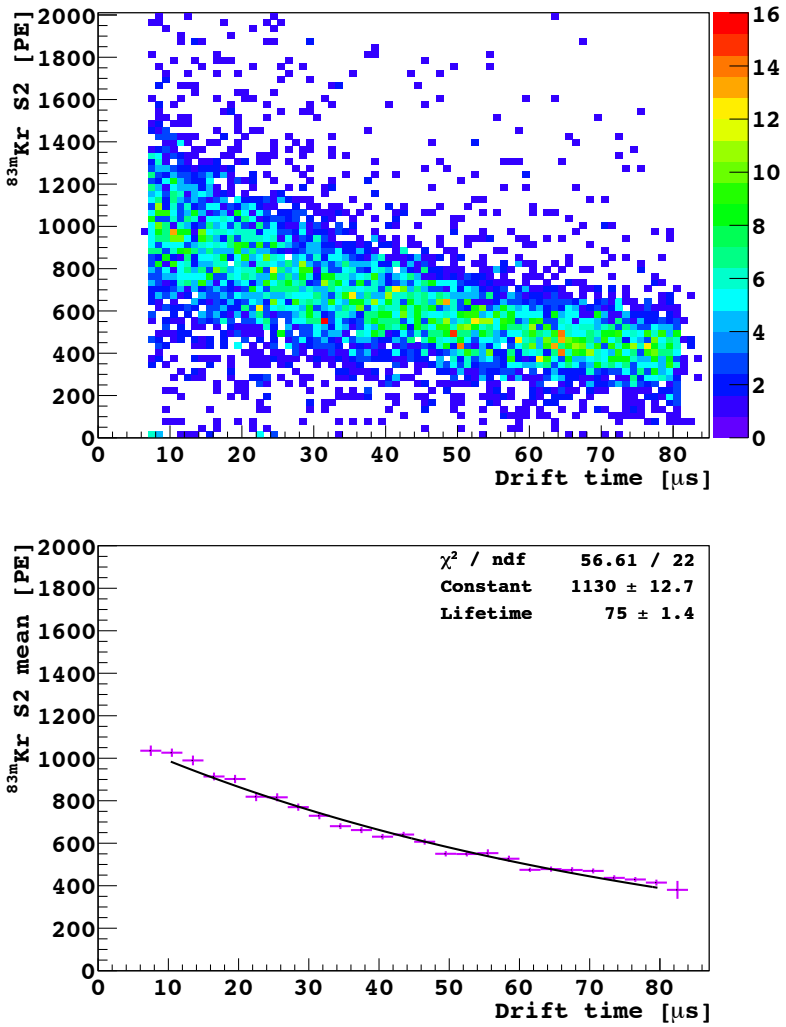

Fig. 2.12: Top: 2D distribution of S2 *vs* drift time using ^{83m}Kr source at 200V/cm. Bottom: S2 mean of 3 µs-wide bins as a function of drift time for the same data set used to make the top plot. An exponential function was fitted to the data points. The "lifetime" parameter represents the electron-drift lifetime. Figures taken from Cao 2014.

which shows the drift lifetime at different electric drift fields during the October run. τ_d was greater that 40 µs at the start of the run and, thanks to the argon recirculation through the getter, improved over the course of the run, reaching 120 µs at the end of the run. Equation (2.4) can also be written as:

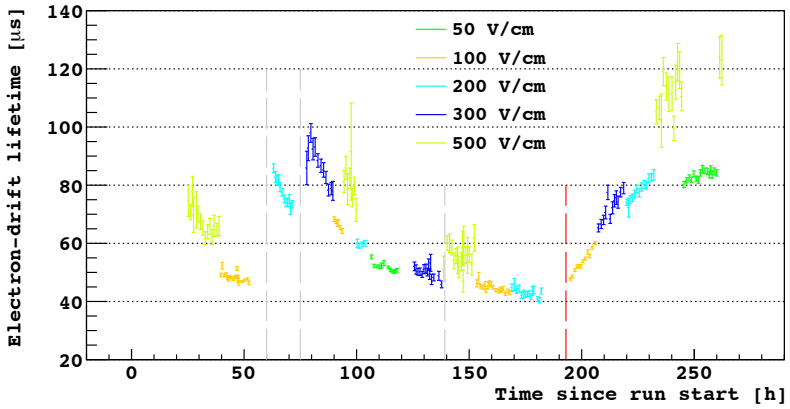

Fig. 2.13: Electron-drift lifetime monitored over the entire run in October. Figure taken from Cao 2014.

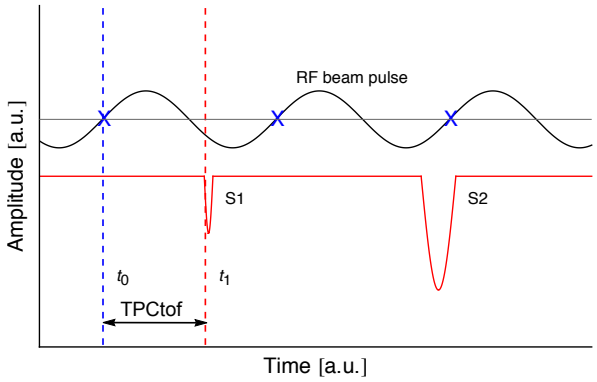

Fig. 2.14: The reference time t_0 is set by the closest rising-edge zero-crossing of the proton-beam-on-target RF pulse the to the S1 signal in the TPC. The time of flight from the target to the TPC, TPCtof, is given by the difference in time between the proton-beam-on-target and the S1 signal.

$$S2(t_d) = S2_0 \exp(-t_d/\tau_d) \tag{2.6}$$

where t_d is the drift time, $S2(t)$ is the actual number of p.e. that reached the PMT, and $S2_0$ is the number of p.e. that would have reached it if no electron capture happened along the drift path. To obtain $S2_0$, hereby accounting for electron capture, we corrected each S2 signal by dividing it by $\exp(-t_d/\tau_d)$.

2.4 Event selection

I describe the event selection by referring to the following data set: 57.3 keV nuclear recoils at 193 V/cm drift field, 3.0 kV/cm extraction field, and 4.5 kV/cm multiplication field. It is worth noting that, despite a single voltage being applied between the mesh and the cathode, the extraction field (between the mesh and the liquid surface) and the multiplication field (in the gas layer) have distinct strengths due to the different dielectric constants of liquid and gas argon.

Figure 2.15 (a) shows the 2D distribution of the pulse shape discrimination parameter $\mathtt{f}_{90}$, defined as the fraction of primary scintillation detected in the first 90 ns of the primary scintillation signal, *vs* the time difference between the proton-beam-on-target and the primary scintillation signal in the TPC (TPCtof). The time of arrival of a pulse is defined as the time when the amplitude reaches 50% of the peak height. As schematically illustrated in Fig. 2.14, the reference time is set by the closest rising-edge zero-crossing of the proton-beam-on-target RF pulse the to the S1 signal in the TPC. Liquid argon luminescence shows roughly a double exponential decay. The fast component, which corresponds to the decay of the LAr singlet excited state ($^1\Sigma_u^+$), is 6 ns for electron recoils and 7.1 ns for nuclear recoils, as measured in 1983 by Hitachi *et al.* under electron and α-particle excitation, respectively. The slow lifetime constant is due to the decay of the LAr triplet excited state ($^3\Sigma_u^+$) and is 1.59 µs for electron recoils and 1.66 µs for nuclear recoils, again as found in 1983 by Hitachi *et al.* under electron and α particle excitation, respectively. The intensity ratios, $\mathrm{I_S/I_T}$, of the singlet states to the triplet states are significantly different for electron and nuclear recoils and were found to be 0.3 and 1.3 for electron and α-particle excitation respectively (Hitachi *et al.*, 1983) (this $\mathrm{I_S + I_T} = 1$ means that for electron recoils $\mathrm{I_S} = 0.23$ and $\mathrm{I_T} = 0.77$, while for nuclear recoils $\mathrm{I_S} = 0.57$ and $\mathrm{I_T} = 0.43$). This explains why $\mathtt{f}_{90}$ is small for electron recoils (photons) and large for nuclear recoils (neutrons), as shown in Fig. 2.15 (a). As for the time of flight between the target and the TPC, γ-like events are clustered around 5 ns and neutron MeV-like events around 45 ns as predicted, given the speed for 1.773 MeV neutrons is approximately 1.8 cm/ns. $^{83\mathrm{m}}$Kr events display $\mathtt{f}_{90}$ and γ-like timing. Some events displayed a time of flight slightly faster than the one of photons and were characterised by $\mathtt{f}_{90}$ close to 1. These events did not exhibit the typical slow component of LAr scintillation and were present even when the TPC did not contain any liquid. Therefore, we concluded these signals must have been independent from any scintillation process in the liquid and we interpreted them as Čerenkov light induced by fast electrons traversing the fused silica windows. Whenever S2 and S1 came too close in time to be resolved, $\mathtt{f}_{90}$ was smaller than usual

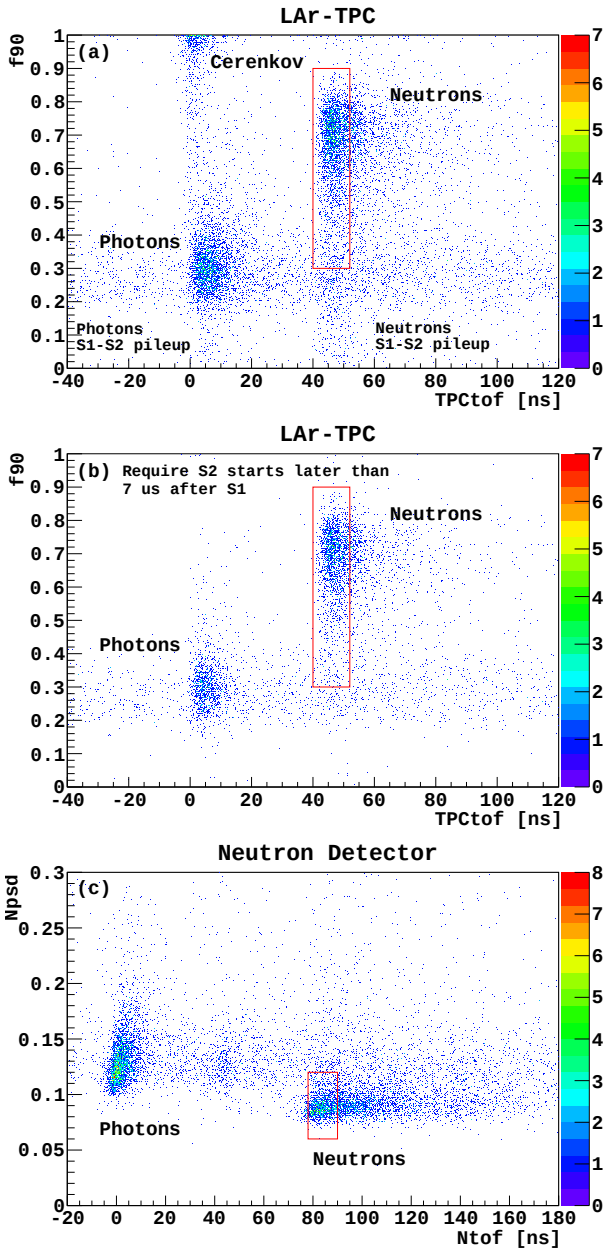

Fig. 2.15: Panel (a) shows the 2D distribution of the pulse shape discrimination parameter $\mathtt{f}_{90}$ against the time of flight between the target and the TPC. Pileup events are removed in panel (b) by requiring the second pulse's $\mathtt{f}_{90}$ to be less than 0.1 and to start 7 µs after the first pulse. Neutrons are characterised by a larger $\mathtt{f}_{90}$ than photons and a greater time of flight. Panel (c) describes the neutron detectors response by showing the neutron pulse shape discriminant *vs* the time of flight between the proton-beam-on-target and the neutron detector (Ntof). Figures taken from Cao *et al.* 2015.

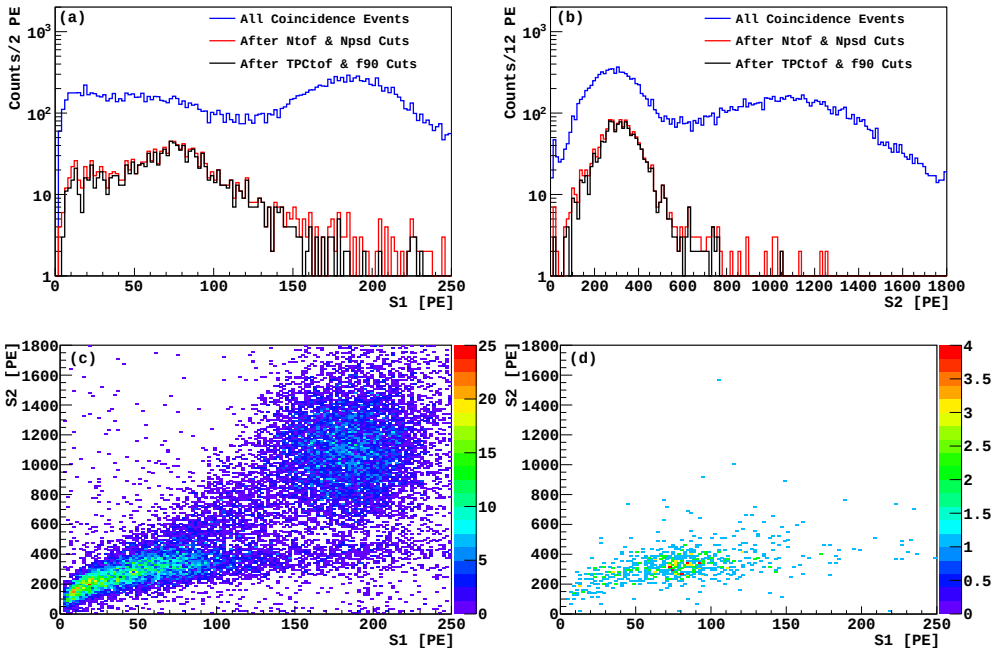

Fig. 2.16: (a) and (b) refer to the S1 and S2 spectra with cuts applied in sequence. Data refer to 57.3 keV nuclear recoils with a 193 V/cm drift field, a 3.0 kV/cm extraction field, and a 4.5 kV/cm multiplication field. (c) S2 *vs* S1 scatter plot for all events without S1-S2 pileup before neutron selection cuts. (d) S2 *vs* S1 distribution after neutron selection cuts. Figures taken from Cao *et al.* 2015.

(S1-S2 pileup). To remove these signals, we required the S2 pulse starting at least 7 µs after S1 and the second pulse $\mathtt{f}_{90}$'s to be less than 0.1. Figure 2.15 (b) shows the same 2D distribution as in 2.15 (a) after cuts have been applied.

Figure 2.15 (c) describes the neutron detectors response by showing the neutron pulse shape discriminant, defined as the peak amplitude over the pulse integral, *vs* the time of flight between the proton-beam-on-target and the neutron detector (Ntof). The population near a Npsd of 0.09 and Ntof of 85 ns represents neutron events, while the cluster near a Npsd of 0.13 and Ntof of 2 ns corresponds to β/γ events. Between the two populations, random coincidences from environmental background are visible.

To retain nuclear recoils only, we selected events with Ntof and TPCtof within ±6 ns from the bin with the maximum number of counts in the neutron-events clusters. The cuts on the pulse shape discrimination parameters were set as follows for all recoil energies examined: $0.06 < \text{Npsd} < 0.12$ and $0.3 < \mathtt{f}_{90} < 0.9$.

Figures 2.16 (a) and (b) show the S1 and S2 spectra respectively, with no cuts in

blue (all coincidence events and TPC alone events at pre-scaled trigger rate), after Ntof and Npsd cuts in red, and after TPCtof and $\mathtt{f}_{90}$ cuts in black. The S1 peak around 187 p.e and S2 peak around 1100 p.e (blue curves) come from ^{83m}Kr which, as explained before, was used for continuous monitoring of the TPC. The bottom plots in Fig. 2.16 show the S2 *vs* S1 scatter plot before (c) and after (d) the nuclear recoil selection cuts.

2.5 Analysis of S1 spectra and determination of $\mathcal{L}_{\mathrm{eff},\,^{83m}\mathrm{Kr}}$

To derive $\mathcal{L}_{\mathrm{eff},\,^{83m}\mathrm{Kr}}$ as a function of nuclear recoil energy and electric drift field, the measured S1 spectrum, for each scattering angle and drift voltage setting, was compared to the simulated S1 distribution. The Monte Carlo simulation computed the energy deposited in liquid argon at a specific scattering angle and electric field configuration, taking into account the complete geometry of the experiment and the TOF selection cuts. To convert the simulated spectrum from keV to p.e., the energy deposition is first multiplied by the free parameter $\mathcal{L}_{\mathrm{eff},\,^{83m}\mathrm{Kr}}$ (keV goes into keV$_{\mathrm{ee}}$) and then by the measured light yield using ^{83m}Kr (this converts keV$_{\mathrm{ee}}$ to p.e.). The number of photoelectrons S1, fluctuates according to a Poisson distribution with standard deviation $\sqrt{\mathrm{S1}}$. If detector energy resolution followed Poisson statistics exactly, the number of photoelectrons S1, would fluctuate with standard deviation $\sqrt{\mathrm{S1}}$. However, energy resolution is also effected by other factors which depend on the applied electric drift field and the specific nuclear recoil energy, such as the variation of the SPE distribution, the position dependent light collection efficiency, and the intrinsic resolution of LAr scintillation. Thus, before fitting, the simulated S1 spectrum was smeared with a Gaussian distribution with mean S1 and standard deviation $R_1(E_{nr},\mathcal{E}_d)\sqrt{S1}$, where R_1 is the second free parameter of the fit. The Monte Carlo is fit to the data by χ^2-minimisation with $\mathcal{L}_{\mathrm{eff},\,^{83m}\mathrm{Kr}}$ and R_1 left as free variables:

$$\chi^2(\mathcal{L}_{\mathrm{eff},\,^{83m}\mathrm{Kr}},R_1)=\sum_{i=1}^{n}\frac{\left[h_i-h_{\mathrm{MC},i}(\mathcal{L}_{\mathrm{eff},\,^{83m}\mathrm{Kr}},R_1)\right]^2}{\sigma^2_{\mathrm{MC},i}} \tag{2.7}$$

where n is the total number of bins in the selected fit region, h_i is the measured number of events in bin i, and $h_{\mathrm{MC},i}$ is the simulated number of events in bin i as a function of $\mathcal{L}_{\mathrm{eff},\,^{83m}\mathrm{Kr}}$ and R_1. Assuming each bin is effected by Poisson fluctuations, $\sigma^2_{\mathrm{MC},i}$ is equal to $h_{\mathrm{MC},i}$. The fit parameters were applied to the MC before binning and the MC spectrum was normalised to the number of events of the data (when determining $\mathcal{L}_{\mathrm{eff}}$, we are only comparing the shapes of the histograms).

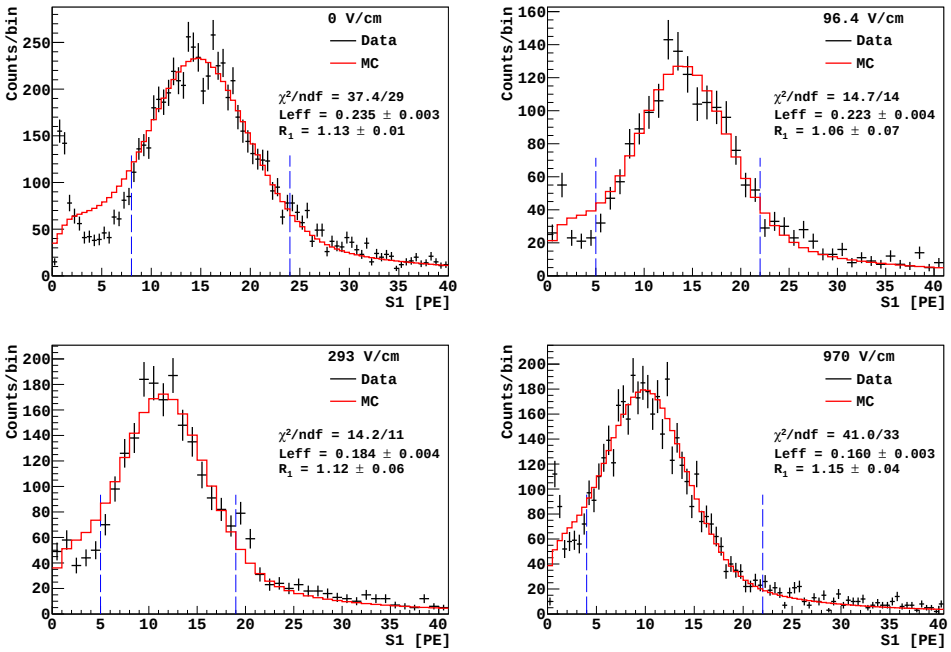

Fig. 2.17: Black: S1 spectra from experimental data taken at 10.3 keV nuclear recoil energy at four drift voltage values. Red: Monte Carlo fit of the data. The range used for the fit is indicated by two vertical blue dashed lines. Figures taken from Cao *et al.* 2015.

As an example, Fig. 2.17 shows the results for the 10.3 keV nuclear recoil data at four different drift fields. For each configuration and with the TPC OR trigger, the lower fit boundary was initially chosen around 3–4 p.e (depending on binning) and the upper boundary as the bin where the number counts would fall below 10% of the peak. Typically, the fit would be poor at the left most or the right most region. We then excluded such region(s) and made sure the fit converged. With TPC AND trigger, we initially set the lower bound at 12 p.e in order to exclude events effected by reduced trigger efficiency.

Figure 2.18 shows our values for $\mathcal{L}_{\text{eff}}$ at zero field along with measurements from other experiments. As already mentioned earlier, despite these results were not obtained using $^{83\text{m}}$Kr as the calibration source for electronic recoil energies, we can still compare them, since light yield in this energy range was measured to be the same regardless of the γ calibration source (i.e. the number of p.e. increases linearly with energy). Figure 2.19 shows the measured values of $\mathcal{L}_{\text{eff},\,^{83\text{m}}\text{Kr}}$ as a function of the nuclear recoil energy, E_{nr}, at 0, 96.4, 193, 293, and 970 V/cm. As can be seen, $\mathcal{L}_{\text{eff}}$ drops

Table 2.4 Summary of error contributions to individual $\mathcal{L}_{\mathrm{eff},\,^{83m}\mathrm{Kr}}$ measurements at $\mathcal{E}_d = 0$. Only minor variations in the magnitude of systematic errors were observed across the range of drift field explored. The combined error (including both systematic and statistical errors) for each measurement is used Fig. 2.19.

Recoil energy [keV]	10.3	14.8	16.9	20.5	25.4	28.7	36.1	49.7	57.3
$\mathcal{L}_{\mathrm{eff},\,^{83m}\mathrm{Kr}}$	0.235	0.239	0.234	0.257	0.251	0.264	0.278	0.291	0.295
Statistical error	0.003	0.005	0.004	0.001	0.005	0.004	0.003	0.005	0.004
Systematic error source									
Fit method	0.001	0.000	0.004	0.004	0.002	0.001	0.003	0.001	0.002
Fit range	0.000	0.002	0.000	0.001	0.002	0.000	0.001	0.000	0.000
TPCtof cut	0.002	0.003	0.003	0.001	0.002	0.001	0.001	0.001	0.001
Ntof cut	0.004	0.002	0.001	0.001	0.002	0.004	0.001	0.003	0.001
f90 cut	0.004	0.004	0.003	0.001	0.000	0.001	0.000	0.000	0.000
^{83m}Kr light yield	0.005	0.005	0.005	0.005	0.005	0.005	0.006	0.006	0.006
Recoil energy									
TPC position	0.001	0.001	0.001	0.001	0.001	0.001	0.001	0.001	0.001
EJ301 position	0.007	0.010	0.005	0.008	0.008	0.005	0.006	0.003	0.006
Combined error total	0.011	0.013	0.010	0.010	0.011	0.009	0.010	0.009	0.010

with increasing electric field and decreasing recoil energy.

Besides the statistical error of the MC fit to the data, many systematic uncertainties effect the measurement of $\mathcal{L}_{\mathrm{eff},\,^{83m}\mathrm{Kr}}$ and must all be added in quadrature in order to find the combined total error.

We investigated for any systematic bias in the fit arising from the nuclear recoil

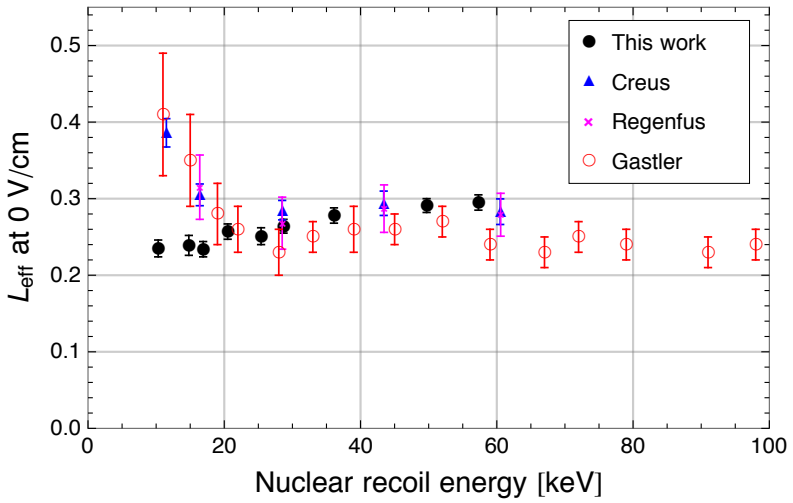

Fig. 2.18: $\mathcal{L}_{\mathrm{eff}}$ relative to the light yield of ^{83m}Kr at zero electric field as a function of nuclear recoil energy at zero field, compared to other measurements.

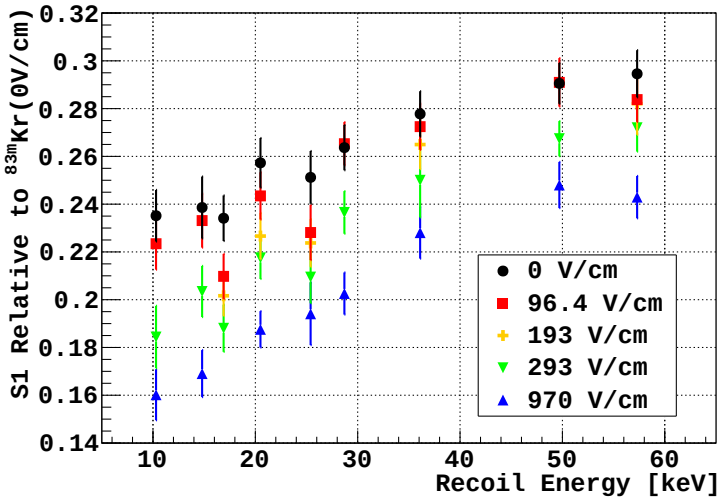

Fig. 2.19: $\mathcal{L}_{\text{eff}}$ relative to the light yield of $^{83\text{m}}$Kr at zero electric field as a function of nuclear recoil energy at five different electric drift fields (0, 96.4, 193, 293, and 970). Figure taken from Cao *et al.* 2015.

energy obtained as the median of the MC single scatter energy deposition (at specific nuclear recoil energy and electric field setting). To do so, we also derived the nuclear recoil energy through a Gaussian plus first order polynomial fit to each MC energy deposition spectrum of all scatters that produced a coincidence between the TPC and the neutron detector and survived the timing cuts (see Fig. 2.20). The difference in $\mathcal{L}_{\text{eff},\,^{83\text{m}}\text{Kr}}$ between the two methods is less than 2% across all recoil energies and is listed in the Table 2.4 in the row "Fit Method" for $\mathcal{E}_d = 0$.

We evaluated the systematic uncertainty due to the choice of the fit range selection by comparing the fit results to those obtained with a reduced fit range ("Fit Range" in Table 2.4). The reduced range was constructed by raising the lower bound by 10% of the original fit range and lowering the upper bound by the same amount.

We computed the systematic error caused by the TOF cuts by advancing or delaying the TPCtof cut by 3 ns while keeping the Ntof cut constant, and vice versa. We estimated the corresponding systematic error as the average of the absolute difference in $\mathcal{L}_{\text{eff},\,^{83\text{m}}\text{Kr}}$ derived by either advancing or delaying the TOF window.

During the data acquisition at a specific recoil energy and electric field configuration, the light yield from $^{83\text{m}}$Kr varied by 1% during. In addition to this, changes in the LAr purity also effect the measured light yield and may be indirectly quantified

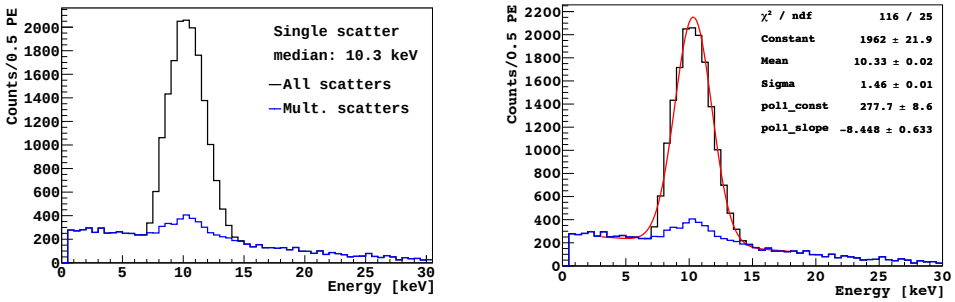

Fig. 2.20: GEANT4-based simulation of the energy deposition in the LAr TPC at the 10.3 keV setting. Black: all events that produced a coincidence between the TPC and the neutron detector and survived the TPCtof and Ntof cuts. Blue: Events undergoing multiple scattering in the TPC. Left: The nuclear recoil energy corresponding to the measured scattering angle at zero field is calculated as the median of the black distribution after subtracting the blue. Right: Alternative method to calculate the nuclear recoil energy using a Gaussian plus first order polynomial fit. Figures taken from Cao 2014.

by looking at the change in the mean life time of the triplet state of S1 scintillation (more on this in Chapter 5, Section 5.3). This corresponds to the slow component in S1 signals, which we measured in the range from 1.39 to 1.48 µs, with 1.45 µs being the most common value. Since $\mathtt{f}_{90}$ is a measure of the relative importance of the slow component in the total luminescence output, a drop in the slow lifetime component (increase in impurities) causes $\mathtt{f}_{90}$to increase (the light output in the first 90 ns stays constant, but the overall scintillation yield diminishes), and vice versa. Figure 2.21 shows the relative scintillation yield as a function of the slow lifetime component for different values of $\mathtt{f}_{90}$. The relative light is equal to 1 at the lifetime nominal value of 1.45 µs. As an example, when $\mathtt{f}_{90}$ is 0.3, for a measured lifetime of 1.38 µs, the light output is reduced by 3.5%. Typical values of $\mathtt{f}_{90}$ for γ-like events from ^{83m}Krare between 0.2 and 0.3, which contributes by to the systematic uncertainty on ^{83m}Kr light yield of $\sim 2\%$, as seen from Fig. 2.21.

Finally, the uncertainty in the nuclear recoil energy due to alignment of the TPC and neutron detectors (which ultimately effect the measurement of the scattering angle) was calculated assuming a 1± error in our determination of their positions relative to the LiF target.

2.6 Analysis of S2 and determination of $\mathcal{Q}_y$

$\mathcal{Q}_y$ is defined as the ionisation yield of nuclear recoils in detector-independent units of extracted electrons per unit of nuclear recoil energy (e^-/keV). Previous measurements

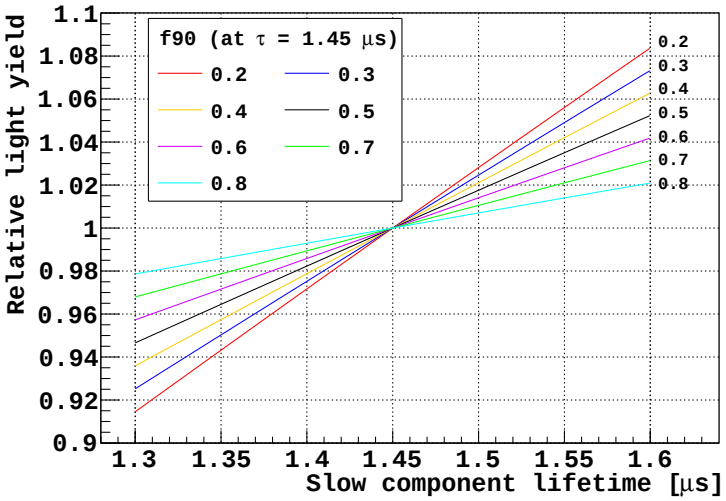

Fig. 2.21: Simulation of the relative light yield as a function of the slow lifetime component in LAr. Each line corresponds to a particular $\mathtt{f}_{90}$ when the triplet lifetime component is 1.45 µs. Figure taken from Cao *et al.* 2015.

have reported that ionisation yield from electrons, relativistic heavy ions, α-particles, fission fragments (Kubota *et al.*, 1978*b*; Doke *et al.*, 1985; Hitachi *et al.*, 1987), and 6.7 keV nuclear recoils (Joshi *et al.*, 2014) increases with stronger electric drift fields. We confirmed this behaviour and I will here present our measurements of $\mathcal{Q}_y$ as a function of nuclear recoil energy and drift voltage taken with an extraction field of 3.0 kV/cm, a multiplication field of 4.5 kV/cm, and an argon gas layer 6 mm thick. With these settings we were not able to resolve single-electron S2 signals and calibrate directly the secondary scintillation gain, g_2, defined as the number of detected photoelectrons per single electron extracted into the gas region (p.e./e^-). Therefore, in order to determine g_2 and convert the measured $\mathcal{Q}_y$ given in detector-dependent units of p.e./keV to detector-independent units of e^-/keV (see eqn 1.40), we used an indirect method which exploits the simultaneous measurement of S1 and S2 (more on this in Section 2.7).

Besides the ionisation yield of nuclear recoils at different drift voltage settings, we also measured the ionisation yield of ^{83m}Kr. Analogously to $\mathcal{L}_{\text{eff},\,^{83m}\text{Kr}}$, the measurement of $\mathcal{Q}_y$ of nuclear recoils relative to $\mathcal{Q}_y$ of ^{83m}Kr allows indirect calibration of nuclear recoil ionisation yield in other LAr TPCs when direct calibration of ionisation yield of ^{83m}Kr is performed.

We obtained $\mathcal{Q}_y$ in a way similar to $\mathcal{L}_{\text{eff},\,^{83m}\text{Kr}}$, that is by comparing experimental

data to Monte Carlo-simulated distributions, but with a few differences. In our S1 fits, when fitting the MC energy deposition spectra to the experimental p.e. distributions, at each nuclear recoil energy and electric field setting we assumed $\mathcal{L}_{\text{eff},\,^{83\text{m}}\text{Kr}}$ as constant in the fit region. This assumption, although sensible for $\mathcal{L}_{\text{eff},\,^{83\text{m}}\text{Kr}}$, does not hold true for $\mathcal{Q}_y$, as its dependence on the recoil energy is much stronger. For this reason, instead of extracting $\mathcal{Q}_y$ independently for each nuclear recoil energy and drift voltage, we modelled the ionisation response at a given drift field, $S2_{\mathcal{E}_d}$, according to the following equation:

$$S2_{\mathcal{E}_d}(E_{nr}) = A_{\mathcal{E}_d}\,\ln(\,B_{\mathcal{E}_d}\,E_{nr}) + C_{\mathcal{E}_d} \tag{2.8}$$

and fit all S2 spectra taken at the same $\mathcal{E}_d$ with the same function described by eqn (2.8), where $A_{\mathcal{E}_d}$, $B_{\mathcal{E}_d}$, and $C_{\mathcal{E}_d}$ are the fit parameters at specific $\mathcal{E}_d$. This procedure improved the goodness of the fit between data and MC, particularly in the low p.e. region.

Practically, we firstly converted the MC energy deposition spectra at each E_{nr} at zero field from keV to p.e. using eqn (2.8). Then, in a similar manner to the S1 analysis, before fitting the MC to the data, we smeared each simulated S2 distribution using a Gaussian distribution with mean S2 and standard deviation given by:

$$\sigma_2 = \sqrt{S2 + a\,S2 + R_2^2\,S2^2} \tag{2.9}$$

where the first term follows from Poisson statistics, the second comes from SPE resolution, which is independent of energy and field, and the third accounts for geometrical effects and recombination fluctuations in LAr. a is the ratio of the width of the SPE distribution to its mean and was measured to be 0.3. Indeed, instead of using $\sigma_1 = R_1(E_{nr}, \mathcal{E}_d)\sqrt{S1}$ in the S1 study, we could as well have used an expression similar to eqn (2.9). However, since for S1 the second order term was not as large as for S2 signals, using $\sigma_1 = R_1(E_{nr}, \mathcal{E}_d)\sqrt{S1}$ was still a good approximation. Finally, we fitted all MC spectra to the data at each specific $\mathcal{E}_d$ by minimising the χ^2 defined as:

$$\chi^2(A_{\mathcal{E}_d}, B_{\mathcal{E}_d}, C_{\mathcal{E}_d}, R_2) = \sum_{j=1}^{m}\sum_{i=1}^{n} \frac{[h_{j,i} - h_{\text{MC},j,i}(A_{\mathcal{E}_d}, B_{\mathcal{E}_d}, C_{\mathcal{E}_d}, R_2)]^2}{\sigma^2_{\text{MC},ji}} \tag{2.10}$$

where m is the number of recoil spectra with the same $\mathcal{E}_d$; n_j is the number of bins in the selected fit region for the j-th recoil spectrum; $h_{j,i}$ is the number of counts measured in bin i for the j-th spectrum; $h_{\text{MC},j,i}$ is the number of simulated events in bin i for the j-th spectrum; $\sigma^2_{\text{MC},ji}$ is equal to $h_{\text{MC},j,i}$ because of Poisson statistics; and $A_{\mathcal{E}_d}$, $B_{\mathcal{E}_d}$, $C_{\mathcal{E}_d}$, and R_2 are the free parameters of the fit. Each MC spectrum was

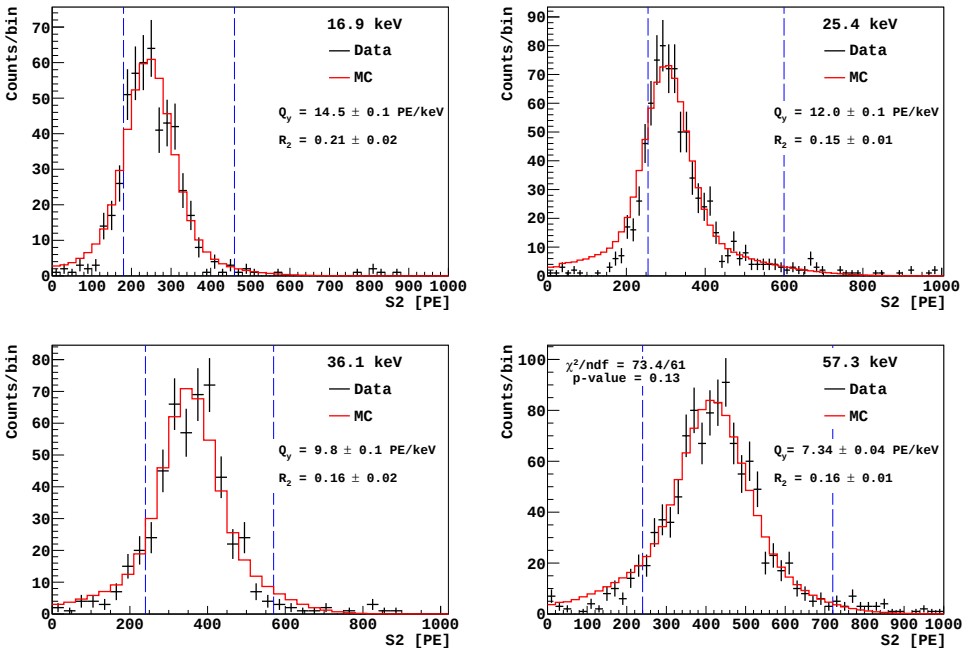

Fig. 2.22: Black: S2 spectra from experimental data taken at $\mathcal{E}_d = 486\,\mathrm{V/cm}$. Red: Simultaneous Monte Carlo fit to data corresponding to four different energies, namely 16.9 keV, 25.4 keV, 36.1 keV, and 57.3 keV. The range used for the fit is indicated by the vertical blue dashed lines. The χ^2 and the total number of degrees of freedom (ndf) is shown in the last panel. Figures taken from Cao *et al.* 2015.

normalised such that the number of event in the fit range was equal to that in the corresponding experimental spectrum. $\mathcal{Q}_y$ in units of p.e./keV is then given by:

$$\mathcal{Q}_y(E_{nr}, \mathcal{E}_d) = \frac{S2_{\mathcal{E}_d}(E_{nr})}{E_{nr}} \tag{2.11}$$

Figure 2.22 shows, as an example, the fit results at $\mathcal{E}_d = 486\,\mathrm{V/cm}$. The fit ranges were chosen according to Table 2.3 and are indicated by the vertical blue dashed lines. The χ^2 and the total number of degrees of freedom (ndf) are shown in the last panel, along with the p-value $P(\chi^2 > \chi^2_{OBS})$. The MC and the data agree fairly well, although the data is systematically lower than the MC on the left side below the lower fit bound. This shortfall is possibly due to a decline in the trigger efficiency for small S2 signals.

Figure 2.23 shows the fitted $\mathcal{Q}_y$ at each nuclear recoil energy as a function of the drift field. The ionisation yield for $^{83\mathrm{m}}$Kr is also plotted in the same figure. Figure 2.24

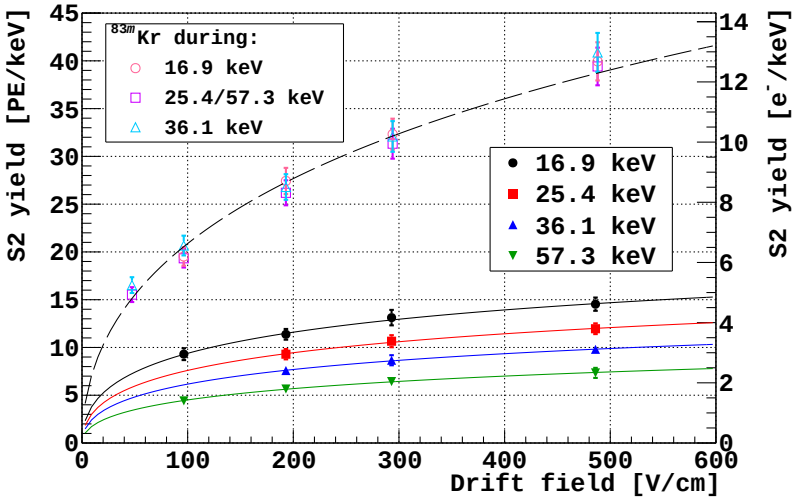

Fig. 2.23: Ionisation yield $\mathcal{Q}_y$ as a function of $\mathcal{E}_d$ at four recoil energies. Left vertical axis is in units of p.e./keV, while the right vertical axis is expressed in detector-independent units of e^-/keV. To account for the error in g_2, an additional 10% systematic uncertainty must be added to the error bars of $\mathcal{Q}_y$ in [e^-/keV]. Figure taken from Cao *et al.* 2015.

shows $\mathcal{Q}_y$ as a function of the recoil energy at the four drift fields for which the S2 peak was resolved and the fitted (96.4, 193, 293, and 486 V/cm). The error bars are given by the combination of the statistical and systematic uncertainties. The latter were evaluated following a similar procedure described in the study of $\mathcal{L}_{\text{eff},\,^{83m}\text{Kr}}$. As an example, Table 2.5 reports the individual contributions and the combined uncertainty for the 193 V/cm drift field setting at each recoil energy. Table 2.6 lists the fit results for $\mathcal{Q}_y$ at each drift field and nuclear recoil energy along with total combined uncertainties.

2.7 S1 and S2 gains

Figure 2.25 shows our simultaneous measurements of scintillation and ionisation signals for both ^{83m}Kr (a) and nuclear recoils (b) at different drift fields. In both cases, a decrease in S1 corresponds to an increase in S2, and vice versa. This anticorrelation has been previously documented for electrons, relativistic heavy ions, α-particles, and fission fragments (Kubota *et al.* 1978*b*; Doke *et al.* 1985; Hitachi *et al.* 1987), but never for nuclear recoils in argon before SCENE's measurements. S1-S2 anticorrelation is not surprising, as the increase in S2 comes at the expense of less electrons available for recombination in the primary scintillation process. If we consider the recombina-

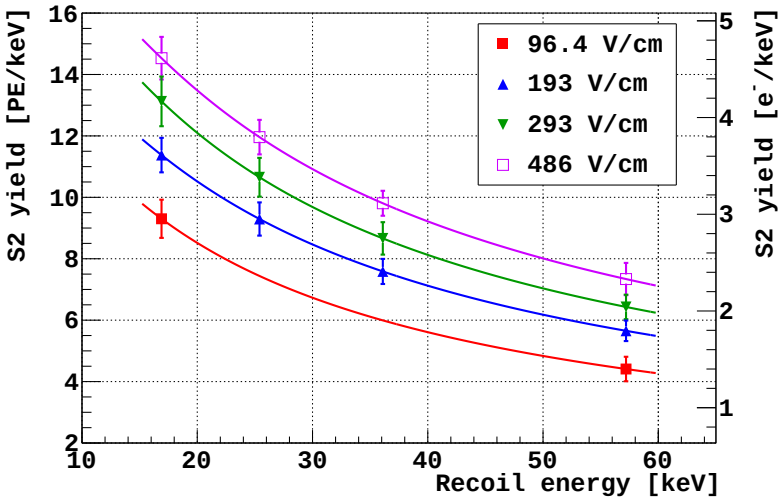

Fig. 2.24: Ionisation yield $\mathcal{Q}_y$ as a function of recoil energy at four different fields. Left vertical axis is in units of p.e./keV, while the right vertical axis is expressed in detector-independent units of e^-/keV. To account for the error in g_2, an additional 10% systematic uncertainty must be added to the error bars of $\mathcal{Q}_y$ in [e^-/keV]. Figure taken from Cao *et al.* 2015.

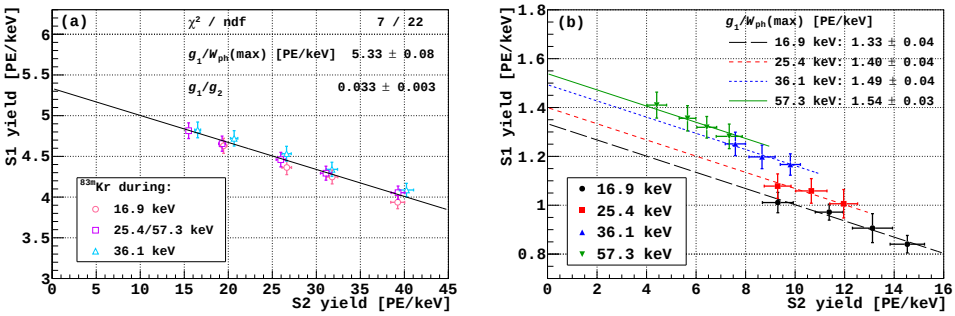

Fig. 2.25: Left: S1 as a function of S2 for ^{83m}Kr. Points of the same colour on the plot correspond to measurements at a specific nuclear recoil energy configuration taken at multiple $\mathcal{E}_d$ values. Right: S1 as a function of S2 for nuclear recoils. Points of the same colour on the plot correspond to measurements at a specific nuclear recoil energy configuration taken at multiple $\mathcal{E}_d$ values. The data in both panels are fit simultaneously, leaving the intercepts free and the slopes as a common parameter. Figures taken from Cao *et al.* 2015.

Table 2.5 Summary of statistical and systematic uncertainties that contribute to the total combined error in $\mathcal{Q}_y$ measurements at $\mathcal{E}_d = 193\,\mathrm{V/cm}$ at four different recoil energies. Only minor variations in the magnitude of systematic errors are observed across the range of drift field explored. The combined error (including both systematic and statistical errors) for each measurement is shown Fig. 2.24. Table taken from Cao *et al.* 2015.

Recoil energy [keV]	16.9	25.4	36.1	57.3
$\mathcal{Q}_y$ [p.e./keV]	11.4	9.3	7.6	5.7
Statistical error	0.2	0.2	0.1	0.1
Systematic errors				
Fit model	0.2	0.2	0.2	0.1
Fit method	0.1	0.2	0.0	0.2
Fit range	0.1	0.1	0.1	0.0
TPC tof	0.1	0.1	0.1	0.1
N tof	0.2	0.2	0.1	0.0
f90	0.2	0.2	0.1	0.0
Kr LY	0.2	0.2	0.2	0.1
Recoil energy				
TPC pos	0.1	0.0	0.0	0.0
EJ pos	0.2	0.3	0.2	0.1
Combined error	0.6	0.5	0.4	0.3

Table 2.6 $\mathcal{Q}_y$ values in units of p.e./keV with total combined errors. Table taken from Cao *et al.* 2015.

Drift field [V/cm]	Recoil energy [keV]			
	16.9	25.4	36.1	57.3
96.4	9.3 ± 0.6			4.4 ± 0.4
193	11.4 ± 0.6	9.3 ± 0.5	7.6 ± 0.4	5.7 ± 0.3
293	13.1 ± 0.8	10.7 ± 0.6	8.7 ± 0.5	6.4 ± 0.4
486	14.5 ± 0.7	12.0 ± 0.6	9.8 ± 0.4	7.3 ± 0.5

tion model valid, the anticorrelation between S1 and S2 proves useful in determining the single quanta gain values for scintillation photons ($[g_1]$ = p.e/ph) and ionisation electrons ($[g_2]$ = p.e./e$^-$).

As reported in 1985 by Doke *et al.*, at zero field the number of scintillation photons, N_{ph}, produced is:

$$N_{ph} = N_{ex} + N_{ir}^0 = N_{ex} + (1 - \chi)N_i \tag{2.12}$$

where N_{ex} is the number of excitons, N_{ir}^0 is the number of ions which through recombination lead to luminescence at zero electric field, and χ denotes the ratio of the number of escaping electrons at zero field to that initially generated by the incident

particle. Assuming $\chi = 0$, eqn (2.12) may be written as follows:

$$\begin{aligned} N_{ph} &= N_{ex} + N_i \\ &= N_i(1 + \frac{N_{ex}}{N_i}) \\ &= \frac{E}{W}(1 + \frac{N_{ex}}{N_i}) \\ &= \frac{E}{W_s^{min}} \end{aligned} \tag{2.13}$$

where W (called W-value) is the average energy required for electron-ion production, which was measured to be 23.6 eV (Miyajima *et al.*, 1974), E is the energy deposited by the impinging particle, and W_s^{min} is the minimum possible energy required to produce a single scintillation photon, which was found to be 19.5 ± 1.0 eV (Doke *et al.*, 2002).

Under electric field some electrons, including the fraction of escaping electrons, are driven into the gas region to undergo electroluminescence. Thus, the number of electrons produced becomes:

$$N_i = N_{ir} + N_{ic} \tag{2.14}$$

where N_{ir} is the number of electrons (ions) that recombine under the electric field and N_{ic} is the number of ionisation electrons which are collected in the gas region. We may also rewrite eqn (2.14) as:

$$N_i = rN_i + (1 - r)N_i \tag{2.15}$$

where r is the fraction of electrons (ions) that recombine under the electric drift field. Hence, for $\mathcal{E}_d \neq 0$, eqn (2.12) becomes:

$$\begin{aligned} N_{ph} &= N_{ex} + (N_i - N_{ic}) \\ &= N_{ex} + N_{ir} \\ &= N_{ex} + rN_i \end{aligned} \tag{2.16}$$

and we can write:

$$\begin{aligned} S1 &= g_1 N_{ph} = g_1(N_{ex} + rN_i) \\ S2 &= g2N_{ic} = g_2(1 - r)N_i \end{aligned} \tag{2.17}$$

where g_1 and g_2 represent the efficiency for photon and electron detection, respectively. Combining eqns (2.13), (2.16), and 2.17 leads to:

$$\frac{S1}{E} = \frac{g_1}{W_s^{min}} - \frac{g_1}{g_2}\frac{S2}{E} \tag{2.18}$$

We simultaneously fitted eqn (2.18) to the data in Figs. 2.25 (a) and 2.25 (b), leaving the y-intercepts as free parameters and the slope (g_1/g_2) as a common parameter. The fit gives $g_1 = 0.104 \pm 0.006\,\mathrm{p.e/ph}$ and $g_2 = 3.1 \pm 0.3\,\mathrm{p.e./e^-}$ (this assumes the measured value of W_s^{min} by Doke *et al.* 2002 also holds for $^{83\mathrm{m}}$Kr).

It is worth noting that, since g_1 is supposed to be a detector constant and independent on the nature of the recoil, the increasing y-intercepts of the nuclear recoil data in Fig. 2.25 (b) implies that W_s^{min} must decrease with increasing nuclear recoil energy.

2.8 Summary

In summary, thanks to this work we have been able to measure for the first time $\mathcal{L}_{\mathrm{eff}}$ as a function of electric drift field, and to measure both $\mathcal{Q}_y$ and $\mathcal{L}_{\mathrm{eff}}$ with unprecedented precision and for a wide range of low-energy nuclear recoils in liquid argon. Values for $\mathcal{L}_{\mathrm{eff}}$ have been determined in the energy range 10.3 to 57.3 keV and the drift field range 0–970 V/cm, while 16.9–57.3 keV and 96.5–486 V/cm for $\mathcal{Q}_y$. Our results suggest that the effects of electric field on scintillation and ionisation in LAr TPCs are more complex than the small, energy-independent variations that have been assumed so far. The data collected are not only valuable to the DM field, but more in general to the design and calibration of any LAr TPC which exploits scintillation and ionisation signals of nuclear recoils in liquid argon.

3
LARA

The Liquid ARgon Apparatus, LARA, was designed and constructed within the High Energy Physics Group at UCL, principally to facilitate tests of novel detector technologies and readouts for dark matter and neutrino physics. Chapter 4 will describe the data reduction system I constructed for LARA, Chapter 5 will present the commissioning and performance, and in Chapter 6 I conclude with the R&D into high-voltage feedthroughs for noble gas TPCs performed using LARA. In the following sections I will describe the LARA gas system and how it operates, the level sensors in the chamber, the TPC design and field simulation, and finally the design and construction of a cryogenic photomultiplier base, as well as the calibration of the photomultiplier tube in liquid argon.

3.1 Gas system

Figures 3.1 and 3.2 show the P&ID ("piping and instrumentation diagram") and the picture of the real setup. The apparatus liquifies filtered and purified gaseous argon through cooling of a stainless steel vacuum chamber (∼9 L) with a surrounding low-grade liquid argon bath.

The gas argon that fills the chamber, hidden in the insulated wooden box on the right of Fig. 3.2, comes from a pressurised GAr bottle of grade 5.0 (99.999% purity) placed behind the aluminium gas system panel. A transfer line feeds the gas to the chamber after passing through a flow meter controller, which sets the flow of the gas, a set of three filters (one for water, one for Oxygen and one for Hydrocarbons) and a SAES MicroTorr getter Model MC 50-903-FV. The purifier works at ambient temperature and removes H_2O, O_2, CO, CO_2, and H_2 up to <100 ppt while acids, bases, and impurities coming from organics and refractory compounds up to < 10 ppt[1]. Both the filters and the getter can be bypassed if valves VA3 and VA5 are opened, with VA2, VA4, VA9 and VA10 being closed. The access to the chamber from the transfer line is provided by a long straight feed-through, equipped with a 4-way and a 6-way CF40 crosses. The gas flowing inside slowly liquifies because the chamber, of inner

[1] https://www.teesing.com/files/downloads/purifiers/purifier-mc2550-spec-torr.pdf

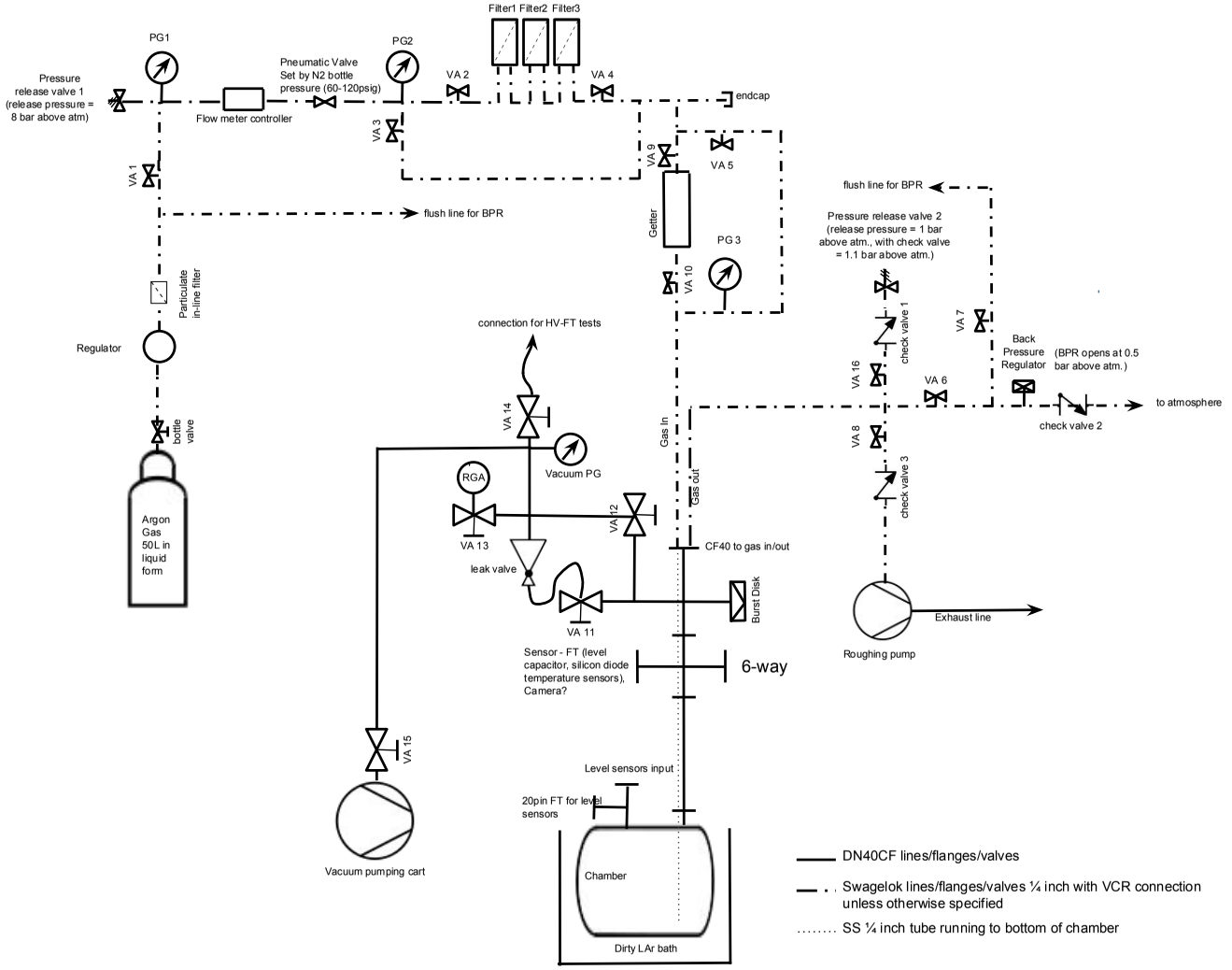

Fig. 3.1: P&ID of the LARA test bench gas system to liquify filtered and purified argon gas.

Fig. 3.2: Photo of the LARA gas system and test chamber. Major components are labelled in the figure.

diameter 200 mm and height 300 mm, is immersed in an external low-grade LAr bath, which also keeps the temperature stable once the argon is liquid (since the bath is open, the pressure is obviously constant at $\sim$1 bar, which guarantees the temperature of the low-grade liquid argon is also constant at 87.2 K).

If the chamber gets over pressurised, the gas escapes outside through a second line by means of a back pressure regulator (BPR). The BPR releases the pressure in excess and guarantees a pressure inside the chamber $\lesssim$1.5 bar. If the BPR cannot keep up with the increase in pressure, there are two safety devices which come into play: a release valve, which starts operating at 2 bar, and a burst disk, which is located on the CF40 4-way and starts operating at 2.7 bar.

The pressure in the system can be constantly monitored by means of three pressure gauges (PG1, PG2, PG3): one before the flow meter and one after, and one after the getter, which measures the pressure inside the chamber. The reading on PG3, combined with the information of the temperature inside, tells us the point on the

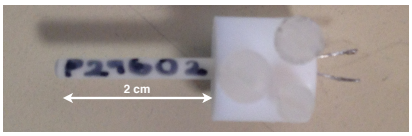

Fig. 3.3: The custom made PTFE holder protects the Pt100 fragile connections.

phase diagram of the argon in the chamber and thus its phase state. By keeping the gas inside the chamber slightly over pressured (0.15–0.25 bar above atmosphere) and a flow of ∼8 stdL/min a liquefaction rate of of approximately 0.4 mm/min can be achieved.

A bellow, fixed to the CF40 4-way, connects the system to the pump cart (model HiCube 80 Eco Pfeiffer Turbo Pump), which can evacuate the chamber down to 1.6×10^{-8} mbar when empty and down to 3.4×10^{-8} mbar with a leak rate of $1.31 \pm 0.1 \times 10^{-6}$ mbar L/s when the level sensors are inside.[2] A Residual Gas Analyser, RGA (model Pfeiffer Vacuum Prisma RGA), visible in white above the cart, can analyse the residual gases left in the chamber, provided the pressure is below 10^{-4} mbar. The RGA has also been used to check that all the connections were leak free from He leak testing.

3.2 Level sensors in LARA

The liquid argon level inside the chamber must be kept constant to provide consistent measurements over time. In fact, a larger or smaller amount of LAr would translate into more or less scintillation light produced for the same recoiling event, and, when the electric field is on, a varying level would correspond to a non uniform extraction process. If one wants to apply a drift and an extraction field, the liquid level needs also to be known precisely, as, in this case, the liquid should be only slightly above the extraction grid. To measure the level of liquid argon in the chamber, two devices have been developed: a temperature sensor based on ladder-level and a capacitive sensor.

3.2.1 Temperature sensor

The temperature sensor consists of a series of Pt100 sensors in PTFE holders (see Fig. 3.3) positioned along a PTFE rod attached to a blank feedthrough. Pt is the symbol for platinum and 100 refers to its resistance in Ohm at 0 °C. The principle

[2] The error given includes only the uncertainty in the calculation of the system volume and the error on the fit of the pressure build-up curve, which is typically small. Systematics on the measurements are potentially a lot larger and may include dependence on the stability of the base pressure, assumption of linearity and a constant slope as well as the definition of the fitting range.

of operation involves correlating the resistance of the platinum element with temperature, which is possible since platinum has a predictable change in resistance with temperature with a highly repeatable, very linear R *vs* T relationship over a wide temperature range.

Before 1968, the Calendar-Van Dusen equations:

$$\begin{aligned} T < 0\,^{\circ}\mathrm{C} \qquad & \frac{R_t}{R_0} = [1 + A \cdot T + B \cdot t^2 + C(T - 100^{\circ}\mathrm{C})T^3] \\ T > 0\,^{\circ}\mathrm{C} \qquad & \frac{R_t}{R_0} = [1 + A \cdot T + B \cdot T^2] \end{aligned} \tag{3.1}$$

were used to describe the relationship between T and R for both standard and industrial platinum resistance thermometers. In 1990, with the introduction of the ITS-90 (International Temperature Scale of 1990), temperature T_{90} (International Celsius Temperatures) was defined by means of a reference function, a logarithmic polynomial equation of 12^{th} order below 0 °C and of 9^{th} order above 0 °C (Ciarlini *et al.*, 2003).

The Pt100 sensors and the temperature monitor we adopted are from Lake Shore. The temperature monitor (Model 224) allows an abbreviated calibration of the sensors, called SoftCal$_{\text{TM}}$, using two calibration points: 77 K, the liquid nitrogen boiling point at atmospheric pressure, and 305 K, usually the room temperature. Five sensors have been deployed in the chamber. One of them was calibrated by Lakeshore using the 2-point SoftCal$_{\text{TM}}$ calibration. To calibrate the others, we immersed all sensors in liquid nitrogen and registered the resistance of the un-calibrated sensors, as well as the temperature of the calibrated one (I assumed this was the "true" temperature of liquid nitrogen at atmospheric pressure). We then used that point as one of the two calibration points needed in the SoftCal$_{\text{TM}}$, the other being room temperature (here again we assumed the temperature registered by the Lakeshore calibrated sensor to be the exact one in the room). A Pt100 sensor has two leads for connection. As suggested in the Lake Shore user's manual, using a four-lead connection instead of two can eliminate effects of lead resistance on the measurement since current is confined to one pair of current leads while sensor voltage is measured across voltage leads. To connect the sensors to the feedthrough we used Quad-Twist$_{\text{TM}}$ cryogenic wires 32 AWG, which provide optimal heat insulation (low thermal conductivity, i.e. no heat will be conducted from the wire to the sensor).

Figure 3.4 shows the Pt100 data taken during the capacitive sensor calibration (for details see Section 3.2.2). The chamber was left open and filled with liquid argon, which was then allowed to evaporate. The top Pt100 clearly stops being submerged at $\sim$ 311 minutes (vertical purple dashed line on graph (a) in Fig. 3.4), which corresponds

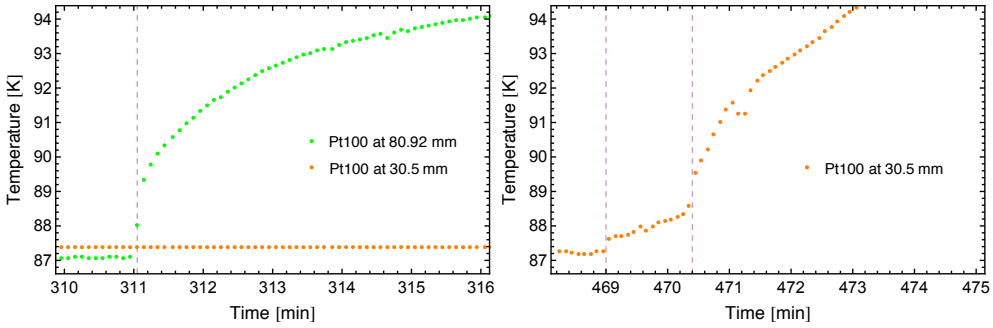

(a) (b)

Fig. 3.4: The top Pt100 sees a sharp rise in temperature as soon as it is not submerged anymore (a). Instead, the bottom Pt100 is subject to a gentler increase in temperature due to cold vapours above the liquid surface (b).

to the liquid level, as measured manually, with a precision of <0.5 mm. Instead, the bottom Pt100 does not show the same sharp rise in temperature once it stops being submerged, which happens anywhere between the two vertical purple dashed lines. This leads to an uncertainty of ∼10 mm in the level measurement and is mostly due to the fact that, by the time the bottom sensor is above the liquid surface, the vapours are cold enough for the temperature not to increase suddenly. This same mechanism, but inverted, happens when the chamber is filled, with the temperature ladder allowing for precise liquid level measurements at the bottom (when the chamber starts being filled) and less precise at the top.

3.2.2 Capacitive sensor

The capacitance of a device depends on its geometry and the dielectric present between the conductive plates. If the capacitor is being filled with some liquid, the capacitance will change as a consequence and the result can be used to measure the level of the dielectric in the capacitor. Instead of measuring the capacitance directly, one can also arrange the capacitor in series with a quartz and exploit a property of the crystal, called pullability, to work as a level sensor.

A quartz behaves like an RCL circuit with a precise resonance frequency:

$$\omega_r = \frac{1}{\sqrt{L_m C_m}} \tag{3.2}$$

This is also called series resonant frequency, because L_m and C_m are in series and cancel each other. This is analogous to a real RCL circuit, where, if an AC voltage of

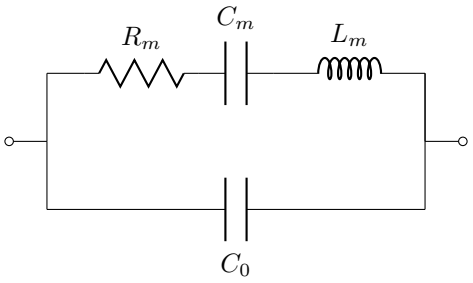

Fig. 3.5: Equivalent circuit of a quartz.

the form $V = V_0 \sin(\omega t)$ is applied, the voltage amplitude across the capacitor will be:

$$V_C = \frac{V_0}{C\sqrt{(\frac{1}{C} - L\omega^2)^2 + (R\omega)^2}} \tag{3.3}$$

thus resulting in the voltage being maximum when the frequency is equal to the resonance frequency of the circuit, namely $\omega = 1/\sqrt{LC}$. The equivalent circuit of a quartz is shown in Fig. 3.5. C_0 is called shunt capacitance or static capacitance and it is the real capacitance of the quartz. It comprises the capacitance due to the electrodes on the crystal plate and the stray capacitance due to the crystal mounting structure. R_m, C_m and L_m are called motional components and they represent the components of the crystal in operation mode (when the crystal is oscillating because of an external force, either mechanical or electrical, applied). R_m is the motional resistance measured in ohms and represents the frictional losses within the crystal. Values of R_m range from $10\,\Omega$ for 20 MHz crystals to $200\,\text{k}\Omega$ for 1 kHz. C_m is the motional capacitance measured in Farad and refers to the elasticity or stiffness of the quartz, its thickness and shape. Values of C_m range in femtofarads (10^{-15} F or 10^{-3} F). L_m is the motional inductance measured in Henrys and represents the vibrating mass of the quartz in motion. Values of L_m range between few Henrys (low frequency crystals with thicker and larger quartz wafers) to few millihenrys (high frequency crystals, with thinner and smaller quartz wafers)[3]. C_m is the only physical quantity in the equivalent circuit and it is present whether the crystal is oscillating or not. The motional components are equivalent quantities (not real) and they are valid only over a narrow range of frequencies (around the resonance).

By adding a load capacitance in series with the crystal, the resonance frequency changes to:

[3] ww1.microchip.com/downloads/en/AppNotes/00826a.pdf

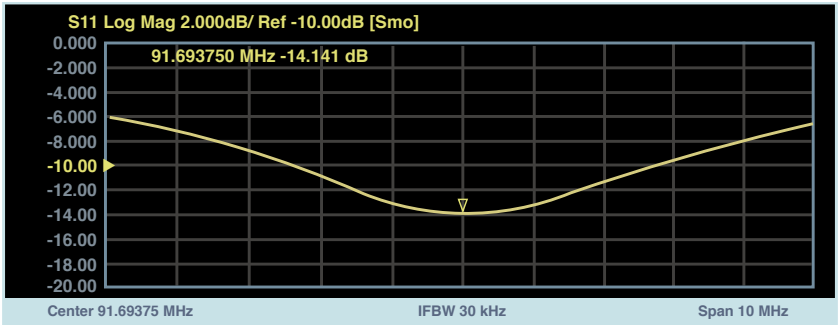

Fig. 3.6: Typical output of the VNA.

$$\omega_L = \omega_r \sqrt{1 + \frac{C_m}{C_0 + C_L}} \tag{3.4}$$

It is apparent from eqn (3.4) that the resonance frequency will increase if the capacitive load is decreased and decrease if the load is increased. The amount of change in the resonance frequency as a function of load capacitance is referred to as the pullability. The pullability increases if one uses two or more quartz in parallel with each other (Matko, 2009). For the sake of completeness, it is worth mentioning that there is also an antiresonance frequency of the form:

$$\omega_a = \frac{1}{\sqrt{L_m \frac{C_0 C_m}{C_0 + C_m}}} \tag{3.5}$$

This is also called parallel resonant frequency, as the motional inductance resonates with the parallel combination of C_m and L_m.

To measure the resonance frequency a Vector Network Analyser (VNA) can be used. The VNA we used at UCL is from Agilent Technologies, Model E5062A. The VNA can measure various quantities, among which the S_{11} parameter:

$$S_{11} = \frac{Y_0 - Y_{1PR}}{Y_0 + Y_{1PR}} \tag{3.6}$$

S_{11} is found by driving port 1 of the VNA with an incident wave of voltage V_1^+ and measuring the reflected wave amplitude V_1^- coming out of the same port. Thus, the measurement is performed in reflection mode (Pozar, 2011). Usually, it is more convenient to work in dB:

$$S_{11}[\text{dB}] = 20 \log_{10} \frac{Y_0 - Y_{1PR}}{Y_0 + Y_{1PR}} \tag{3.7}$$

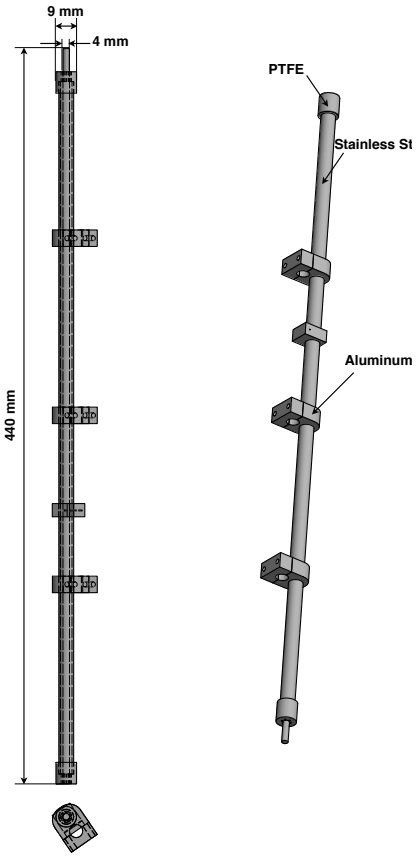

Fig. 3.7: CAD design of the capacitive sensor.

where $Y_0 = 1/50\,\Omega^{-1}$. Y_{1PR} is the total admittance of the device under test:

$$Y_{1PR} = \frac{1}{Z_0} + \frac{1}{Z_m} = j\omega C_0 + \frac{1}{R_m + j\omega L_m + \frac{1}{j\omega C_m}} \tag{3.8}$$

Since the motional and the real arms are parallel to each other, the sum is between the the inverse ratio of their impedance. The graph of the magnitude of the reflection coefficient S_{11} is shown in Fig. 3.6.

As the load capacitance we used a cylindrical stainless steel capacitor, 420 mm tall, with a 3 mm gap between the outer surface of the inner conductor and the inner wall of the outer conductor (see Fig. 3.7 for CAD design), and 9 quartz in parallel (to increase the pullability), each with nominal resonance frequency 11.0592 MHz. The

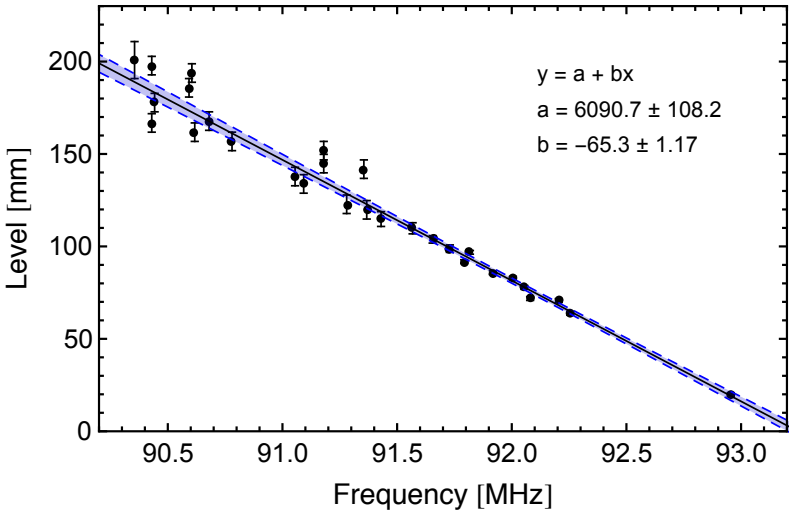

Fig. 3.8: Capacitive sensor calibration. The first points to the left have a greater uncertainty due to the fact that the liquid argon was initially boiling and only after sometime it settle down, allowing for a better measurement of the liquid depth. The blue dashed confidence bands enclose the area which contains the true curve at 95% confidence level.

capacitive sensor has been anchored to the PTFE rod that hosts the Pt100s in the chamber using aluminum clamps, while the 9 quartz, whose resonance frequency is temperature dependent, have been placed in a metal box and kept outside at ambient temperature. It is worth pointing out that when more than one quartz is used, more than one resonance frequency will be present. We chose the resonance frequency around 92 MHz as by eye it showed the greatest pullability when using the VNA. We obtained a calibration curve for the LAr level in the chamber as a function of the resonance frequency by filling the open chamber to the top and recording the resonance frequency and the liquid depth while the LAr was evaporating. Figure 3.8 shows the data and the linear fit performed on them. 95% confidence bands (blue dashed lines) are plotted along the linear fit, which was obtained by minimising the chi-squared function:

$$\chi^2 = \sum_{i=1}^{n} \frac{(y_i - (\hat{a} + \hat{b}x_i))^2}{\sigma_{y_i}^2} \tag{3.9}$$

where y_i are the liquid depths sampled with σ_{y_i} being their errors, x_i are the measured frequencies, and $(\hat{a}, \hat{b})$ the parameters of the model to fit.

From one test to another, a shift upwards or downwards of the curve might occur.

This means that while the slope of the fit remains approximately constant, the intercept needs to be determined periodically, particularly if the internal arrangement of the TPC changes. When liquifying we used the bottom Pt100 to calculate the offset. When the bottom Pt100 was at 87 K, we knew the LAr level inside the chamber was at 3.5 mm. The error on the level measured (σ_L) is a function of the uncertainties of the parameters and, given the uncertainty on the resonance frequency (ν_r) is negligible, is calculated as follows:

$$\sigma_L = \sqrt{\sigma_a^2 + \nu_r^2 \cdot \sigma_b^2} \tag{3.10}$$

which leads to an average uncertainty of 6 mm.

As mentioned above, while the temperature ladder is very precise in measuring the liquid level in the first stage of the filling, after a few hours the precision becomes smaller, as the cold vapours tend to reach equilibrium with the liquid. On the contrary, the capacitive sensor gives measurements with low (∼6 mm), but constant precision all the way to the top of the chamber. For more precise measurements around the extraction grid, a shorter, but wider capacitor should be used instead.

3.3 LARA's TPC

The TPC, shown in Fig. 3.9, is in polytetrafluoroethylene (PTFE) and has been machined by the MAPS workshop at UCL. The choice of the material is the one commonly employed for TPCs, and is dictated by several PTFE properties:

1. High density, which in our case prevents the TPC from floating in LAr.
2. Low outgassing, which is good to achieve a low vacuum.
3. High reflectance, which allows higher photon collection efficiency.

As can be seen from the CAD design in Fig. 3.9, the bottom of the TPC, a cylinder with inner diameter 83 mm for the upper part and 60 mm for the lower one, functions as the holder of the 3" R6091 Hamamatsu photomultiplier tube (PMT), which serves the purpose of light readout. The head of the PMT sits on the inner edge of the cylinder, with the body encapsulated in the bottom of the case. The inner diameters are chosen to be greater than the PMT head and body to take into account contractions of PTFE in LAr. A set of six feet disposed circularly on the bottom of the case allows the cables from the PMT base to bend and exit the structure. The PMT sits at the bottom of the TPC, with nothing at the top by design, to allow test of other readouts (e.g. SiPMs or other PMTs) and assess performance relative to the PMT (while also using the PMT to monitor the system stability). At a distance of 9.5 mm from the photocathode a series of four rings and a solid lid are fixed by means of three PolyetherEtherKetone (PEEK)

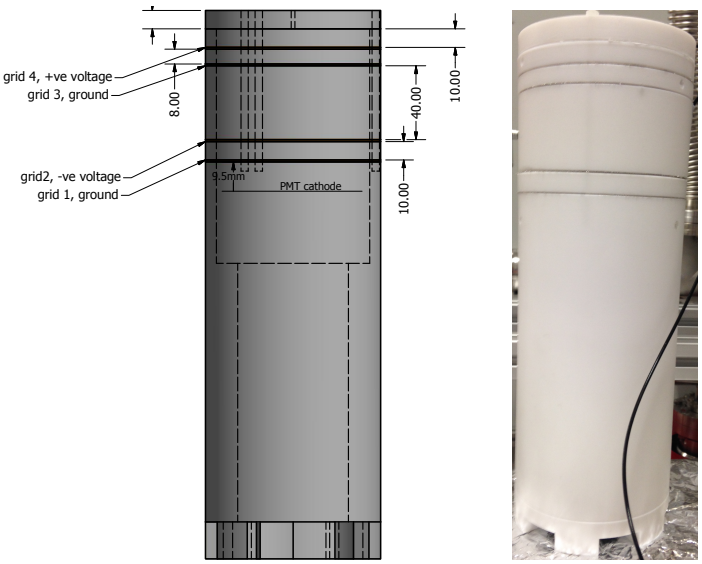

Fig. 3.9: Left: TPC design using CAD. Right: picture of the TPC.

long screws. Four stainless steel grids are also set thanks to the screws. The choice of the grid aperture is a trade off between transparency and electric field uniformity: the wider the aperture, the more transparent the grid, but also the less uniform the electric field. For a first construction of the prototype, where stability was required over transparency, a mesh of 600 µm aperture and wire diameter 160 µm with 62% transparency was chosen. The first grid, at a distance of 9.5 mm from the photocathode, screens the PMT from the drift and extraction fields, and is kept at ground. The second grid, 10 mm above the first one, is at negative high voltage (HV). The third, 40 mm from the second one, is at ground and the third one, 10 mm above the third, is at positive HV.

The maximum values for the drift field and the extraction field are constrained by the distance between the grids and the maximum voltage allowed by the HV cables[4], that is 2 kV. Thus, by design, the highest drift field is 500 V/cm and the highest extraction field 2 kV/cm. Practically, we could only achieve 475 V/cm for the drift field before breakdown, while the extraction field could not be turned on, possibly because of a faulty connection to the grid. The fact that the extraction grid was not working was not too much of a concern at this stage of the experiment, as the first

[4]This is a 50 Ohm coaxial cable, consisting of single conductor, 30 AWG, braid shielded, with a FEP jacket.

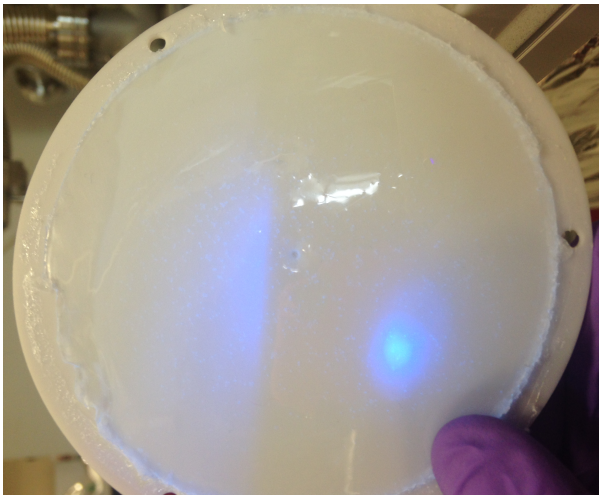

Fig. 3.10: TPB coating on the TPC lid.

measurement performed with LARA only required the drift field.

A stationary simulation of the electric fields has been carried out using COMSOL. Figure 3.11 shows that the field across the drift and the extraction regions is uniform within ∼0.96 V/cm along the radius of the TPC when the maximum HV is applied (-2 kV on the second grid and +2 kV on the fourth). Figure 3.12 reports the result of the simulation at the same voltages with a system of shaping field stainless steel electrodes (race tracks). As the difference between the two configurations was minor, we decided to opt for the simplest one in terms of construction.

3.3.1 TPB coating

Since the PMT is not sensitive to the the scintillation light from LAr, the bottom layer of the lid and the PMT window have been coated with the wavelength shifter TetraPhenylButadiene (TPB), which converts the LAr scintillation light into the blue range (∼420 nm). The TPB coating has been prepared following the procedure presented in Jerry *et al.* 2010 by dissolving 7.97 g of polystyrene pellets and 0.3 g of TPB in 100 mL of toluene. Half of the mixture was applied directly onto the PMT window and half on the PTFE lid for evaporation. After one night the toluene dissolved, leaving behind a thin plastic skin with embedded TPB. This allowed to have 0.0021 g/cm^2 TPB on the lid and 0.0033 g/cm^2 on the PMT window. Given the TPB density is approximately 1.08 g/cm^3, one can calculate the thickness l of the TPB layer according to the following equation:

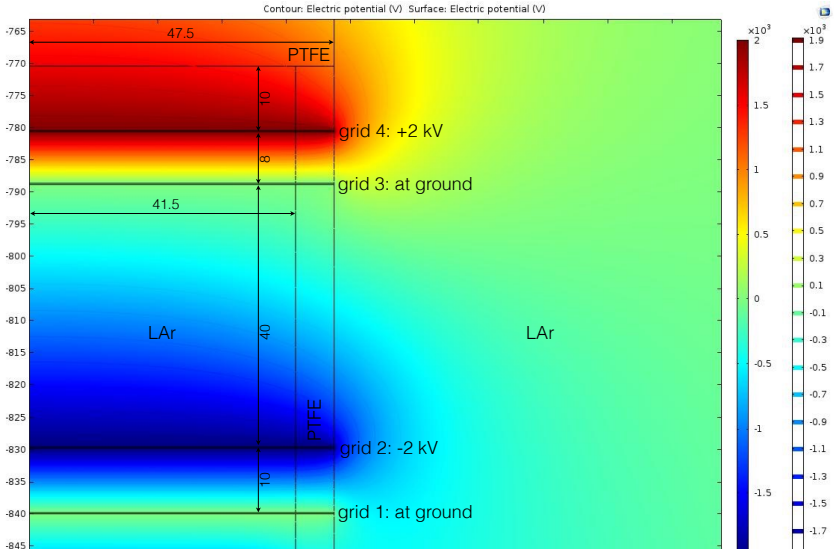

Fig. 3.11: Cross sectional view of COMSOL simulation of the electric field in LARA's TPC with no shaping field rings. The field is uniform within ∼0.96 V/cm along the radius of the TPC. All dimensions are in mm.

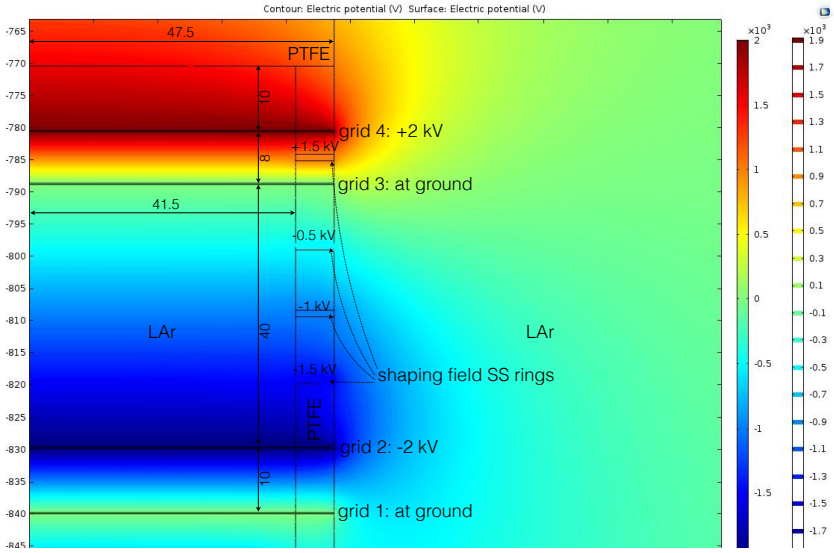

Fig. 3.12: Cross sectional view of COMSOL simulation of the electric field in LARA's TPC with stainless steel shaping field rings. All dimensions are in mm.

$$l = \frac{\rho_A}{\rho_V}$$

where ρ_A is the area density of the TPB mixture, and ρ_V is the TPB density. This yields to a deposited layer of TPB of 5.11 µm on the lid and of 8.03 µm on the PMT window above the photocathode. These are the values used for the TPB in the Monte Carlo simulation of the TPC, as, for simplicity, the polystyrene was not taken into account. To roughly check that the TPB has been deposited uniformly across the PMT window, it is sufficient to shine the surface with a UV LED (we used 350 nm): if the light reflected is visible, it means the TPB is present (see Fig. 3.10). We also experimented painting and evaporating the mixture without polystyrene, but results were not satisfactory as, when immersed in LAr, the TPB layer would partially fall in flakes. To allow SPE calibrations in the chamber, light from a 400 nm LED is transmitted via an optical fibre through a hole in the lid.

3.4 Photomultiplier tube in LARA

Since the PMT has to operate at LAr temperature and Hamamatsu does not provide cryogenic bases, an in-house printed circuit board (PCB) has been designed and developed.

Photomultipliers consists of an input window, a photocathode, focusing electrodes, a set of dynodes for electron multiplication and an anode, all contained in an evacuated glass tube. A PMT detects light and produces an output voltage in the following way:

1. Photons impinge on the glass window and are partially reflected and partially transmitted through
2. The photons transmitted hit the photocathode and are converted into electrons via the photoelectric effect with a quantum efficiency of typically 25%.
3. The electrons emitted into the vacuum are accelerated and focused by the focusing electrode and sent to the first dynode with a collection efficiency of typically 80-90%. Here, they are multiplied by means of secondary electron emission, which occurs at each of the following dynode stages.
4. The multiplied secondary electrons emitted from the last dynode are collected by the anode, the output being an AC voltage.

The photocathode is a semiconductor of multialkali or bialkali (the latter in our case) and can be described by the band theory for solids. When photons hit the photocathode, the electrons in the valence band (which in a semiconductor is fully occupied) absorb photon energy, become excited, diffuse toward the photocathode surface and, if the energy is sufficient, can jump to the conduction band and be emitted into the

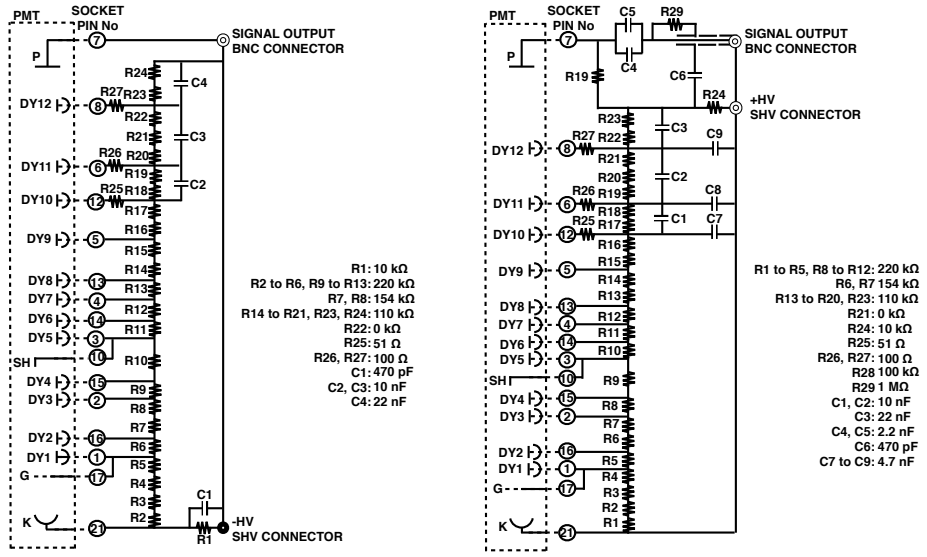

Fig. 3.13: Negative base schematic (left) and positive base schematic (right) as suggested by Hamamatsu for the R6091 PMT model.

vacuum as photoelectrons (p.e.). The probability for the photoelectric conversion to happen is called quantum efficiency and it depends on the specific semiconductor and the wavelength of the incident light (Hamamatsu Photonics K. K., 2007). The electron trajectory across the PMT tube responds to the electric field applied, which is set by the electrodes configuration, arrangement, and the voltage distribution between the dynodes. The voltage-divider circuit sets the voltage drops and is used to divide the high voltage and provide a gradient from the first to the last dynode.

The PMT used is a Hamamatsu R6091 MOD with a platinum substrate below the photocathode, whcih allows phototube to work at cryogenic temperatures.

3.4.1 Design and construction of the cryogenic voltage-divider circuit

For an electron to move from the photocathode to the anode the difference in voltage between anode and cathode needs to be positive. Two operating modes may be used: either grounding the cathode and applying a positive high voltage to the anode (positive HV base), or supplying a negative high voltage to the photocathode and grounding the anode (negative HV base). I will now briefly outline the advantages and disadvantages of the two base configurations.

Positive bases have lower dark current and as such give better performance. The

fact that no high voltage is applied to the thin cathode layer prevents field emissions, a phenomenon for which electrons are emitted from the cathode into vacuum via quantum tunnelling. On the other hand, negative high voltage schemes eliminate the potential difference between external circuits and the anode, facilitating the connection of ammeters or current-to-voltage conversion operational amplifiers, which operate at low voltage, to the anode. Another advantage of negative high voltage bases is that they are better suited for high rate pulses (e.g. at a collider), as positive high voltage bases feature a decoupling capacitor, which sets a limit on the output signal rate.

To explain why this is the case, it is necessary to look at the configuration of both circuits in more detail. Figure 3.13 shows the circuit schematic for the negative (left) and positive (right) bases recommended for the R6091 PMT used in the TPC. The schematic for the negative configuration is slightly simpler: before the cathode, where the high voltage is applied, a capacitor (C1) and a resistance (R1) are mounted in parallel and act as a low pass filter (i.e. it lets through signals with a frequency lower than the cutoff frequency $\omega_c = 1/RC$). The DC voltage coming from the high voltage power supply has often AC components. Since:

$$V_{OUT} = \frac{Z_C}{Z_C + Z_R} V_{IN} = \frac{j\omega C}{R + j\omega C} V_{IN} \tag{3.11}$$

it follows that:

$$\left| \frac{V_{OUT}}{V_{IN}} \right| = \sqrt{\frac{1}{1 + \omega^2 R^2 C^2}} \tag{3.12}$$

From the last equation it is apparent that this is a low-pass filter network, because it tends to block high-frequency signals, while passing low-frequency signals. For frequencies below the cutoff frequency $1/RC$ the magnitude of the ratio goes to zero, as does the output. For frequencies above the cutoff frequency, the magnitude of the ratios tends to unity, and the output equals the input. After the RC chain, a series of resistors provides the correct voltage drops across each dynode. The capacitors C2, C3 and C4 across the final few dynodes are called reservoir capacitors and are needed in case of high light levels seen by the PMT. They are able to store some of the charge, such that the voltage across the dynodes is more stable. After the last dynode the signal output is finally read out. The differences between the negative and the positive base are mainly two: the low pass filter in the positive configuration is before the anode and a "decoupling capacitor" (C5 and C4) is mounted before the output reading. Since the high voltage is applied to the anode, where the output signal is also read, the decoupling capacitor serves to decouple the AC output from the high voltage DC input. In this way there is no risk for the high voltage to be sent to the signal output

Fig. 3.14: R6091 Hamamatsu photomultiplier tube with in-house made PCB. The platinum underlay below the photocathode makes this PMT suitable to work at cryogenic temperatures.

and, subsequently, to the oscilloscope.

Before proceeding with the design of the base, one needs to select the specific electrical parts, as the PCB will heavily depend on the size of the individual elements. Our major constrains on the components were set by the the operating temperature and the voltage rating. Since there do not exist commercial components which are rated at liquid argon temperatures, the maximum being −55 °C, choosing components with low thermal coefficient becomes crucial. The thermal coefficient, expressed in units of ppm/°C, specifies the change in resistance (or capacitance) nominal value, if the temperature is taken below or above the operating temperature. For our specific base, only components with operating temperature from −55 °C to 125 °C and thermal co-

efficient between 15 and 25 ppm/°C have been selected. The components must also be chosen according to their working voltage, i.e. the voltage they have to withstand continuously during normal operation (1 kV–1.5 kV on the PMT high voltage), as well as their absolute maximum rated voltage, which is set by the maximum high voltage that can be applied to the PMT without breaking them (2.5 kV for the R6091). To derive the working and absolute voltage required, the voltage drop across each component along the entire chain was calculated[5] No calculation is necessary for the decoupling capacitors, as they simply have to be rated to whatever is the maximum high voltage allowed on the PMT (2.5 kV).

Given its better performance, we initially opted for the positive base. During our first liquid argon liquefaction test, the PMT often tripped because of voltage breakdown occurring due to bubble formation around the PMT base (details are presented in Chapter 5). This ultimately led to a malfunction of the base and also a break in one of the oscilloscope channels. This has to be ascribed to the failure of the decoupling capacitor, which caused the circuit to short and the high voltage to be dumped directly onto the output readout. Thus, we decided to go for the negative base, which prevents any damage to the oscilloscope in case the PMT trips and the high voltage supply is not paused promptly.

Figure. 3.15 shows a real image of the PCB and its design using the CadSoft EAGLE PCB design software[7]. The material used for the PCB is FR-4. A special cryogenic solder made of 63% Tin, 36.65% Lead and 0.35% Antimony[8] was used to manually solder all the components and the cables.

Before mounting the PCB onto the PMT, several tests have been carried out. The voltage drop across each dynode was tested manually with a multimeter up to 100 V and not higher for safety reasons. The circuit was stress tested in LAr several times to check the components and the voltage distribution remained unaltered after the immersion and applying a 2 kV high voltage. All the three bases built passed the stress test. Figure 3.14 shows one of the bases mounted on the PMT.

[5] To do this, calculate the current across the circuit at 1.3 kV and 2.5 kV (assuming these are respectively the operating and absolute voltages applied to the PMT) using:

$$I = V_{HV} / \sum_i R_i$$

where $\sum_i R_i$ is the sum of all the resistances in series in the circuit. Then, multiply the resistance of each component with the current to obtain the voltage drop across it.

[7] www.cadsoftusa.com

[8] Part number 361A-20R from Vishay Precision Group.

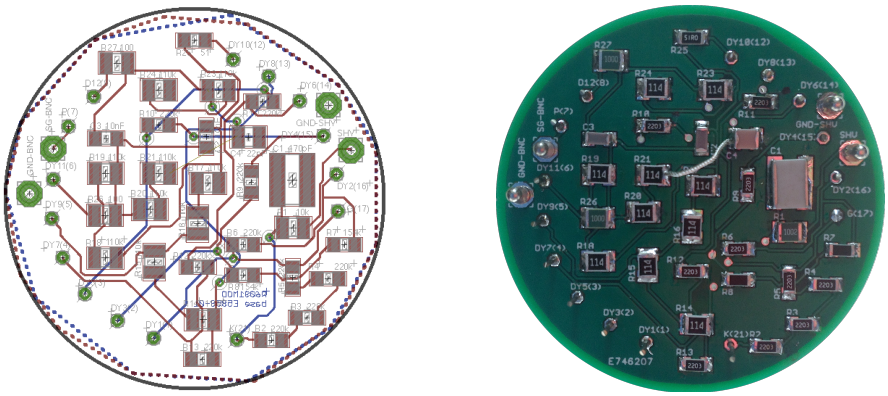

Fig. 3.15: Left: PCB design using CadSoft EAGLE. Right: Real PCB, printed by Eurocircuit[6], surface-mount component soldering performed by the author.

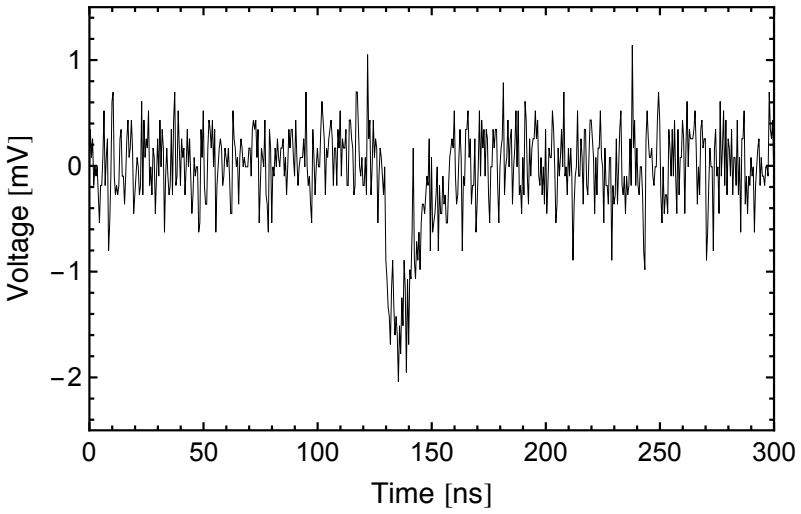

Fig. 3.16: Typical PMT output (in LAr) as seen by the oscilloscope when the LED is on.

3.4.2 Photomultiplier tube calibration

In Chapter 5 I report on the quenching of liquid argon scintillation for electron recoils when a drift field is applied, S_e. S_e is expressed as the fraction of scintillation light at a given electric drift field, $\mathcal{E}_d \neq 0$, relative to the scintillation light at zero field $S_0$for electron recoils:

$$S_e = \frac{L_y(\mathcal{E}_d)}{L_y(\mathcal{E}_d = 0)} \tag{3.13}$$

where L_y is the measured light yield expressed in units of p.e./keV$_{\text{ee}}$ relative to a specific source (in this work ^{137}Cs and ^{60}Co). The number of photoelectrons produced by a crossing particle in the scintillator is not directly measurable, but can be extracted from the output signal of the photomultiplier tube. When observing the output signal of a photomultiplier tube with an oscilloscope, the output pulse looks like the one in Fig. 3.16 The area of the pulse, a, is equal to:

$$a = \int_{\Delta T} V(t)dt \tag{3.14}$$

where V is the voltage and ΔT is the pulse width. The area is linearly related to the number of photoelectrons n for that pulse:

$$n = A \cdot a + B \tag{3.15}$$

Thus, if one wants to express the scintillation yield in terms of number of photons produced per unit of energy, it is necessary to first know the conversion between area and number of p.e. It is worth pointing out that:

$$\frac{a(\mathcal{E})}{A} \neq \frac{n(\mathcal{E})}{n} \tag{3.16}$$

and that is why we still need to convert from [mV ns] to [p.e.] even though we are calculating a ratio.

To do this, a single photoelectron (SPE) calibration on the specific PMT must be performed. This is generally done by shining a low intensity pulsed light source against the PMT and plotting the relative pulse area spectrum. The pulsed light source is usually an LED driven by a pulse generator with short pulse widths ($\leq$20 ns). An optical fibre is commonly employed to transmit the light from the LED to the PMT. If the light intensity is low enough, it is possible to obtain a pulse area spectrum for a single photoelectron. This looks like the one in Fig. 3.17 and can be explained using the model of the photomultiplier response as given in (Bellamy, 1994). The first peak is called pedestal and is associated to background processes. These can be of two kinds:

(I) low charge processes, which are always present even when no photoelectrons are emitted from the photocathode (e.g. leakage current)

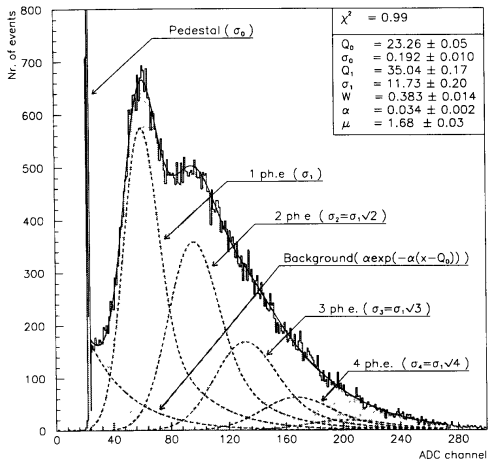

Fig. 3.17: Typical deconvoluted LED spectrum (EMI-9814B photomultiplier). Image taken from Bellamy 1994.

(II) discrete processes which can accompany the measured signal (e.g. thermoemission and noise caused by the measured light)

The first type of process is described by a Gaussian and the second by an exponential function.

$$B(x) = \frac{1-w}{\sigma_0\sqrt{2\pi}} \exp\left(-\frac{(x-\mu_0)^2}{2\sigma_0^2}\right) + w\,\theta\,\alpha\,\exp(-\alpha x) \tag{3.17}$$

where x is the pulse area variable, μ_0 is the average pulse area when 0 p.e. arrive to the first dynode, σ_0 is the the standard deviation of the type I background, w is the probability that the background will be of type II, α is the coefficient of the exponential decay in background II and θ is the step function. If the noise of type II is small, its effect will be to shift the Gaussian distribution due to background of kind I by some additional constant:

$$B(x) = \frac{1}{\sigma_0\sqrt{2\pi}} \exp\left(-\frac{(x-\mu_0-\mu_{sh})^2}{2\sigma_0^2}\right) \tag{3.18}$$

The other peaks come from single, double, triple... photoelectrons events and their Gaussian distribution is due to the response of the multiplicative dynode system.

To fully describe the PMT response, we also need to take into account the photo collection and the photoemission from the photocathode. Together these processes are described by a Poisson distribution:

$$P(n;\nu) = \frac{\nu^n e^{-\nu}}{n!} \tag{3.19}$$

with ν is defined as:

$$\nu = m \cdot QE \tag{3.20}$$

where $P(n;\nu)$ is the probability that n photoelectrons will be observed with mean ν, m is the mean number of photons hitting the photocathode and QE the quantum efficiency associated to the PMT.

Thus, the PMT response can be summarised by the following equation:

$$S(x) = B(x)e^{-\nu} + \sum_{n=1}^{\infty} \frac{\nu^n e^{-\nu}}{n!} \times \frac{1}{\sigma_1\sqrt{2\pi n}} \times \exp\left(-\frac{(x-(\mu_0 + n\mu_{spe} + \mu_{sh}))^2}{2n\sigma_{spe}^2}\right) \tag{3.21}$$

μ_{spe} is the average pulse area for an SPE with σ_{spe} being its the standard deviation, and $\mu_n = \mu_0 + n\mu_{spe}$ is the mean related to the peak in the histogram initiated by n photoelectrons.

Practically the pedestal is often approximated with a Gaussian. This implies that the mean pulse area for one SPE is the mean of the 1 p.e. peak, μ_1, minus the pedestal mean, μ_0, where both means are found via a Gaussian fit:

$$\mu_{spe} = \mu_1 - \mu_0 \tag{3.22}$$

To obtain the average charge at the PMT output for an SPE, it will be sufficient to divide μ_{spe} by the resistance of the circuit (50 Ω for an oscilloscope). Especially with small PMTs (like the 3 inch one we use), it is often not easy to resolve down to the SPE level without using an amplifier. In this case to estimate μ_{spe}, another approach which relies on measuring the linearity of the PMT response to multiple photoelectrons can be employed.

For large number of photoelectrons ν (i.e. high intensity source) the Poisson distribution in eqn (3.21) goes over into a Gaussian with standard deviation $\sqrt{\nu}$, and thus eqn (3.21) becomes:

$$\lim_{\nu\to\infty} S(x) = \int \left(\frac{e^{-(n-\nu)^2/2\nu}}{\sqrt{\nu 2\pi}} G_n(x)\right) dn \tag{3.23}$$

with

$$G_n(x) = \frac{1}{\sigma_{spe}\sqrt{2\pi n}} \times \exp\left(-\frac{(x-(\mu_0 + n\mu_{spe} + \mu_{sh}))^2}{2n\sigma_{spe}^2}\right) \tag{3.24}$$

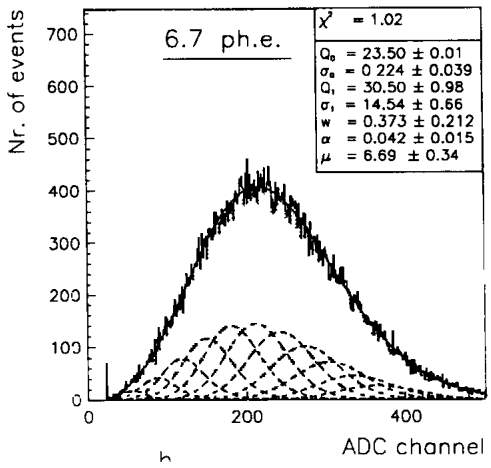

Fig. 3.18: Typical LED spectrum at high light intensities. Image taken from Bellamy 1994.

Because we are in the limit of large light pulses, the pedestal distribution in eqn (3.23) has been neglected.

In eqn (3.23), the Gaussian with mean and variance ν is the weight assigned to each $G_n(x)$ function. The largest contribution to the integral comes from the G_n function for which $n = \nu$, with less and less contribution as n moves away from ν. Practically, only the G_n functions with $n < \nu - \sqrt{\nu}$ or $n > \nu + \sqrt{\nu}$ will contribute, as expressed visually by Fig. 3.18.

Thus, in the limit of large pulses, the final distribution will be a Gaussian with mean and variance equal to ν. If we call m^* and σ^* the mean and standard deviation obtained from the fit (in units of [area×time]), it follows that their ratio to the second power will approximate the average number of photoelectrons arriving to the first dynode:

$$\left(\frac{m^*}{\sigma^*}\right)^2 = \left(\frac{\nu}{\sqrt{\nu}}\right)^2 = \nu \tag{3.25}$$

By shining different light intensities on the PMT, one can extract the mean number of photoelectrons at each data point from the pulse area spectrum. The mean number of photoelectrons seen by the PMT is then plotted against the mean of the peak (in units of [area×time]), which represents the light output of the LED. The relation between the PMT output signal and the number of photoelectrons collected by the first dynode is linear.

The R6091 photomultiplier tube was calibrated at 1000 V in liquid argon firing

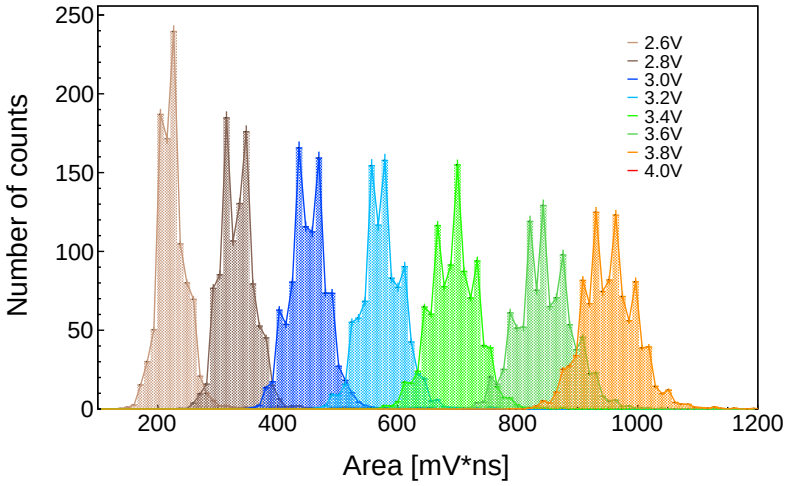

Fig. 3.19: Histogram of the pulse area at different voltages intensities on the pulse generator. Distributions normalised to 1000 counts.

light pulses of 400 nm and 20 ns width from a pulse generator at a rate of 100 Hz through an optical fibre. The pulse generator provided the trigger, such that the PMT output was measured only when the LED was on. Data were acquired using a DT5751 Caen digitizer, which comes with a GUI, where one can visually monitor the input, and saves data in the form of a text file. The text file contains the x and y value (respectively time and voltage) of the waveform. Figure 3.19 shows the pulse area spectrum at several light intensities. The plot of the of the number of photoelectrons, calculated as explained above, as a function of the mean pulse area at different LED intensities is shown in Fig. 3.20. From the linear fit we obtain the parameters, and their uncertainties, to use when converting from [area $\times$ time] to p.e. Along with the linear fit (performed using the least square method), Fig. 3.20 shows the 95% confidence interval on the fit, which says that there is a 95% probability that the true best-fit line for the data sample lies within that band. This gives a visual sense of how well the data define the best-fit curve. The band tends to be narrow around the mean x-value of our sample ($\bar{x}$) and larger around the minimum and maximum values. Let us try to explain this intuitively. The least square regression has to pass though $(\bar{x}, \bar{y})$, where the terms $\bar{x}$ and $\bar{y}$ refer to the arithmetic mean of the independent and dependent variables respectively (in our case x represents the area and y the number of p.e.). If we take into account the uncertainty in the slope, i.e. the slope were a little higher or lower than the estimated one, the new line would move further away from the current

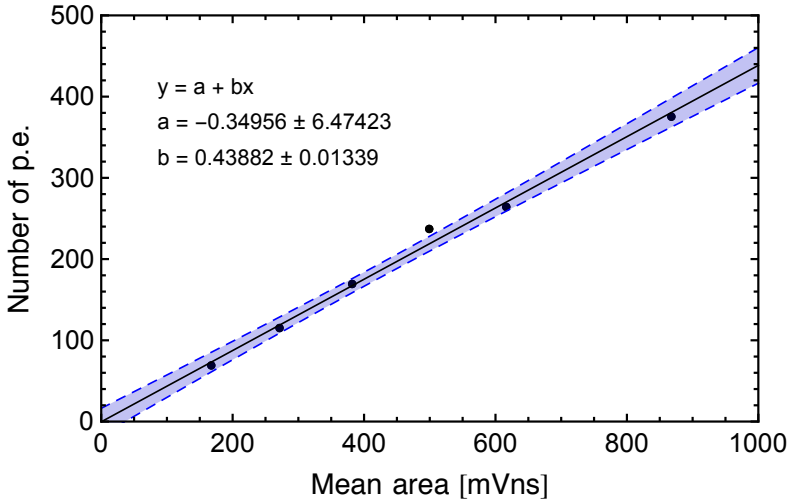

Fig. 3.20: Photomultiplier linearity plot. On the x axis the mean value of the pulse area at different light intensities obtained via a Gaussian fit on the distributions in Fig.3.19. On the y axis the number of photoelectrons as calculated in eqn (3.25). 95% confidence bands are plotted along the fitted regression line calculated via the method of least squares.

line near the ends than near the middle, always crossing $(\bar{x}, \bar{y})$. If instead we take into account the uncertainty in the intercept, such that the line will pass only close to $(\bar{x}, \bar{y})$, the new line will move upwards or downwards from the current line. When we take into account both uncertainties, the new line will fan out around the mean, $\bar{x}$, because of the uncertainty in the intercept, with some additional spread peaking at the minimum and maximum x-values because of the uncertainty in the slope. If the intuitive argument is not sufficient, one can look at the formula for the variance of the estimate of the mean value at a specific x, say, x_0, which has been used to construct the confidence interval around the fit curve:

$$V[\hat{\mu}_{Y|x_0}] = \sqrt{\hat{\sigma}^2 \left(\frac{1}{n} + \frac{(x_0 - \bar{x})^2}{\sum_{i=1}^{n} (x_i - \bar{x})^2} \right)} \tag{3.26}$$

where $\hat{\mu}_{Y|x_0}$ is the estimate of the mean of Y (this is the random variable representing the number of p.e. in our case) at x_0, $\hat{\sigma}^2$ is the estimator of the variance of Y, and n is the number of points of the data sample. The summation runs over these n observations $(x_1, ..., x_n)$ and $\bar{x}$ is the mean x-value of such n observations. It follows from the formula that the variance is minimum for $x_0 = \bar{x}$ and increases as x_0 departs

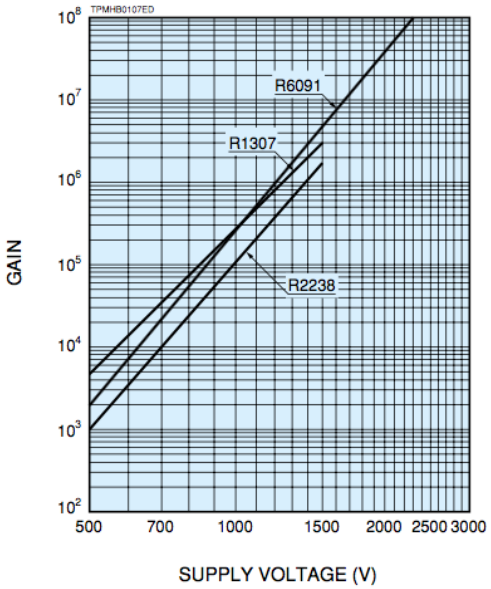

Fig. 3.21: Gain curve for R6091 PMT by Hamamatsu.

from $\bar{x}$.

3.4.3 Photomultiplier tube gain

To assess the correct calibration of the PMT, we measured the gain of the PMT and compared it to the one reported by Hamamatsu at the same supply voltage value. We calculated the gain at 1000 V as the average gain $\langle G \rangle$ across all light levels (these correspond to different voltage intensities on the pulse generator, as shown in Fig. 3.19) according to the following formula:

$$\langle G \rangle = \sum_{i \in \text{light levels}} \frac{Q_i}{q_{e^-}\, n_i} \tag{3.27}$$

where q_{e^-} is the electron charge and n_i is the number of photoelectrons at the i^{th} light level as calculated in eqn (3.25). Q_i is the charge collected at the i-th light level, and is calculated as follows:

$$Q_i = \frac{m_i^*}{50\,\Omega} \cdot 10^{-12} \tag{3.28}$$

where m_i^* is the fitted mean in units of [mV ns] of each distribution in Fig. 3.19, 50 Ω is the resistance of this oscilloscope and Q_i is expressed in units of Coulomb. The gain at 1000 V, calculated according to eqn (3.27), is $\sim 2.87 \times 10^5$, that is of the same

order of magnitude as the one reported by Hamamatsu at the same supply voltage, i.e. $\sim 1.8 \times 10^5$ (see Fig. 3.21). As our calculated gain is roughly 1.6 times smaller than the one from Hamamatsu, it follows that we are slightly underestimating the number of photoelectrons. Although this discrepancy is not extremely significant, let us investigate the reasons behind the result. Let us call m the "true" mean of the pedestal-subtracted charge distribution and σ the "true" RMS of the Poisson fluctuation of the number of photoelectrons reaching the photocathode, such that:

$$n = \left(\frac{m}{\sigma}\right)^2 \tag{3.29}$$

where m and σ are here unitless[9]. Then, the following holds true:

$$\begin{aligned} m &= G\, n \\ \sigma &= G\, \sqrt{n} \end{aligned} \tag{3.30}$$

What is actually measured though is:

$$(\sigma^*)^2 = \sigma^2 + \sigma_{ped}^2 + \sum_{i=1}^{k} \sigma_i^2 \tag{3.31}$$

where σ_i is the RMS of the photoelectron distribution at the i^{th} dynode (with k being the total number of dynodes) and σ_{ped} is the RMS of the pedestal. As the total gain is given by:

$$G = \prod_{i=1}^{k} g_i \tag{3.32}$$

where g_i is the gain at dynode i^{th}, it follows that the contribution to the final RMS from the first dynode is given by:

$$\begin{aligned} \sigma_1 &= (g_2 g_3 ... g_i ... g_k)\sqrt{g_1 n} = \\ &= \frac{G}{\sqrt{g_1}}\sqrt{n} \end{aligned} \tag{3.33}$$

For a generic dynode i, the above equation becomes:

[9] If m is measured in [mV ns], like in eqn (3.25), simply multiply by 10^{-12} and divide by 50 Ω and by the electron charge in Coulomb

$$\begin{aligned}\sigma_i &= \left(\prod_{j=i+1}^{k} g_j\right)\left(n \times \prod_{j=1}^{i} g_j\right)^{1/2} \\ &= \frac{G}{\left(\prod_{j=1}^{i} g_j\right)^{1/2}}\sqrt{n}\end{aligned} \tag{3.34}$$

Thus, we can rewrite eqn (3.31) as:

$$\begin{aligned}\sigma^{*2} &= G^2 n\left(1 + \frac{1}{g_1} + \frac{1}{g_1 g_2} + ... + \frac{1}{g_1 ... g_k}\right) + \sigma_{ped}^2 \\ &= G^2 n\left(1 + \sum_{j=1}^{k} \frac{1}{\prod_{i=1}^{j} g_i}\right) + \sigma_{ped}^2\end{aligned} \tag{3.35}$$

Since for 1 photoelectron there are no Poissonian fluctuations (i.e. σ^2 in eqn 3.31 equals zero as n is exactly equal to 1), for 1 photoelectron eqn (3.31) becomes:

$$\begin{aligned}{\sigma^*_{\text{1p.e.}}}^2 &= \sigma_{ped}^2 + \sum_{i=1}^{k} \sigma_i^2 \\ &= \sigma_{ped}^2 + G^2\left(\frac{1}{g_1} + \frac{1}{g_1 g_2} + ... + \frac{1}{g_1 ... g_k}\right)\end{aligned} \tag{3.36}$$

If we neglect the pedestal contribution in eqn (3.36), the measured RMS of eqn (3.31) can be rewritten in terms of $\sigma^*_{\text{1p.e.}}$ as:

$$\sigma^{*2} = G^2 n\left[1 + \left(\frac{\sigma^*_{\text{1p.e.}}}{G}\right)^2\right] \tag{3.37}$$

and the number of photoelectrons at a generic light level is then equal to:

$$n = \left(\frac{m^*}{\sigma^*}\right)^2\left[1 + \left(\frac{\sigma^*_{\text{1p.e.}}}{G}\right)^2\right] \tag{3.38}$$

In the limit of ${\sigma^*_{\text{1p.e.}}}^2 \to 0$ (this case for relatively high supply voltage values for which g_1 is large) eqn (3.38) reduces to eqn (3.25). As such, it can be seen from eqn (3.38) that by not taking into account $\left(\frac{\sigma^*_{\text{1p.e.}}}{G}\right)^2$, we are in fact underestimating the number of photoelectrons.

4
LArView

For the data analysis of S_e in Chapter 5 and future measurements with LARA, we developed a software package called LArView, which stands for Liquid Argon Viewer. LArView reads in the raw data formats, operates as a pulse finder, and performs parameterisation, reducing the waveforms to a set of physical variables whose distributions can be easily accessed given ROOT compatible ntuple output. LArView is implemented in `C++`, features a class-oriented architecture and is also provided with a Graphical User Interface (GUI).

Data can be acquired directly from the oscilloscope in the form of a text file, which contains the x and y values (respectively time and voltage) of the waveform displayed on the screen of the oscilloscope. For the statistics to be significant, an appropriate number of waveforms needs to be acquired. To speed up this process a digitiser can be used instead. The digitiser samples the input signals at constant frequency (sampling rate of 1 GS/s) and records all the waveforms in a single text file. This can be split afterwards in n text files (needed for LArView), each one representing one of the n waveforms acquired.

One key plot in my analysis is the charge distribution for the waveforms collected. To get the charge one needs to integrate a waveform over a specific range of time (V s) and then divide that number by the resistance of the circuit (V s/Ω). It is worth pointing out that to go from a pulse area distribution to a charge distribution it is sufficient to scale the first by the resistance in the circuit, which is a constant of the setup. To get a reasonable charge spectrum one needs to specifically integrate the charge over the signal region. The simplest way to get a charge distribution is to integrate each waveform over a fixed region, that is where the signal is expected to be. If the voltage output is driven by a pulsed light source, this is easy, as the signal will always fall within a specific time after the light turns on. This type of analysis can be very useful to get preliminary results, especially if one does not want to write any fancy and complicated algorithm. On the other hand, a lot of noise will also be included (the signal might be embedded with noise or no pulse might be present all over the integral range); and, most importantly, the signal region needs to be known

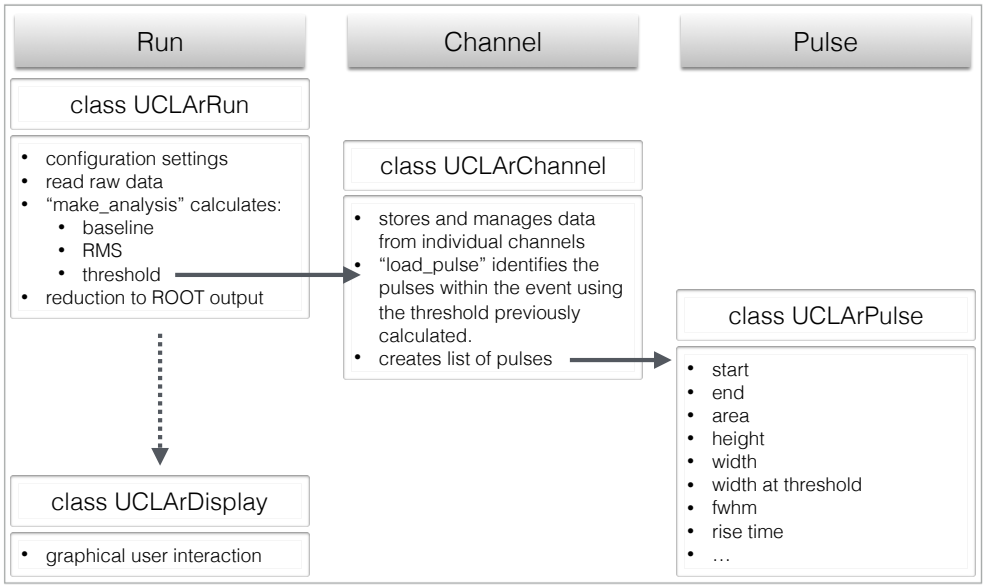

Fig. 4.1: Schematic of the LArView software architecture.

a priori. Without knowing this, one can make no use of this method. These are the motivations that led to the development of the LArView software.

4.1 Software architecture

LArView's architecture is illustrated schematically in Fig. 4.1 and includes the following classes:

- **UCLArRun:** The UCLArRun class manages the configuration settings and the reduction of the data into ROOT ntuples. Its class member *make_analysis* analyses each event timeline and calculates the waveform's baseline, RMS and threshold.
- **UCLArChannel:** The UCLArChannel class stores and manages data from individual channels (one in our case) and all contained structures. In particular, the threshold calculated for each waveform by UCLArRun is used by *load_pulse*, class member of UCLArChannel, to identify the pulses in the event. Once the pulses have been found (as we shall see later a pulse is defined by a start and end time), they are added to the class member *add_pulse* and then passed to the class UCLArPulse.

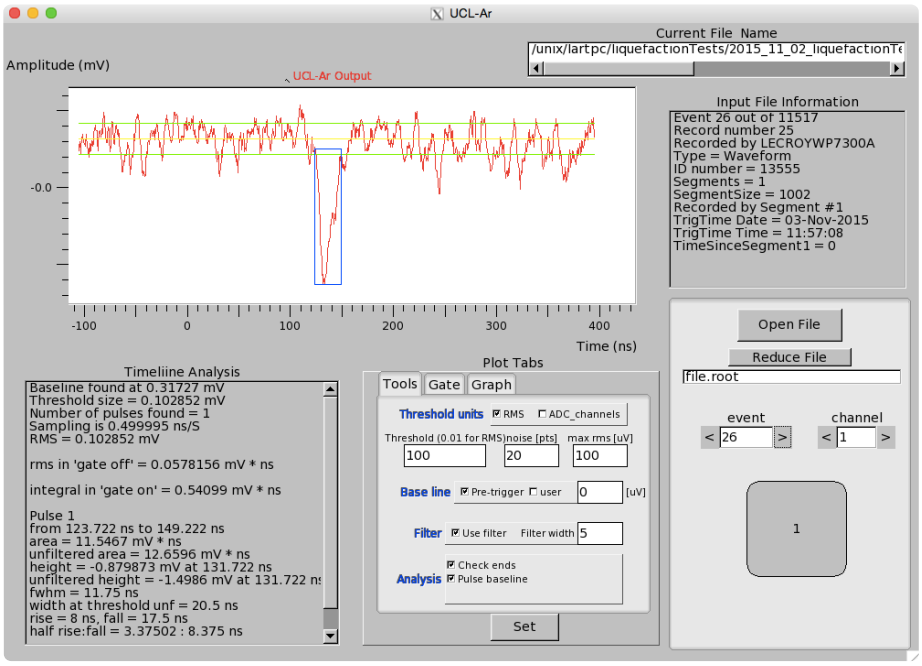

Fig. 4.2: Graphical User Interface of LArView.

- **UCLArPulse:** The UCLArPulse class calculates and stores all the information related to individual pulses, such as height, area, width, rise time, fall time, etc.
- **UCLArDisplay:** Finally, the UCLArDisplay class takes care of the graphical user interaction while interacting with the classes which manage the analysis and holds both the raw and the reduced data files.

4.2 Baseline and threshold characterisation

Two things are needed before LArView can start looking for a pulse within a waveform: a baseline and a threshold. The baseline is constant all over the waveform and it is calculated into two steps. First, a rough calculation is performed by taking the average voltage on the whole waveform:

$$\mu_b = \sum_{i=1}^{n} \frac{y_i}{n} \tag{4.1}$$

where y_i is the voltage amplitude for the sample point i and n is the total number of sample points. A more accurate estimation is then carried out by re-averaging the

waveform a second time after taking out "obvious" pulses. This is done by averaging over the sample points y_i whose amplitude is within 1 RMS from the baseline:

$$|y_i - \mu_b| < |\sigma_b - \mu_b| \tag{4.2a}$$

$$\text{where} \quad \sigma_b = \sqrt{\sum_{i=1}^{n} \frac{y_i^2}{n} - \left(\sum_{i=1}^{n} \frac{y_i}{n}\right)^2} \tag{4.2b}$$

If the "pretrig" option is selected in the GUI (see Fig. 4.2), the baseline is calculated only using the first sample points for which the root mean square (RMS) does not exceed the pre-defined user value "max rms (uV)" (expressed in µV) shown in the GUI (so with sensible tuning, this is at the start of a pulse):

$$\mu_b = \sum_{i=1}^{k} \frac{y_i}{n} \qquad k \text{ such that } \mu_b < \text{"max rms"} \tag{4.3}$$

This option is likely to be valuable when only noise is present in the first part of a waveform, before any pulse starts. One can also choose to set the baseline manually by ticking the box "user" in the GUI.

The threshold is measured in terms of number of RMS from the baseline. This number can be set in the graphical interface in the box "Threshold (0.01 for RMS)". For example, to set the threshold twice above and below the baseline, one has to choose 200. The formula for the RMS is the one in eqn (4.2b), where the sum is calculated over the sample points in the pre-trigger region if the "pretrig" option is selected and over the entire waveform if it is not.

4.3 Pulse finding

With a baseline and a threshold defined, LArView can then identify the pulses within a waveform. A pulse is described by a start and end. These are defined as follows: the timeline increasing above the threshold indicates the pulse start, the timeline falling below the threshold indicates the pulse end. The option "check ends", selectable in the GUI, might adjust the pulse start and end to be respectively a bit earlier and further in time (the code checks if sample points before [after] the start [end] get any closer to the baseline or not—this is irrespective of the threshold). This allows optimisation of pulse finding.

Once a pulse is found (i.e. its start time and end time are known), its width is calculated. The pulse is then loaded onto the timeline by the public member *loadPulses*

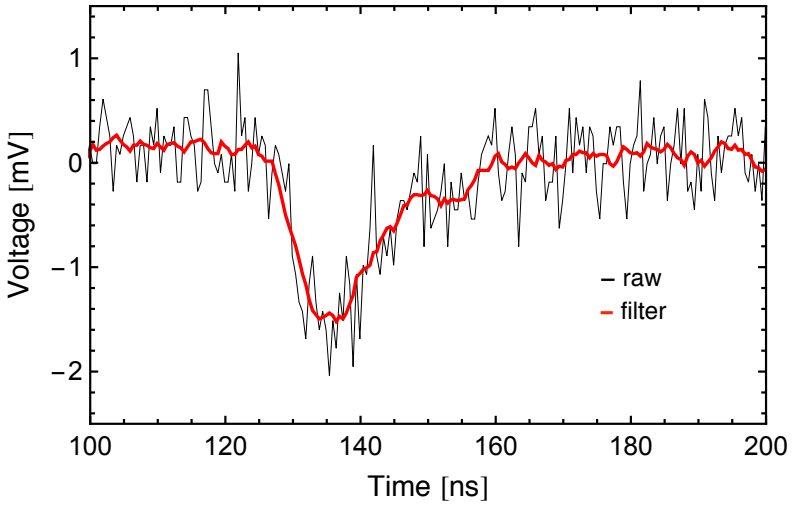

Fig. 4.3: Comparison between raw data and the same waveform obtained using the moving average with width filter width equal to 11 ($m = 5$).

of the class UCLArChannel only if its width is greater than the user defined parameter "noise" (which in the GUI is expressed in number of sampling points).

4.4 Raw data filtering

One important feature of LArView is the possibility of filtering the raw data. This is convenient when waveforms are particularly noisy and one needs to enhance the signal-to-noise ratio in order to identify relevant pulse structures. If the "filter" box is ticked and a "filter width" f is specified in the GUI, LArView will apply a moving average algorithm to the raw waveform which is defined as follows:

$$\tilde{y_i} = \sum_{j=i-m}^{i+m} \frac{y_j}{2m+1} \tag{4.4}$$

where m is the parameter chosen by the user, with $2m + 1$ being the filter width f, and $\tilde{y}$ and y represent the filtered and the raw data amplitudes. The original text file will be converted into a filtered version, in which the amplitude of each sample point is replaced by the average of that point and the m points before and after. The pulses start and end points will be defined using the filtered text file. It should be pointed out that the DAQ raw data is never modified, as an extra buffer containing all the filtered data is created instead. Figure 4.3 shows a raw waveform and the smoothed one obtained using the moving average.

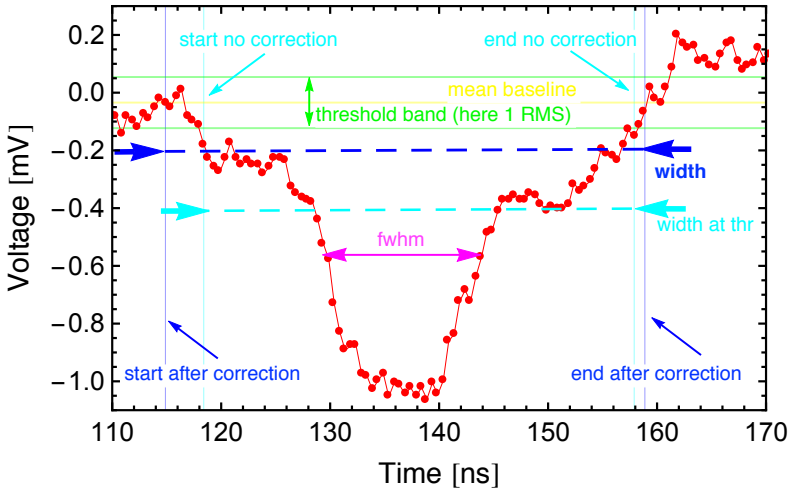

Fig. 4.4: Pulse parametrisation in LArView.

4.5 Physical variables

Once the pulses are identified, LArView parametrises each pulse by means of physical variables. Below is the complete list of the variables.

- **pulse start and pulse end:** As explained above, the pulse start and end are respectively defined by the timeline growing above and decreasing below the threshold. Practically, the pulse start is found by looping over all the sample points in the waveform until the following condition is satisfied:

$$|y_i - \mu_b| < |y_{thr} - \mu_b| \tag{4.5}$$

where the voltage threshold, y_{thr}, is given by:

$$y_{thr} = N\sigma_b \tag{4.6}$$

where N is set by the user. The start point will then correspond to the i^{th} point for which (4.5) is true. Once a pulse start is found, a loop is done over the remaining sample points to look for the pulse end by requiring that:

$$|y_i - \mu_b| > |y_{thr} - \mu_b| \tag{4.7}$$

Analogously, the end point is the one for which eqn (4.7) applies. Sometimes it might happen that the amplitude value of one of the sample points preceding

the start is actually closer to the baseline than the start's amplitude itself. As anticipated above, if the option "check ends" in the GUI is activated, LArView checks for this and can correct the pulse start and end, as can be seen in Fig. 4.4. The same is done for the pulse end. Once a pulse is found (i.e. its start and end are defined), the search continues over the rest of the waveform.

- **pulse width:** Once the pulse start and end have been computed, LArView checks that the pulse width is greater than the noise width chosen by the user. If it is, then the pulse is included in the pulses' list.
- **pulse area:** The pulse area, expressed in units of mV ns, is a positive defined quantity and it is the absolute value of the integral of the amplitude of the pulse over its width. Practically it is calculated by looping over the sample points of the pulse and summing over the difference between the amplitude and the mean baseline:

$$\text{area} = \left(\sum_{i=\text{start}}^{\text{end}} |y_i - \mu_b| \right) \cdot \Delta t \tag{4.8}$$

  where Δt is the sampling time in ns.
- **pulse height and pulse maximum at:** The height is computed by looping over all the y_i amplitudes of the pulse and finding the maximum amplitude. Once the maximum is found, the corresponding time value for that point is also stored in "pulse maximum at".
- **pulse width at threshold:** This is found by searching the sample points in the pulse whose amplitude increases above the threshold (left edge) and decreases below it (right edge) and taking their difference. The width at threshold can be seen as the difference between end and start before any correction is applied.
- **pulse fwhm:** This is the the width of the pulse when the amplitude is half the of the pulse maximum amplitude.
- **pulse rise time and fall time:** The rise time is the time it takes for the pulse to reach its maximum (that is the difference between the start and the "maximum at" variable). Similarly, the fall time is the time it takes for the pulse to reach the end from its maximum (that is the difference between the end and the "maximum at" variable).

Except for the pulse start and end, all the other quantities are calculated twice using the unfiltered and filtered data files. All quantities which are dimensionally a time are expressed in ns and in mV when they are dimensionally a voltage. For each waveform the following variables, of which a description was already given above, are also stored:

- **number of pulses**
- **baseline**
- **RMS**
- **sampling time**
- **noise width**

The sampling time depends on the oscilloscope/digitiser settings and it is expressed in ns. The noise width is set by the user in the GUI and it is also in ns. Before using LArView for the actual analysis, the software has been validated using a set of data of known characteristics created by a pulse generator. All the distributions agreed with what was expected.

Figure 4.6 shows the distributions for the variables most relevant to our analysis. The data refers to the PMT submerged in liquid argon with a 400 nm LED pulsed at 100 Hz with width 20 ns (data were taken with an oscilloscope). Since in this case the response of the PMT is driven by a known source, one can reject part of the noise by selecting only the pulses whose start time falls within the "light on" time window. For these plots the following settings have been used: no pre-trigger option selected, filter equal to 5, noise width equal to 20 ns, and threshold set to 1 RMS above and below the baseline. With this choice not all the noise pulses are rejected (as can be seen from the area distribution in Fig. 4.6, where the small peak to the left comes from noise). One can opt for increasing the threshold, but this would result in a worse identification of the pulse start and end: part of the pulse would be regarded as noise (see Fig. 4.5) as it falls within the wider threshold band. To avoid this, one technique is to still choose 1 RMS band threshold and require later in the analysis that the pulse height is greater than 2 (or more) RMS. Another simple, yet effective technique to further discard noise is requiring the height to be negative and the rise time to be smaller than the fall time (as it should be for a pulse coming from the PMT).

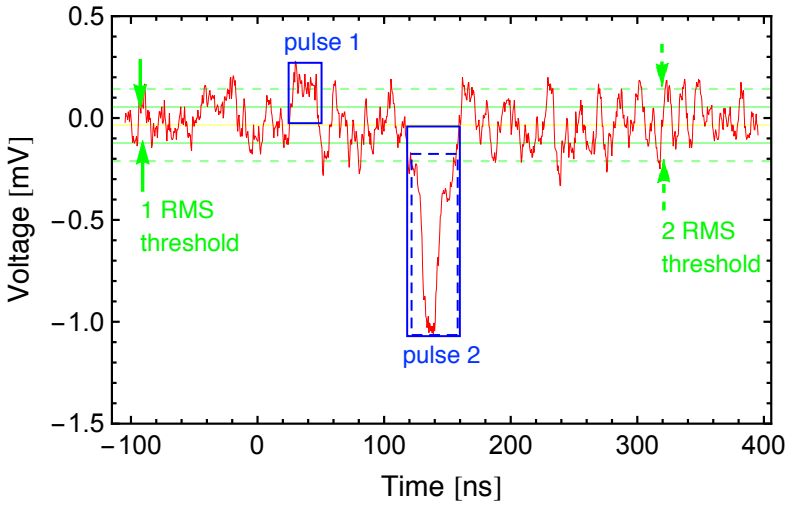

Fig. 4.5: Green solid lines refer to 1 RMS threshold band, while the green dashed ones to 2 RMS threshold band. With the first choice, two pulses are identified: one positive and one negative (coming from the PMT response to the LED). With the second choice, only the negative pulse is found, at the expense of a worse identification of the pulse start and end, which leads to nearly 40% of the pulse area being lost.

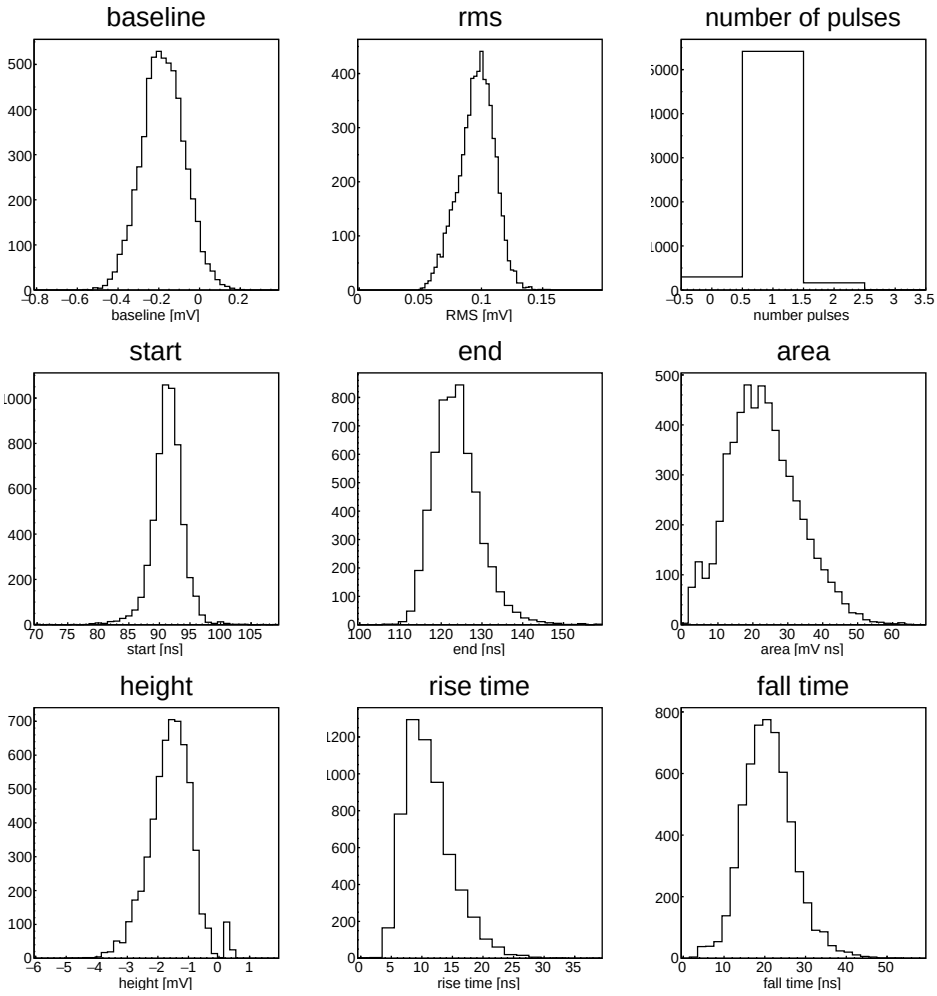

Fig. 4.6: Distributions for some of the variables in LArView. On the y axis is the number of counts. The data refers to the PMT submerged in liquid argon with a 400 nm LED pulsed at 100 Hz with width 20 ns (data were taken with an oscilloscope).

5
Measurement of scintillation quenching for ER in LAr

The quenching of LAr scintillation for electron recoils when a drift field is applied, S_e, is the first measurement performed with LARA. Given extensive data on S_e (Kubota *et al.*, 1978*b*; Hitachi *et al.*, 1987; Doke *et al.*, 2002) this measurement serves the purpose of validating the TPC operation and stability.

5.1 Liquefaction and TPC monitoring

Before the liquefaction, the chamber was pumped down to 10^{-4} mbar and the system was flushed with purified gas argon. Fifteen minutes after filling the external bath with low-grade LAr, the argon bottle was opened and gas argon started to fill the chamber. By continuously keeping the external liquid level just below the chamber edge, the gas inside the chamber, kept slightly over pressured at 0.15–0.25 bar above atmosphere, is liquified almost instantaneously, at an average rate of approximately 0.4 mm/min. The filter system was bypassed, such that a GAr flow of 9 stdL/min could be achieved (the filters restrict the flow down to 2.5 stdL/min). Resonance frequency readings from the capacitive sensor were taken automatically every 60 seconds thanks to the VNA remote control. Four Pt100s were inserted in the temperature ladder at 3.5 mm, 20.66 mm, 150.47 mm, and 401.57 mm. Another one was placed above the top grid at 281.38 mm in a hole in the PTFE and a sixth one was laid on top of the lid at 293.38 mm. All the distances are relative to the bottom of the chamber (see Fig. 5.1). The temperature data combined with the pressure inside the vessel constantly locates the system in the phase diagram showed in Fig. 5.2. The diagram is only approximate and was made by the author. To derive the boundaries of the gas region, Antoine's equation has been used. This takes the following form:

$$\log_{10} P = A - \frac{B}{T + C} \tag{5.1}$$

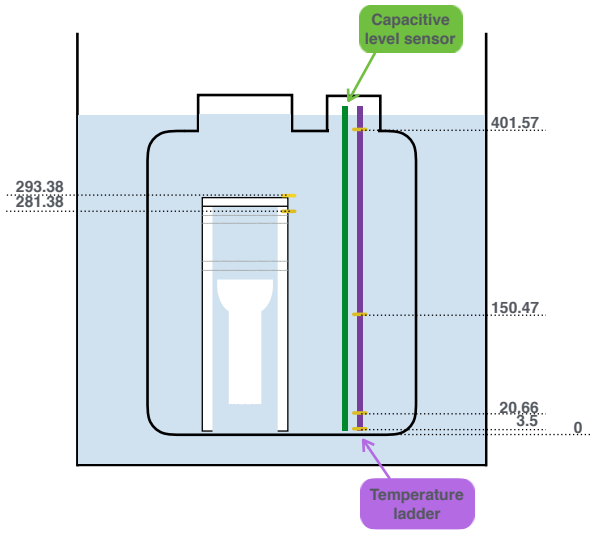

Fig. 5.1: Schematic drawing of the installations inside the chamber: the TPC, the capacitive level sensor (green) and the Pt100 temperature ladder (purple) made of PTFE and equipped with four Pt100 sensors. Two extra Pt100s are mounted in the TPC: one above the top grid and one above the lid. All dimensions are given in units of mm and are relative to the bottom of the chamber (0 mm).

where P is the gas pressure in bar, T is the temperature in K, and A, B, and C, called "Antoine's coefficients", are constants. For argon the National Institute of Standards and Technology (NIST) reports the following values[1] in the temperature range between 83.78 and 150.72 K: $A = 3.29555$, $B = 215.24$, and $C = -22.233$. The line which separates the liquid from the gas phase has been approximated to a vertical line passing through the triple point $T_T = 83.8\,\mathrm{K}$ (as also reported by NIST).

5.2 About voltage breakdown in LAr

To avoid electrical breakdowns around the PMT base, the high voltage must be turned on only when the base is fully immersed in LAr. In fact, it is easier to develop discharges in gas, due to the fact that argon gas has a much lower dielectric strength compared to the liquid. This follows directly from Paschen's law, which states that the breakdown voltage V_B of a uniform field gap is a unique function of the product of the gas pressure P and the gap length d (Wadhwa, 2007):

[1] http://webbook.nist.gov/cgi/inchi?ID=C7440371&Mask=4#ref-4

$$V_B = f(P, d) \tag{5.2}$$

For an ideal gas:

$$\begin{aligned} PV = nRT &= \frac{m}{M}RT \\ \implies P = \rho T \frac{R}{M} &= \rho T R_{\text{specific}} \end{aligned} \tag{5.3}$$

where the symbols have their usual meaning. Thus, Paschen's law can also be rewritten as:

$$V_B = f(\rho, d) \tag{5.4}$$

which means that the lower the density, the lower the breakdown voltage. As the density of argon gas is lower than the liquid, the breakdown voltage will be lower for gas, making it easier to spark.

Even if the base of the PMT is fully immersed in LAr, breakdown can still be triggered by thermal bubble formation in the liquid. When something in the liquid is being heated (the PMT voltage divider in this case), the latent heat is dissipated through several mechanisms, convection being the most important. When normal convection is not sufficient to remove the heat produced in the liquid, bubbling formation starts occurring. In fact, as described in Lakkaraju *et al.* 2013, boiling is an extremely effective way to promote heat transfer from a hot surface (the PMT base) to the liquid. With

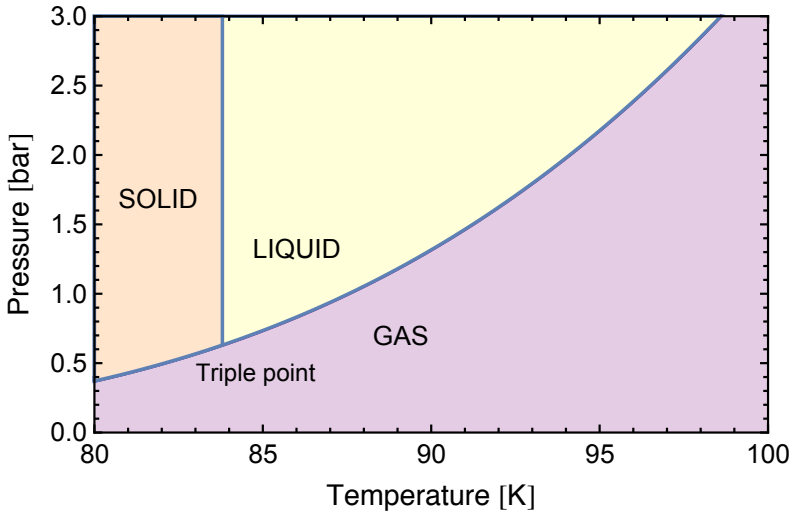

Fig. 5.2: Phase diagram for argon made by the author.

their formation, bubbles cause a micro-convective motion of the heat on the surface and, as they detach by buoyancy, the volume they vacate tends to be replaced by cooler liquid. Not only this process provides for the direct transport of latent heat, being able to bypass the low-velocity liquid region at the heated surface boundary due to the no-slip condition[2], but also bubbles, with their buoyancy, enhance convective circulation inside the liquid beyond the level caused by the Rayleigh-Bénard convection (in turn Rayleigh-Bénard convection[3] is a more effective heat transfer mechanism compared to the molecular heat conduction). The situation in a real chamber is further complicated by the fact that there are many nonuniformities, like resistors, pins, wires, etc., which means that the heat can be produced in very small regions and bubble formation is very sensitive to nonuniformities.

To make existing bubbles collapse, pressure needs to be increased. At the P-T saturation curve, where the liquid and gas coexist in equilibrium, to every T_s corresponds some P_s. If for some reason the pressure drops below P_s (while $T = T_s$), liquid boils until the amount of evaporated gas is sufficient to restore the original P_s. Oppositely, if the pressure increases above P_s (with the temperature being constant), part of the gas will condense (i.e. pre-existing bubbles will collapse) to rebuild equilibrium, $P = P_s$. It should be noted that these are transition processes. If there are bubbles at certain conditions, they can be made disappear by increasing pressure, however this does not mean that their formation can be prevented forever after equilibrium is reached at new values along the saturation curve.

In our setup, we found that we had to constantly let argon gas flow (1–3 stdL/min) into the chamber in order to make bubble collapse. Instead, if the argon bath is not kept constant and the liquid inside evaporates slowly and steadily (such that the change in temperature over time is very small), no flow is required (the pressure naturally rises as the liquid evaporates).

5.3 Data taking and pulse shape analysis

Data were acquired with the TPC fully immersed in liquid argon. Scintillation light is constantly emitted by liquid argon because of cosmic muons traversing the chamber. If the photons are wavelength-shifted by the TPB, they can be collected at the PMT photo-cathode. If the pulse amplitude is greater than the threshold set on the digitiser, the waveform is recorded over a time window of 800 ns, with sampling time of 1 ns.

[2]The slip condition for viscous fluids states that at the solid boundary the fluid will have zero velocity relative to the boundary.

[3]The Rayleigh-Bérnard convection is a type of natural occurring convection for which the heated fluid exhibits a regular pattern of convection cells called Bérnard cells.

Figure 5.3 shows an averaged waveform from cosmic muons when no source is present (logarithmic scale on the y-axis). Nearly 50,000 waveforms have been processed in the following way: (1) for each event the baseline is calculated over a pre-trigger region of 40 ns and subtracted to the each amplitude sample in the waveform, (2) the waveforms are time equalised at the same peak position and averaged. The curve shows the presence of a fast component ($\tau_S \sim 4$–7 ns as reported in literature) and a slow component ($\tau_T \sim 1$–1.7 µs as reported in literature), corresponding to liquid argon light emission from an initial singlet or triplet state. An intermediate component (τ_I), which has been already reported in literature with decay time of 20–40 ns (Hitachi *et al.*, 1983), is also visible. A fit (linear as the the y-axis is in logarithmic scale) has been performed independently over the fast, intermediate and slow component of the curve, giving the following results:

$$\begin{aligned} \tau_S &= 9.0 \pm 0.2\,\text{ns} \\ \tau_I &= 10.3 \pm 0.3\,\text{ns} \\ \tau_T &= 408 \pm 5\,\text{ns} \end{aligned} \tag{5.5}$$

The components are not compatible with the range of values reported in literature. The largest discrepancy is with the slow component and may be primarily explained

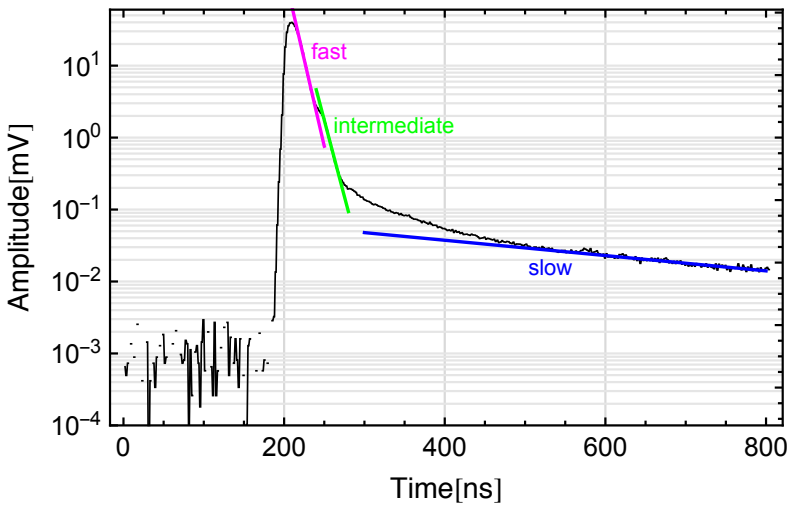

Fig. 5.3: Averaged waveform from cosmic muons when no source is present (logarithmic scale on the y axis). Three independent linear fits have been performed to extrapolate the fast, intermediate and slow component of liquid argon.

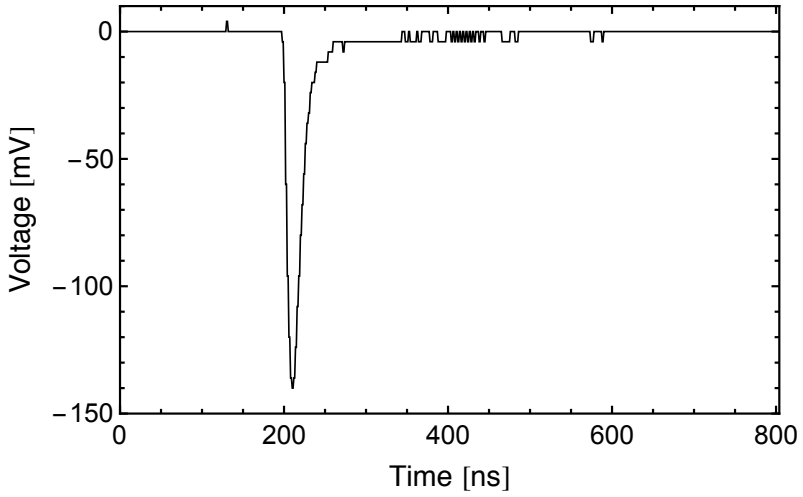

Fig. 5.4: Waveform from a high energy cosmic muon event acquired with the digitiser.

by the relatively small time window set on the digitiser, which causes a cut off on the late light component of the curve. The decay constants can also be effected by impurities in the LAr, which induce a non negligible quenching of the scintillation light (electrons may be prevented from recombining following electron capture by impurities, for example oxygen). Variations in the time constants are significant especially for the slow component. To a first approximation, the quenching effect of impurities on the slow component can be described by the following equation:

$$\frac{1}{\tilde{\tau}} = \frac{1}{\tau} + k[\rho] \tag{5.6}$$

which gives:

$$\tilde{\tau} = \frac{\tau}{1 + k\rho} \tag{5.7}$$

where $\tilde{\tau}$ is the value of the time decay constant when impurities are present, τ for is the same constant, but for zero impurities, ρ is the concentration of impurities and k is a constant. From eqn (5.7) and given $\tau_T > \tau_S$, it follows that, for the same amount of impurities, τ_T will be more affected than τ_S. Figure 5.4 shows a single waveform from a high energy cosmic muon event. Due to quenching of the slow component by impurities, the signal pulse primarily consists of light from the fast scintillation component, although single p.e. pulses due to slow scintillation processes are also visible.

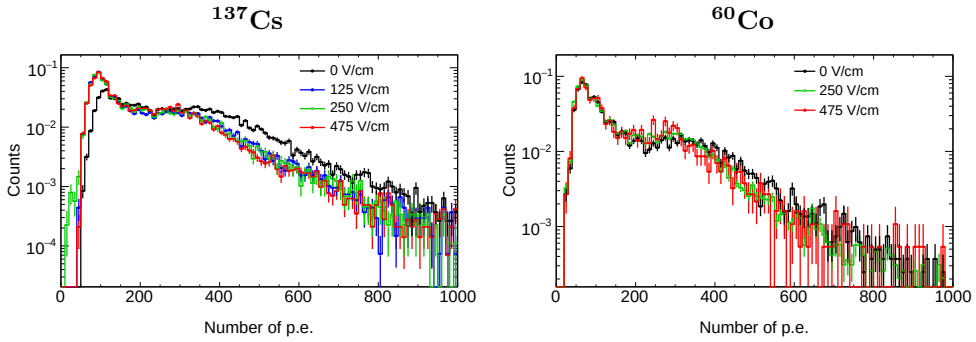

(a) (b)

Fig. 5.5: (a) Caesium-137 and (b) Cobalt-60 p.e. spectra at different drift fields applied.

5.4 Measurement of $\mathcal{S}_e$

After the PMT calibration using a pulsed LED (see Chapter 3, Section 3.4.3), data were taken with the PMT voltage bias at 1 kV, using gamma rays from Caesium-137 (^{137}Cs) and from Cobalt-60 (^{60}Co), with the gamma source placed in a plastic box on top of the chamber. These mainly induce single and multiple Compton scatterings in the liquid argon. A minimum of 10,000 waveforms has been recorded for each run at different trigger thresholds, ranging from 5 to 15 LSB. LSB stands for "least significant bit", and practically 1 LSB = 1 V/1024 $\simeq$ 1 mV. To measure the light quenching, the drift field was varied from 0 to 475 V/cm (when breakdown occurred), with data being taken at the following electric field values: 0 V/cm, 125 V/cm (only for ^{137}Cs), 250 V/cm, 475 V/cm.

Data were then reduced to ROOT ntuples using the following settings in LArView: threshold at 0.5 RMS, noise at 10 ns, pre-trigger option selected with "*max rms*" at 1 mV, no filter applied and no "*check ends*" option selected. Cuts were applied to discard noise, by requesting the pulse height to be negative and fall time to be greater than rise time, and to discard low energy events, by requiring only one pulse within a waveform (waveforms with more pulses exhibit low energy pulses after the main signal).

Each data set was normalised to 1, as for the S_e estimation only the shape of the spectrum matters. Figure 5.5 shows the histogram for the number of p.e. using ^{137}Cs and ^{60}Co at different drift fields. According to the definition of S_e:

$$S_e^{^{137}\mathrm{Cs},^{60}\mathrm{Co}}(\mathcal{E}_d) = \frac{S1_{^{137}\mathrm{Cs},^{60}\mathrm{Co}}(\mathcal{E}_d \neq 0)}{S1_{^{137}\mathrm{Cs},^{60}\mathrm{Co}}(\mathcal{E}_d = 0)} \tag{5.8}$$

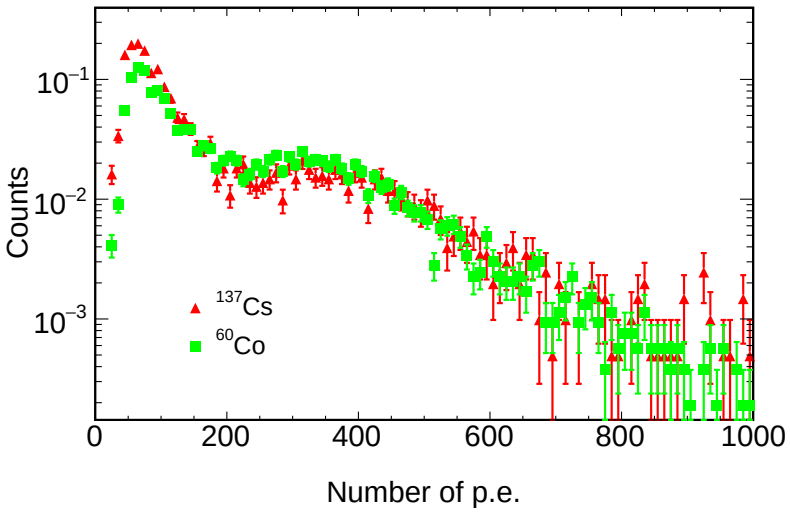

Fig. 5.6: ^{137}Cs and ^{60}Co spectra at zero field.

the ratio between the scintillation signal in p.e. at $\mathcal{E}_d \neq 0$ and the scintillation signal in p.e. at zero field gives S_e at that field. As the scintillation yield may not be linear with the energy deposited, S_e is specific to the gamma source used in the measurement. Each bump in the spectra has been fitted with a Gaussian in the arbitrary range of 200–500 p.e. and the ratio between the mean value of the distribution at $\mathcal{E}_d \neq 0$ and $\mathcal{E}_d = 0$ has been calculated. As per eqn (5.8), such ratio gives S_e as a function of $\mathcal{E}_d$.

Since S_e is a function of the energy deposited, the energy range of the peak must be known in order to specify at what energy the quenching factor is calculated. If the peak corresponded to the Compton edge of ^{137}Cs and ^{60}Co that would be easy. The Compton edge corresponds to the case in which the photon scattering off the electron in the medium deflects at 180°. At this scattering angle, the energy transferred E_T is maximum and is equal to:

$$E_T = E_0 \left(1 - \frac{1}{1 + 2E_0/m_e C^2}\right) \tag{5.9}$$

where E_0 is the incident energy and m_e is the mass of the electron. Figure 5.6 shows the ^{60}Co and ^{137}Cs spectra at zero field. Since both peaks appear in the same position, doubts on the true nature of the spectrum shape arose. In fact, as the theoretical Compton edge for ^{137}Cs is at ∼480 keV and for ^{60}Co at ∼960 keV, the Cobalt Compton edge should appear at double the energy of Ceasium (i.e. double number of p.e.).

One plausible explanation is that the digitiser threshold was just too high to be able

to see the sources and that the bump is due to cosmic muons. To test such hypothesis we can calculate the rate of the events in Fig. 5.6 and compare it with the expected rate from muons. To do so, we divide the number of events in the spectrum by the acquisition time in seconds (corrected for the efficiency in the event selection, i.e. the ratio between the number of events that passed our cuts and the total number of events collected). This gives roughly 1.9 Hz. The muon expected rate is instead calculated as follows.

Let us assume that the cosmic ray vertical intensity of muons (above 1 GeV/c) at sea level is as given in Olive *et al.* 2014:

$$I_{SV} = 70\,[\mathrm{m}^{-2}\,\mathrm{s}^{-1}\ \ \mathrm{sr}^{-1}] \tag{5.10}$$

This energy-averaged intensity at sea level has an overall angular distribution proportional to $\cos^2\theta$, where θ is the azimuthal angle:

$$I_S(\theta) = \begin{cases} I_{SV}\cos^2\theta = 7 - \cos^2\theta\,[\mathrm{m}^{-2}\,\mathrm{s}^{-1}\,\mathrm{sr}^{-1}], & \text{if } 0 < \theta < \pi/2 \\ 0, & \text{if } -\pi/2 < \theta < 0 \end{cases} \tag{5.11}$$

The muon rate R_μ can be obtained by integrating the muon intensity over the solid angle and the detector area:

$$R_\mu = \int_S \int_\Omega I_S(\theta)(\hat{\mathbf{n}}\cdot\hat{\mathbf{r}})d\Omega d\Sigma \tag{5.12}$$

where $\hat{\mathbf{n}}$ is the normal to the detector infinitesimal surface and $\hat{\mathbf{r}}$ is the direction of the muon. In our case the detector area is reduced to the top surface and the lateral surface of the sensitive liquid argon cylindrical volume. The rate through the top is then:

$$\begin{aligned} R_S^{top} &= \Sigma_{top}\int_0^{2\pi} d\phi \int_0^{\pi/2} I_S(\theta)\cos\theta\sin\theta\ d\theta \\ &= \Sigma_{top}\int_0^{2\pi} d\phi \int_0^{\pi/2} I_{SV}(\theta)\cos^2\theta\cos\theta\sin\theta\ d\theta \\ &= \Sigma_{top} I_{SV}\frac{\pi}{2} = \frac{\pi}{2} I_{SV}\Sigma_{top} = \frac{\pi}{2}\left(\pi R^2\right) I_{SV} \end{aligned} \tag{5.13}$$

with Σ_{top} being the top surface of the LAr volume, $d\Omega = \sin\theta d\theta d\phi$, $\hat{\mathbf{n}} = (0,0,1)$, $\hat{\mathbf{r}} = (\cos\phi\sin\theta, \sin\phi\cos\theta, \cos\theta)$, and $(\hat{\mathbf{n}}\cdot\hat{\mathbf{r}}) = \cos\theta$. We have here assumed that there is no angular dependence on Σ_{top}, i.e. the muon flux is the same on all the infinitesimal

surfaces $d\Sigma_{top}$.

The rate through the side:

$$\begin{aligned}
R_S^{side} &= \Sigma_{side} \int_0^{2\pi} d\varphi \int_0^{\pi} d\phi \int_{-\pi/2}^{\pi/2} I_S(\theta) \\
&\quad \times (\cos\phi \sin\theta, \sin\phi\cos\theta, \cos\theta) \cdot (\cos\varphi, \sin\varphi) \sin\theta \; d\theta \\
&= \Sigma_{side} \int_0^{2\pi} \cos\varphi d\varphi \int_0^{\pi} \cos\phi d\phi \int_0^{\pi/2} I_{SV} \cos^2\theta \sin^2\theta \; d\theta \\
&\quad + \Sigma_{side} \int_0^{2\pi} \sin\varphi \; d\varphi \int_0^{\pi} \sin\phi \; d\phi \int_0^{\pi/2} I_{SV} \cos^2\theta \sin^2\theta \; d\theta \\
&= \Sigma_{side} \frac{\pi}{16} I_{SV} \left(\int_0^{2\pi} (\cos\varphi + \sin\varphi) \; d\phi + \int_0^{\pi} (\cos\phi + \sin\phi) d\phi \right) \\
&= \Sigma_{side} \frac{\pi}{16} I_{SV} (0 + 2) \\
&= (2\pi RH) \frac{\pi}{8} I_{SV}
\end{aligned} \tag{5.14}$$

where φ is the polar angle that identifies $\hat{\mathbf{n}}$ and runs from 0 to 2π; ϕ is the planar angle that characterises $\hat{\mathbf{r}}$ on the xy-plane and spans from 0 to π (muons coming from the "other" side of the cylinder are not considered); θ is the azimuthal angle for the muon direction and goes from $-\pi/2$ to $\pi/2$, although only the integral from 0 to $\pi/2$ contributes (see eqn 5.10). Plugging in the values $R = 41.5\,\text{mm}$ and $H = 67.5\,\text{mm}$ gives a total rate of 1.08 Hz. This is in agreement with the rate of events expected within a factor of 2. A possible explanation for the measured rate being larger could be the presence of events in the low p.e. region coming from the source.

In the next section I present the results of the simulation of the setup, which further support the assignment of the bump to muons. With this explanation, it follows that the measurement of S_e has been performed in the energy range of 16 MeV. In fact, as muons deposit approximately 2 MeV/cm and the sensitive argon volume (between the TPB below the lid and the PMT photocathode) is ∼8 cm, a peak in the deposited energy spectrum of muons is expected around 16 MeV.

The values obtained are shown in Fig. 5.7 and summarised in table 5.1. The calculation of S_e has been performed using ^{137}Cs and ^{60}Co data, and then averaging the two results at each electric field. In fact, as the bump is ascribed to muons, which source has been used to collect the data becomes irrelevant.

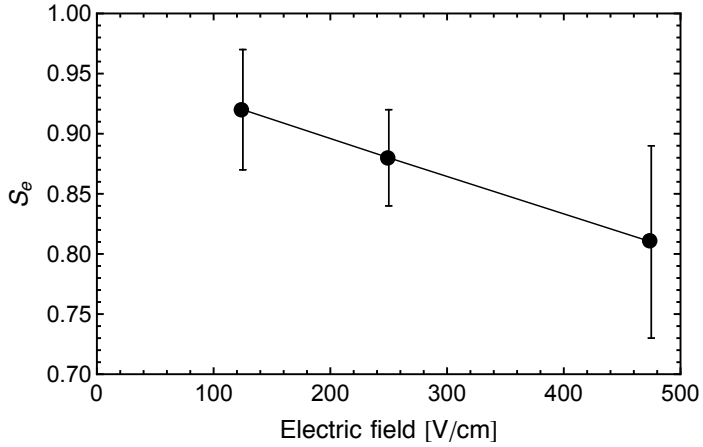

Fig. 5.7: Values obtained for S_e at different electric fields using data from cosmic muons. The line is to guide the eye only.

5.5 Monte Carlo simulation

To assess our understanding of the detector and compare the data acquired with a prediction on them, a simulation of the setup, performed using the GEANT4 Monte Carlo framework, has been carried out.

To simulate the passage of particles through the detector, GEANT4 requires the user to define the geometry, specify the material (chemical composition, temperature, density, pressure, etc.), assign optical properties to the materials (reflectivity, absorption length, etc.) and select the particle to simulate (type of particle, initial position and energy).

A simplified geometry of the setup, shown in Fig. 5.8, has been used, with no electric field being applied. The TPC closely resembles the real one, except for the PMT, which only consists of two empty 1 mm thick borosilicate glass cylinders with diameters 76.2 mm and 50.29 mm on top of each other, a bialkali photocathode (of thickness 50 Å), a quartz window (of thickness 1 mm), and the TPB layer. The polystyrene used to make the TPB mixture used on the PMT window and the PTFE lid has not been

Table 5.1 Values of S_e at different electric fields in the 16 MeV energy range in LARA.

$\mathcal{E}_d$ [V/cm]	S_e
125	0.92 ± 0.05
250	0.88 ± 0.04
475	0.81 ± 0.08

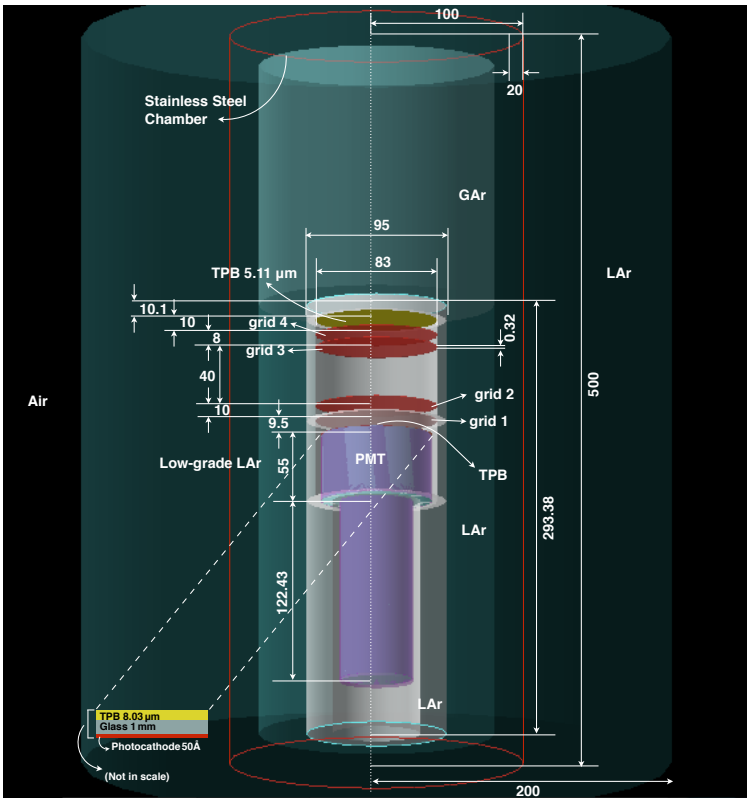

Fig. 5.8: GEANT4 visualisation of the TPC and stainless steel chamber. All dimensions are in mm.

included in the simulation. Instead, the equivalent thicknesses for a $0.0033\,\mathrm{g/cm^2}$ TPB deposition on the PMT window and $0.0021\,\mathrm{g/cm^2}$ on the lid have been calculated and used (see Chapter 3, Section 3.3.1).

The chamber that hosts the TPC has been reduced to a stainless steel cylinder with no feedthroughs and has been filled with liquid argon up to the top of the TPC and with gaseous argon above. Nothing outside of the low-grade liquid argon bath, where the chamber is immersed, has been simulated (i.e. no insulator, no wooden box, etc.) The low grade liquid argon bath reaches the top of the chamber as was in reality.

Optical properties were defined for all materials that might interact with scintillation photons—whether directly from the LAr or from the TPB having been wavelength shifted and reemitted. In our detector these are: the stainless steel for the grids and the chamber; the PTFE for the TPC structure and PMT holder; the liquid argon; the

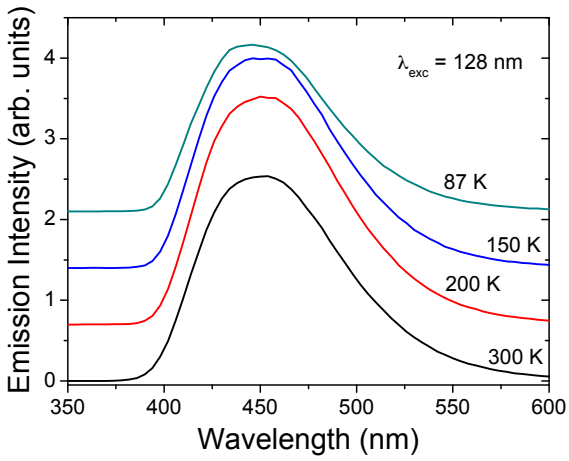

Fig. 5.9: Photoluminescence spectra of TPB in polystyrene on glass substrate excited at 127 nm in liquid argon as taken from Francini *et al.* 2013). The line at 87 K has been used in the simulation.

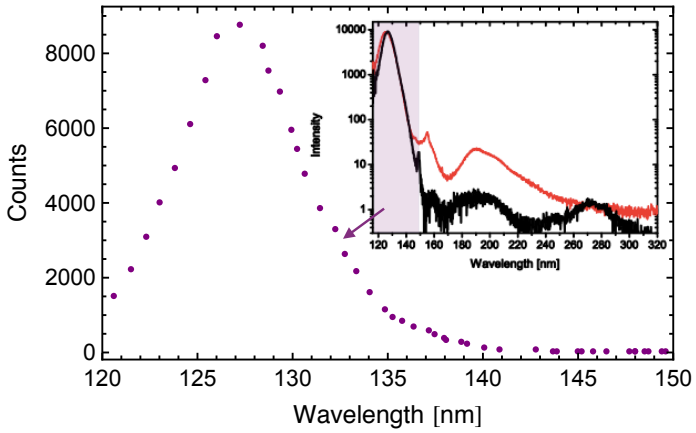

Fig. 5.10: VUV emission spectrum of liquid argon used in the simulation as taken from Heindl *et al.* 2010. The original spectrum is also shown. In red is the fluorescence spectrum from gaseous argon and in black from liquid argon. Weak emission features in the wavelength range from 145 to 300 nm can be observed.

TPB; the borosilicate glass for the PMT body and window; and finally the photocathode.

For all the materials the refractive index and the absorption (attenuation) length are defined in the energy range 2.1–10.5 eV (580–118 nm). This range is required since

photons from argon fluorescence are (predominantly) in the 120–150 nm range (see Fig. 5.10), reaching a peak around 126.8 nm (9.8 eV), but, if absorbed by the TPB, they are wavelength shifted into the visible range 300–580 nm (4.1–2.1 eV). To accommodate both cases, energy dependent optical properties were defined for the complete range. A wavelength dependent absorption length, λ_{abs}, is specified for all photons absorbed by the TPB. A high λ_{abs} is associated with 127 nm, so that for 127 nm a 100% shift efficiency is guaranteed. Once the photon is absorbed, the TPB reemits it at a shifted wavelength with a specific intensity (emission spectrum, see Fig. 5.9, taken from Francini *et al.* 2013). The TPB emission time was initially set arbitrarily and varied to yield agreement with data at 1.68 ns, in excellent agreement with literature (Chepel and Araújo, 2013). This time constant is not insignificant when compared to the liquid argon time constants (τ_S and τ_T).

Besides the refractive index and the absorption length, the PTFE is also set with a custom reflection mechanism, defined through four constants that parameterise the specular spike, specular lobe, diffuse lobe and back scatter.

The absorption length of the stainless steel that makes up the grids is calculated though the Beer-Labert law using a nominal transparency of 62% and a measured thickness of 0.32 mm:

$$\begin{aligned} I(x = 0.32\,\text{mm}) = 0.62 &= e^{-(0.32\,\text{mm})/\lambda_{\text{abs}}} \\ \implies \lambda_{\text{abs}} &= -(0.32\,\text{mm})/\ln(0.62) \end{aligned} \tag{5.15}$$

which means that the intensity of an electromagnetic wave traveling through the whole grid will go down to 62%.

The liquid argon fast and slow components, τ_S and τ_T, for electron recoils are taken from Hitachi *et al.* 1983, and set to:

$$\begin{aligned} \tau_S &= 6\,\text{ns} \\ \tau_T &= 1.59\,\mu\text{s} \end{aligned} \tag{5.16}$$

The fraction with which the fast and slow components occur are also according to the measurement performed in Hitachi *et al.* 1983. These are:

$$\begin{aligned} F_S &= 0.23 \\ F_T &= 0.77 \end{aligned} \tag{5.17}$$

The (maximum) scintillation yield for liquid argon is set to 51.3 ph/keV, and follows from:

$$\frac{dL}{dE} = \frac{1}{W_s^{min}} = 51.3\,\text{ph/keV} \tag{5.18}$$

Recall that W_s^{min} corresponds to the minimum possible energy needed to produce a scintillation photon (maximum number of photons) with no quenching processes:

$$W_s^{min} = \frac{W}{1 + N_{ex}/N_i} \tag{5.19}$$

The ratio between excitons and number of ionised atoms was set to $N_{ex}/N_i = 0.21$, as measured in 1978 by Kubota *et al.* for electron recoils, and the average energy expended per ion pair was fixed to $W = 23.6\,\text{eV}$, as reported in 1974 by Miyajima *et al.*.

The scintillation efficiency for electron recoils at zero field is set to $\eta_0 = 0.75$, as measured for 1 MeV electrons in 1988 by Doke *et al.*, assuming the scintillation efficiency for alpha particles from ^{210}Po is unity. It is worth recalling from Chapter 1, Section 1.1.5 that the relative scintillation efficiency of electron recoils $(dL/dE)_{\text{rel}} \in (0, 1)$:

$$(dL/dE)_{\text{rel}} \equiv (dL/dE)_{e^-}/(dL/dE)_{^{210}\text{Po}} \tag{5.20}$$

is not simply equal to η_0, but instead (see eqn 1.35):

$$(dL/dE)_{\text{rel}} = (dL/dE)_{\text{rel,v}} + \eta_0 \tag{5.21}$$

where $(dL/dE)_{\text{rel,v}}$ is the relative scintillation efficiency generated from recombination between electrons and ions other than the parents[4]. By saying that $(dL/dE)_{\text{rel}}$ is $\eta_0 = 0.75$, we are implying that $(dL/dE)_{\text{rel,v}}$ does not contribute to observable light, i.e. scintillation comes only from geminated recombination or direct excitation. This is strictly true only in the limit of low LET, that is:

$$\lim_{dE/dx \to 0} (dL/dE)_{\text{rel}} = \eta_0 \tag{5.22}$$

The absorption length for borosilicate glass is set to 10 m and is constant through the entire energy range (2.1–10.5 eV). This means that the PMT window is effectively transparent to all photons, including the UV range. The cut-off on UV photons, which is thus not included in the material properties, is applied at a later stage. The simulation output consists of a ROOT ntuple, which includes the following variables:

[4] In Chapter 1 we referred to $(dL/dE)_{\text{rel,v}}$ simply with $(dL/dE)_{\text{v}}$, dropping the "*rel*" subscript.

- event number
- initial source position (x, y, and z coordinate)
- position of the first scattering (x, y, and z coordinate)
- incident energy
- deposited energy and number of hits in the sensitive liquid argon volume (set to be the volume above the PMT window within the PTFE structure)
- position of the first photon within the event hitting the photocathode
- average kinetic energy of photons hitting the photocathode
- and, finally, number of photocathode hits before and after smearing.

It is precisely before filling these last variables (at the photocathode level) that a cut-off on UV photons is applied and photons with a kinetic energy above 4 eV (i.e. below ∼300 nm) are rejected. Since no photon are emitted from liquid argon below this energy, it follows that only wavelength-shifted photons are selected.

After the cut-off on the kinetic energy, the number of visible photons is multiplied by the PMT quantum efficiency, which for simplicity is set to a constant 20%. This represents the PMT average quantum efficiency in the wavelength range to which the photocathode is exposed, that is 400–500 ns, as shown in TPB emission spectrum in Fig. 5.9.

After the number of photons hitting the photocathode (n) has been reduced by QE (n_{QE}) a smearing is applied. The simplified smearing follows a Poisson distribution with mean n_{QE} if n_{QE} is less than 10, and a Gaussian distribution with mean n_{QE} and standard deviation $\sqrt{n_{QE}}$ otherwise.

5.6 Monte Carlo and data comparison

Before comparing the data acquired at zero field with the simulation results, MC results from ^{137}Cs and ^{60}Co have been studied separately to better understand the behaviour of the detector. For ^{137}Cs[5] two million gammas with energy ∼662 keV have been fired isotropically from the top centre of the stainless steel chamber. For ^{60}Co[6], two million events with energy 1.17 MeV and other two million with energy 1.33 MeV have also been fired isotropically from the same location in the detector. Figure 5.11 shows the GEANT4 visualisation when a particle generates scintillation light. The top left plot in Fig. 5.12 shows the energy deposited in the sensitive liquid argon volume

[5] Caesium-137 decays by beta emission to to a metastable nuclear isomer of barium, which in turn decays to its ground state by emitting a gamma at 662 keV.

[6] Colbalt-60 decays by beta decay to an excited state of the isotope nickel-60, which in turn emits two gamma rays with energies of 1.17 and 1.33 MeV.

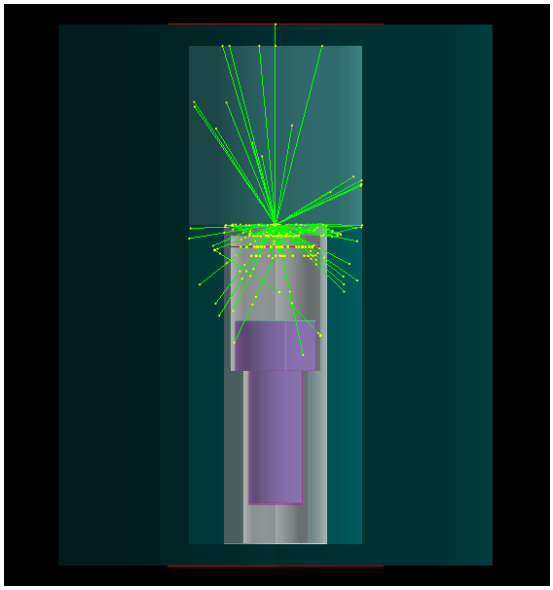

Fig. 5.11: A gamma event of 662 keV fired from the top centre of the stainless steel chamber generates scintillation light in the TPC.

in logarithmic scale for ^{137}Cs. As expected, it displays the Compton edge at ∼480 keV and a few events for the photoelectric peak at 662 keV. This corresponds to the case where the photon releases all of its energy in the medium and can happen via photoelectric effect or multiple scattering. The second plot to the right shows the position along the z and x axis of the first hit of the gamma in liquid argon. As the TPC is symmetric along the z axis, a similar result is obtained when plotting the z and y coordinates. The number of hits correctly decreases when moving away (vertically and radially) from the top of the chamber where the source is located. The third plot shows the number of p.e. collected at the photocathode for different cuts on the energy deposited in the liquid argon. In magenta are the number of p.e. collected when no cuts are applied; in blue are the events for which the energy deposited falls outside the photoelectric peak and Compton edge ranges (i.e. background); in green the number of p.e. for those events that contribute to the Compton edge; and, finally, in yellow the number of p.e. for "photoelectric-like" events. While the cut off corresponding to ∼480 keV is visible at around 10 p.e., it is also evident that only few photons make it to the photocathode. The bottom right plot, which shows the collection efficiency C_e *vs* the energy deposited, gives a possible explanation for this. The collection efficiency encapsulates the position dependent probability for a photon to reach the photocathode

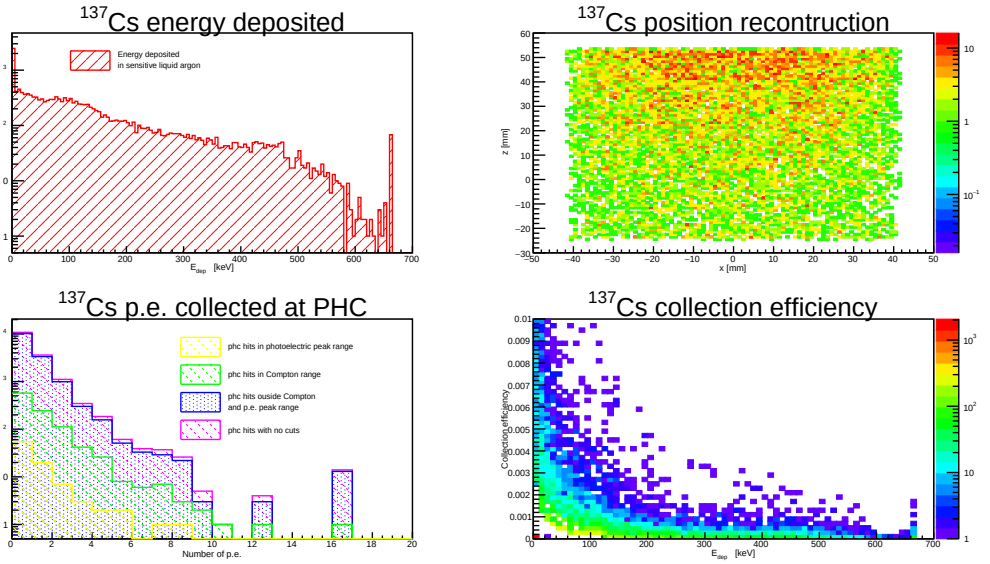

Fig. 5.12: MC results when firing 662 keV gammas from the top centre of the stainless steel chamber. *Top left*: energy deposited in sensitive liquid argon above the PMT. *Top right*: position reconstruction along z and x for the first hit. *Bottom left*: p.e. collected at photocathode when different energy cuts are applied. *Bottom right*: Collection efficiency as a function of the energy deposited.

after it has been produced and can be extrapolated in the following way:

$$C_e = \frac{n_{ph_{PHC}}}{E_{dep} \times \frac{dL}{dE} \times \eta_0} \tag{5.23}$$

where $n_{ph_{PHC}}$ is the number of photons collected at the photocathode without any smearing and before the PMT QE is applied; $\frac{dL}{dE}$, as defined in eqn (5.18), is maximum number of photons produced per keV deposited; and η_0 is the scintillation efficiency for 1 MeV electrons (and gammas) at zero field. As the collection efficiency is very low, not many photons reach the photocathode. Analogous results are also obtained for ^{60}Co.

Let us now discuss the simulation of the cosmic ray muon induced background. The sea level differential muon intensities as a function of muon momentum at 0 degrees, taken from Kempa 2006 (see Fig. 5.13), has been used to fire muons downwards to the detector, from a 1×1 m plane placed 50 cm above the SS chamber. Given cosmic muons are in the 10^{-1}–10^{4} GeV range, it takes a lot of computational time to simulate the full tracking of the scintillation process. That is why we decided to simulate only

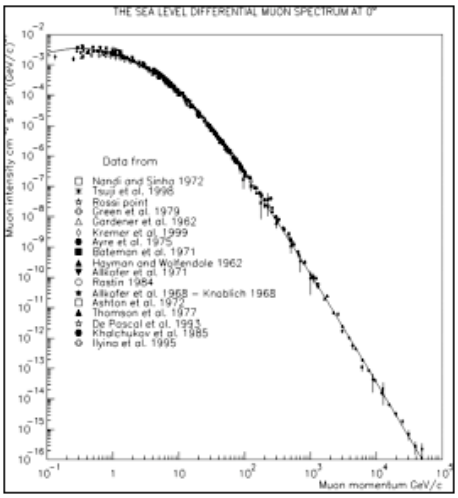

Fig. 5.13: Sea level differential muon intensity as a function of muon momentum at 0 degrees as taken from Kempa 2006.

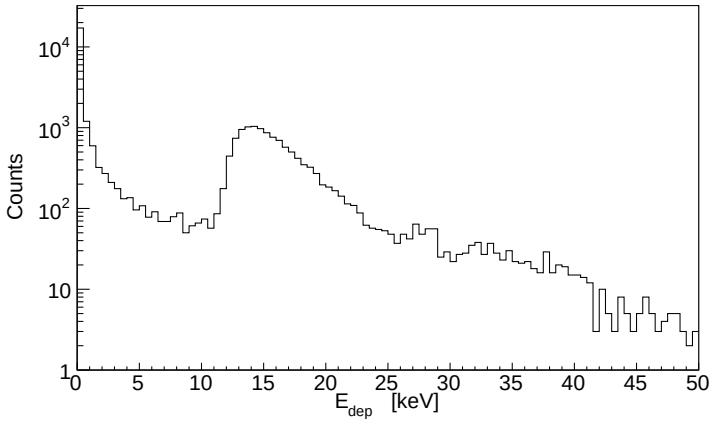

Fig. 5.14: Energy deposited by cosmic muons in the LAr sensitive volume in LARA.

scatterings in liquid argon, while "turning off" the optical tracking. Fig. 5.14 represents the muon energy spectrum, which shows a peak around 16 MeV as expected.

To calculate the number of p.e. at the photocathode using the energy deposition, the following relation may be used:

$$n_{p.e.} = E_{dep} \times \frac{dL}{dE} \times \eta_0 \times C_e(x, y, z) \times QE \tag{5.24}$$

where QE is the PMT quantum efficiency and the dependency of C_e on the position of the particle interaction with the liquid has been written explicitly. We can roughly estimate the C_e by averaging across all energies the collection efficiency simulated for ^{137}Cs. The number of p.e. collected at the photocathode is then smeared afterwards in a ROOT macro, in the same way it is done in the GEANT4 simulation, to take into account statistical fluctuations in the photon-electron conversion at the photocathode.

To convert the ordinate in the MC spectra from counts to counts per second (i.e. a frequency), the histograms must be scaled by 1/DAQ time (ΔT):

$$\begin{aligned} N_{ev} &= \int f(x)dx = \nu \Delta T \\ \implies \nu &= \frac{\int f(x)dx}{\Delta T} \end{aligned} \tag{5.25}$$

To find ΔT for the gamma sources, one needs to divide the number of MC events generated (e.g. two million for Caesium) by the current activity of the source in Bq. Given the sources were rated at 450 kBq in 1991 and the decays constants for ^{137}Cs and ^{60}Co are respectively $\tau_{^{137}Cs} = 43.53\,\text{y}$ and $\tau_{^{60}Co} = 7.61\,\text{y}$, one can easily calculate the current rate, R_{2015} as follows:

$$R_{2015} = R_{1991} e^{-(2015-1991)/\tau} \tag{5.26}$$

For the muons we use the rate of 1.08 Hz calculated in the section before. Dividing the number of muon events seen by the LAr volume by such rate gives the muon DAQ time.

Each data set was normalised to its DAQ time multiplied by the event selection efficiency (recall that this is equal to the ratio between the number of waveforms passing the selection cuts over the total number of waveforms recorded). It is worth noting that the DAQ time should be corrected for the digitiser dead time. This is the time in which the instrument is essentially blind to any pulse activity, as it is busy processing the previous signal acquisition. Dead time is especially important for oscilloscopes, but digitisers allow for basically dead-timeless acquisitions. In fact, they have the ability to accept two consecutive signals thanks to multi buffer memory management. The waveforms samples are continuously read and stored in a circular memory buffer. At the arrival of a trigger the buffer is frozen and is transferred into the host computer memory, while the acquisition continues in a new buffer. Despite continuos acquisition, there is maximum trigger rate the digitiser can handle, which is set by the read out speed. For our digitiser this is 30 MB/S. Assuming each sample

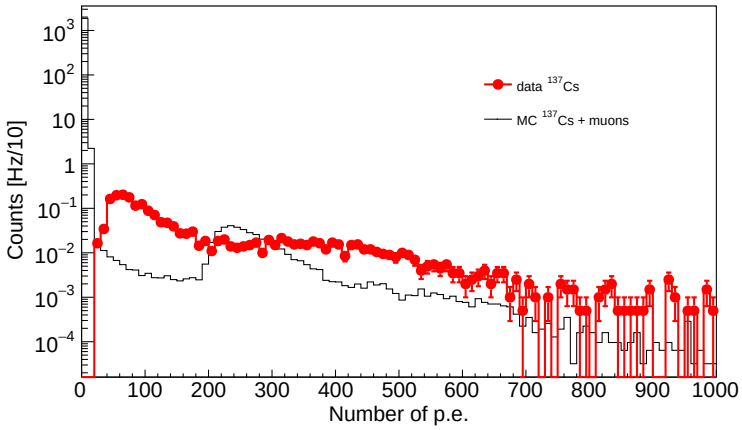

Fig. 5.15: Comparison between MC p.e. spectra from ^{137}Cs and cosmic muons (black) with data (red) in LARA.

is 1.5 byte and given our time window is 800 ns, with 1 GS/s sampling rate this means 1200 bytes per event, which gives a maximum trigger rate of 25 MHz, well above the 1–2 events per second we experience.

Figure 5.15 shows the spectrum of the number of p.e. for the simulated ^{137}Cs with cosmic muons in black (the ^{137}Cs has been included for completeness, but could have actually been neglected given the small contribution compared to muons) and the ^{137}Cs acquired data in red. A slight underestimation of the light yield in number of p.e. arising from the PMT calibration, but especially a simplified MC simulation for the muons and a lack of knowledge of the collection efficiency could explain the discrepancy in shape between the data and MC.

However, given the numerous evidences presented in the chapter, we may safely interpret the bump in the data in the 200–500 p.e. range as arising from muons. The results reported in Fig. 5.7 then hold for the 10–20 MeV range and establish a correct electric field operation, which was one of the primary targets of this work.

Our results are compatible with what found by Doke *et al.* 2002 for 1 MeV conversion electrons from ^{207}Bi. Since, as already mentioned in Chapter 2, the light yield for electron recoils shows a linear response above 30 keV as reported by Creus *et al.* 2015, our results for S_e relative to ∼10–20 MeV can be directly compared with Doke *et al.*'s S_e measurements relative to ^{207}Bi, shown in Fig. 5.17.

5.7 Recommendations for future R&D

The lesson learnt from this experiment is that an amplifier should surely be employed next time when using radioactive sources. In fact, despite triggering in the ∼5-10 mV range, i.e. minimally above the noise level, we were only able to detect events from cosmic muons. With the aid of an amplifier we would be able to amplify the signal, while keeping a large signal to noise ratio, and to further lower the trigger. As such, we would detect lower energy events from ^{137}Cs and ^{60}Co, whose activity is also several orders of magnitude larger than muons. Another improvement could be the use of more transparent grids, that, while marginally affecting the uniformity of the electric drift field, would enhance the number of photons collected at the photocathode (i.e. larger collection efficiency). Finally, to increase the energy deposited in the sensitive liquid argon volume, the radioactive source should be placed inside the detector, below the stainless steel flange.

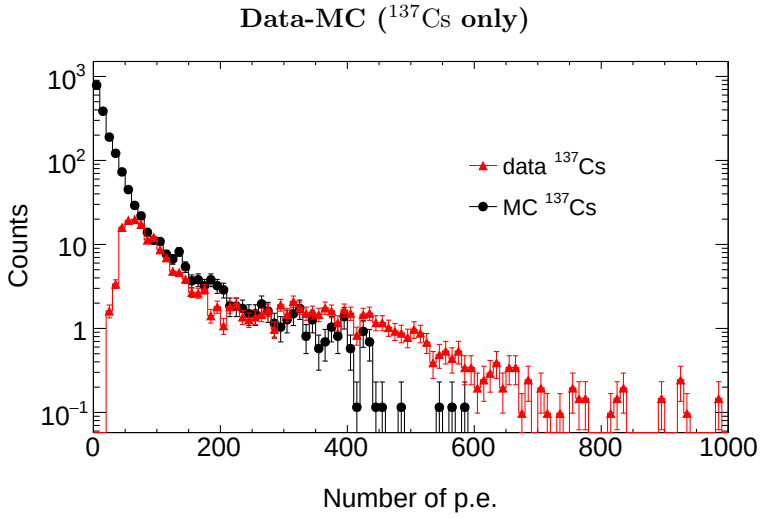

Fig. 5.16: ^{137}Cs data and MC with^{137}Cs only events after reducing the data time acquisition by a 100.

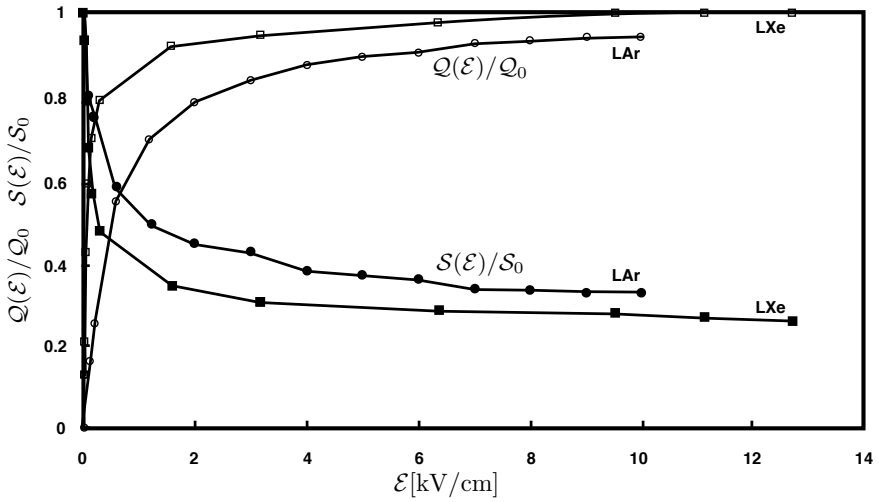

Fig. 5.17: Saturation curves of ionisation (open symbols) and scintillation (close symbols) for 1 MeV conversion electrons from ^{207}Bi in liquid argon (●, ○) and liquid xenon (□, ■) as a function of the electric field strength. Graph taken from Doke *et al.* 2002.

6
Cold high-voltage feedthrough

The LARA test stand has been used for testing a novel cold high-voltage feedthrough design part of the dark matter R&D, with a focus on LZ in particular. The cold feedthrough is designed to deliver high voltage through the LZ cryostat directly into the cryogenic noble liquid. It has been investigated as an alternative to the warm (gas-phase) feedthrough being developed by Yale University (LZ baseline), but it may be adopted for other cryogenic detectors, including LAr TPCs, given the design and sealing methodology developed.

Two consecutive prototypes of the cold high voltage feedthrough have been developed using the technique of sealing plastic to stainless steel by exploiting the different thermal expansion coefficients. The first prototype has been tested for its sealing properties at room temperature, achieving unacceptably high leak rates of $\sim 10^{-5}$ mbar L/s. The leak rate improved significantly upon cooling of the feedthrough to a level of $\sim 10^{-8}$ mbar L/s, though still one order of magnitude above the vacuum requirement for the LZ detector. A second prototype was developed based on the lessons learned during the first development phase and addressing identified issues. An improvement in leak rate at room temperature, as well as at liquid argon temperatures, was observed to $\sim 10^{-7}$ mbar L/s and $\sim 10^{-9}$ mbar L/s, respectively.

In this chapter I will give a full description of all design, construction and assembly stages for both prototypes. The focus of this work was vacuum sealing rather than HV delivery. Subsequently, measurement results and test procedures for the sealing capability are laid out and discussed for each of the prototypes individually, and finally plans for the continuation of the R&D programme through the Rutherford Appleton Laboratory (RAL), including tests for high voltage application, are summarised.

6.1 Warm or cold high-voltage feedthrough?

High voltage (HV) delivery to the cathode of a noble liquid time projection chamber to establish an electron drift field across the liquid target presents several challenges. The voltage must be fed from air into a hermetically sealed cryogenic system and subsequently into the liquified noble gas space of the detector, for delivery of sev-

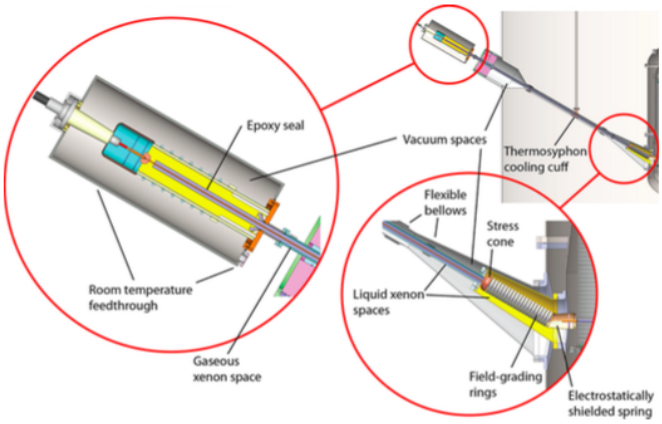

Fig. 6.1: CAD rendering of the LZ baseline design of a warm, gas-phase feedthrough, developed by Yale University. The top right shows part of a cross-section of the LZ cryostat and the water tank with the protruding HV umbilical reaching all the way through the water tank to the HV-FT.

eral hundred kilovolts using only low-radioactivity materials. All materials used in the construction of a custom feedthrough (FT) must fulfil stringent radio-purity requirements, such that it contributes negligibly to the overall radioactivity budget of the experiment. This includes radioactivity from fixed contaminant producing gamma and neutron backgrounds and, equally important, outgassing of radioactive krypton and radon that may diffuse throughout the xenon (argon) volume. Typical materials used in commercial FTs, such as ceramics, may not be employed for these reasons. Although radiopurity is of fundamental importance in dark matter experiments, it should be emphasised that it is a less stringent requirement in neutrino experiments.

Two solutions present themselves for the delivery of HV generated externally to the detector. The first is to locate the FT far from the sensitive volume, outside the water tank shielding in the case of LZ, and feed the voltage from the room-temperature air-side into gaseous xenon. Commercial cabling through an umbilical conduit will be used to finally couple directly to the cathode within the liquid. This is the baseline solution for LZ, as deployed in the LUX experiment, using an epoxy-based FT. The design and technical details of the default solution are already progressed to an advanced stage (see CAD renderings shown in Fig. 6.1) and high voltage tests with a first FT prototype, applying up to 200 kV, have been performed at Yale University.

An alternative is to mount a compact FT, constructed from low background materials, directly onto the detector cryostat, penetrating through the liquid xenon to

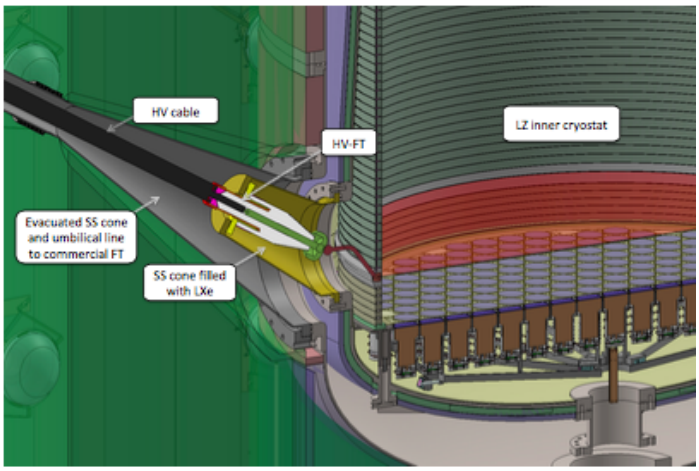

Fig. 6.2: CAD rendering of the cold HV-FT backup solution coupling directly to the inner cryostat of LZ. Liquid xenon will only fill the volume of the cone-shaped extension housing the cold HV-FT (yellow). The rest of the HV umbilical line, holding the HV-cable and extending outside the water tank, can be evacuated in this type of setup. At the room-temperature end, outside the water tank, a second FT will be needed. This could either be the warm FT or a commercial solution.

the cathode (as shown in the schematic in Fig. 6.2). This significantly reduces contact surfaces with xenon to only those between the cryostat and the cathode contact, rather than throughout the entire umbilical conduit, reducing risk from radon emanation and outgassing of electronegative species, and obviating the requirement for non-trivial purification of the xenon in the conduit. It also reduces the total non-active xenon, otherwise filling the umbilical, lowering costs as well as heat load through the commercial HV cable in the umbilical, which is now delivered to the cryostat under vacuum. Though configurations of such compact FTs have been successfully deployed through air into gaseous xenon or argon, the LZ design requires the FT to enter the cryostat through the umbilical located at the bottom of the detector, close to the cathode. Consequently, the FT must enter liquid xenon directly rather than gas, which generates additional complexity in design and construction of such a "cold" FT in producing a reliable vacuum seal at liquid xenon temperatures, as well as at room temperature. Here we summarise progress towards development of a cold HV-FT as a backup solution for LZ, dimensioned for delivery of 200 kV,with general design applicable to all noble gas TPCs operating in rare event searches.

6.2 Design concept

The strict requirements on radio-purity constrain the selection of possible construction materials, which not only have to fulfil the general properties of an excellent insulator for HV applications, such as a high breakdown voltage, but must also withstand very low temperatures ($\sim -110\,°\mathrm{C}$ for LXe or $\sim -186\,°\mathrm{C}$ for LAr). Ultra high molecular weight polyethylene (UHMW-PE) has the required characteristics for construction of the cold HV-FT. It is a robust insulator (electric field breakdown at $\sim$900 kV/cm) and has a thermal expansion coefficient of $\sim 2 \times 10^{-4}\,\mathrm{K}^{-1}$ (non-linear), more than an order of magnitude greater than that of stainless steel ($1.5 \times 10^{-5}\,\mathrm{K}^{-1}$), which is chosen as the conductor material for the FT construction. Utilising this difference, i.e. the increase or decrease in size of the plastic under the influence of different temperatures relative to the stainless steel (SS), a vacuum seal may be achieved between these two low-activity materials without the addition of any extra sealing materials that might become brittle at cryogenic temperatures or introduce impurities that poison the xenon (argon). The challenges of this design are to maintain its vacuum seal at all times from room temperature down to liquid xenon (argon) temperature, whilst delivering high voltage safely directly to the cathode of the detector.

6.3 First cold high-voltage prototype

Figure 6.3 (left) shows the schematic drawings of the 1$^{\mathrm{st}}$ prototype. The main parts of the design are a plastic insulator (grey) with a long hole penetrating through the full length to accommodate the SS conductor (green) and a double-sided zero-length reducer DN100CF flange (reduced to DN60CF), which is welded to the SS ground cylinder (yellow). The critical dimensions, primarily the ratio in diameter between the central conductor and the surrounding insulator, are set to minimise the electric field across the insulator assuming application of 200 kV, maintaining less than 200 kV/cm throughout the UHMW-PE insulator. While it would be preferable to have large diameters for the reduction of electric fields, the main diameter must retrofit the LZ cryostat and kept to a reasonably standard Conflat flange size (DN100CF). A smaller diameter, in turn, reduces the amount of overall material introduced into the LXe cryostat (radioactivity, outgassing) and keeps the thermal load to a minimum. The same reasoning applies to the SS conductor, which is fabricated from a hollow tube, which is welded and closed off on both ends, to reduce its overall weight and thermal conductance. The regions highlighted in red in Fig. 6.3 indicate surfaces between the SS and the UHMW-PE where the seal is made, along the conductor as well as on a "lip" structure between the SS ground cylinder and the plastic. To maintain the

seals in this first prototype only the technique of fitting through heating of the plastic was employed. The expansion of UHMW-PE was measured repeatedly to allow the successful fitting due to the non-linear behaviour of the thermal expansion coefficient and to ensure maximum volume overlap between the metal and plastic parts at room temperature and lower, resulting in a volume overlap of up 2.5% on the components' radii. The assembly procedure for the 1st prototype is outlined below:

- The plastic was heated in an upright position to a temperature of 105 °C (over 4 hours) to expand it to dimensions compatible to fit it onto the pre-machined SS parts. This temperature was chosen to stay well away from the crystalline melting point of 135 °C[1] and maximum short-term service temperature (120 °C) whilst accommodating for possible temperature fluctuations of the oven during the heating process.
- Conductor core and the outer SS grounding cylinder sheath are fitted into the hot insulator.
- Finally, the assembly was put into a custom-made spring-loaded jig (see Fig. 6.4) to ensure the insertion depth of the central conductor as well as the constant positioning of the SS parts during cool down to room temperature and subsequent contraction of the plastic.

Upon cooling of the hot-fitted FT back to room temperature, the restricting dimensions of the metal parts result in a firm seal between the two materials. Further cooling of the FT, e.g. to LXe temperatures, improves this seal. The corrugated cone-shaped tip of the FT is designed to trap charged particles in the groove, inhibiting charge paths along the surface. The finished fitted FT is shown on the right hand side of Fig. 6.3.

6.3.1 Conductive coatings

The design of the plastic incorporating a plastic lip to enclose the grounded SS cylinder is advantageous in terms of sealing, but presents a challenge in sustaining reasonable electrical fields at the tip of the ground sheath, deep within the groove of the plastic. The grounding sheath is machined to incorporate maximum allowable thickness such that the inner edge of the grounding cylinder may be rounded to reduce the electric field at that interface. However, the gap between SS and UHMW-PE generated at that interface may allow charge build-up along the surface of the insulator at vacuum. As a result, either the volume must be backfilled with transformer oil, or a conductive

[1] http://www.directplastics.co.uk/pdf/datasheets/UHMWPE%20Data%20Sheet.pdf

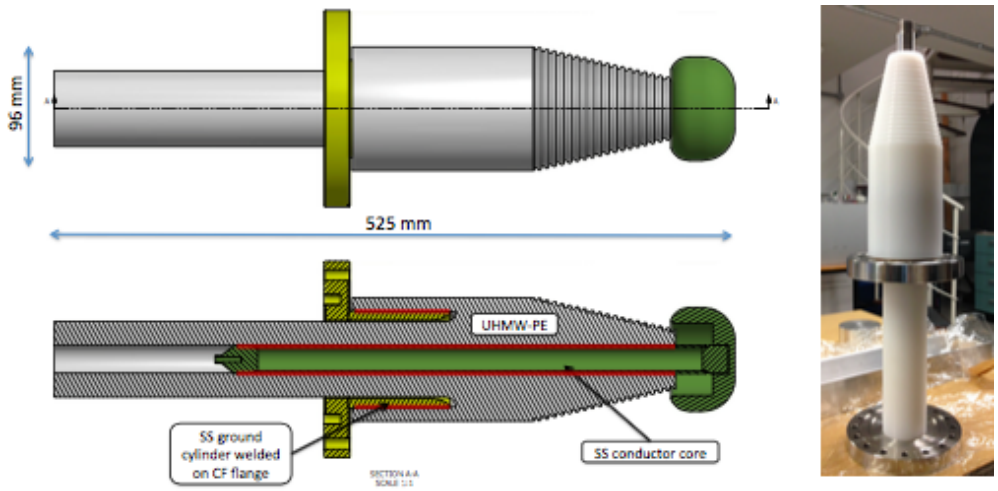

Fig. 6.3: Left: Schematic drawing of the 1st cold HV-FT prototype featuring a central SS conductor (22 mm in diameter) surrounded by a UHMW-PE insulator (fitted by thermal expansion) and a SS cylinder that extends into the plastic, providing the ground for the HV-FT. Right: Finished machined and fitted 1st cold HV-FT prototype. The bottom flange is not part of the assembly.

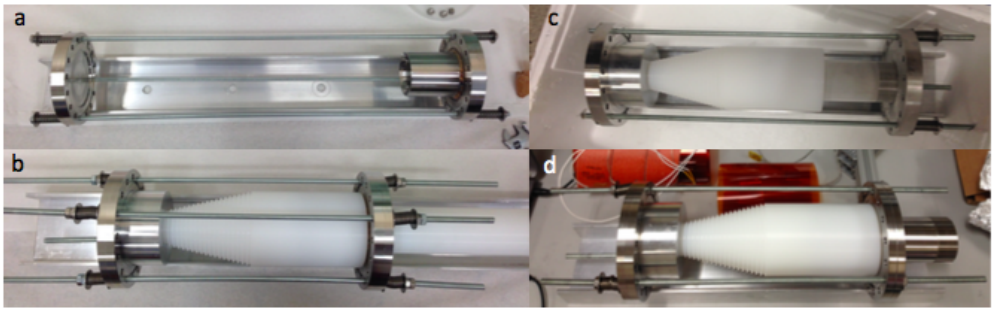

Fig. 6.4: Pictures of using the spring loaded fitting jig for various assembly steps of the first (left) and second (right) HV-FT prototypes: a) empty fitting jig set up for the 1st FT prototype assembly, here one of the flanges available is replaced by the flange-grounding-cylinder welded SS part; b) closed fitting jig with the completely assembled 1st FT prototype; c) warm up of the 2st FT prototype and jig in flowing nitrogen gas after fitting the inner SS compression cylinder of the 2st prototype; d) cool down of the 2st FT prototype in the fitting jig after expansion fitting with the heating jacket to fit the flange-cylinder SS part. Similar to the case of the 1st prototype fitting, one of the flanges of the jig is replaced by the welded flange-cylinder SS part.

paint or coating needs to be applied to the surface of the insulator to create a field-free region. We have assessed insulating oil and conductive paints for their low temperature characteristics, and identified silver paint (SCP03B from Electrolube) as the most promising candidate given its reasonable adhesion properties to UHMW-PE from room to liquid xenon temperatures. These tests were conducted on the inside of a plastic lip, with the outside cooled with either boil-off nitrogen or liquid nitrogen. Care was taken that the silver conductive paint never came into direct contact with the boiling cryogenic liquid, as this would always induce peeling of the conductive layer. Sufficient adhesion was confirmed and successfully tested to a temperature of −150 °C, measured on the surface of the silver paint. The silver paint can be applied on the necessary surfaces of the FT in its assembled stage by pouring the liquid paint directly into the gap between the flange and the plastic and by turning the FT upside down to let access paint run off. Accessible plastic surfaces can either be covered by dunking or painting by brush. There was no significant difference observed in adhesion of the paint when baking it for 4 hours at 100 °C. However, baking of double layers of paint should be avoided. Another conductive coating tested was Aquadag E. Despite difficulties with homogenous application at room temperature, if failed immediately upon cooling of the plastic test piece and started to peel off in large sheets. Investigation into conductive epoxies revealed similar problems of adhesion. Transformer oil (Midel 7131) was also tested for its properties at low temperatures. Problems with crystallisation upon solidifying and the resulting cracks (reducible through low cool-down rates), but more importantly the immediate proximity of the liquid xenon in the LZ detector led us to exclude this possibility of controlling the electric fields.

6.3.2 Sealing tests

Room temperature sealing tests

A two-compartment vacuum chamber setup at UCL (which then became part of the LARA test stand described in Chapter 3) was used to test the vacuum seal across the HV-FT, which was mounted between the top and the main chamber. The leak rate of the empty upper chamber was measured to be $(3.9 \pm 0.1) \times 10^{-10}$ mbar L/s. This is below the design requirement for the LZ cryostat, which needs to be rated at 10^{-9} mbar L/s. An image of the setup is shown in Fig. 6.5 on the left hand side and a corresponding schematic on the right hand side. The FT points vertically downwards into the main vessel (depicted in red), sealed in the stainless steel pipework shown, with vacuum gauge and Residual Gas Analyser (RGA) connected to the top of the FT vacuum space. The top and bottom half of the FT, across the seal, could be evacuated

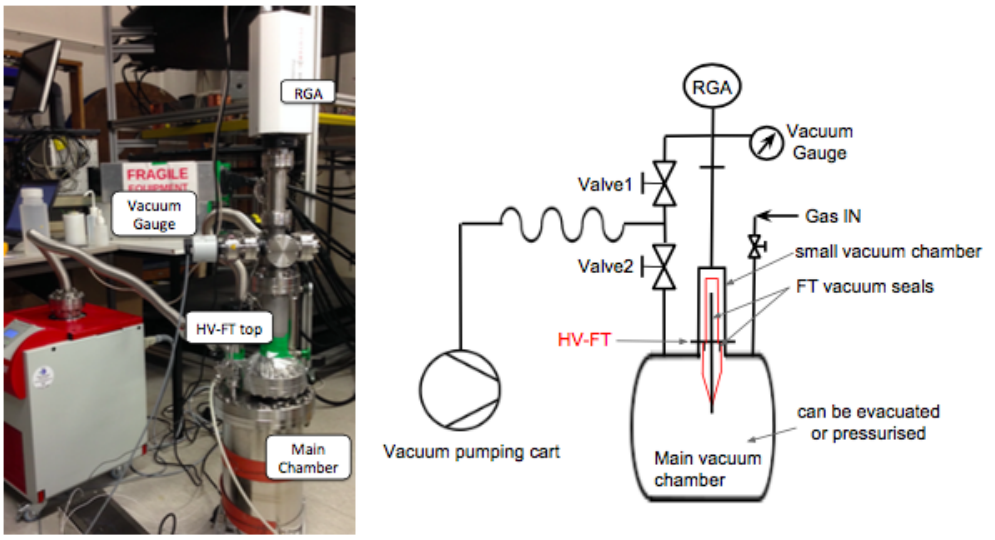

Fig. 6.5: Left: Image of the room temperature sealing test setup for the 1st HV-FT prototype at UCL. Right: Corresponding schematic of the "warm" sealing test setup. All lines and the small vacuum chamber holding the top of the HV-FT (red) are evacuated. The main chamber, in which the FT points down into can be evacuated, left at atmospheric pressure, or over-pressurised with suitable gasses whilst maintaining the vacuum on the top of the FT.

independently from one another. This setup was chosen to, firstly, be able to simulate a more realistic situation with vacuum at the top of the FT, the HV cable connection side, and approximately atmospheric pressure (or slightly above) at the bottom, the cathode connection side. Secondly, it addresses a problem with the welding of the SS ground cylinder onto the CF-flange performed at the UCL workshop, which caused the flange to warp. The more problematic concave side of the flange was used to connect the FT to the vacuum chamber only, and is not part of the seal between the UHMW-PE and the SS. By evacuating the top half of the FT we exclude any potential leak through the flange during the UHMW-PE to SS sealing tests. The risk of warping during welding of the 2nd prototype was mitigated by the use of a specialist contractor.

The base pressure reached at the top of the FT in the first set of tests was 1.5×10^{-5} mbar, with atmospheric pressure below the seal, demonstrating this sealing technique, but nevertheless some three orders of magnitude above the baseline vessel pressure. However, it is expected that some of this residual pressure will be from outgassing of the UHMW-PE, a slow diffusion process that continues for long periods whilst pumping on the FT after exposure to air.

To assess the contribution from outgassing, a small (22 g) test piece of UHMW-PE from the same batch as used for the FT was inserted into the empty chamber and its outgassing increased the pressure above the baseline for this measurement by two orders of magnitude to 1.4×10^{-5} mbar after 18.5 h of pumping. Subsequently, the plastic was baked under the same conditions as the FT plastic for the fitting procedure, for 4 h at 105 °C, and a reduction in outgassing by one order of magnitude relative to the pre-baking measurement after one day of pumping was observed. The base pressure of the chamber was reached after approximately a week of continuous pumping. Baking forces outgassing of the plastic, and this step will be crucial for the HV-FT before fitting it into a vacuum system.

To distinguish the residual outgassing from the FT plastic from a leak through the seal the partial pressures of the individual components in the vacuum were analysed with an RGA. The measurements clearly indicated, from a ratio of the molecular nitrogen to oxygen of 4:1, that atmospheric air is leaking into the system. Common leak test procedures with helium are not feasible for this type of FT due to the porosity of the plastic and susceptibility to permeation of light gases. Another diagnostic tool is the so-called rate-of-rise curve, which is simply a measurement of the pressure increase when decoupling the system from the vacuum pumps. The plot given in Fig. 6.6 (left) shows a steep linear increase in pressure when closing the vacuum valve to the pump, indicating a leak in the system. The measured leak rate is $(2.20 \pm 0.09) \times 10^{-5}$ mbar L/s, that is four orders of magnitude away from the LZ vacuum requirement. The presence of a residual leak through the FT was further confirmed by over-pressurising the chamber, to which the bottom of the FT is exposed, with argon and nitrogen gas at 0.5–1 bar above atmospheric pressure, with the top of the FT still being pumped. Instantaneous pressure increase observed at the top part of the FT excludes permeation, as shown in Fig. 6.7.

Sealing tests at cryogenic temperatures and thermo-cycling tests

To assess the robustness and reproducibility of the seal under thermal cycling between cryogenic and room temperatures, the bottom of the FT was removed from the vacuum vessel and inserted directly into liquid nitrogen (LN2) with the FT cooled at a rate of approximately 40 °C per hour (see temperature plot in Fig. 6.9), whilst monitoring pressure changes at the top of the FT, held under vacuum and being continuously pumped on. A picture of the setup (left), as well as a schematic (right) are shown in Fig. 6.8. Improvement in vacuum as the bottom of the FT is cooled is expected by design, as further contraction of the UHMW-PE compresses the SS conductor and

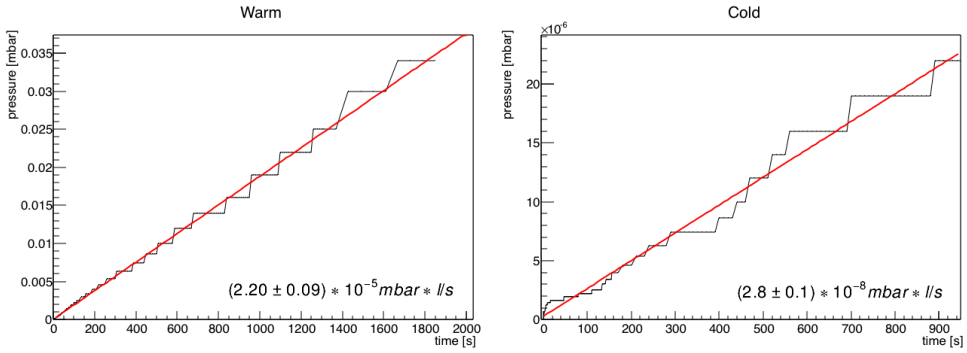

Fig. 6.6: Rate-of-rise curves for evaluating the leak rate of the system with the 1$^{\text{st}}$ prototype HV-FT. Left: Measurement at room temperature. Right: Measured with the FT cooled down with liquid nitrogen.

ground sheath. RGA data from a typical cooling cycle is shown in Fig. 6.9. Cooling is maintained by actively re-filling the LN2 dewar over the course of a day (in this case ∼8 h), with a minimum pressure of $\sim 5 \times 10^{-7}$ mbar achieved after ∼12 h. Total pressures were monitored throughout the cycle and temperatures taken at the top of the FT (as indicated in Fig. 6.8 (right) by the blue arrow, T2) and near the vacuum gauge (see T1 in Fig. 6.8, right). The latter temperature remains constant throughout the thermal cycling of the bottom of the FT, indicating the improved vacuum is due to an improved vacuum seal at low temperatures, rather than, for example, water condensation. Variations in the pressure on short time scales are due to the contraction and the resulting movement of the plastic. These are more pronounced just after each re-fill of the LN2 dewar, which is correlated with the liquid level, covering only for a short period of time the full height of the plastic sealing lip of the FT. The continuously decreasing liquid level soon exposes this part of the plastic-to-SS seal leading to high temperature gradients on the outside of the plastic in this region. To ensure more stable liquid levels and controlled cooling rates in the subsequent sealing tests for the 2$^{\text{nd}}$ cold HV-FT prototype, the LARA liquid argon test facility, built in the meantime, was employed.

Outgassing is suppressed at low temperatures and would lead to improved vacuum, but this effect can be decoupled from the efficacy of the vacuum seal by monitoring nitrogen to oxygen ratios with the RGA. The increasing ratio indicates the reduction of atmospheric air coming through the seal to the top of the FT and into the RGA, giving further confidence that the improved vacuum is due to the improvement of the seal at low temperatures, confirming the achievement of this sealing technique.

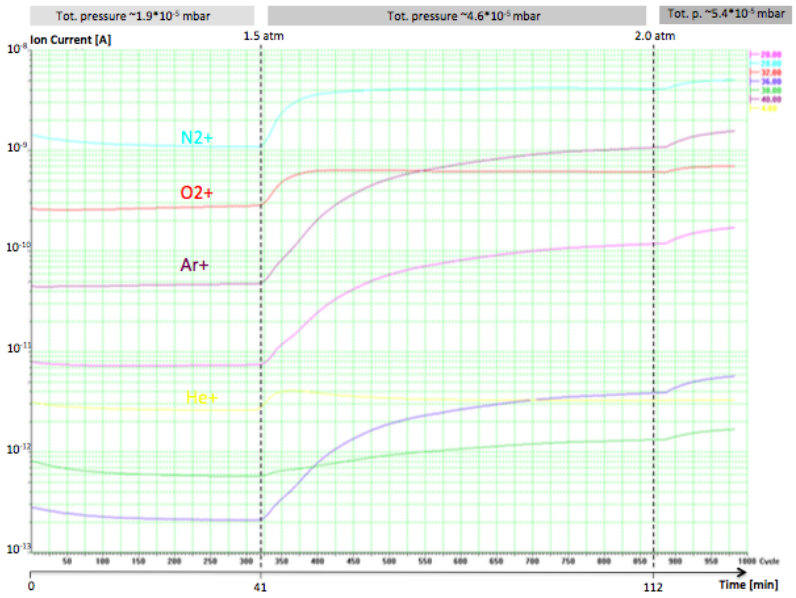

Fig. 6.7: Rate-of-rise curves from over pressurising the bottom half of the HV-FT with argon gas, for different gas constituents in the vacuum at the top of the FT measured with the RGA.

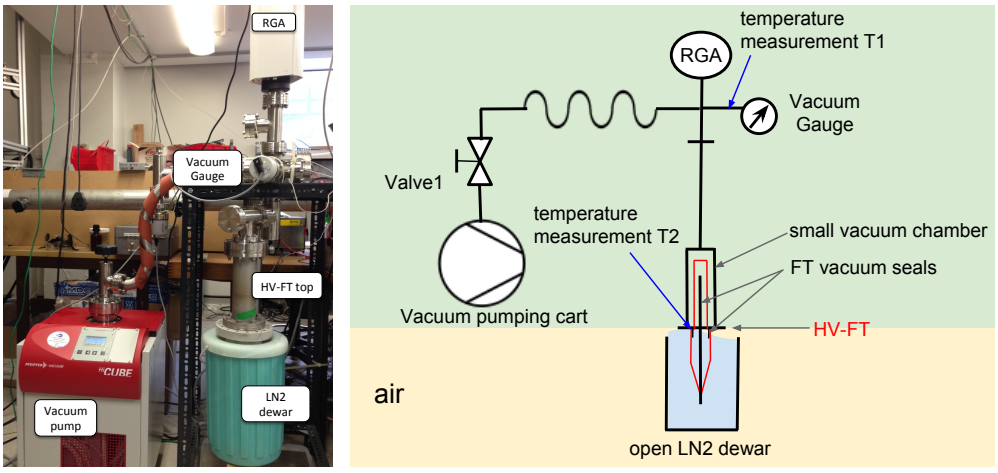

Fig. 6.8: Left: Image of the thermo-cycling and cold sealing test setup for the 1st FT prototype at UCL. Right: Corresponding schematic of the cold sealing test setup. All lines in the upper part of the schematic (green), including the small vacuum chamber housing the top of the HV-FT, are evacuated. The bottom part of the FT is at atmospheric pressure and points downwards into an open liquid nitrogen dewar.

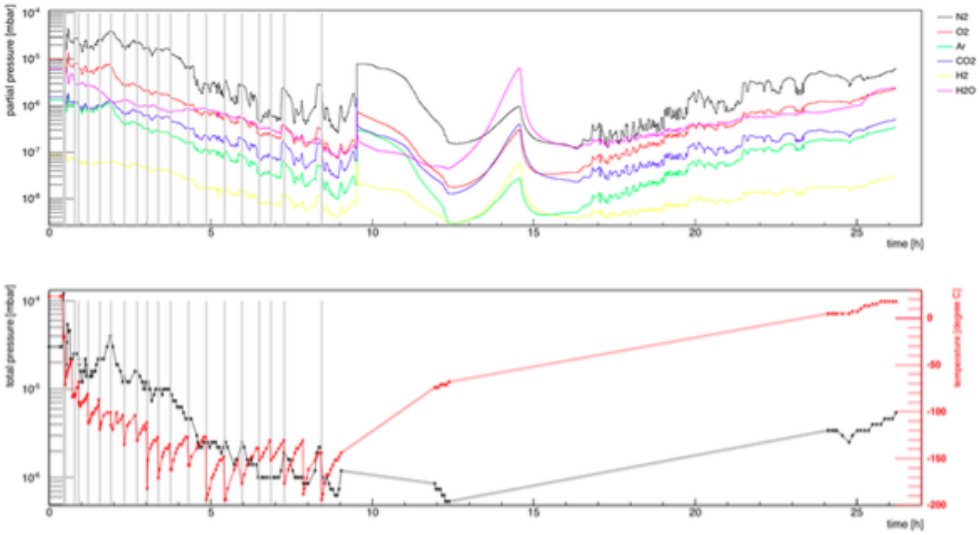

Fig. 6.9: Typical RGA data taken from a thermo-cycle run, cooling the bottom half of the HV-FT in an open LN2 dewar. The top shows the partial pressure (nitrogen equivalent pressures) for different species of the residual gas components. The bottom shows the corresponding total pressure measurements and the temperature measured on the external surface of the UHMW-PE (at the top of the lip, just below the flange, indicated in Fig. 6.8, right, by T2). The grey lines indicate when the dewar was re-filled/topped up with liquid nitrogen. Note: The various small spikes in the partial and total pressure are due to the movement and contraction of the plastic upon cooling in the beginning of the run and expansion and warming up towards the end. The shape of noisier parts in the timelines may also be influenced by the light and activity in the laboratory during daytime, as the observed quiet time correlates with part of the night. The large H_2O spike, when water rises above all other species, at around 14 hours is the result of reaching the melting point of water after continuous warm-up during the night. The lowest pressure point of 5.4×10^{-7} mbar was recorded approximately 12 hours after starting to cool and ∼3.5 hours after the active cooling has stopped.

Importantly, after each of the 5 cooling cycles performed, the pressure at the top of the FT returned to its original, room temperature, value, i.e. the seal returns to its original state indicating no permanent deformation or shattering of the plastic when exposed to these high stresses, and confirming reproducibility under thermal cycling with low cooling and warm-up rates.

Rate-of-rise curves to evaluate the residual leak when the FT is cold resulted in a leak rate of $(2.8 \pm 0.1) \times 10^{-8}$ mbar L/s (shown in Fig 6.6, right), approximately one order of magnitude above the LZ requirement. Attempts to flush the cold plastic to SS seals with argon gas while monitoring the RGA output to confirm the nature of

the leak were inconclusive.

The residual leak through the 1st prototype FT has been traced to the insufficient surface quality and finish of the machined construction parts. UHMW-PE is difficult to machine, and the requirement of a long bore through the cylinder complicates this further. Since production of this 1st prototype, the Edinburgh mechanical workshop, where the piece was machined, has refined the procedure with iterative testing. The surface quality of the SS parts, produced at UCL, was compromised primarily due to the insufficient quality of the welding. This led to non-uniform surfaces on the conductor and grounding sheath, as well as the warped flange mentioned earlier. All of these mentioned failure modes have been addressed in the design and construction of the 2nd prototype and are outlined in the following section, and summarised in Table 6.1.

Following evaluation of the leak rate at cryogenic temperatures, a higher thermo-cycling frequency, and as such also higher temperature gradients within the FT, was adopted for more rigorous stress tests, evaluating if fracture or permanent deformation can be induced. Before this could be taken any further, an increase to two consecutive cooling cycles within ∼30 hours induced a fracture in the bottom region of the plastic lip (see Fig. 6.10), through the full depth, and as such breaking the vacuum seal. The tension at this point has been noticed previously from a permanent deformation of the plastic in this region. Increased lip thickness of the UHMW-PE piece for the 2nd prototype was adapted. This also initiated us to perform a comprehensive FEA study of the stresses within the plastic for the 2nd prototype, described in more details in section 6.4.3.

6.4 Second cold high-voltage feedthrough prototype

A 2nd cold HV-FT prototype has been designed, constructed and tested. Though based on the same general construction and sealing methodologies, the new design addresses identified issues of the first prototype regarding the machining process, the assembly methods and the sealing tests. A major change in the design of the seal is the use of a double compression seal, whereby seals are created through both heat expansion and cryo-fitting of the plastic in equal parts. In addition, modifications in the machining processes helped to further improve upon the surface quality. A shorter UHMW-PE insulator simplifies the bore production, and reduction of the number of welds helps to eradicate potential error traps. The unavoidable weld between the CF flange and the ground sheath cylinder was performed by a specialist company. Table 6.1 provides a summary of the changes made to the previous design.

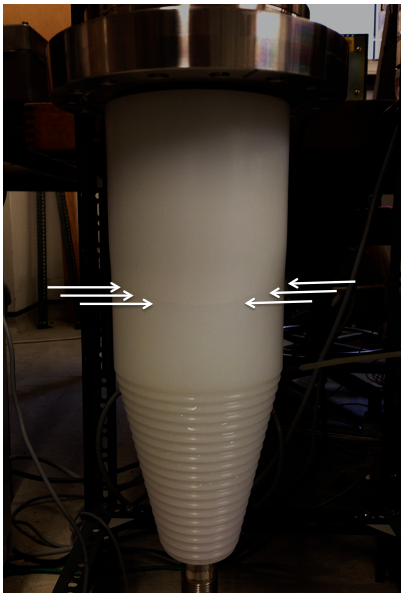

Fig. 6.10: Image of the 1st prototype after material break down. The white arrows point to the fracture that follows the line of the bottom of the plastic lip. The fracture is through the full depth of the lip to the inserted SS, but only reaches around half of the circumference of the plastic.

To improve the sealing properties of the FT at room temperature the design evolved into a double compression seal. By alternating heat-expansion and cryo-fitting procedures, seals on both sides of the plastic are created, with SS sheaths constricting both diameters, creating a nested design of SS cylinders in and around the plastic insulator. This compresses, especially at room temperature, the plastic from both sides, improving the sealing properties of the FT. Figure 6.11 shows the design drawings (left) of the 2nd FT prototype, with the sealing/compression interfaces indicated in red. The additional cryo-fitted SS cylinders are the Inner and Outer SS compression cylinder/ring coloured in orange and pink, respectively. A step-by-step description of the assembly procedure for this nested design is given in section 6.4.1.

Similar to the 1st prototype, the general dimensions are designed to fit the predefined standard flange size (DN100CF). To increase the lip thickness of the plastic insulator, as well as to accommodate the double compression seal, the diameter of the insulator between the conductor and the SS ground (formed here by the inner compression cylinder) has been reduced to 2 inches. The conductor diameter (18 mm) has then been chosen to keep the field within the insulator to a maximum of just

Table 6.1 Lessons learned from the 1st prototype feeding into the design of the 2nd FT.

Problem	Cause	Mitigation
Insufficient surface finish of the plastic.	Difficult machining of the long bore hole.	Reduced length of UHMW-PE insulator. Selected workshop that performed best in the previous machining of the plastic. Additional experience in working with this specific material also improved the overall quality.
Insufficient surface quality of the metal parts.	Hand-performed welds.	Reduced necessary welds overall in the design. E-beam weld unavoidable joints. Use of external contractor.
Leak through metal-plastic seal.	Insufficient surface quality.	See above. Evolved sealing technique using both heat expansion and thermal contraction properties of the plastic (double compression seal).
Leak through the FT connection flange.	Warped flange due to heat load of welding.	E-beam weld connection between ground cylinder and flange. Use of external contractor.
High field region at tip of SS ground cylinder and gap between insulator and ground.	Design.	To first order designed away (below 100 kV no additional measures such as conductive paint or epoxy necessary).
Large thermal gradient across one of the sealing region of the FT during thermo-cycling tests.	Rapidly changing liquid levels due to open LN2 dewar setup.	Perform test in a stable environment, such as the UCL LAr test facility.
Fracture of plastic.	Large thermal gradient across sealing region during thermo-cycling tests. Insufficient plastic lip thickness for the volume overlap enforced due to the fitting procedure.	See above for a more stable test environment. Increased thickness of the plastic lip and decreased volume overlap. Fine element stress analyse of 2nd prototype.

above 200 kV/cm when applying 200 kV (see Fig. 6.12). For the 2nd prototype it was decided to machine the conductor from one solid piece, and as such, neglect for this prototype development the advantages gained from the decreased thermal load and reduction of material overall when using a hollow tube. This reduces the number of welds necessary and therefore helps in maintaining a good surface quality, essential for the vacuum sealing technique. Considerations of thermal load will be re-addressed in future iterations of the FT design.

The design also includes a SS "bullet" machined at the end of the central conductor

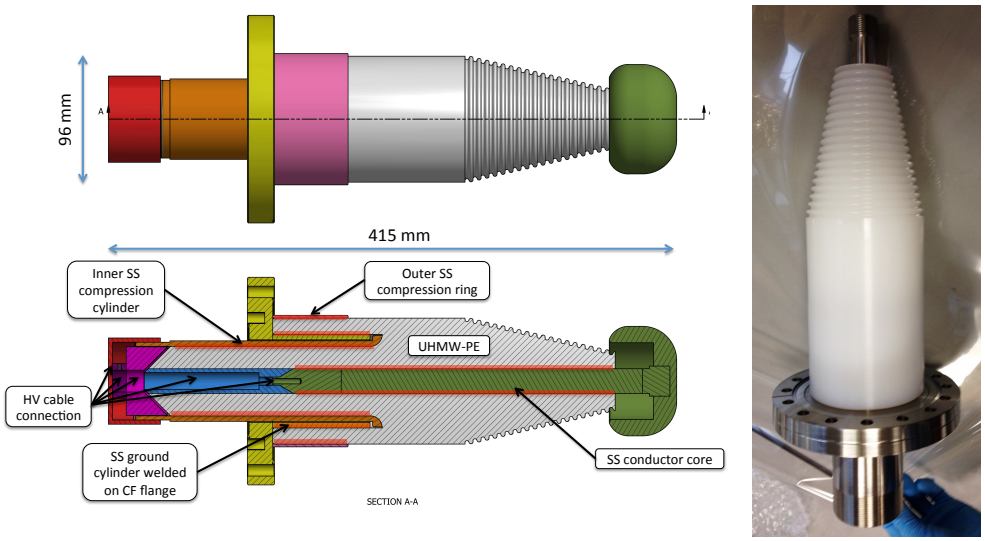

Fig. 6.11: Construction drawing for the second cold HV-FT prototype (left) featuring, in addition to the components also present in the 1st prototype, two SS compression rings that are cryo-fitted by immersing the plastic part in LN2. The sealing interfaces are indicated in red. The insulator (grey) and the sleeve for the HV cable (blue) are made from UHMW-PE. All other parts are machined from SS. Finished assembled prototype (right). The Outer SS compression ring could not be fitted in its original dimensions (for more details see section 6.4.1).

SS piece to accommodate connection to the HV cable that will be used for testing. Here, a spring loaded inverted cone will push the grounding braid of the HV cable onto the UHMW-PE part. At the other end of the conductor, a threaded large area rounded tip screws onto the SS core to create a field free region at the end of the central cylinder within the tip and to lower the surrounding local field.

In addition to improving the seal, the chosen method of nested seals shapes the electric field in the region of the intruding SS steel ground (bottom of the groove) such that additional coating of the plastic surfaces with conductive paints or filling of the evacuated gaps with insulator oils or epoxies can be completely avoided up to moderate high voltages of ∼100 kV, as can be seen in the electric field simulations shown in Fig. 6.13. Here the electric field of the tip of the inner compression cylinder, which provides the important direct contact of ground to insulator, reaches ∼70 kV/cm. At an applied voltage of 200 kV the resulting maximum field at the tip of the SS parts reaches ∼140 kV/cm in the insulator plastic and the vacuum space, which might be an area of breakdown if no conductive silver paint is used. Application of the paint

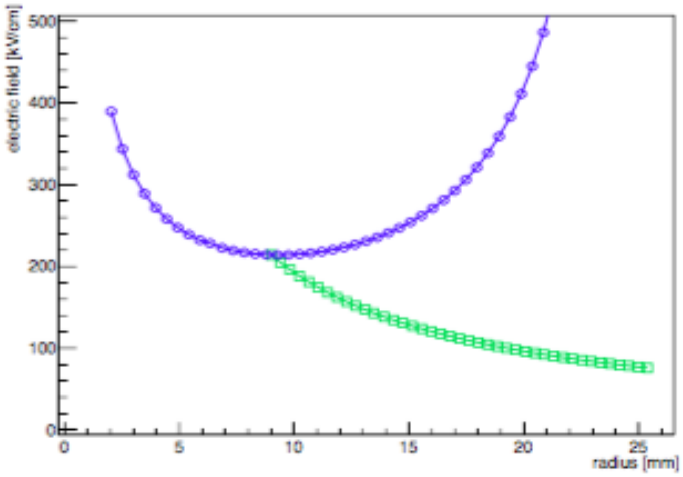

Fig. 6.12: Green squares: Calculation of the electric field as a function of radius within an ideal plastic insulator of 2 inch diameter and a conductor radius of 9 mm. Blue circles: Electric field at the inner diameter of the insulator as a function of different conductor radii, motivating the choice of the inner conductor size (courtesy to Dr. Hanguo Wang, University of California at Los Angeles).

can be achieved in a similar way, as described earlier for the case of the 1st HV-FT prototype.

6.4.1 Construction and assembly

The majority of the parts have been procured, machined and welded from external companies and universities. All metal parts are made from SS grade 304L. As described in the previous section, the seal for the 2nd prototype is formed by alternating layers of SS and plastic. This nested design does not only significantly complicate the assembly procedure of the individual components, but requires very accurately specified dimensions with minimal tolerances to allow the two different fitting methods to work together. It is an imperative to clearly specify and check tolerances with the external companies for all machined parts. Already apparent in the development of the 1nd FT prototype, but even more pronounced for the 2nd one (due to the tighter fittings), is the necessity of test pieces made from UHMW-PE of the same dimensions as the final prototype to evaluate accurately the shrinkage and expansion properties. The temperature behaviours can be very difficult to correctly scale from one size and shape to another. Below, we describe step-by-step the final assembly procedure, developed from the previously conceived assembly guides and various test trials. In addition, we

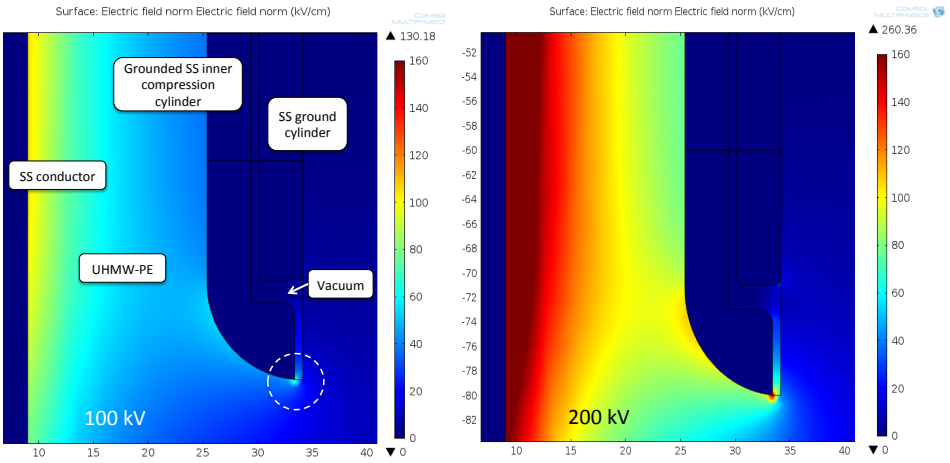

Fig. 6.13: Electric field simulations using COMSOL of the tip of the grounded inner compression ring and SS ground cylinder. The maximum electric field measured at the tip of the inner compression cylinder is 70 kV/cm and 140 kV/cm when applying 100 kV(left) and 200 kV(right), respectively.

list encountered issues and lessons learned along the way:

- The UHMW-PE is heated at 105 °C in a vertical position for 3 hours to expand and allow the seal between insulator and central conductor to be made as it cools. The custom-made spring-loaded jig shown in Fig. 6.4 ensures the insertion depth of the central conductor as well as a constant position during cool down to room temperature and contraction of the plastic.
- Next, the assembly is cooled down using liquid nitrogen to shrink the plastic to fit the dimensions of the inner compression cylinder. Best results are achieved by pouring LN2 over the top into the lip groove and the inner bore of the FT, which is placed in an upright position inside an open dewar or insulated container. This delivers the cryogenic directly to the surfaces and parts of the plastic to be shrunk. The inner compression cylinder can then be fitted from the top while the groove is filled with LN2. During warm-up the FT assembly is continuously flushed with gaseous warm nitrogen to prevent condensation of water and again the custom jig ensures the correct positioning upon warm-up.
    - The largest outer as well as the inner diameter of the inner SS compression cylinder need to be exactly dimensioned and machined, as the groove formed by the plastic lip does not only shrink on its inner diameter but at the same time also on the outer diameter. This behaviour during shrinkage of the plastic

can be marginally counteracted by pouring the LN2 into the groove only, rather than cooling the whole insulator. This leaves the outside of the lip at a higher temperature and as such the outer circumference will not shrink proportionally to the inner diameter of the plastic.

  - Never force the SS parts to fit, especially during cryo-fitting where the time scales are very short, i.e. the time span for fitting is very limited once the cooling source is removed. This can lead to parts being stuck half-way. Due to very exact fittings, even the slightest miss alignment can result in parts being jammed. These parts are then not removable even when trying to immerse the assembly instantaneously in cryogenic liquid. Only after warming the ill-fitted assembly up and repeated cooling the parts usually come loose. This is to avoid as the plastic will deform permanently at an unwanted location from the high stresses upon warm-up.
  - Never try to assemble the SS and UHWW-PE parts in reversed order, i.e. by cryo-fitting first the inner SS compression cylinder and subsequently heating of the FT for heat expansion fitting of the SS conductor and flange-cylinder. The UHMW-PE part undergoes severe permanent deformation when heated up from the constriction on the outer diameter; so much, that the inner compression cylinder can become loose at room temperatures. In addition, the expansion from heating manifests itself in a different way than the usual. Instead of the hole plastic part getting bigger on the outer circumference, as well as the diameter of the bore, the inner diameter starts to reduce due to the high compression stresses form the constriction. Furthermore, removal of the previously cryo-fitted part and subsequent heating of the plastic part on its own, showed that the deformations are of such extend that even then the bore of the diameter can not be expanded large enough to allow the SS conductor to be inserted.

- The best method found to fit the SS cylinder-flange into the UHMW-PE is, similarly to the cryo-fitting procedure described above, through localised application of the heat source. Here, we expand only the lip of the plastic by using a heating jacket constructed from three layers of Kapton foil and a standard baking tape wrapped around the assembly in the region of the lip. A thermocouple temperature sensor is mounted on the surface of the plastic underneath the heating jacket to monitor and control the temperature of the plastic to avoid reaching the critical temperature (120 °C). Once the sensor reaches the required temperature for sufficient expansion of the lip (usually around 100 °C), the SS cylinder with the

welded flange can be inserted. Again, the fitting jig ensures the correct positioning during cool-down.

  * Carefully monitor your heating controller. The thermal transport through the Kapton foil is a relatively slow process and even after the baking tape has been switched off the temperature of the plastic will keep rising by up to 30%.

- The final step to finish the FT assembly is the fitting of the outer SS compression ring by exposing the whole FT to LN2 temperatures, sliding over the SS ring and letting it warm up in a nitrogen environment.

  * In this instances correct dimensioning and keeping to machining tolerances is of utmost importance. This is a very tight fit around the lip region with only a very small total volume overlap achievable. Unfortunately, we could not fit the outer compression ring in its original design dimension for the 2^{nd} FT prototype. The SS ring has since been re-machined (with a larger inner diameter) and the fit can be tested again in the continuation of the R&D programme.

The finished assembled 2^{nd} cold HV-FT prototype is shown on the right hand side of Fig. 6.11. As mentioned above, the final assembly step could not be completed, and as such, the SS outer compression ring is missing and not shown in the image. This is also the FT configuration that has been tested for its sealing properties, described in the following section.

6.4.2 Sealing tests

Room temperature sealing tests

Tests similar to those for the 1^{st} FT prototype have been performed to evaluate the sealing properties of the 2^{nd} cold HV-FT prototype. In this instance, we were using LARA. An image (left) as well as a P&ID schematic of the room temperature sealing test setup is shown in Fig. 6.14. The larger main chamber, hidden in the insulated wooden box on the right hand side of the image is used to hold the bottom of the FT (cathode connection side) and remains at atmospheric pressure. The top of the FT (cable connection side) is contained within the smaller top chamber, which is evacuated. The vacuum system, including the top chamber without the FT, reached a vacuum pressure of 4×10^{-8} mbar and a leak rate of $(8.6 \pm 0.2) \times 10^{-10}$ mbar L/s after a very short pumping time of only two and a half days. All connections have been shown to be leak free from He leak testing with the RGA. An analog scan taken with the RGA of the empty top chamber revealed that there are no unexpected compounds

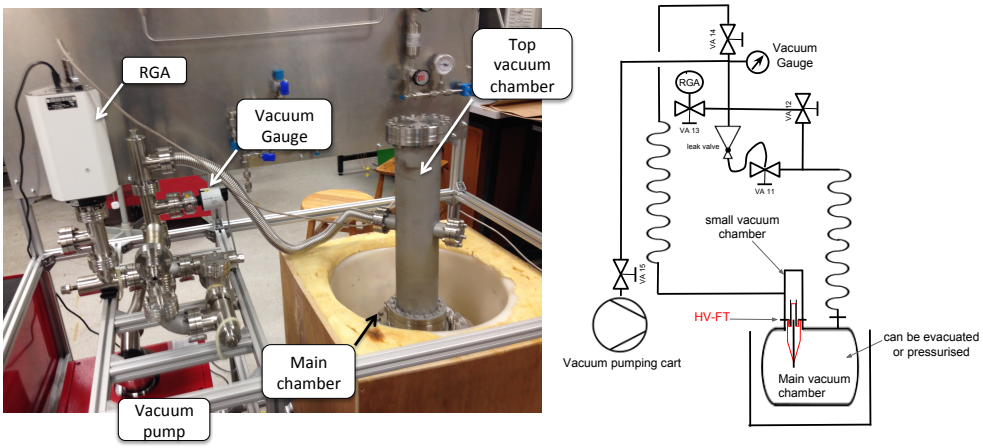

Fig. 6.14: Image (left) and schematic (right) of the room temperature sealing test setup of the 2nd HV-FT prototype. For the test we utilised the LARA test stand. The FT is pointing downwards into the same 9 L SS vessel as previously used (sitting in the wooden box – used to hold liquid argon for cooling the SS vessel for cryogenic testing). The top of the FT (cable connection end) is inside the top vacuum chamber. The top chamber is evacuated to measure the sealing properties of the FT.

to be found in the residual gas, which is composed of the usual candidates such as water, oxygen, nitrogen, carbon dioxide and some low mass hydrocarbons.

Room temperature sealing tests of the 2nd FT have been measured several times over the course of 10 days of pumping on the top vacuum chamber (with atmospheric pressure in the main chamber, and as such, ∼1 bar pressure difference across the FT). The final rate-of-rise curve taken, by monitoring the vacuum gauge after closing the valve to the vacuum pump, is shown on the left hand side of Fig. 6.15. The starting pressure read 7.4×10^{-7} mbar and the calculated leak rate from the fit to the second half of the rate-of-rise curve is $(1.10 \pm 0.04) \times 10^{-7}$ mbar L/s. The plot on the right in Fig. 6.15 shows distinctively two different regions. The first part of the curve with the steep gradient is dominated by the outgassing of the FT, which is levelling off once outgassing and vapour pressure inside the chamber reach equilibrium. The shallower gradient represents the rate of the leak through the FT. Due to the small leak rate and the relatively small total pressure, it is possible to record the rate-of-rise curve for different species simultaneously with the RGA (see right hand side of Fig. 6.15). The leak rate measured from a fit to the nitrogen curve in the RGA spectrum, assuming the vacuum gauge measures nitrogen equivalent vacuum pressure, is $(4.7 \pm 0.1) \times 10^{-8}$ mbar L/s. These measured leak rates are still one to two orders of magnitude

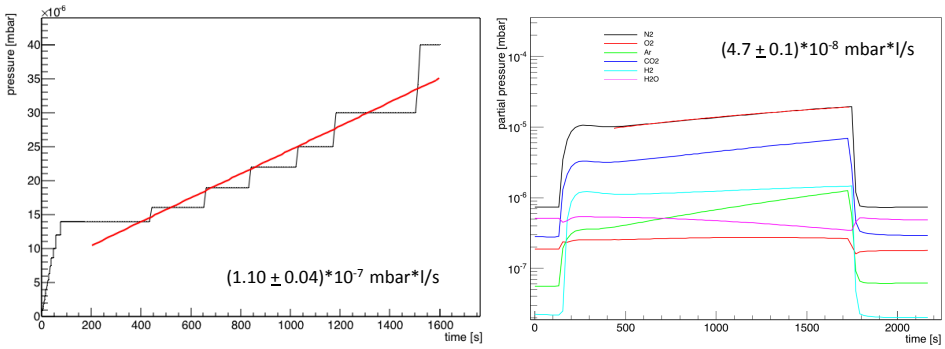

Fig. 6.15: Rate-of-rise curves taken at room temperature, measuring the leak rate across the 2nd prototype FT. Left: Measured directly with the vacuum gauge. Right: Data taken with the RGA.

above the required baseline for the LZ experiment. However, the 2nd FT prototype achieved an improvement over the 1st one of over two orders of magnitude for the sealing tests at room temperature. A scan over the full mass scale with the RGA of the top chamber with the FT attached (leaving the vacuum pump running) is shown in Fig. 6.16. The outgassing of the hydrocarbons from the plastic is clearly visible. Other compounds found are isopropyl alcohol (used in the cleaning process) and the usual ones, such as water and the components of air. The nitrogen to oxygen ratio (mass 28:32) decreased over the 10 days from 7:1 to 5:1, confirming the small residual leak.

Sealing at cryogenic temperatures

Following the evaluation of the leak rate at room temperatures, the FT was put to the test under cryogenic temperature conditions. The capacitive sensor and the temperature ladder installed in the LARA's main chamber allowed for better control cooling rates. An image of the experimental setup is shown on the left hand side of Fig. 6.17. The schematic of the setup is almost identical to the one from the warm sealing test (Fig. 6.14) with the addition of the connections to the full auxiliary gas system which allows to evacuate and fill the bottom main chamber with argon gas.

Figure 6.18 displays the full temperature and pressure profile (middle pane) with the corresponding liquid levels (bottom pane) inside the chamber during the liquefaction process. The temperatures are measured by three Pt100 sensors mounted on a PTFE rod (temperature ladder) with the levels inside the chamber indicated on the

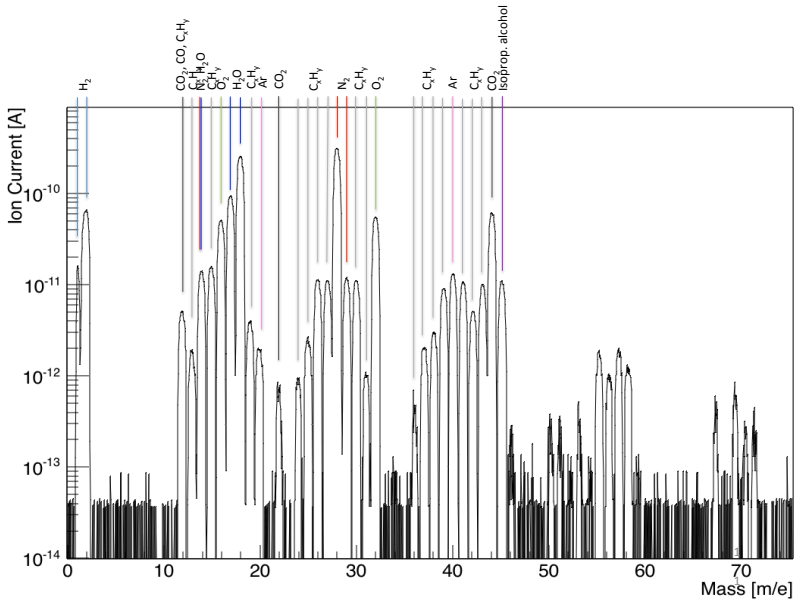

Fig. 6.16: Scan over the full mass range with the RGA (shown up to mass 75, with no recorded significant peaks beyond that point) of the vacuum in the top chamber with the 2nd HV-FT. Most of the lines originate from outgassing of hydrocarbons from the plastic.

schematic drawing on the right hand side of Fig. 6.17. The location of the sensors differs from the one used in Chapter 5. Next to the temperature ladder the capacitor sensor is mounted for continuously monitoring of the liquid level, running though the full length of the chamber. The top panel of Fig. 6.18 shows the partial pressures as measured with the RGA in the evacuated top chamber which is connected via the FT to the main vessel. The chamber was cooled by liquid argon on the outside from ∼40 min onwards. The large spikes in pressure at the very beginning of the cool down process are similar to those previously observed in the cold down of the 1st prototype FT and correspond to movements in the UHMW-PE (accompanied with audible cracking noise). The pressure spikes went up to a pressure of $\sim 10^{-3}$ mbar, and as such, the RGA had to be temporarily disabled. After ∼4 h of cooling the strong movement subsided and the pressure started to fall gradually. Active refilling, to keep the low-grade liquid argon level in the outer box above the flange of the FT, stopped after ∼11.5 h. After that, the argon on the outside of the chamber was allowed to boil off slowly and the chamber to warm-up very gradually over the next two days. At around ∼50 h the FT warmed up enough to enter again the regime of strong movements in the plastic.

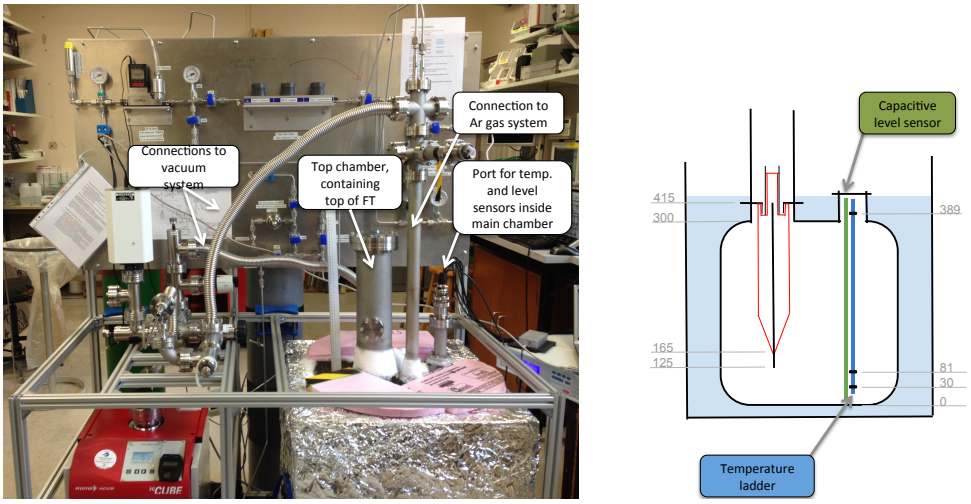

Fig. 6.17: Left: Image of the 2nd HV-FT prototype cold sealing test setup taken during the experiment. The FT is mounted between the small top and the bottom main chamber. Right: Schematic drawing of the installations inside the liquefaction chamber, the FT, the capacitor level sensor (green) and the temperature ladder (blue). The dimensions given (units mm) are measured from the bottom of the chamber.

Despite the high leak rates and increased pressures at times during the warm-up, it was confirmed that the FT returned to its original leak rate once it reached room temperature.

The visible spikes at approximately 12 h, 26 h, and 73.5 h are due to rate-of-rise curve measurements (and as such decoupling from the vacuum pump for a short period of time) to establish the leak rates at a given pressure and temperature. Two consecutive rate-of-rise curves have been taken at ∼12 h, when the liquid inside the chamber covered the FT over its full length. The two measurements were consistent with each other and the second one is shown in Fig. 6.19, demonstrating a leak rate at the order of the LZ vacuum requirement, of $(1.66 \pm 0.06) \times 10^{-9}$ mbar L/s ($(1.07 \pm 0.03) \times 10^{-9}$ mbar L/s when fitting the nitrogen line from the partial pressure plot taken with the RGA). The minimum pressure in the top chamber was reached some hours later and was measured to be 7.4×10^{-8} mbar. For completeness, we have also measured the baseline pressure and leak rate of the empty top chamber at room temperature before conducting the cold sealing test, which resulted in 5.4×10^{-8} mbar and $(8.2 \pm 0.3) \times 10^{-10}$ mbar L/s, respectively.

Due to time constrains, only one cycle of cryogenically testing the 2nd cold HV-FT prototype could be performed and completed. However, the results of this run are very

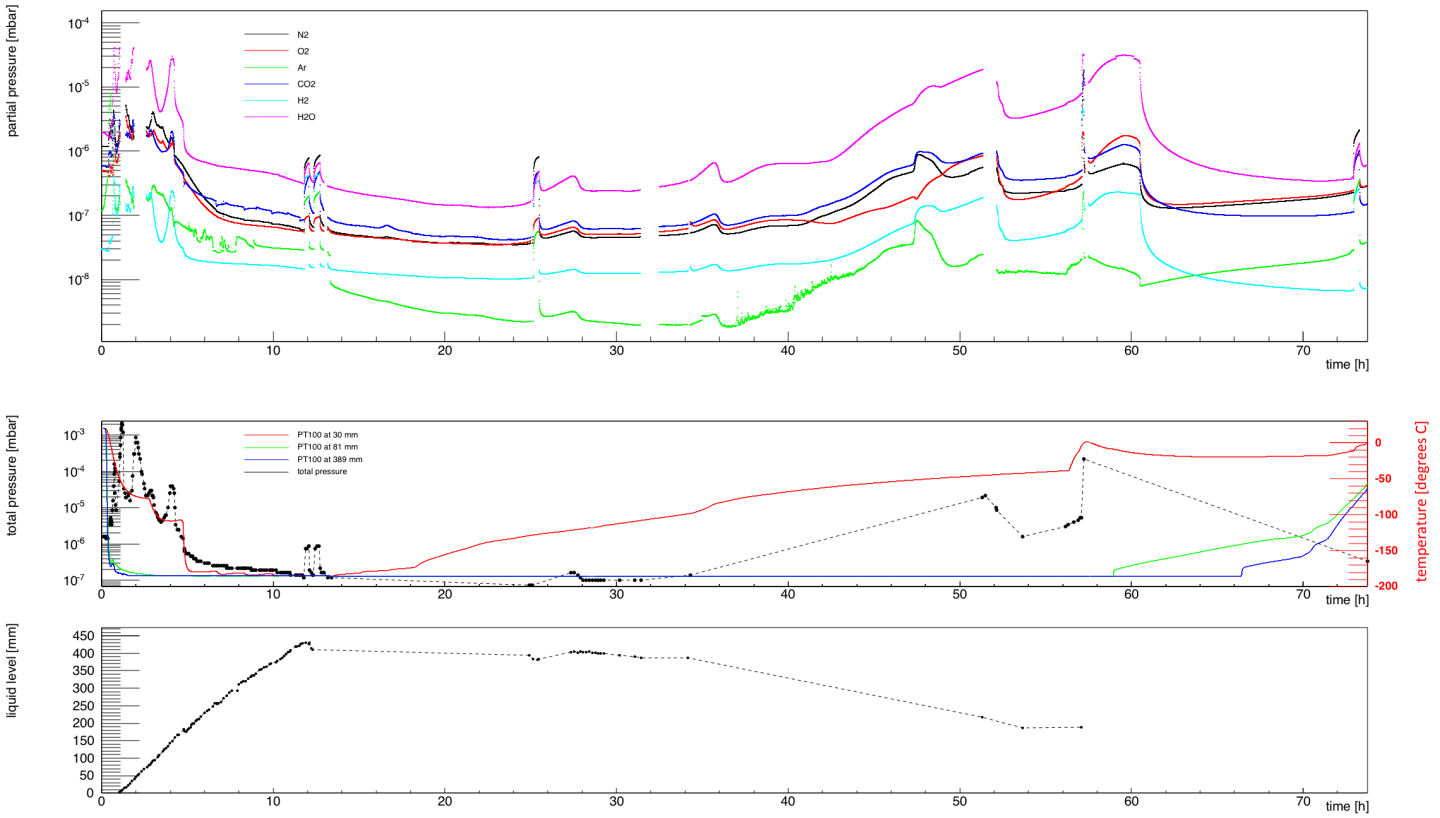

Fig. 6.18: Data from the cold sealing test of the 2nd HV-FT prototype. Top: Partial pressures measured with the RGA from the evacuated top chamber, which is sealed off on one end by the to be tested FT. For more details see text. Middle: Corresponding total pressure profile in the top chamber (black dots—the line is there to guide the eye only) and temperatures measured with the three PT100 sensors mounted in the main liquefaction chamber (red, green and blue solid lines). To increase the warming up rates a heat gun (at a low temperature setting) was employed at the end of the run (at ∼56 h and again at ∼72 h), visible by the sudden increase in the gradients of the temperature curves. Bottom: Liquid level inside the main argon chamber measured with the capacitor level sensor. At the time of this test resonance frequency readings had not been automatised yet, and had to be taken by hand. Therefore, there are only a few measurements after the first cool-down period available and the error on the level is of the order of 10 mm. This is greater than the 6 mmuncertainty quoted in Chapter 5, and it has to do with the fact that at the time of this test the pipe feeding the gas to chamber was almost reaching the its bottom, causing the LAr to bubble. A line is plotted for guiding the eye only.

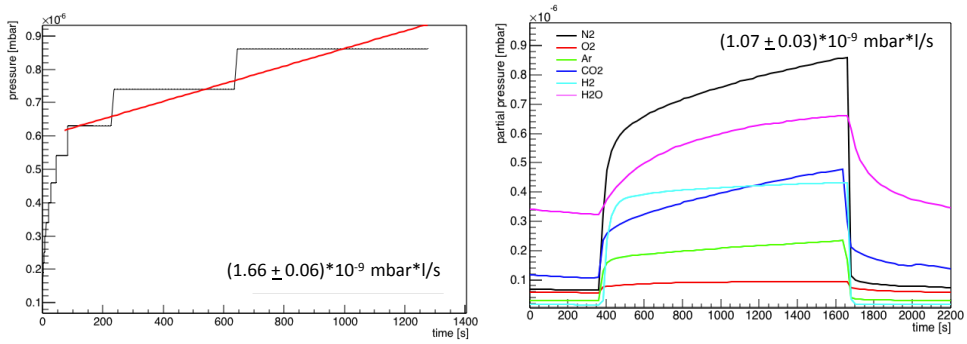

Fig. 6.19: Rate-of-rise curve measurements to establish the leak rate of the 2nd HV-FT prototype at liquid argon temperatures. Left: Measurement taken with the vacuum gauge. Right: Partial pressure plot from the RGA.

encouraging and the leak rate measured across the FT is in line with the LZ vacuum requirement of 10^{-9} mbar L/s. Further cryo-cycling tests are to be performed at RAL to show and understand the durability of the FT under extreme conditions.

Finally, from testing both FT prototypes we find that the transition period from warm to cold is problematic, due to movement in the plastic opening up pockets and leak paths through the FT for short periods of time. The nested sealing technique used for the 2nd prototype did not help significantly in preventing these. Further research into controlling these transition periods should be considered and to this end the stresses evoked in the plastic of the 2nd HV-FT prototype, in the first instance due to the compression seals, but also during cool-down periods, have been studied with a finite element stress analysis. The main results summarised in the following section.

6.4.3 Finite element stress analysis

We have completed thermo-mechanical analyses to improve our understanding of the stresses and deformations manifested under the three scenarios experienced by the feedthrough components and finished assembly, and identify areas for improvement in design, assembly procedure, and tolerance definition to address the residual leak rate through the feedthrough.

- Assembly case: This scenario assessed the mechanical stress and deformation as a result of feedthrough assembly where components require heating and cooling, such that expansion and contraction permits assembly. Following assembly, parts return to nominal, room temperatures, and are hence in a pre-loaded and

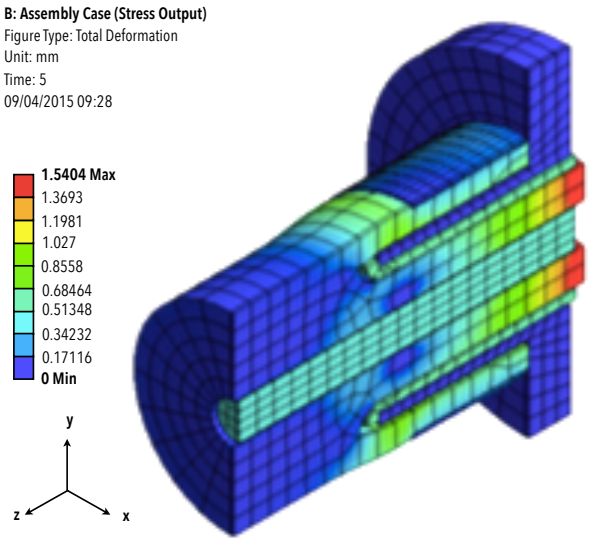

Fig. 6.20: Deformation during assembly of the feedthrough. Maximum deformation of 1.5 mmoccurs on the UHMW-PE along the z coordinate, but with littles consequences, since axial motions are not externally constrained. However, deformations of the inner cylinder and and UHMW-PE adjacent to the outer compression cylinder are not negligible.

elastically stressed state. Defining this precondition is necessary since it provides supplementary stresses to all subsequent analyses.

- Cooling case: To provide input in terms of ramp times required for cooling cycles, this scenario assessed the rate of normalisation of thermal loads during cooling of the feedthrough for normal operation by performing a transient thermal computation of component temperatures until nominal, steady-state is achieved.
- Cold case: Stresses and thermally-induced deformations as a result of thermal loading in line with typical use of the feedthrough, with a vacuum applied to the cable side and feedthrough immersed in a cryogen, were analysed in this scenario. A static thermal computation of component stresses provides understanding of thermal gradients and assessment of the feedthrough with respect to glass transition temperatures.

The most significant result from these analyses is identification of significant stress on the stainless steel inner compression barrel and outer compression sleeve during the

assembly sequence. The stainless steel is subject to sufficient stress during thermal normalisation subsequent to fitting the components, up to about 340 MPa in some areas, that exceeds the elastic limit yield strength of 241 MPa for stainless steel 304L. The cylinders undergo plastic deformation (as seen in Fig. 6.20) that results in low subsequent elastic response during the cool down cycle, in which the UHMW-PE contracts enough such that pass-through gaps are formed due to separation of UHMW-PE and sleeves through which pressure differentials may normalise. These gaps are identified as the likely cause of the residual leaks through the 2nd prototype feedthrough.

Improvements to the design such that only elastic deformation occurs during assembly would allow stress to normalise with respect to temperature, but contact between components would remain continuous such that no gaps would form. Specific steps to achieve this with further iterations of the feedthrough have been identified through this FEA study:

- The outer compression sleeve and inner barrel should be manufactured from materials with higher yield stress or lower modulus than the stainless steel 304L used presently.
- Stringent requirements on tolerances of all interference fit components should be met during hardware procurement.
- Material with a lower coefficient of thermal expansion than UHMW-PE could be used demonstrating similar electrical properties.
- Perform feasibility assessments of the use of static sealing methodologies as part of the assembly sequence.

6.5 Continuation of R&D programme

In order to further develop the cold HV-FT, address the areas for improvement identified with the FEA study, and perform tests with voltage delivery under LZ running conditions, the work presented in this chapter will be followed up by R&D at Rutherford Appleton Laboratory, due to the availability of HV power supplies and infrastructure for testing to 200 kV. Nonetheless, this research progressed designs for novel cold feedthroughs to the state of satisfying the critical vacuum sealing aspect. This opens up gains for noble gas TPCs in terms of low background and compact constructions that could greatly simplify HV delivery in future experiments.

7
Conclusions

This work has shown the contribution of the author to experiments using LAr TPC technology. This final chapter summarises what has been presented, underlying the results achieved.

After an introduction to the the fields of dark matter and neutrino physics, where LAr TPCs are widely employed, the results of the SCENE experiment have been reported. These comprised the scintillation efficiency, $\mathcal{L}_{\text{eff}}$, and the ionisation yield, $\mathcal{Q}_y$, of nuclear recoils in LAr. While previous measurements only included $\mathcal{L}_{\text{eff}}$ at zero electric field, SCENE measured $\mathcal{L}_{\text{eff},\,^{83\text{m}}\text{Kr}}$ (i.e. relative to $^{83\text{m}}$Kr) in the drift field range 0–970 V/cm, for energies between 10.3 and 57.3 keV. $\mathcal{Q}_y$ was also measured by SCENE with unprecedented precision and for a wide range of low-energy nuclear recoils, namely 16.9–57.3 keV, between 96.5 and 486 V/cm. SCENE's results suggest that the effects of electric field on scintillation and ionisation in LAr TPCs are more complex than the small, energy-independent variations that have been assumed so far. The data collected are not only valuable to the DM field, but more in general to the design and calibration of any LAr TPC which exploits scintillation and ionisation signals of nuclear recoils in liquid argon.

After SCENE's results, the description of the LARA liquid argon test facility and the software package LArView have followed. LARA has been constructed by the author within the High Energy Physics Group at UCL in order to facilitate tests of novel detector technologies and readouts for dark matter and neutrino physics, while LArView has been developed—also by the author—for data analysis with LARA.

The first measurement performed with LARA has been the scintillation quenching for electron recoils in LAr, S_e using cosmic muons. For the purpose, a TPC and a cryogenic PMT have been designed and built by the author. The measurement of S_e has established correct electric field operation of the TPC in the chamber. For future recommendation, an amplifier should be used when using radioactive sources to allow detection of energy events below the cosmic muon range. If possible the source should also be placed inside the detector.

Finally, the LARA test stand has been used for testing a novel cold high-voltage

feedthrough design, part of the dark matter R&D, with a focus on LZ in particular. The research progressed designs for novel cold feedthroughs to the state of satisfying the critical vacuum sealing aspect. This opens up gains for noble gas TPCs in terms of low background and compact constructions that could greatly simplify HV delivery in future experiments.

References

Aartsen, M. G. et al. (2015). **??***Search for Dark Matter Annihilation in the Galactic Center with IceCube-79.* Eur. Phys. J., **C75***(10), 492.*

Acciarri, R. (2015). Measurement of muon neutrino and anti-muon neutrino Neutral Current $\pi_0 \to \gamma\gamma$ Production in the ArgoNeuT Detector. arXiv:1511.00941.

Acosta-Kane, D. et al. (2008). Discovery of underground argon with low level of radioactive ^{39}Ar and possible applications to WIMP dark matter detectors. Nuclear Instruments and Methods in Physics Research A, **587***, 46–51.*

Agostinelli, S. et al. (2003, August). Geant4–a simulation toolkit. Nuclear Instruments and Methods in Physics Research Section A: Accelerators, Spectrometers, Detectors and Associated Equipment, **506***(3), 250–303.*

Agostino, L. et al. (2014). LBNO-DEMO: Large-scale neutrino detector demonstrators for phased performance assessment in view of a long-baseline oscillation experiment. arXiv:1409.4405.

Ahlen, S. et al. (2009, November). The case for a directional dark matter detector and the status of current experimental efforts. International Journal of Modern Physics A, **25***(1), 1–51.*

Ahmad, Q. R. et al. (2001, July). Measurement of the Rate of $\nu_e + d \to p + p + e^-$ Interactions Produced by ^{8}B Solar Neutrinos at the Sudbury Neutrino Observatory. Phys. Rev. Lett., **87***(7), 071301.*

*Alexander, T. et al. (2013*a*). Observation of the Dependence of Scintillation from Nuclear Recoils in Liquid Argon on Drift Field.* Phys. Rev. D, **88***, 092006.*

*Alexander, T. et al. (2013*b*). Light yield in DarkSide-10: A prototype two-phase argon TPC for dark matter searches.* Astroparticle Physics, **49***, 44–51.*

Amar, J. et al. (2015, June). Background analysis and status of the ANAIS dark matter project. arXiv:1506.03210.

AMS Collaboration (2013, April). First Result from the Alpha Magnetic Spectrometer on the International Space Station: Precision Measurement of the Positron Fraction in Primary Cosmic Rays of 0.5–350 GeV. Physics Review Letterss, **110***, 141102.*

Angle, J et al. (2008, September). Limits on spin-dependent WIMP-nucleon cross-sections from the XENON10 experiment. Physics Review Letters, **101***, 091301.*

Ankowski, A. M. et al. (2015). Comparison of the calorimetric and kinematic methods of neutrino energy reconstruction in disappearance experiments. Phys. Rev. D, **92***, 073014.*

Antonello, M. et al. (2015). Operation and performance of the ICARUS-T600 cryogenic plant at Gran Sasso underground Laboratory. arXiv:1504.01556.

Aprile, E. et al. (2014). Measurements of proportional scintillation and electron multiplication in liquid xenon using thin wires. Journal of Instrumentation, **9***, 11012.*

Aprile, E. and Doke, T. (2010, July-September). Liquid xenon detectors for particle physics and astrophysics. Reviews of Modern Physics, **82***, 2053.*

Arazi, L. et al. (2013). First observation of liquid-xenon proportional electroluminescence in THGEM holes. arXiv:1310.4074.

Arazi, L. et al. (2015). Liquid Hole Multipliers: bubble-assisted electroluminescence in liquid xenon. arXiv:1505.02316.

ATLAS Collaboration (2014). Search for dark matter in events with a hadronically decaying W or Z boson and missing transverse momentum in pp collisions at $\sqrt{s} = 8$ TeV with the ATLAS detector. Physics Review Letters, **112***, 041802.*

Babcock, H. W. (1939). *The rotation of the Andromeda nebula.* Lick Observatory bulletin, **19***(498), 41–51.*

Bakale, G. et al. (1976). *Effect of an Electric Field on Electron Attachment to SF_6, N_2O, and O_2 in Liquid Argon and Xenon.* The Journal of Physical Chemistry, **80***(23), 2556.*

Ballou, R. et al. (2015, November). *New exclusion limits on scalar and pseudoscalar axionlike particles from light shining through a wall.* Phys. Rev. D, **92**, *092002.*

Barabash, A. S. and Bolozdynya, A. I. (1989, March). *How to detect the dark matter of the galaxy if it made up of weakly interacting neutral particles with masses 1–10 GeV/c^2.* Pis'ma Zh. Eksp. Teor. Fiz., **49***(6), 356–359.*

*Baudis, L. (2014*a*).* *WIMP dark matter direct-detection searches in noble gases.* Physics of the Dark Universe, **4**, *50–59.*

*Baudis, L. (2014*b*, June).* *XENON and DARWIN. In* SWAPS meeting Cartigny.

Bauer, D. et al. (2015, March). *Dark Matter in the Coming Decade: Complementary Paths to Discovery and Beyond.* Physics of the Dark Universe, **7-8**, *16–23.*

Bekenstein, J. D. (2004). *Relativistic gravitation theory for the MOND paradigm.* Phys. Rev. D, **70**, *083509.*

Bellamy, E. H. (1994, February). *Absolute calibration and monitoring of a spectrometric channel using a photomultiplier.* Nuclear Instruments and Methods in Physics Research A, **339**, *468–476.*

Bernabei, R. (2010). *New results from DAMA/LIBRA.* Eur. Phys. J. C, **67**, *39–49.*

Bertone, Gianfranco (ed.) (2010). Particle Dark Matter. *Cambridge University Press.*

Birks, J. B. and Black, F. A. (1951). *Deterioration of Anthracene under α-Particle Irradiation.* Proceedings of the Physical Society. Section A, **64***(5), 511–512.*

Breskin, A. (2013). *Liquid Hole-Multipliers: A potential concept for large single-phase noble-liquid TPCs of rare events.* Journal of Physics: Conference Series, **460**, *012020.*

Breskin, A. et al. (2009). *A concise review on THGEM detectors.* Nuclear Instruments and Methods in Physics Research A, **598***(1), 107–111.*

Breskin, A. et al. (2011). *CsI-THGEM gaseous photomultipliers for RICH and noble-liquid detectors.* Nuclear Instruments and Methods in Physics Research A, **639**, *117–120.*

Bringmann, T. and Hofmann, S. (2007). *Thermal decoupling of WIMPs from first principles.* Journal of Cosmology and Astroparticle Physics, **2007***(04), 016.*

Bunemann, O. et al. (1949). *Design of grid ionization chambers.* Canadian Journal of Research, **27**, *191–206.*

Buote, D. A. et al. (2002). *Chandra Evidence for a Flattened, Triaxial Dark Matter Halo in the Elliptical Galaxy NGC 720.* Astrophysical Journal, **577**, *183–196.*

Burbidge, E. M. et al. (1959). *The Rotation and Mass of NGC 2146.* Astrophysical Journal, **131**, *549–552.*

Buzulutskov, A. et al. (2000). *The GEM photomultiplier operated with noble gas mixtures.* Nuclear Instruments and Methods in Physics Research A, **443**, *164–180.*

Cao, H (2014, November). A Study of Nuclear Recoils in Liquid Argon Time Projection Chamber for the Direct Detection of WIMP Dark Matter. *Ph.D. thesis, Princeton University.*

Cao, H et al. (2015). *Measurement of scintillation and ionization yield and scintillation pulse shape from nuclear recoils in liquid argon.* Phys. Rev. D, **91**, *092007.*

Carroll, S. M. et al. (1992). *The Cosmological Constant.* Annual Review of Astronomy and Astrophysics, **30**, *499–542.*

Casper, D. (2002). *The nuance Neutrino Simulation, and the Future.* Nucl. Phys. Proc. Suppl., **112**, *161–170.*

CAST Collaboration (2015, July). *New solar axion search using the CERN Axion Solar Telescope with ^{4}He filling.* Phys. Rev. D, **92**, *021101.*

Chepel, V. and Arajo, H. (2013). *Liquid noble gas detectors for low energy particle physics.* Journal of Instrumentation, **8***(04), R04001.*

Church, E. D. (2014). *LArSoft: A Software Package for Liquid Argon Time Projection Drift Chambers.* arXiv:1311.6774.

Ciarlini, P., Cox, M. G., Pavese, F., and Rossi, G. B. (2003, September). Advanced Mathematical and Computational Tools in Metrology *(Sixth edn). World Scientific.*
Clowe, D. et al. (2006). A direct empirical proof of the existence of dark matter. Astrophysical Journal Letters, **648***(2), 109–113.*
Corti, C. (2014). The cosmic ray electron and positron spectra measured by AMS-02. arXiv:1402.0437.
Cowan, C. L. et al. (1956). Detection of the Free Neutrino: a Confirmation. Scinece 20, **124***(3212), 103–104.*
Cressler, John D. and Mantooth, H. Alan (ed.) (2013). Extreme Environment Electronics. *CRC Press.*
Creus, W. et al. (2015, Aug). Scintillation efficiency of liquid argon in low energy neutron-argon scattering. Journal of Instrumentation, **10**, *08002.*
Cushman, P. et al. (2013). Snowmass CF1 Summary: WIMP Dark Matter Direct Detection. arXiv:1310.8327.
Davis, R. et al. (1968). Search for Neutrinos from the Sun. Phys. Rev. Lett., **20***(21), 1205.*
Dehnen, W. and Binney, J. (1998). Mass models of the Milky Way. Mon. Not. R. Astron. Soc., **294**, *429–438.*
Doke, T. et al. (1985, March). Estimation of the fraction of electrons escaping from recombination in the ionization of liquid argon with relativistic electrons and heavy ions. Chem. Rev. Lett., **115***(2), 164–166.*
Doke, T. et al. (1988). LET dependence of scintillation yields in liquid argon. Nuclear Instruments and Methods in Physics Research, **A269**, *291–296.*
Doke, T. et al. (2002). Absolute Scintillation Yields in Liquid Argon and Xenon for Various Particles. Japanese Journal of Applied Physics, **41**, *1538–1545.*
Dolgoshein, B. A. et al. (1970). New method of registration of ionizing-particle tracks in the condensed matter. JETP Lett., **11***(11), 351.*
Donato, F. et al. (1998). Effects of galactic dark halo rotation on WIMP direct detection. Astroparticle Physics, **9***(3), 247–260.*
Drukier, A. K. et al. (1986, June). Detecting cold dark-matter candidates. Phys. Rev. D, **33***(12), 3495–3508.*
DUNE Collaboration (2016, January). Long-Baseline Neutrino Facility (LBNF) and Deep Underground Neutrino Experiment (DUNE). arXiv:1512.06148v2.
EDELWEISS Collaboration (2007). Measurement of the response of heat-and-ionization germanium detectors to nuclear recoils. Nuclear Instruments and Methods in Physics Research A, **577**, *558–568.*
Einasto, J. (2010). Dark Matter. arXiv:0901.0632.
Engel, J. et al. (1992). Nuclear physics of dark matter detection. International Journal of Modern Physics E, **1***(1), 1–37.*
Erdal, E. et al. (2015). Direct observation of bubble-assisted electroluminescence in liquid xenon. Journal of Instrumentation, **10***(11), P11002.*
Fan, Y. et al. (2010). $e^{\pm}$ Excesses in the Cosmic Ray Spectrum and Possible Interpretations. International Journal of Modern Physics D, **19**, *2011–2058.*
Feldman, Gary J. (1992). The Discovery of the tau, 1975-1977: A Tale of three papers. In Stanford 1992, The third family and the physics of flavor, *Number C9207131, pp. 631–646.*
Feng, J. L. (2010). Dark Matter Candidates from Particle Physics and Methods of Detectionrticle Physics and Methods of Detection. Annual Review of Astronomy and Astrophysics, **48**, *495–545.*
Feng, J. L. et al. (2011). Isospin-Violating Dark Matter. Phys. Rev. B, **703***(2), 124–127.*
Fermi-LAT Collaboration (2012). Measurement of separate cosmic-ray electron and positron spectra with the Fermi Large Area Telescope. Physics Review Letters, **108**, *011103.*
Foreman, W. (2015, November). First Run of the LArIAT Testbeam Experiment. arXiv:1511.0030.
Formaggio, J.A. and Zeller, G.P. (2012). From eV to EeV: Neutrino Cross Sections Across

Energy Scales. Reviews of Modern Physics, **84**, *1307.*

Francini, R. et al. (2013). VUV-Vis optical characterization of Tetraphenyl-butadiene films on glass and specular reflector substrates from room to liquid Argon temperature. Journal of Instrumentation, **8***(09), P09006.*

Freedman, D. Z. (1974, March). Coherent effects of a weak neutral current. Phys. Rev. D, **9***(5), 1389.*

Galymov, V. (2015). LBNO-DEMO (WA105): a large demonstrator of the liquid argon dual-phase TPC. In Proceedings, 2015 European Physical Society Conference on High Energy Physics (EPS-HEP 2015), *Volume EPS-HEP2015, p. 052.*

Gastler, D. et al. (2012). Measurement of scintillation efficiency for nuclear recoils in liquid argon. Phys. Rev. C, **85**, *065811.*

Gelmini, G. B. (2015). TASI 2014 Lectures: The Hunt for Dark Matter. arXiv:1502.01320.

Geuzaine, C. and Remacle, J. (2009). Gmsh: a three-dimensional finite element mesh generator with built-in pre- and post-processing facilities. International Journal for Numerical Methods in Engineering, **79***(11), 1309–1331.*

Goodman, M. W. and Witten, E. (1985). Detectability of certain dark-matter candidates. Phys. Rev. D, **31**, *3059–3063.*

Grace, Emily and Nikkel, James A. (2016). Index of refraction, Rayleigh scattering length, and Sellmeier coefficients in solid and liquid argon and xenon. arXiv:1502.04213.

Graham, P. W. et al. (2016). Experimental Searches for the Axion and Axion-like Particles. Annual Review of Nuclear and Particle Science, **65**, *485–514.*

Green, A. (2012). Astrophysical uncertainties on direct detection experiments. Mod. Phys. Lett. A, **27**, *1230004.*

Guenette, R. (2011). The ArgoNeuT experiment. In Particles and fields. Proceedings, Meeting of the Division of the American Physical Society, DPF 2011, Providence, USA, August 9-13, 2011 *(ed. T. Speer), Number C11-08-09.*

Gutlein, A. et al. (2010). Solar and atmospheric neutrinos: Background sources for the direct dark matter searches. Astroparticle Physics, **34**, *90–96.*

Hamamatsu Photonics K. K., Editorial Committee (ed.) (2007, August). Photomultipliers Tubes - Basics and Applications *(3a edn). Hamamatsu Photonics K. K., Electron Tube Division.*

Heindl, T. et al. (2010). The scintillation of liquid argon. EPL, **91**, *62002.*

Hitachi, A. et al. (1983). Effect of ionization density on the time dependence of luminescence from liquid argon and xenon. Phys. Rev. B, **27***(9), 5279–5285.*

Hitachi, A. et al. (1987, May). Scintillation and ionization yield for a particles and fission fragments in liquid argon. Phys. Rev. A, **35***(9), 3956–3958.*

Hitachi, A. and Doke, T. (1992, November). Luminescence quenching in liquid argon under charged-particle impact: Relative scintillation yield at different linear energy transfers. Phys. Rev. B, **46***(18), 11463.*

Hollas, J. Michael (2004). Modern Spectroscopy *(Fourth edn). John Wiley and Sons, Ltd.*

Hutchinson, G. W. (1948, October). Ionization in Liquid and Solid Argon. Nature, **162**, *610–611.*

Jerry, R. et al. (2010). A study of the Fluorescence Response of Tetraphenyl-butadiene. arXiv:1001.4214.

Joshi, J and Qian, X. (2015). Signal Processing in the MicroBooNE LArTPC. arXiv:1511.00317.

Joshi, T. H. et al. (2014, May). First measurement of ionization yield of nuclear recoils in liquid argon. Phys. Rev. Lett., **112**, *171303.*

Jungman, G. et al. (1996). Supersymmetric Dark Matter. Phys. Rept., **267**, *195–373.*

Kamionkowski, M. (1997). WIMP and Axion Dark Matter. arXiv:hep-ph/9710467.

Karagiorgi, G. (2013). Current and Future Liquid Argon Neutrino Experiments. arXiv:1304.2083.

Kayser, B. (2008). Neutrino Mass, Mixing, and Flavor Change. arXiv:0804.1497.

Kempa (2006). Low energy muons in the cosmic radiation. Nucl.Phys.Proc.Suppl., **151**,

299–302.

Kohri, K. et al. (2015, February). Can we explain AMS-02 antiproton and positron excesses simultaneously by nearby supernovae without pulsars or dark matter? Prog. Theor. Exp. Phys..

Kubota, S. et al. (1976, February). Evidence of the existence of exciton states in liquid argon and exciton-enhanced ionization from xenon doping. Phys. Rev. B, **13***(4), 1649.*

*Kubota, S. et al. (1978*a*, February). Evidence for a triplet state of the self-trapped exciton states in liquid argon, krypton and xenon.* Journal of Physics C: Solid State Physics, **11***(12), 2645–2651.*

*Kubota, S. et al. (1978*b*, March). Recombination luminescence in liquid argon and in liquid xenon.* Phys. Rev. B, **17***(6), 2763–2765.*

*Kubota, Shinzou et al. (1978*c*). Variation of scintillation decay in liquid argon excited by electrons and alpha particles.* Nuclear Instruments and Methods, **150**, *561–564.*

Kubota, S. et al. (1979). Dynamical behaviour of free electrons in the recombination process in liquid argon, krypton, and xenon. Phys. Rev. B, **20***(8), 3486–3496.*

Kubota, Shinzou et al. (1982). Liquid and solid argon, krypton and xenon scintillators. Nuclear Instruments and Methods, **196***(9), 101–105.*

LAGUNA-LBNO Collaboration (2014). The mass-hierarchy and CP-violation discovery reach of the LBNO long-baseline neutrino experiment. arXiv:1312.6520.

Lakkaraju, R. et al. (2013, April). Heat transport in boiling turbulent Rayleigh-Bnard convection. Proc. Natl Acad. Sci. USA, **110***(23), 9237–9242.*

Lewin, J. D. and Smith, R. F. (1996). Review of mathematics, numerical factors, and corrections for dark matter experiments based on elastic nuclear recoil. Astroparticle Physics, **6**, *87–112.*

Lightfoot, P. K. et al. (2008). Characterisation of a silicon photomultiplier device for applications in liquid argon based neutrino physics and dark matter searches. Journal of Instrumentation, **3**, *10001.*

LIGO Collaboration (2016, February). Observation of Gravitational Waves from a Binary Black Hole Merger. Physics Review Letters, **116**, *061102.*

Lindhard, J. et al. (1963). Integral equations governing radiation effects. Mat. Fys. Medd. Dan. Vid. Selsk., **33***(10), 1–42.*

LUX Collaboration (2013). The Large Underground Xenon (LUX) Experiment. Nuclear Inst. and Methods in Physics Research A, **704**, *111 – 126.*

LUX Collaboration (2014, March). First Results from the LUX Dark Matter Experiment at the Sanford Underground Research Facility. Phys. Rev. Lett., **112**, *091303.*

*LUX Collaboration (2016*a*, January). Improved WIMP scattering limits from the LUX experiment.* arXiv:1512.03506.

*LUX Collaboration (2016*b*, March). Results on the spin-dependent WIMP-nucleon cross section from LUX Run 3 data.* arXiv:1602.03489.

Manalaysay, A. (2010). Towards an improved understanding of the relative scintillation efficiency of nuclear recoils in liquid xenon. arXiv 1007.3746.

Matko, V. (2009). Major Improvements of Quartz Crystal Pulling Sensitivity and Linearity Using Series Reactance. Sensors, **9***(10), 8263.*

Meszaros, Peter (2010). The High Energy Universe: Ultra-High Energy Events in Astrophysics and Cosmology. *Cambridge University Press.*

MicroBooNE Collaboration (2008). Unexplained Excess of Electron-Like Events From a 1-GeV Neutrino Beam. Phys. Rev. Lett., **102**, *101802.*

MicroBooNE Collaboration (2012). The MicroBooNE Technical Design Report. Technical report, Fermilab.

Milgrom, M. (2015). MOND theory. Canadian Journal of Physics, **93***(2), 107.*

Miyajima, M. et al. (1974). Average energy expended per ion pair in liquid argon. Phys. Rev. A, **9***(3), 1438–1443.*

Moffat, J. W. (2005). Scalar-Tensor-Vector Gravity Theory. Journal of Cosmology and Astroparticle Physics, **2006***(03), 004.*

Moffat, J. W. and Toth, V. T. (2007). *Testing Modified Gravity with Globular Cluster Velocity Dispersions.* Astrophysical Journal, **680**, *1158.*

Moffat, J. W. and Toth, V. T. (2012). *Modified Gravity: Cosmology without dark matter or Einstein's cosmological constant.* arXiv:0710.0364.

*Mozumder, A (1995*a*).* *Free-ion yield in liquid argon at low-LET.* Chemical Physics Letters, **238***(1), 143–148.*

*Mozumder, A (1995*b*).* *Free-ion yield and electron-ion recombination rate in liquid xenon.* Chemical Physics Letters, **245***(4), 359–363.*

Northrop, J. A. et al. (1958). *Further Work with Noble Element Scintillators.* IRE Transactions on Nuclear Science, **5**, *81–87.*

Nunokawa, H. (2007). *Resolving the octant θ_{23} degeneracy by neutrino oscillation experiments.* Nucl.Phys.Proc.Suppl., **168**, *212–214.*

Olive, K. A. et al. (2014). *Review of Particle Physics.* Chin.Phys. C, **38**, *090001.*

Oort, J. H. (1932, August). *The force exerted by the stellar system in the direction perpendicular to the galactic plane and some related problems.* Bulletin of the Astronomical Institutes of the Netherlands, **6**, *249.*

Oort, J. H. (1940, April). *Some Problems Concerning the Structure and Dynamics of the Galactic System and the Elliptical Nebulae NGC 3115 and 4494.* The Astrophysical Journal, **91***(3), 273–306.*

Palamara, O. (2011). *The ArgoNeuT LAr-TPC: a dedicated experiment for neutrino cross section measurement at FNAL.* Nuclear Physics B (Proc. Suppl.), **217**, *189–192.*

PAMELA Collaboration (2009, February). *Observation of an anomalous positron abundance in the cosmic radiation.* Nature, **458**, *607–609.*

Pauli, Wolfang (1978). *Dear radioactive ladies and gentlemen.* Phys. Today, **31***(9), 27.*

Peccei, R. D. (2008). *The Strong CP Problem and Axions.* Lecture Notes in Physics, **741**, *3–17.*

Perl, M. L. et al. (1975). *Evidence for Anomalous Lepton Production in $e^+ - e^-$ Annihilation.* Phys. Rev. Lett., **35**, *1489.*

PICASSO Collaboration (2005). *Response of Superheated Droplet Detectors of the PICASSO Dark Matter Search Experiment.* Nucl.Instrum.Meth. A, **555**, *184–204.*

*PICO Collaboration (2016*a*, March).* *Improved dark matter search results from PICO-2L Run 2.* Phys. Rev. D, **93**, *061101.*

*PICO Collaboration (2016*b*, March).* *Dark matter search results from the PICO-60 CF3I bubble chamber.* Phys. Rev. D, **93**, *052014.*

Planck Collaboration (2015, February). *Planck 2015 results. XIII. Cosmological parameters.* arXiv:1502.01589.

Plante, G. et al. (2011). *New Measurement of the Scintillation Efficiency of Low-Energy Nuclear Recoils in Liquid Xenon.* Phys. Rev. C, **84**, *045805.*

Pointecouteau, E. and Silk, J. (2005). *New constraints on MOND from galaxy clusters.* Mon. Not. Roy. Astron. Soc., **364**, *654–658.*

Pozar, D. M. (2011). Microwave Engineering. *Wiley.*

Quinn, Helen R. (2004). *CP Symmetry Breaking, or the Lack of It, in the Strong Interactions.* *In* 5th Rencontres du Vietnam: New Views in Particle Physics (Particle Physics and Astrophysics) Hanoi, Vietnam, August 5-11, 2004, *Number SLAC-PUB-10698.*

Radeka, V. et al. (2009, June). *R&D on Readout for Very Large Liquid Argon TPCs. Director's Review of Fermilab's Integrated LAr/TPC R&D Plan.*

Read, J. I. (2014). *The Local Dark Matter Density.* Journal of Physics G: Nuclear and Particle Physics, **41***(6), 063101.*

Regenfus, C. et al. (2012). *Study of nuclear recoils in liquid argon with monoenergetic neutrons.* Journal of Physics: Conference Series, **375***(1), 012019.*

Roberts, M. S. (1965). *A High-Resolution 21-cm Hydrogen-Line Survey of the Andromeda Nebula.* Astrophysical Journal, **144**, *639–656.*

Roberts, M. S. and Rots, A. H. (1973, August). *Comparison of Rotation Curves of Different Galaxy Types.* Astronomy and Astrophysics, **26**, *483–485.*

Rubin, V. C. and Ford, W. K. Jr. (1970). Rotation of the Andromeda Nebula from a Spectroscopic Survey of Emission Regions. Astrophysical Journal, **159**, *373.*
Sauli, F. (1997). GEM: A new concept for electron amplification in gas detectors. Nuclear Instruments and Methods in Physics Research A, **386**, *531–534.*
Schenk, Michael (2015). Studies with a Liquid Argon Time Projection Chamber. *Springer Spektrum.*
Schneider, M. D. et al. (2012). The Shapes and Alignments of Dark Matter Halos. Journal of Cosmology and Astroparticle Physics, **30**.
Schwarzschild, M. (1954, September). Mass distribution and mass-luminosity ratio in galaxies. The Astronomical Journal, **59***(8), 273–284.*
Sikivie, P. (1996). The Pool-Table Analogy to Axion Physics. Phys.Today, **49***(12), 22.*
Skordis, C. et al. (2006). Large Scale Structure in Bekenstein's theory of relativistic Modified Newtonian Dynamicsucture. Phys. Rev. Lett., **96**, *011301.*
Smirnov, A. Yu. (2003). The MSW effect and Solar Neutrinos. arXiv:hep-ph/0305106.
Smith, M. C. et al. (2007, August). The RAVE Survey: Constraining the Local Galactic Escape Speed. Monthly Notices of the Royal Astronomical Society, **379***(2), 755–772.*
Smoot, George F. et al. (1992). Structure in the COBE differential microwave radiometer first year maps. Astrophys. J., **396**, *L1–L5.*
Soderberg, M. (2009). ArgoNeuT: A Liquid Argon Time Projection Chamber Test in the NuMI Beamline. In Proceedings of the DPF-2009 Conference, Detroit, MI, July 27-31, 2009.
Solovov, V.N, Chepel, V, Lopes, M.I, Hitachi, A, Marques, R Ferreira, and Policarpo, A.J.P.L (2004). Measurement of the refractive index and attenuation length of liquid xenon for its scintillation light. Nuclear Instruments and Methods in Physics Research Section A: Accelerators, Spectrometers, Detectors and Associated Equipment, **516***(2?3), 462 – 474.*
Sorensen, Peter and Dahl, Carl Eric (2011, Mar). Nuclear recoil energy scale in liquid xenon with application to the direct detection of dark matter. Phys. Rev. D, **83**, *063501.*
Spooner, N. J. C. et al. (2011). Optical readout of liquid argon ionisation. Journal of Physics: Conference Series, **308***(1), 012019.*
Steigman, G. (1979, December). Cosmology Confronts Particle Physics. Annual Review of Nuclear and Particle Science, **29**, *313–338.*
Steigman, G. et al. (2012, Jul). Precise Relic WIMP Abundance and its Impact on Searches for Dark Matter Annihilation. Phys.Rev. D, **86***(2), 023506.*
Suzuki, S. et al. (1993). Detection of energy deposition down to the keV region using liquid xenon scintillation. Nuclear Instruments and Methods in Physics Research A, **327**, *203–206.*
Takahashi, T., Konno, S., Hamada, T., Miyajima, M., Kubota, S., Nakamoto, A., Hitachi, A., Shibamura, E., and Doke, T. (1975, Nov). Average energy expended per ion pair in liquid xenon. Phys. Rev. A, **12**, *1771–1775.*
van Albada, T. S. et al. (1985). Distribution of dark matter in the spiral galaxy NGC 3198. Astrophysical Journal, **295**, *305–313.*
van de Hulst et al. (1954). The Spiral Structure of the Outer Part of the Galactic System Derived from the Hydrogen Emission at 21 *cm Wavelength.* Bull. Astr. Inst. Netherlands, **12**, *117–149.*
van de Hulst et al. (1957). Rotation and Density Distribution of the Andromeda Nebula Derived from Observations of the 21-cm line. Bull. Astr. Inst. Netherlands, **14**, *1–16.*
Wadhwa, C.L. (2007). High Voltage Engineering. *New Age International.*
Wolfenstein, L. (1978). Neutrino oscillations in matter. Phys. Rev. D, **17***(9), 2369.*
Yin, P. et al. (2013, July). Pulsar interpretation for the AMS-02 result. Phys. Rev. D, **88**, *023001.*
Zwicky, F. (1933). Spectral displacement of extra galactic nebulae. Helvetica Physica Acta, **6**, *110–127.*